The growth of multilayer systems, consisting of thin oxidic (Ga_2O_3, Al_2O_3) and metallic (Ga, Al, Co, Au) films on Ni(100) and Cu(111) surfaces

Inaugural – Dissertation

zur

Erlangung des Doktorgrades der

Mathematisch-Naturwissenschaftlichen Fakultät

Der Heinrich-Heine-Universität Düsseldorf

vorgelegt von

Yanka Martcheva Jeliazova

aus Dimitrovgrad – Dobritch (BULGARIEN)

August 2002

Gedruckt mit der Genehmigung der Mathematisch-Naturwissenschaftlichen Fakultät der Heinrich-Heine-Universität Düsseldorf

Referent:
Prof. Dr. René Franchy

Korreferent:
Prof. Dr. Klaus Schierbaum

Tag der mündlichen Prüfung:
11.11.2002

„Das Volumen des Festkörpers schuf Gott,
ihre Oberfläche wurde vom Teufel gemacht“

Wolfgang Pauli

На моите родители,
сестра ми,
баба и дядо

To my parents,
my sister,
my grand- ma and pa

Für meine Eltern,
meine Schwester,
Oma und Opa

Contents

Introduction

If one would like to investigate the crystals not only the structure of the bulk is interesting, but also that of the surface, which offers a multiplicity of new aspects. The surface science describes the Interfaces of the solid state and tries to explain the processes, which are found there. It is situated between the physics and the chemistry [1] and adapts one spectrum, which covers the area from the basic research to application problems. An industrial challenge is the manufacturing of smaller and smaller components, and thus surface effects may play an important role.

In general, the oxidation behavior of metal and metal alloys is of great interest [2]. The growth of thin films of metals in the range of 1 – 10 nm is a very active area of research. Thin metal films and their oxides are used, e.g., for gas sensors and microelectronics [3], as high temperature resistant materials [4, 5] and as well they find applications in heterogeneous catalysis [6-8]. Very often the catalytic, electronic, and magnetic properties of thin films made from transition metals differ appreciable from those of the bulk, e.g., due to band hybridization with the substrate or due to boundary layers effects which may dominate the overall behavior of a thin film. The magnetic properties of thin films of the 3d transition metals (1-10 monolayers, ML) [9-11] are of course, of crucial importance for magnetoelectronic structures. The properties of these thin films depend strongly on their surface cleanliness, bulk purity, and physical structure. Thus, the deposition has to be performed under ultrahigh vacuum (UHV) conditions, with the possibility for *in situ* controlling and characterization of the surface structure and composition.

In the past few years, the tunneling magneto resistance (TMR) effect and related phenomena were extensively studied in magnetic tunnel junctions (MTJs) [12, 13], leading to important applications such as magnetic field sensors and magnetic

random access memory (MRAM) [14, 15]. Since Julliere [16] observed the tunneling magneto resistance (TMR) effect with a value of 14% at 4.2 K for the Fe/Ge/Co tunneling junction, different kind of tunneling junctions, such as Ni/NiO/Co [17], Fe/MgO/Fe [18], Ni/Al_2O_3/Co [19], Co/Cu/Co/Al_2O_3/Co[20], NiFe/Al oxide/NiFe [21], CoFe/Al_2O_3/CoFe/MnIr [22], and CoFe and Co or $Ni_{0,8}Fe_{0,2}$ as ferromagnetic films and AlN or Al_2O_3 as a tunnel barrier [23] were investigated. However, in most of these cases, the tunneling magneto resistance effect was very low at room temperature. Moodera et. al [13] and Miyazaki and Tezuka [12], respectively, observed TMR effect over 10% at room temperature in their samples.

Today, thin gallium and aluminium oxide layers are used also as a tunnel barrier between ferromagnetic metal layers in magnetic tunnel junctions (MTJ) [12, 24, 25]. Gallium oxides are used as oxygen sensors at high temperature [26], as well as for the detection of reducing gases [27], it has proven to be also an useful material for many other applications as metal-insulator structures on GaAs [28], and facet coatings for GaAs based lasers [29].

Intermetallic compounds such as transition-metal aluminides and silicides have attracted much attention in resent years, particularly as high-temperature structural materials [30]. Ordered compounds with $L1_2$ structure belong to a group of intermetallic phases and typically, they are formed in alloys of Ni, Fe and Pt. The nickel-containing compounds of the type Ni_3X are the most promising materials for engineering applications due to their excellent mechanical parameters and their corrosion resistance. Binary intermetallic compounds that contain a transition metal and a group-III metal display also interesting electronic and magnetic properties. For instance, Ni_3Al demonstrates weak itinerant ferromagnetism with T_C = 71 K and a very small magnetic moment (0.23 mB per cell) [31] while Ni_3Ga is an exchange enhanced paramagnetic metal [32], and Ni_3In and NiGa are nonmagnetic.

In general, it is very difficult to characterize oxides by means of electron spectroscopies due to the insulating behavior of the oxides. One method to avoid these difficulties of charging is to use ultra thin oxide films instead of bulk oxides

[33]. Experimental studies have shown that oxide films, which are several monolayers thick, simulate bulk samples in many respects [34].

The main goal of this thesis work was to investigate the elementary steps and the bases of the growth and characterization of ultra thin oxide layers (e.g. Al_2O_3 and Ga_2O_3). Thin oxide films between magnetic materials (e.g. Co, Cu, Ni and their alloys) for setting up of multilayer systems are applicable for tunneling junction, thereby the electrical conductivity (tunneling current, electrical resistance) depends on the relative magnetization of the neighbouring magnetic layers. On the other hand the tunneling current is considerably affected by the layer thickness and the band gap (tunnel barrier) of the oxide layer.
The preparation of the oxide layers was performed by deposition of Al and Ga layers on a ferromagnetic substrate and their oxidation with oxygen. At room temperature, amorphous Ga oxide and Al oxide layers are formed which become ordered after annealing at elevate temperatures. The growth of the layers was performed in ultra-high vacuum chambers and for their characterizations the following surface sensitive techniques were used: High-Resolution Electron Energy Loss Spectroscopy (EELS), Auger Electron Spectroscopy (AES), Low Energy Electron Diffraction (LEED) and Scanning Tunneling Microscopy (STM). By means of EELS the vibrational properties as well as the electronic transitions (band gap and metal-semiconductor states) are investigated. LEED and STM give informations about the surface morphology and by means of AES the chemical composition of surface layers could be determined.

The present work is organized as follows: The first four Chapters give an overview of the experimental methods and setups, the magneto resistance effects and some aspects of the film growth. In Chapter 5 an outline of the used materials is presented. Chapter 6 deals with the setup of the evaporation sources. In Chapter 7 the growth and characterization of an ultra thin film of Al_2O_3 on a Cu(111) substrate is described. The growth and properties of ultra thin Ga_2O_3 films on Ni(100) substrate are presented in Chapter 8. The preparation of a TMR – model

system Au/Co/Ga_2O_3/Ni(100) is presented in Chapter 9. Chapter 10 deals with the formation of a Ni_3Ga surface alloy.

Chapter 1

Basic Concepts of the Experimental Methods

1.1 Ultra-High Vacuum (UHV)

To successfully study the properties of a surface on an atomic scale, the surface must be atomically clean for the duration of an experiment. Hence, the rate of arrival of contaminants at the surface must be kept to a minimum for a period of several hours. From the kinetic theory of gases it is relatively straightforward to determine that at a pressure of ~ 1×10^{-6} mbar, a surface will be covered by one monolayer (ML) of a reactive species in around one second, if all incident atoms (molecules) are *adsorb on* the surface (with a sticking coefficient of 1). From an experimental perspective it is clear, that better vacua are required to ensure that samples remain clean on a practical time-scale. At a pressure of around 10^{-9} mbar a monolayer will be adsorbed in a time of the order of a quarter of one hour. It is only since the early 1960s when commercial high-vacuum pumps, stainless-steel vessels and components became available, that the pressure regime known as *ultra-high vacuum* (UHV), of around 10^{-9} - 10^{-11} mbar has been regularly attainable. Such vacua, used in modern surface science, reduce the problems of ambient contamination. Nonetheless, UHV still implies major constraints on the types of experimental work possible. In particular, it is essential to be able to clean the sample surface within the vacuum system to an atomic level. For a general discussion of vacuum physics, the reader is referred to appropriate books [35, 36].

1.2 Surface Science Analytical Techniques

A range of UHV-compatible techniques have been developed over the years to study the properties of the surfaces. These techniques are broadly sensitive to at least one of the following properties of the surface: crystallography, periodicity, morphology, chemical state, elemental composition, vibrational and electronic structure. They may give information on the surface properties over a short range, and may characterize both surfaces and their adsorbates. It is therefore usually necessary to use a combination of two or more techniques to fully characterize the surface. A description of these techniques can be found in the book of Woodruff and Delchar [37]. In this PhD Thesis only those techniques will be briefly reviewed which are used in this study.

1.2.1 High Resolution Electron Energy Loss Spectroscopy (HREELS)

1.2.1.1 Introduction

High resolution electron energy loss spectroscopy (abbreviations HREELS and EELS) relies on the inelastic energy loss of a monochromatic electron beam (of energy 1 – 100 eV with a spread of ~1 – 10 meV FWHM) due to coupling with the long range dipole electric fields induced by excitation of surface vibrations or/and with the vibration of the lattice (phonons) itself. As a result, HREELS is a non-invasive technique; electrons need not even to penetrate the surface (in the dipole scattering regime). Most of the electrons are elastically reflected, i.e. the incident and scattered electrons have the same energy (typically 1 – 15 meV FWHM). On the energy-loss side of the elastic peak, features can be observed due to excitation of surface vibrations (usually < 400 meV). These excitations may occur as a result of adsorbate vibrational modes; however, they may also be due

to collective excitations of the lattice or charge carriers close to the surface (surface phonons and surface plasmons, respectively).

The technique involves interaction of the surface with a monochromatized beam of low energy electrons (E_0 = 1 – 10 eV for dipole scattering and up to few hundreds eV for impact scattering), the energy spread of which should be as narrow as possible. For this reason the technique is often referred to as high-resolution electron energy loss spectroscopy (HREELS). Energy loss results from the excitation of a chemical bond which like a spring possesses a resonant frequency, ν leading to an energy loss equal to hν suffered by electrons of the primary beam (Fig. 1.1.).

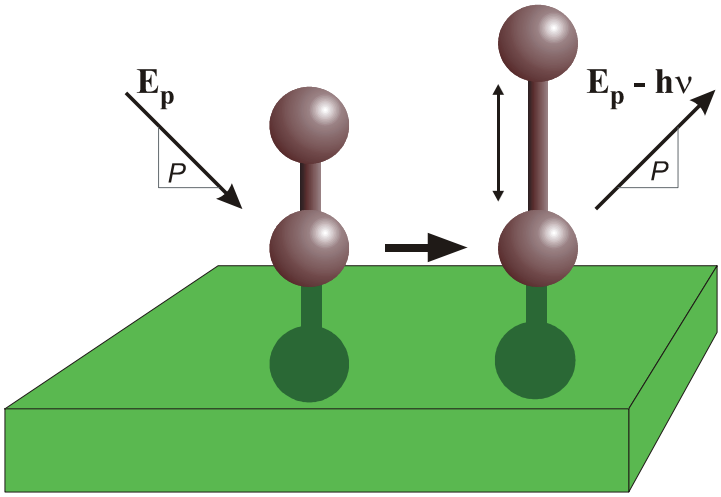

Figure 1.1. Mechanism of a vibrational loss in EELS.

In 1967, Propst and Piper [38] published the first vibrational energy loss spectrum of small molecules (CO, H) chemisorbed on a tungsten surface, significant improvements in the technique particularly concerning resolution were later developed by Ibach [39, 40].

1.2.1.2 Electron Scattering Mechanisms in EELS

There are three basic scattering modes for electrons, each with own selection rules:

- **Dipole scattering** The scattering mechanism of the primary electron beam by the excitation of a vibrational mode is known as dipole scattering and occurs in the specular direction, i.e. equal angles of incidence and excidence. The incident electrons are scattered while they are around 100 Å [41] above the surface. Dipole scattering involves negligible change in the wave vector of the electron thus producing a *"dipole scattering lobe"* sharply centred around the specular direction (Fig. 1.2, see also section 1.2.1.3).

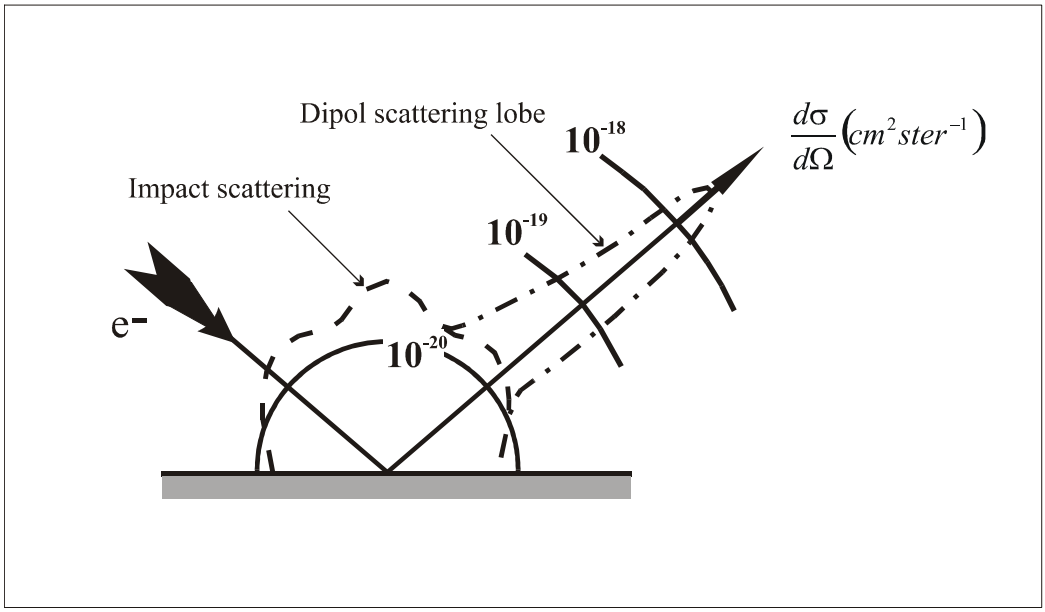

Fig. 1.2. The cross-section of dipole and impact scattering

The excitation of a molecular vibration is achieved with long-range forces and as such every oscillating dipole *on* a metallic surface is accompanied by an image dipole *within* the substrate as shown schematically in Figure 1.3. A dipole perpendicular (or a perpendicular components of a dipole) to the surface will be reinforced by the image dipole effectively doubling the amplitude of the response

and quadrupling the scattering intensity [42]. However, a dipole laying parallel to the surface will be effectively neutralised by the opposite image, thus only those dipoles which have some component perpendicular to the surface will be observed. These are vibrations which belongs to the total symmetric representation of a point group (***A*** and ***A´***).

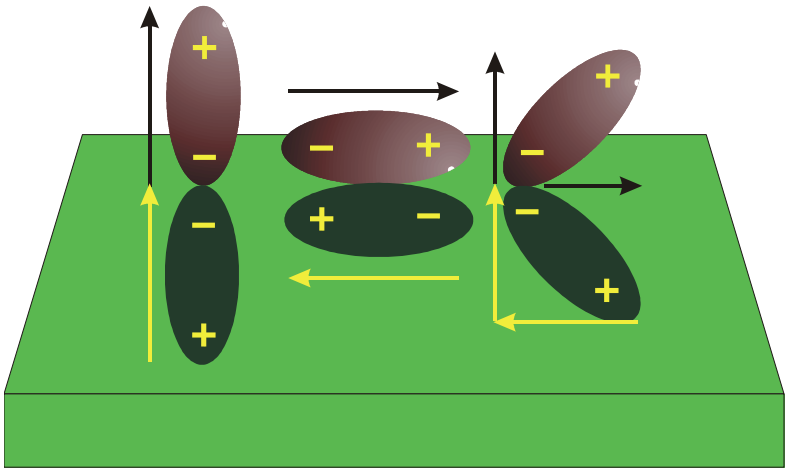

Figure 1.3. Image dipole configurations and the surface normal dipole selection rule on a metallic substrate.

- In **impact scattering**, the incident electrons are scattered by short range interactions on the order of atomic dimensions. This short-range scattering mechanism produces a broad angular distribution of inelastically scattered electrons which are not confined to the dipole scattering lobe (approximately isotropic). Impact and dipole scattering mechanisms can be distinguished therefore by an angular dependent measurement which is performed by moving the detector away from the specular direction. The scattering cross-section varies with incident beam energies. Impact scattering usually has a much lower cross section than dipole scattering and has a less well-developed theory than dipole scattering.

- In **negative ion resonance scattering**, the incident electrons are temporarily captured by empty electronic energy levels of molecules on the surface. The lifetime of one of these states may by femtoseconds to nanoseconds and the electrons are scattered in preferential directions depending on the symmetry of the excited state. Resonance scattering and the formation of short-lived negative ions is well developed in the gas phase. At surfaces, in general, resonance scattering was observed only for weakly bond physisorbed molecules.

1.2.1.3 The Dielectric Theory

A theoretical description of the scattering of electrons from the solid surface offers the dielectric theory, whose in principle approach for the dipole scattering is briefly introduced in the following. In order to provide a better understanding of the observed EEL spectra and the calculations presented in the next sections, we would like to give a short description of the theoretical background. The intense loss (and gain) peaks which are observed in EEL spectra of oxides (or other poorly conducting, ionic materials) are long wavelength optical surface phonons, referred to as Fuchs-Kliewer (FK) phonons [43, 44]. The interaction between the probe electron with wave vector **k** and the sample is dominated by long-range Coulomb fields. The electrons are scattered in the so-called dipole lobe around the specular direction. The maximum of the dipole lobe is located a small angle away from the specular direction [45] and the momentum transfer $\mathbf{q} = \mathbf{k}_{||} - \mathbf{k}'_{\perp}$ ($\mathbf{k}'$ = scattered wave vector) is very small (≈ 0.05 nm^{-1}). The response of the solid sample surface to the external electric field of the probe electron can be described in terms of the so-called surface dielectric response $g(\mathbf{q},\omega)$, with frequency ω of the external electric field.

According to the classical electrodynamics this energy loss per unit volume amounts to [46, 47]

$$W = \int_{-\infty}^{+\infty} dt \int d\mathrm{r} \mathrm{E}(\mathrm{r},t) \cdot \dot{\mathrm{D}} \qquad (1.1)$$

where **E** is the electric field and **D** the electrical displacement. Using the classical scattering probability $P(\mathrm{q}_{\parallel}, \hbar w)$ for transfer of one energy quantum $\hbar w$ and wave vector $\mathrm{q}_{\parallel}$ parallel to the surface, the total loss of energy will be:

$$W = \int \hbar w \, P(\mathrm{q}_{\parallel}, \hbar w) \, d\mathrm{q}_{\parallel} \, d\hbar w \tag{1.2}$$

After calculation of (1.1) we obtain the classical scattering probability [46]

$$P(\mathrm{q}_{\parallel}, \hbar w) = \frac{e^2}{2p^3 e_0 \hbar^2} \frac{q_{\parallel} v_{\perp}^2}{\left[(q_{\parallel} v_{\perp})^2 + (\mathrm{q}_{\parallel} \cdot \mathrm{v}_{\parallel} - w)^2\right]^2} \mathrm{Im}\left\{-\frac{1}{e(w)+1}\right\} \tag{1.3}$$

where $v_{\parallel}$ and $v_{\perp}$ are the parallel and perpendicular components of the velocity of the electrons. For the dipole scattering the loss of energy is much smaller than the primary energy, thus

$$\hbar w << E_0 \tag{1.4}$$

generally well performed. Including the energy and momentum conservation the differential scattering cross section are computed in the form [46]

$$\frac{d^2 S}{d(\hbar w) d\Omega} = \frac{m_e^2 v_{\perp}^2 e^2 |R|^2}{2p^3 e_0 \hbar^4 \cos q} P(\mathrm{q}_{\parallel}, \hbar w). \tag{1.5}$$

The differential cross-section indicates the number of electrons, which are scattered with an energy loss $\hbar w$ into a solid angle $d\Omega$. The additionally introduced reflection coefficient R in the equation (1.5) implies that not each electron is reflected, but a part penetrates into the solid state and it is measurable as a sample current. For the practical computation of EEL spectra in the equation (1.5) must be integrated the acceptance angle of the analyser $\Omega_{aperture}$ of the EEL - spectrometer. The dielectric scattering of electrons of small energy is essentially characterized by the so-called surface energy loss function (see equation 1.3)

$$\mathrm{Im}\left\{-\frac{1}{e(w)+1}\right\} \tag{1.6}$$

and the kinematic prefactor

$$\frac{q_{\parallel} v_{\perp}^2}{\left[(q_{\parallel} v_{\perp})^2 + (\mathrm{q}_{\parallel} \cdot \mathrm{v}_{\parallel} - w)^2\right]^2} \tag{1.7}$$

The surface energy loss function specifies the fundamental spectral structure of the loss spectra. The kinematic prefactor has the structure of a resonance term. In the case of granzing incidence $\left(v_{\perp} << v_{\parallel}\right)$, the prefactor shows a sharp maximum of the scattering probability if the following resonance condition is fulfilled:

$$\frac{w}{q_{\parallel}} = v_{\parallel} \tag{1.8}$$

For realistic values one receives the preferential scattering of the electrons into a small angle (1 - 2°) around the specular direction [46, 47]. The maximum of the dipole cone is shifted due to the wave vector transfer to a little smaller angles.

The equation of the differential scattering cross section (equation (1.5)), deduced in the classical approximation, differs from that obtained on the basis of a quantum-mechanical approach only with a Bose factor.

$$\left[1 + n\left(\hbar w\right)\right] = 1 + \left[\exp\left(\frac{\hbar w}{k_B T}\right) - 1\right]^{-1} \tag{1.9}$$

[41, 46]. Thereby multiple scattering and energy gains are considered in the description.

1.2.2 Auger Electron Spectroscopy (AES)

Auger Electron Spectroscopy (*Auger spectroscopy* or AES) was developed in the late 1960's. It is a surface specific technique utilizing the emission of low energy electrons in the *Auger process* and is one of the most commonly employed surface analytical techniques for determining the chemical composition of the surface layers of a sample.

Auger electron spectroscopy (AES) gives surface compositional information integrated over a depth of two to ~ 10 atomic layers. A beam of primary electrons (typically 3 – 5 keV in energy) is incident to the sample surface and an energy-resolving detector is used to record the energy spectrum of electrons ejected from the surface.

The basic Auger process starts with removal of an inner shell electron to form a vacancy. Several processes are capable of producing the vacancy, but bombardment with an electron beam is the most common. The inner shell vacancy is filled by a second electron from a higher shell. Energy must be simultaneously released. A third electron, the Auger electron, escapes carrying the excess energy in a radiationless process. The process of an excited ion decaying into a doubly charged ion by ejection of an electron is called Auger process. Alternatively, X-ray photon removes the energy. If, for example, a K-level electron is ejected by the primary beam, than L-level electron drops into the vacancy, and another L-level electron is ejected. Such a process is called KLL transition.

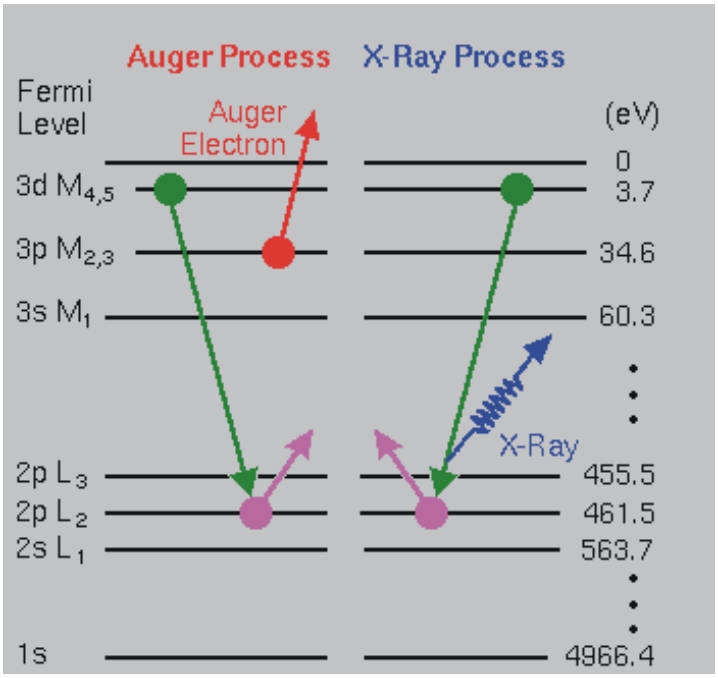

Figure 1.4. Illustration of the Auger process ($E_{kin} = E_{L_2} - E_{M_{4,5}} - E_{M_{2,3}} - \Delta E$), where D*E* is a correction term [48].

Figure 1.4 illustrates two competing paths for energy dissipation with titanium as an example. The kinetic energy of the electron of the illustrated $L_2M_{4,5}M_{2,3}$

transition is ~ 423 eV ($E_{AES} = E_{L2} - E_{M4} - E_{M3} - \Delta E$) and the X-ray photon energy is ~ 457.8 eV ($E_{hv} = E_{L2} - E_{M4}$). ΔE is a correction term which describes the many electron effects, related to the rearrangement of the electrons after excitation.

Auger spectroscopy can be considered as involving three basic steps :

- Atomic ionization (by removal of a core electron)
- Electron emission (the Auger process)
- Analysis of the emitted Auger electrons.

The last stage requires the analysis of the kinetic energies of the emitted electrons with high sensitivity.

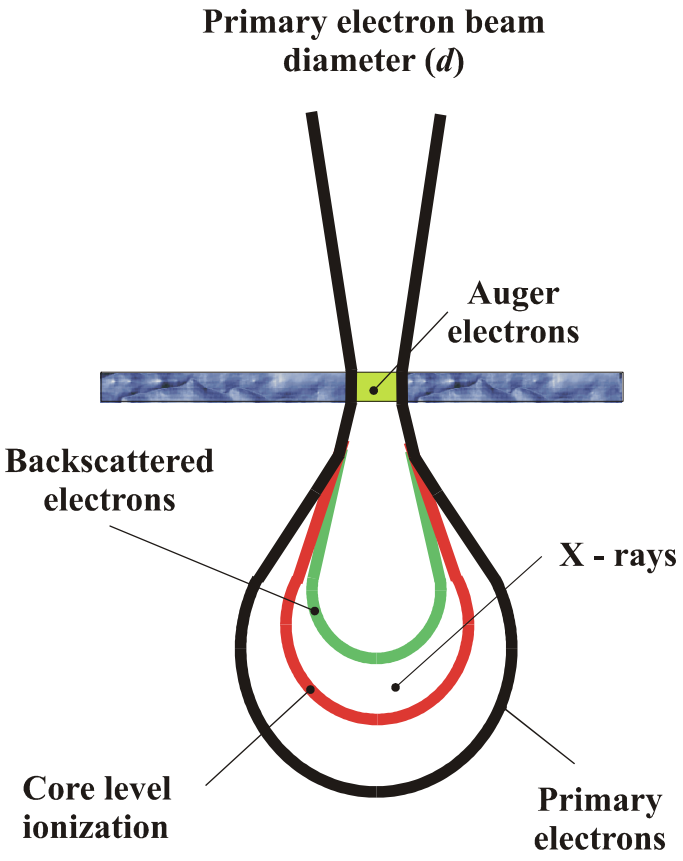

Fig.1.5. Distribution (schematic) of primary, backscattered and Auger electrons together with emitted X-rays.

Fig. 1.5 shows schematically the distribution of electrons, i.e. primary, backscattered and Auger electrons together with the emitted characteristic X-rays under electron bombardment. Under the typical experimental conditions the latter have a larger escape depth due to a much smaller ionization cross section with the matter, i.e. a higher probability to escape matter. Auger electrons with energies up to 2000 eV, however, have a high probability to escape only from the first few monolayers because of their restricted kinetic energy. Consequently, they are much better suited for surface analysis.

Before leaving the crystal, the electrons have to pass a certain amount of material. Thus, the AES intensity ***I*** of the observed signal outside the film depends on the mean free path λ (IMFP) of electrons depending on their particular energy. The AES process can be used to determine the growth mode and the thickness of a deposited layer. In order to determine the AES intensity as a function of film thickness, the growth mechanisms are to be considered. For layer-by-layer growth the change of the AES intensity d***I*** is related to the change dh in the film thickness by

$$\frac{dI}{I} = -\frac{dh}{l} \tag{1.10}$$

During film growth, the intensity of the film material depends in an approximation exponentially on the coverage

$$\frac{I^F}{I_\infty^F} = 1 - \exp\left(\frac{-h}{l}\right) = 1 - \exp\left(\frac{-q'd}{l}\right) \tag{1.11}$$

where I_∞^F is the intensity measured on bulk film material, and q' the number of monolayers (thickness of monolayers, *d*). The intensity originating from substrate atoms after deposition of q' monolayers is then

$$\frac{I^s}{I_0^s} = \exp\left(\frac{-q'd}{l}\right) \tag{1.12}$$

where I_0^s is the intensity of the signal originating from the substrate material without any deposited film. During the film growth of a monolayer, the intensity changes linearly with q'. But, the envelope of the curves being composed of several linear pieces is to a good approximation, given by an exponential function [46].

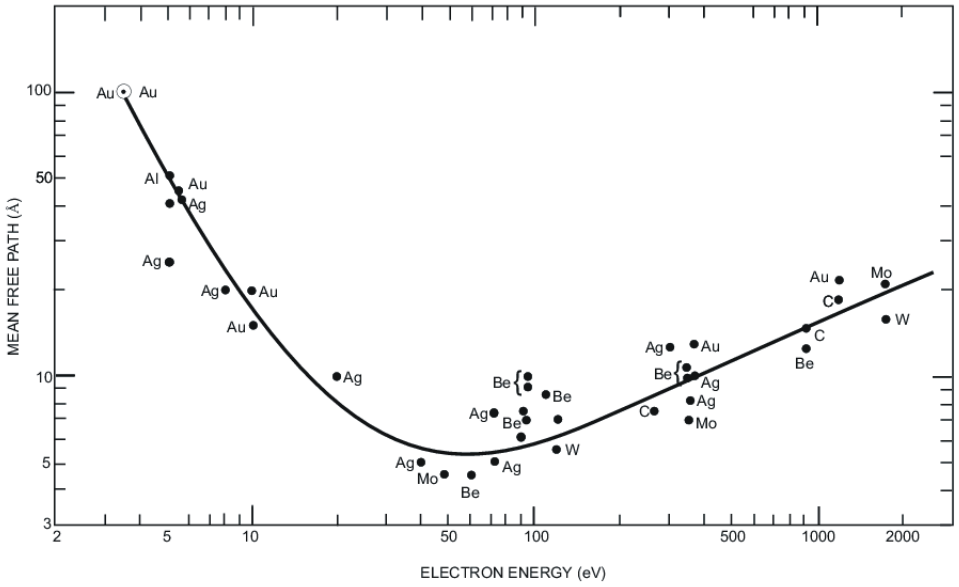

Fig. 1.6. The inelastic electron mean free path (escape depth) is plotted versus initial kinetic energy [49].

The mean free path of electrons depends on their kinetic energy. Fig. 1.6 shows this dependence, the so called “universal curve”. For electron energies between 50 and 3000 eV, the IMFP of electrons varies from ~5 to ~25 Å. For elements IMFP depends on the electron energy as [50]:

$$l = \frac{538}{E^2} + 0.41(a \cdot E)^{1/2} \qquad (1.13)$$

and for inorganic compounds the relation is

$$l = \frac{2170}{E^2} + 0.72(a \cdot E)^{1/2} \qquad (1.14)$$

where the parameter *a* is given by:

$$a = \sqrt[3]{\text{volume of an atom}} = \sqrt[3]{\frac{\text{unite cell volume}}{\text{number of atoms per unit cell}}} \qquad (1.15)$$

1.2.3 Low Energy Electron Diffraction (LEED)

Low energy electron diffraction (or LEED) [51] gives information on the long-range translational periodicity of a surface. Electrons are accelerated through a potential of around 50 – 200 eV, and are directed onto the surface at normal incidence. The elastically scattered (diffracted) electrons hit a hemispherical phosphorescent screen, forming a diffraction pattern of spots representing the reciprocal lattice.

LEED may also be used quantitatively, whereby the intensities of the diffraction spots are measured as a function of incident electron energy, typically over a range of about 40 - 300 eV. This quantitative LEED technique is known as LEED I-V analysis. The determination of the structure is only possible by comparison with simulations of I-V curves for each diffracted spot and for a range of possible models using a calculated reliability factors (*R-factor*) analysis.

By the principles of wave-particle equality, the beam of electrons may be regarded as a succession of electron waves incident normally on the sample. These waves will be scattered by regions of high localized electron density i.e. the surface atoms, which can therefore be considered to act as point scatters. The wavelength of the electrons is given by the de Broglie relation $l = h/mv$. In the case of wave scattering at an periodic array in one dimension, constructive

interference takes place when the scattered waves from neighboring lattice points have “path difference” (pd) of multiples of the wavelength λ. By considering a one dimensional (1-D) chain of atoms (with atomic separation *a*) and an electron beam incident at angle j_0 to the chain, interference of the backscattered waves occurs in directions j (Fig. 1.7), where j is given by the condition

$$a(\sin j - \sin j_0) = n l \,, \qquad (1.16)$$

where *n* is integer denoting the order of diffraction.

An arrangement of lattice points which is periodic in two dimensions may be considered as an ensemble of parallel rows of scatters with directions $[h'k']$ and mutual distance $d_{h'k'}$. In this case the interference maxima are to be expected in direction given by

$$n l = d_{h'k'}(\sin j - \sin j_0). \qquad (1.17)$$

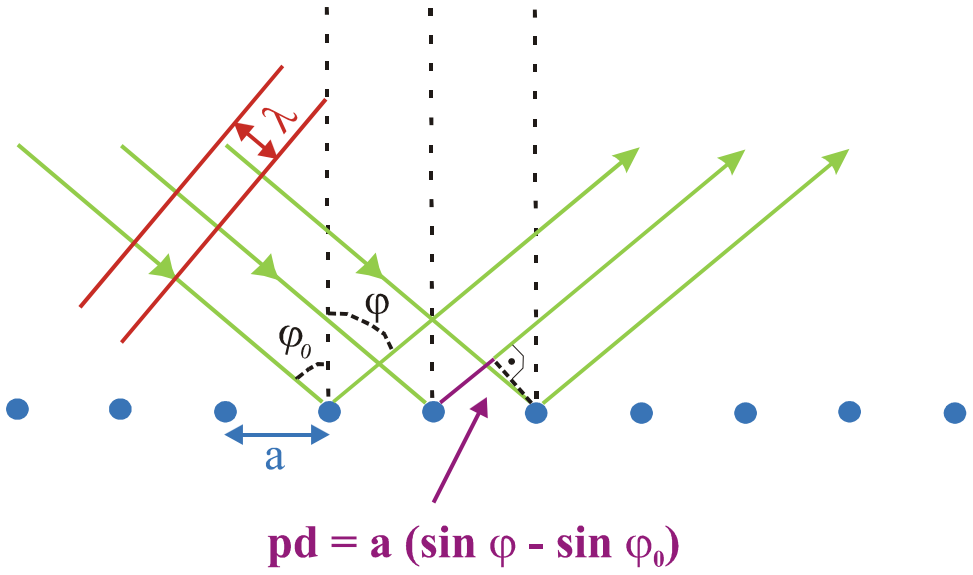

Fig.1.7. Scattering of a plane wave at a one-dimensional periodic lattice.

For normal incidence to the surface $(j_0 = 0)$, as is frequently the case of LEED experiments, equation (1.17) becomes

$$\sin j = \frac{n l}{d_{h'k'}}.$$

A much better method of looking at LEED diffraction patterns involves the concept of reciprocal space: more specifically, it can be readily shown that – *"The observed LEED pattern is a (scaled) representation of the* ***reciprocal net*** *of the pseudo-2D surface structure"*

The *reciprocal net* is determined by the reciprocal basis vectors $\bar{a}_1^*, \bar{a}_2^*$ which are defined by the equations

$$\bar{a}_i \cdot \bar{a}_j^* = d_{ij}(i, j = 1,2): \qquad (1.18)$$

where $\bar{a}_i$ represents the basis vectors of the real surface structure. The Kronecker symbol $d_{ij} = 0$ if $i \neq j$, and $d_{ij} = 1$ if $i = j$, i.e. $\bar{a}_1^* \perp \bar{a}_2, \bar{a}_2^* \perp \bar{a}_1$.

Considering this definition: $\bar{a}_1^*$ is perpendicular to $\bar{a}_2$ (Fig.1.8), and the length a_1^* is derived from the condition $\bar{a}_1 \cdot \bar{a}_1^* = 1$. Hence, $a_1 \cdot a_1^* = \left[\cos\left(\frac{p}{2} - g\right)\right]^{-1}$, where γ is the angle between $\bar{a}_1$ and $\bar{a}_2$, or

$$a_1^* = 1/a_1 \sin g \ . \qquad (1.19)$$

By analogy $a_2^* = 1/a_2 \sin g$, where $\bar{a}_2^* \perp \bar{a}_1$. The angle γ^* between a_1^* and a_2^*, is given by $g^* = g + 2\left(\frac{p}{2} - g\right) = p - g$, which means $\sin g^* = \sin g$.

If a surface structure with basis vectors $\bar{b}_1$ and $\bar{b}_2$ is superimposed on a substrate lattice with the vectors $\bar{a}_1, \bar{a}_2$, then both lattices $\bar{a}$ and are related by

$$\begin{aligned} \bar{b}_1 &= m_{11}\bar{a}_1 + m_{12}\bar{a}_2 \\ \bar{b}_2 &= m_{21}\bar{a}_1 + m_{22}\bar{a}_2 \end{aligned} \qquad (1.20)$$

The reciprocal lattice $\bar{b}^*$ is related to the reciprocal lattice $\bar{a}^*$ in a similar manner:

$$\begin{aligned} \bar{b}_1^* &= m_{11}^*\bar{a}_1^* + m_{12}^*\bar{a}_2^* \\ \bar{b}_2^* &= m_{21}^*\bar{a}_1^* + m_{22}^*\bar{a}_2^* \end{aligned} \qquad (1.21)$$

The coefficients m_{ij}^{*} may be obtained from an inspection of the diffraction pattern formed on the LEED screen. The coefficients of the two matrices are related by the following equations:

$$m_{11} = \frac{m_{22}^{*}}{m_{11}^{*}m_{21}^{*} + m_{21}^{*}m_{12}^{*}} \tag{1.22}$$

$$m_{12} = \frac{-m_{21}^{*}}{m_{11}^{*}m_{21}^{*} - m_{21}^{*}m_{12}^{*}} \tag{1.23}$$

$$m_{21} = \frac{-m_{12}^{*}}{m_{11}^{*}m_{21}^{*} - m_{21}^{*}m_{12}^{*}} \tag{1.24}$$

$$m_{22} = \frac{m_{11}^{*}}{m_{11}^{*}m_{21}^{*} - m_{21}^{*}m_{12}^{*}} \tag{1.25}$$

so that when the ones of the matrix is known the others may be readily calculated.

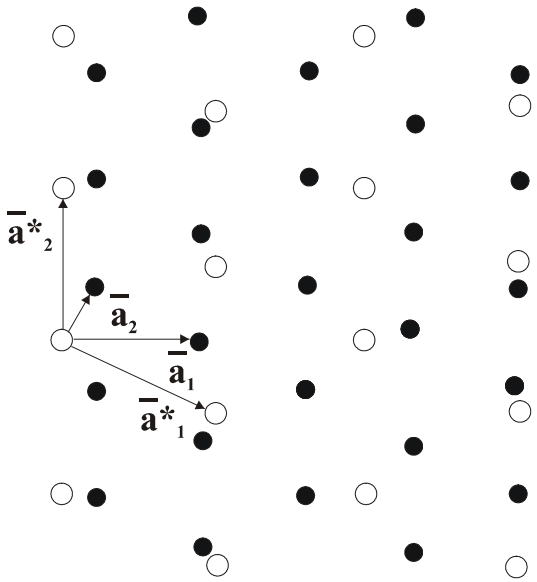

Figure 1.8. A two-dimensional real lattice(dark circles), described by the vectors $\bar{a}_1$, $\bar{a}_2$, and its reciprocal lattice (open circles), described by the vectors $\bar{a}_1^{*}$, $\bar{a}_2^{*}$.

1.2.3 Scanning Tunneling Microscopy (STM)

New techniques for studying surface structure have been developed and have become widely used within the last fifteen years. There are the Scanning Probe Microscopy (SPM) that originated with the device developed by Bining and Rohrer around 1980, the Scanning Tunneling Microscopy (STM) [52-54].

The “observation” of individual atoms has become a commonplace event in many modern laboratories. The consequence of this is the application of SPM techniques across a broad spectrum of scientific research, from biological processes to solid state physics.

Scanning tunneling microscopy (STM) is a technique reliant upon the wave-like nature of electrons. If two conductors are brought close together (to a separation of the order of around few Å) and a potential applied between them, then the overlap of the electron wave functions permits quantum mechanical tunneling and a current flow across the gap.

The main differences between the STM and all other microcopies are that there is no need for lenses and special light or electron sources. Instead the electrons (in empty or filled states) already existing in the sample and tip under the investigation serve as the exclusive source of excitation [55].

The tunneling current I_t (which was first described by Fowler and Nordheim in 1928 [56]) through the potential barrier between a surface and a probing metal tip (Fig. 1.9a), usually made of W- or PtIr-wires, sets the fundamental basement of STM. If a small bias is applied between the sample surface and the tip (in the best case, an atomically sharp tip), a tunneling current will flow between these when the gap between them is reduced to a few atomic diameters (Fig. 1.9b). The key point resides on the strong dependence of the tunneling current probability of electrons on the electrode separation. The tunneling current (at low bias voltage V_t) behaves as [55]:

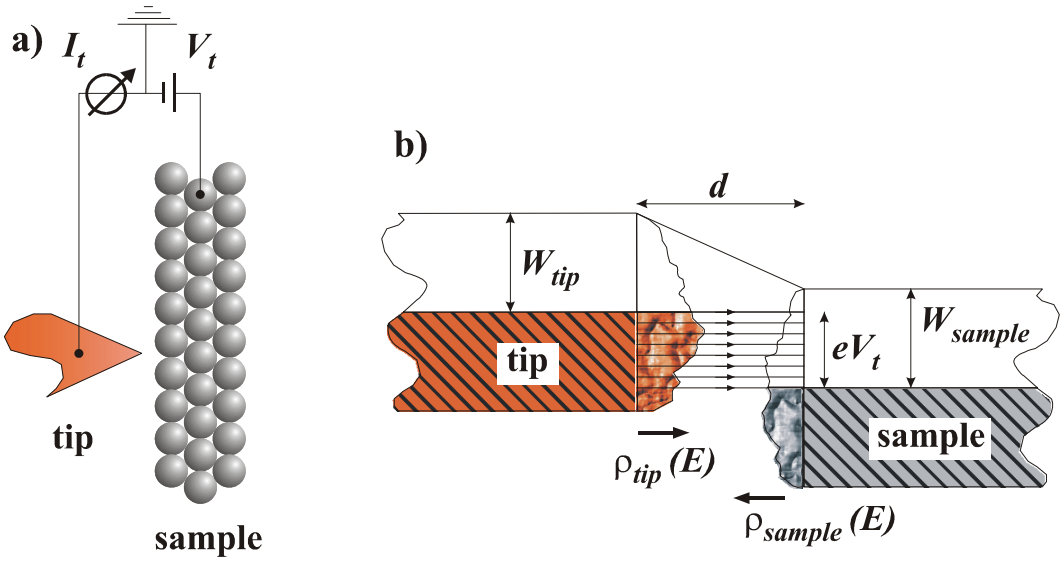

Fig. 1.9. (a) The principle of STM. (b) The corresponding potential energy diagram.

$$I_t = 18 \cdot \frac{V_t}{10^4\,\Omega} \cdot \frac{k}{d} \cdot A_{eff} \cdot e^{-2kd} \qquad (1.26)$$

where $2k\left[\text{Å}^{-1}\right] = 1.025 \cdot \sqrt{\Phi}\left[eV\right]$, F is the average work function, assumed equal to the mean barrier height between the two electrodes. $A_{eff} = p \cdot \left(L_{eff}/2\right)^2$ is the effective area determining the lateral resolution $L_{eff} \approx 2 \cdot \left(\left(R_{tip} + d\right)/k\right)^{1/2}$ which applies when the separation *d* becomes smaller than the radius R_{tip} of the tip. For typical metals $\left(\Phi \approx 5eV\right)$ I_t change by one order of magnitude for a change of ~ 1 Å of the separation distance.

In the case of a positively biased sample (as in the Fig. 1.9b), the net current comes from electrons tunneling from occupied states in the tip to unoccupied states of the sample. The current per energy unit, *i*, is represented by the density of horizontal arrows in Fig. 1.9b. It is intuitively clear from Fig. 1.9b, that the tunneling current depends on the density of occupied and unoccupied states of the tip and sample (ρ_{tip} and ρ_{sample}) respectively. Compared to the "classical"

tunneling model, from which equation (1.24) has been derived, the exact calculation of the tunneling current starting from the electronic structures of the tip and of the sample is a difficult task.

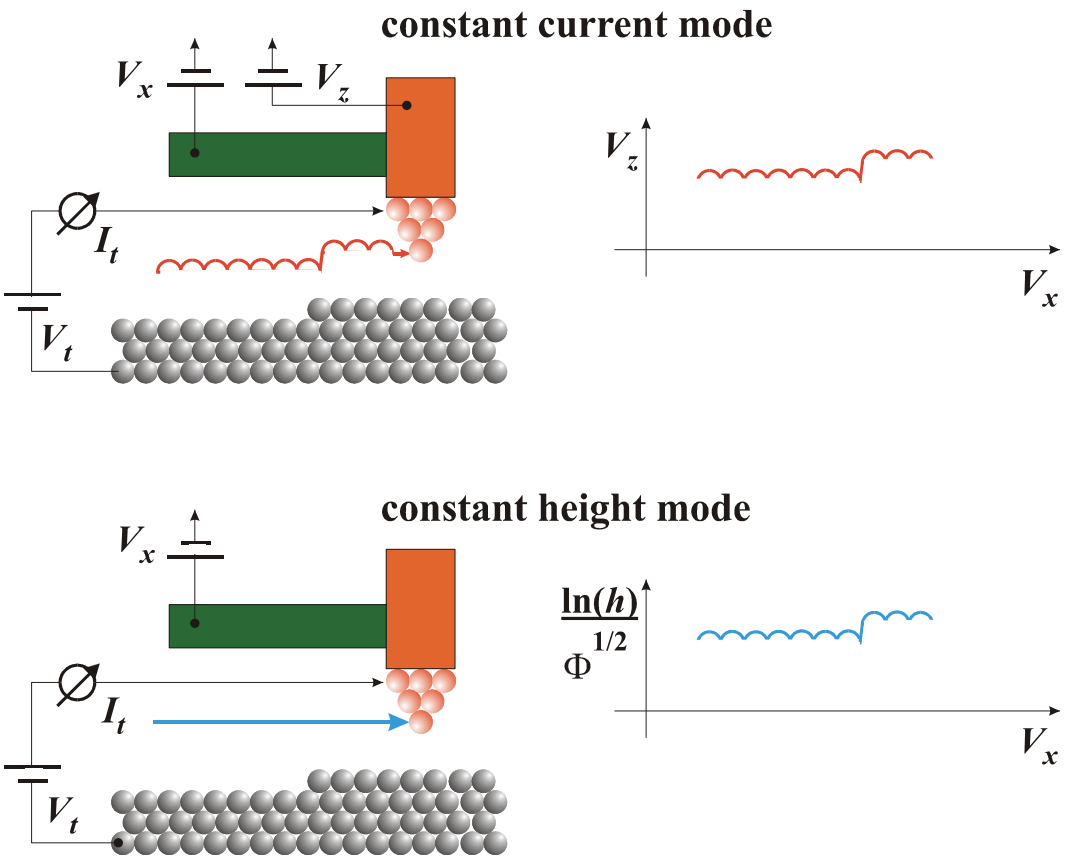

Fig. 1.10. The two operation modes of STM. I_t is the tunneling current, V_t – the bias voltage, V_z – the feedback voltage controlling the tip height along the z-direction and V_x – the voltage applied to the x-piezo.

As a consequence, the tunnel current is very sensitive to height difference. The tip is mounted on a piezoelectric tube to allow scanning with atomic scale precision. During scanning, the tunnel current is kept constant by changing the distance between tip and surface using a negative feed back system. The changes in the height are recorded by a data system and a topographical image of the surface is obtained. This mode is called *constant current imaging (CCT)*. It is also possible to keep the height between the tip and the surface constant, and to measure the changes in the tunnel current during the scan. This is called *constant height imaging*, as shown on Fig. 1.10.

Chapter 2

Magneto Resistance Effects and Magnetic Multilayer Systems

This thesis deals with the growth and characterization of multilayer systems for the magnetoelectronics. The main goal was not to grow devices for the magnetoelectronic, rather to find conditions for the growth of well defined (well-ordered, crystalline) layers and the characteristics of the individual layers which are used in multilayer systems. Therefore, a brief introduction of the two most important magneto resistance effects (GMR – giant magneto resistance and TMR – tunneling magneto resistance) is presented in this section.

Recently the interest in magnetic random access memory (MRAM) devises has been renewed with the possibility of using spin-dependent tunnel junction as a memory cell element [57-62]. MRAM possesses the attractive properties of nonvolatility, radiation hardness, nondestructive readout, low voltage, and unlimited read and write endurance. MRAM devices have been fabricated using the anisotropic magneto resistance (AMR) effect, finding niche markets in satellite and military applications [63] due to comparatively poor performance. With recent advances in GMR and TMR materials higher signal levels became available and a renewed interest has arisen in MRAM fabrication. By replacing AMR cell structures with GMR cell structures has some obvious advantages such as larger signals because of the higher magnetoresistive (MR) values. The larger

signals can lead to a faster read time. In order to achieve reasonable memory array density, many GMR cells have to be connected.

2.1 The Giant Magneto Resistance (GMR) Effect

The observation of the giant magneto resistance (GMR) effect has given rise to immense experimental and theoretical effort to understand the origin of GMR. The understanding of the intrinsic fundamental physical phenomena and the study of these artificial superstructures will lead to the next generation of electronic devices. The GMR effect was independently discovered in 1988 by P. Grünberg (Jülich) [64] and A. Fert (Paris) [65]. By changing the relative magnetization of the ferromagnetic layers a large resistance change was observed. A GMR devise consists of a stack of several alternating very thin layers (ferromagnetic and nonmagnetic) of various metallic elements, each of which is only a few nanometres thick (Fig. 2.1). The coupling of adjacent ferromagnetic layers leads to an antiparallel alignment of the magnetization, if the thickness of the spacer layer (non magnetic) is chosen properly.

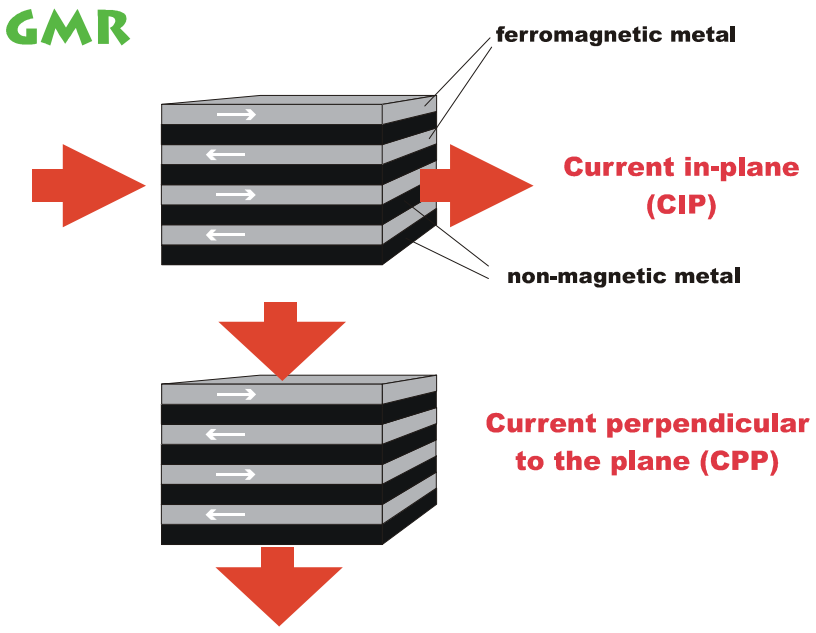

Fig. 2.1. Giant magneto resistance effect.

An external magnetic field can override this coupling, decrease the angle between the magnetic alignments, which in turn reduces the electrical resistance. Fig. 2.1 shows the two different configurations “current in plane” (CIP) and “current perpendicular to the plane” (CPP), respectively, for which the GMR effect can be observed. The origin of the effect lies in the spin-dependent transmission of conduction electrons between the magnetic layers through the nonmagnetic spacer. The effect increases with the number of ferromagnetic and nonmagnetic layers. The effect is observed in antiferromagnetically coupled layers, as well as systems where an antiparallel alignment is achieved by other means, such as exchange biasing of one magnetic layer by an antiferromagnet. Also magnetic clusters in a nonmagnetic matrix or combinations of layers and clusters display a GMR effect. GMR sensors are used in the latest-generation read heads for magnetic hard disks and spin valves [66].

2.2 The Tunneling Magneto Resistance (TMR) Effect

A TMR system consists in two ferromagnetic layers which are separated by an insulating layer (tunnel barrier). Such junctions exhibit a magnetic field dependent tunneling resistance and have a great potential for applications both in the digital storage and magnetic sensor technologies [13, 16, 67]. A simple model of a TMR structure (Fig. 2.2) relates the tunneling probability to the relative orientation of the magnetization in the two ferromagnetic (FM) layers, and the magneto resistance (MR) can in this model be expressed in terms of the electron spin polarizations

$$P_i = \frac{n_{i,up} - n_{i,down}}{n_{i,up} + n_{i,down}}, \qquad (2.1)$$

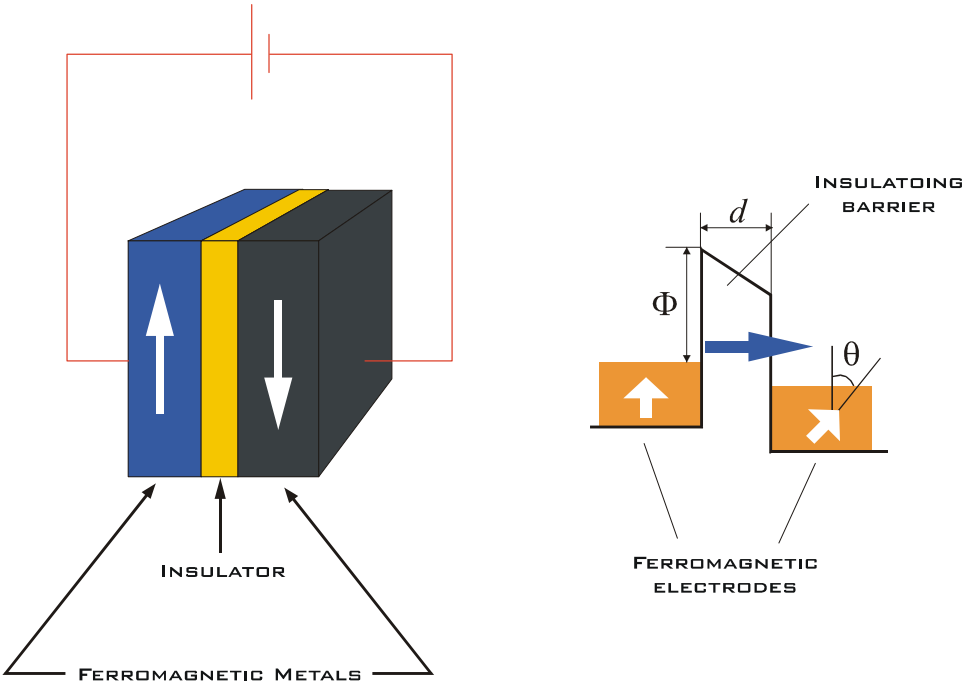

Fig. 2.2. Model of Tunneling Magneto Resistance (TMR).

where $n_{i,up}\left(n_{i,down}\right)$ is the density of states at the Fermi energy for majority (minority) electrons of the FM_i electrode; a larger spin polarization yields a larger magnetoresistive effect.

The tunneling probability T depends on the height of the tunneling barrier Φ and its width d:

$$T \propto \exp\left(-4p\frac{\hbar}{l}\right), \qquad \text{where } l = \frac{\hbar}{\sqrt{2m\Phi}} \tag{2.2}$$

Consequently, also the density of the tunneling current depends exponentially on d and $\sqrt{\Phi}$ [68]. From this arise the requirements on the quality of the tunneling barrier which has to be a fully closed, homogeneous insulator layer (usually an oxide) with an uniform thickness in the order of about 1 – 2 nm. Only then, the electrons can tunnel through the barrier, an entirely quantum-mechanical transport process. The magnetic alignment of one layer (weak magnetic layer) has to be changed without affecting the other. There is not a spin-dependent scattering like

at GMR, but there is a spin-dependent tunneling between the two electrodes. For both the GMR and TMR effects the amplitude of the MR-effect is given by [69]:

$$\frac{\Delta R}{R} = \frac{R_{\uparrow\downarrow} - R_{\uparrow\uparrow}}{R_{\uparrow\uparrow}} \qquad (2.3)$$

$R_{\uparrow\downarrow}$ and $R_{\uparrow\uparrow}$ indicate the electrical resistance of the layer system at antiparallel and, respectively, parallel magnetization of the FM electrodes.

Fig. 2.3 shows a typical TMR-curve [70]. For the parallel magnetization of the two FM electrodes a small resistance is obtained, while for the antiparallel magnetization an increase of ~ 16% is observed. This TMR-curve was found for a Co-Al_2O_3 – permalloy system [70].

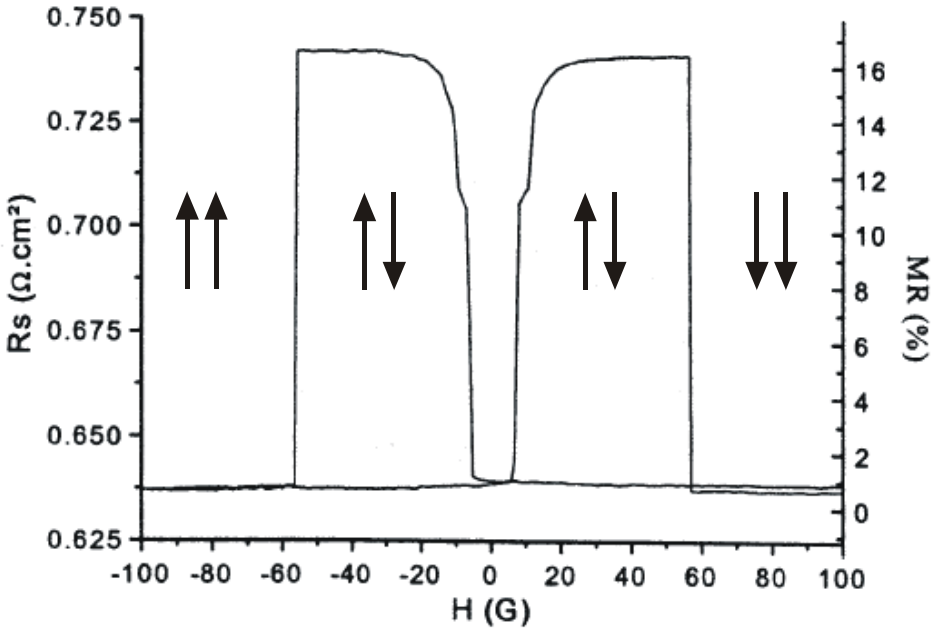

Fig. 2.3. $\Delta R/R$ **measurements as a function of the magnetic induction** $\mu_0 H$ **in a Co-Al_2O_3 - permalloy TMR structure** [70]**.**

Although in most cases the term TMR is associated with memory cells (MRAMs) it has a similar technological potential as spin valve systems. The advantage is the typically higher resistance of TMR elements compared to that of spin valves. The high requirements on the quality of the tunnel barrier ask for a very good control of its preparation process.

Chapter 3

Aspects of the Film Growth

When atoms of a material A are deposited on another material B then a film of A grows on B. The following questions arise:

- What happens when a single atom arrives on the substrate surface?
- How do they move on the surface?
- How to explain their behavior to form islands?
- What happens when the surface is exposed to oxygen?

The answer of all this questions can be found behind the well understanding of thermodynamics, diffusion, nucleation, growth and oxidation processes on the surface.

3.1 Thermodynamics

Thermodynamics parameters are used in order to be understand qualitatively the macroscopic processes of the film growth.

- **Surface free energy and modes of the film growth**

The surface free energy is an important parameter for the thermodynamic classification of the growth modes (which will be discussed below). Bauer [71] introduced a classification of the growth modes on the base of the balance of interfacial and surface free energy. Bauer's criterion, the so called wetting condition, is given by [72]:

$$\Delta g = g_F + g_S - g_{S/F} \qquad (3.1)$$

where g_S is the surface tension of the *substrate/vacuum* interface, g_F that of the *film/vacuum*, and $g_{S/F}$ that of the *substrate/film* interface. Eq. (3.1) gives a formal distinction of the three growth modes depending of Δg. If $\Delta g \leq 0$, i.e. "wetting" of the surface by the deposited film takes place and a two-dimensional (2D) growth occurs. For $\Delta g \geq 0$, the "wetting" condition is no longer fulfilled and several layers grow simultaneously which results in a three dimensional (3D) growth.

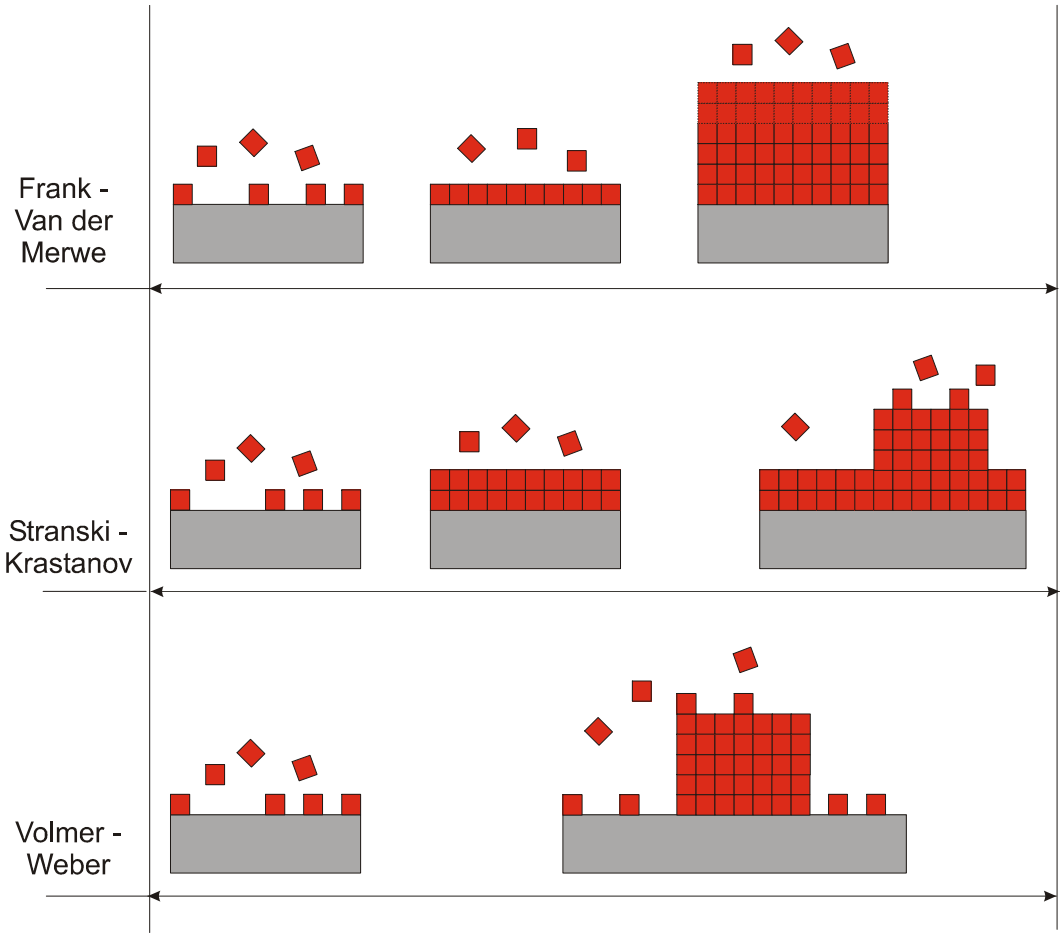

Fig. 3.1. Schematic view of the three topologically distinct growth modes [73].

Fig. 3.1. shows a schematic representation of the common modes of growth one observes under typical deposition conditions (MBE, MOCVD, etc.). In the *layer-by layer* growth mode (Frank – Van der Merwe (FM)) the interaction between the substrate and layer atoms is stronger than that between neighboring layer atoms. Each new layer (n) starts to grow only when the last one (n – 1) has been completed. The opposite case, in which the interaction between neighboring atoms exceeds the overlayer substrate interaction, leads to *island growth* (Volmer – Weber (VW)). In this case an island deposit always means a multilayer conglomerate of adsorbed atoms.

The *layer-plus-islands* growth mode (Stranski – Krastanov (SK)) is an interesting intermediate case. After formation of one, or sometimes several complete monolayers, island formation occurs; 3D islands grow on top of the first full layer(s). Many factors might account for this mixed growth mode: A certain lattice mismatch between the substrate and deposited film may not be able to be continued into the bulk of the epitaxial crystal. Alternatively, the symmetry or orientation of the overlayers with respect to substrate might be responsible for producing this growth mode.

From a thermodynamical point of view, a simple distinction between the conditions for the occurrence of the various growth modes can be made in terms of surface or interface tension, i.e. the characteristic surface free energy γ (per unit area) to create an additional piece of surface or interface. Since γ can also be interpreted as a force per unit length of boundary, force equilibrium at a point where substrate and a 3D island of the deposited film touch (Fig. 3.2) requires

$$g_S = g_{S/F} + g_F \cos f\,, \qquad (3.2)$$

where g_S is the surface tension of the *substrate/vacuum* interface, g_F that of the *film/vacuum*, and $g_{S/F}$ that of the *substrate/film* interface. Using (3.2) then two limiting growth modes, *layer-by-layer* (FM) and *islands* (VW), can be distinguished by the angle f, i.e.

layer-by-layer growth: $\quad f = 0\,, \quad g_s \geq g_F + g_{S/F}\,;$ (3.3a)

island growth: $f > 0$, $g_s < g_F + g_{S/F}$; (3.3b)

f represents the angle between the surface plane and the direction of g_F (see Fig. 3.2). The mixed Stranski-Krastanov growth mode can easy be explained in this picture by assuming a lattice mismatch between deposited film and substrate. The lattice of the film tries to adjust to the substrate lattice, but at the expense of elastic deformation energy. The transition from *layer-by-layer growth* to *island growth* occur when the spatial extent of the elastic strain field exceeds the range of the adhesion forces within the deposited material. The relations (3.3) are not complete if one do not considers the equilibrium condition for the whole system including the gas phase above the deposited film.

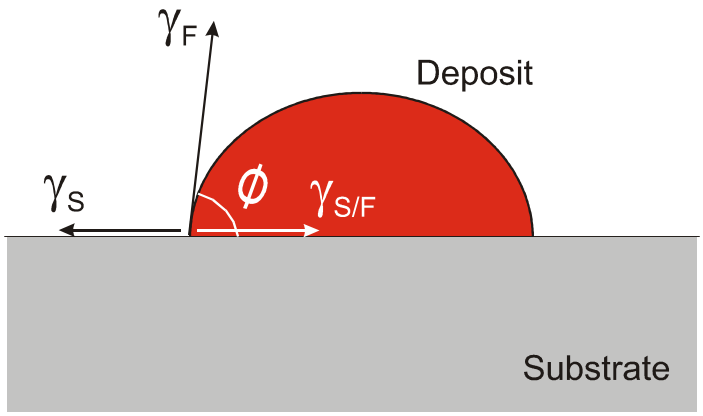

Fig. 3.2. Simplified picture of an 3D-island of a deposited film on a surface [46].

In our study we use the following values for surface free energy: $650 \le g_{Al_2O_3 (Ga_2O_3, respectively)} \le 925 mJ/m^2$ [74], $g_{Ga} = 720 mJ/m^2$, $g_{Ni} = 2364 mJ/m^2$, $g_{Co} = 1870 mJ/m^2$, $g_{Cu} = 1934 mJ/m^2$ [75].

♦ **Heat of formation**

The heat of formation ΔH_f is the change in the total energy of the system when two materials are combined to form a compound [76]. When a metal A is

deposited onto an oxide BO, then A reduces the surface of BO to metallic B and itself become oxidized to AO if the reaction

$$A(s) + BO(s) \rightarrow AO(s) + B(s)$$

is thermodynamically downhill (i.e., if it has a negative standard free energy change; (s) refers to solid). Neglecting differences in formation entropies of the oxides, which are usually almost negligible [77], this occurs when the standard heat of formation of the oxide A, $\Delta H^0_{f,AO}$ is more negative than that of the oxide B. To take more complex stoichiometries like A_3O_4 into account, one has to make this comparison using heats of formation *per mole of oxygen*, using the most negative value amongst all oxides of A (i.e., the value for the most stable oxide of A). The values, with which we are dealing in this work are listed in Table 3.1.

Table 3.1. Heats of formation of some oxides [78]**.**

Oxide	Heat of formation of oxide (ΔH^0_f in kJ per mole O)
Ga_2O_3	- 1080.0
Al_2O_3	- 1675.7
NiO	- 240.0
Cu_2O	- 168.6
CuO	- 157.3

3.2 Surface Diffusion

In thermodynamic equilibrium all processes proceed in two opposite directions at equal rates, as required by the principle of “detailed balance”. Thus, for example, surface processes such as condensation and re-evaporation, decay and formation of 2D clusters must obey detailed balance. Therefore, in equilibrium, there is no net growth of a film and so crystal growth must clearly be a non-equilibrium kinetic process.

The growth of a crystalline film from a molecular or atomic beam, commonly referred to as Molecular Beam Epitaxy (MBE), is a simple example of a self-assembly process. In contrast to crystallization from the melt, which often leads to dendrites and other ramified patterns [79], MBE growth can be described without reference to the transport of matter, latent heat or impurities in the fluid phase. The remarkable richness of patterns forming during MBE is determined solely by processes which occur locally at the surface. Moreover, in the case of *homoepitaxial* growth, in which a film is grown on a substrate of the same material, energetic determinants such as interfacial free energies and misfit strain are absent, so that the film morphology is governed primarily by growth kinetics.

The main steps in the growth process can be summarized as follows. Atoms are deposited at a rate *F*. They migrate (diffuse) along the surface with a two-dimensional diffusion coefficient *D*. When two atoms meet they form a dimer. Dimers may subsequently disintegrate, or they may grow by aggregation of further atoms into trimers and larger clusters. Once a substantial fraction of the surface is covered by two-dimensional island clusters, these begin to coalesce and a full atomic layer forms, on which the processes involved in producing the first layer repeat themselves. At this stage of the growth process, the fate of atoms deposited on top of first layer islands becomes important. Such atoms may either descend from the island, thus contributing to the growth of the island edge, or they may remain on the island, promoting the nucleation of the next layer. On many crystal surfaces, the diffusion of atoms between different atomic layers is suppressed due to additional energy barriers (ΔE_s, Schwoebel barrier), which an atom crossing a step has to overcome.

This phenomenon was first observed experimentally by Ehrlich and Hudda [80], and some of its consequences for the growth of stepped surfaces were analyzed by Schwoebel and Shipsey [81]. The atomistic origin of the additional step edge barrier is illustrated in Fig. 3.3: An atom descending from a step edge passes through a transition state of very low coordination, which implies poor binding and thus a higher energy.

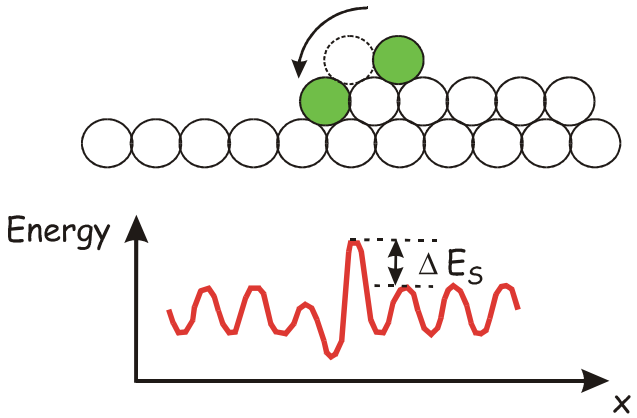

Fig. 3.3. An atom descending from a step edge experiences an additional energy barrier DE_s [82].

This picture is oversimplified, because in many cases descent by concerted exchange is more facile than hopping [83]. Nevertheless, it is generally true that the rate for interlayer diffusion is smaller than the in-layer diffusion constant *D*.

In-layer and interlayer diffusion, as well as all other atomic processes involved in the growth, decay and shape changes of two-dimensional islands, are *thermally activated.* This can be explained in the following way. To a good approximation, the motion of an adsorbed atom (an *adatom)* on a crystal surface can be viewed as a two-dimensional random walk between adsorption sites. In hopping from one adsorption site to another, the adatom has to overcome an energy barrier E_D. The energy is provided by thermal substrate vibrations. This implies an Arrhenius equation

$$D = D_0 e^{-E_D/k_B T} \qquad (3.4)$$

for the diffusion coefficient. In (3.4), T is the substrate temperature, k_B the Boltzmann constant, and D_0 is an attempt frequency with a typical magnitude around 10^{13} s^{-1}. The main role of temperature in MBE growth is that it regulates, through expressions like (3.4), the relative rates of the different activated processes on the surface.

3.3 Oxidation

The oxidation of a surface and the formation of an oxide layer on top of a metal, alloy or semiconductor surface is a growth process which is much more complicated than the simple metal on metal or metal on oxide growth.

The preparation of clean and well-ordered single-crystalline oxide surface remains one of the great experimental challenges of surface science. A variety of techniques have been used with varying degrees of success, depending on the oxide. [3]. The ordering of oxides is not as easily achieved as on single-crystal metals. This is probably because the necessary diffusion of metal atoms has very low activation barrier on metal surfaces, whereas both the oxygen and metal atoms must diffuse to form oxides, and this may require scaling large energy barriers. Also, desorption of oxygen or the metal can occur, which creates non-stoichiometric surfaces and disorder. We have to determine the temperatures needed for achieving a high degree of order, and whether the presence of an oxidizing gas (e.g., O_2, H_2O, N_2O) can improve this.

There are different ways for preparation of one well-ordered oxide. An oxide surface can be formed by mechanically cutting a crystallographic plane of a single crystal oxide or by spark erosion and after that polishing the surface [3]. Oxide surface can be prepared also on a base of growth of thin films on metallic substrates or metallic alloy surfaces [84], which results in a determination to a large extent of the structure of the oxide film from the crystallographic structure of the substrate [85]. Oxide can be grown by oxidation of a metal substrate or by oxidation of a deposited metal layer on a metal or intermetallic alloy substrate. One of the most important property of the substrate is its structure and lattice constant, because it may determine the structure of the oxide layer. Oxide grows also by oxidation of alloy surfaces. In this case thin oxide films grow by the adsorption and reaction of oxygen atoms with substrate atoms which segregate (preferentially) from the bulk of intermetallic alloys like NiAl [86-92] and CoGa [84, 93-95] to the surface, a process which is called “preferential segregation oxidation” (epitaxy, at appropriated temperature) [84]. Oxygen adsorption at

room temperature usually leads to the formation of a thin amorphous oxide layer, which becomes well-ordered after annealing to elevated temperature. One of the advantages of using alloys as substrate instead of pure metals is, that higher annealing temperatures can be used for ordering of the oxide films without melting of the substrate. Very often the temperature of ordering is much higher as the melting temperature of the pure metal. This is crucially important for ordering of the grown oxide layers. Of course, if there is a large mismatch between the lattice of the alloy surface and the oxide lattice, the film may be defect rich.

In general, oxidation is the reaction of a metal (or a semiconductor) with a nonmetal (chalcogenide, halogen, water or a combination) to produce a compound on the surface. The reactants, a metal or semiconductor having delocalized bonding and a gas having covalent bonding, are converted into a product, an oxide having partially ionic, partially covalent bonding. When the product of the reaction is a solid, it separates the two reactants. Further growth requires that atoms of the metal and/or of the oxidant moves through the growing oxide (see Fig. 3.4).

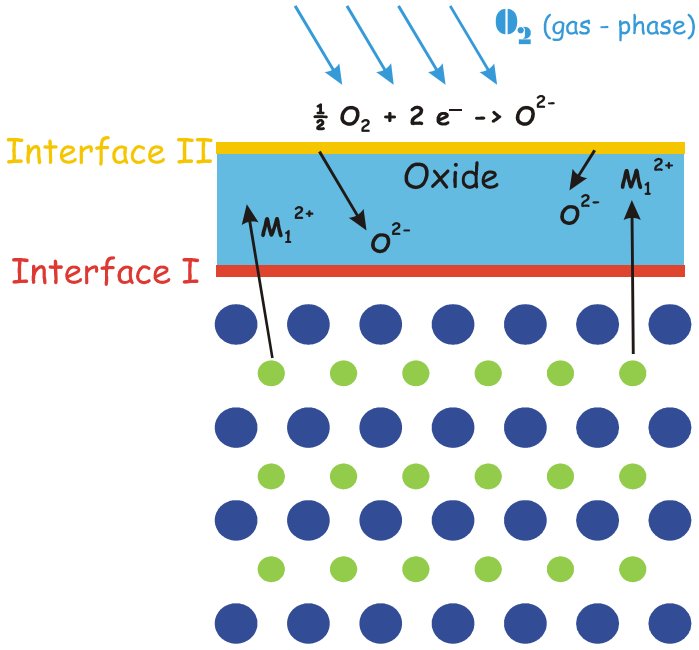

Fig. 3.4. Schematic of oxide growth on the interfaces *gas - phase - oxide* (I) or *oxide - metal* (II) [84].

In Fig. 3.4, the substrate consists of a binary alloy (small and large circles represent the two different atoms). During oxidation only atoms of one metallic constituents moves from the substrate to the interfaces I or II and reacts with oxygen. Of course, oxygen ions can also move to the interface I to form an oxide. In general, it is assumed that oxygen is in an ionic state but there is evidence that, at least in the case of silicon oxidation, the migrating species also can be molecular oxygen [96].

Charge neutrality during the passage of a single ionic species is achieved by the movement of electrons or holes through the oxide in the same or opposite direction. Barriers to ion movement into and through the oxide exist (see Fig. 3.5, [97]). *U* represents the energy which must be overcome by an ion moving from one equilibrium site in the oxide to an adjacent one separated by a distance *2a*, while *W* is the sum of *U* plus W_i. W_i is the heat of solution of a metallic ion.

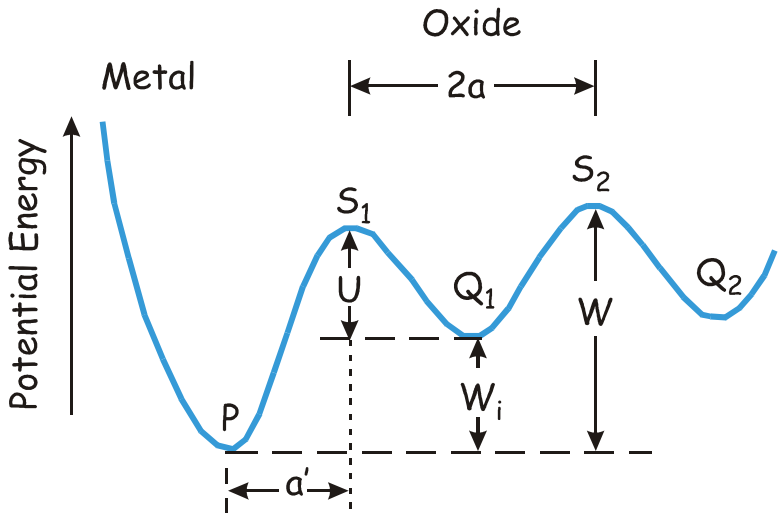

Fig. 3.5. Potential energy diagram at a *metal - oxide* interface. *P* is the position of an ion at rest in the interface, while Q_i is a lattice or network site in the oxide. S_i is the top of the potential energy barrier separating the Q_i sites. W_i is the heat of solution of a metallic ion, *U* is the activation energy for diffusion in the oxide, and $W = W_i + U$. The distance *a´* is considered to be equal to *a* ([96], Fig. 1.1).

Thus, *W* represents the energy change which occurs when an ion is removed from the oxide surface into the bulk of the oxide.

The process of oxidation can be divided conveniently into two regimes, high-temperature and low temperature, depending on the metal and *time - temperature - pressure* relationship during oxidation. The products of high-temperature oxidation are often polycrystalline, and as such, contain paths of easy ion diffusion. However, in some cases the oxidation of single crystal surfaces leads to the formation of single crystalline (well-ordered) oxide layers. In high-temperature oxidation, thermal energy is sufficient to account for ion generation and movement through the oxide even though a small electric field may be present. A parabolic growth rate is generally followed.

In low-temperature oxidation the thermal energy is insufficient to allow existing ions or electrons (or holes) to surmount the energy barrier and therefore, the driving force for the formation of oxides is an electric field. A logarithmic growth rate is found for this case. The actual temperature of transition from low- to high-temperature oxidation is a function of the material, its perfection, and purity.

Oxidation at high temperatures, is more dependent on inherent material properties. In Wagner [98] theory the growth of oxide films obey a parabolic kinetics

$$x^2 = k_p t\,, \tag{3.5}$$

where x is the film thickness and k_p the parabolic rate constant. The parabolic kinetics can be seen to be consistent with the rate of growth being controlled by transport down a gradient of driving force, which becomes proportional smaller as the film thickness increases.

Fig. 3.6 shows various species which can move through an oxide, e.g., ions, electrons and holes. In general, oxide are compounds having predominantly ionic bonding, and therefore, it is appropriate to consider the separate transport of ions and electrons or holes.

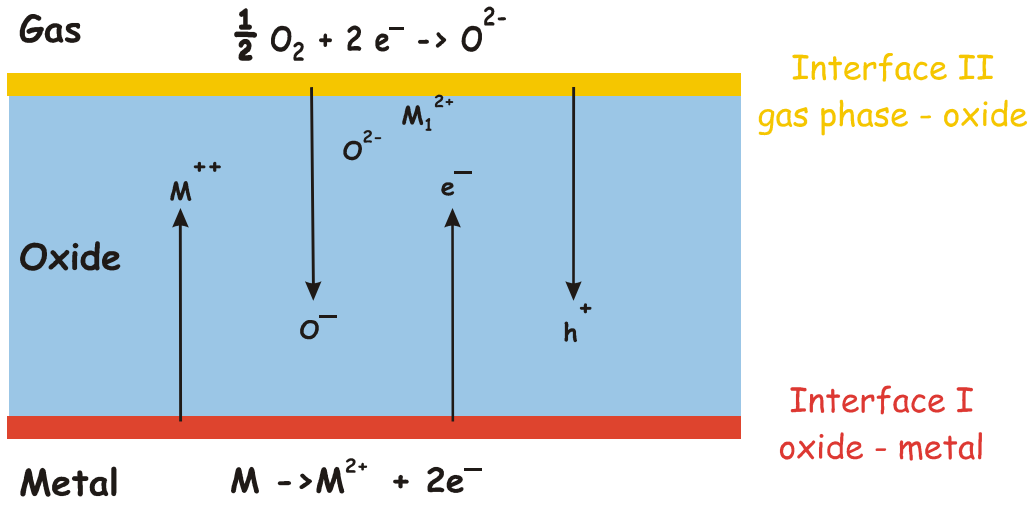

Fig. 3.6. Transport of ions, electrons and holes in gradients of oxygen activity and electrical potential across a growing oxide film [2].

The high-temperature oxidation or Wagner's theory [98] assumes that there is no net electrical current flowing across the whole film and that local chemical equilibrium exists throughout the film and that there is no divergence in the ionic and electronic currents.

Cabrera and Mott [97, 99], in a general treatment of oxidation, derived a parabolic rate law for oxidation limited by cation diffusion in the bulk oxide

$$x^2 = 4\Omega D n_c t\,, \qquad (3.6)$$

where O is the oxide volume per metal ion, n_c the concentration of ions at the *metal - oxide* interface, and D the diffusion coefficient for ions. The concentration of metal ions at the *gas - oxide* interface was assumed to be zero. Cabrera and Mott found a criterion to distinguish between this parabolic growth based on bulk oxide control from other modes of growth based on interface control.

Chapter 4

Experimental Setup

4.1 The UHV Systems

The growth and characterization of thin films was performed under the UHV conditions in two different apparatus. Both apparatuses were equipped with an Auger Electron Spectrometer (AES), LEED optics and evaporators for metal deposition. The first system contains, in addition, an EEL-Spectrometer (EELS) and a Quadruple Mass Spectrometer (QMS). In the second system a variable temperature STM is integrated. The evaporators will be described separate in a Chapter 6.

4.1.1 UHV Apparatus I

This system consists of a two level UHV chamber, which after 48 hours bake-out at ~ 450 K has a basic pressure of 5.10^{-11} mbar. It is evacuated with a pumping chain, consisting of titanium sublimation pump, turbo-molecular pump and rotary pump. The titanium sublimation pump is equipped with a so called “cold wall”, which was cooled down by liquid nitrogen. At normal operation every one hour a new Ti-film is evaporated.

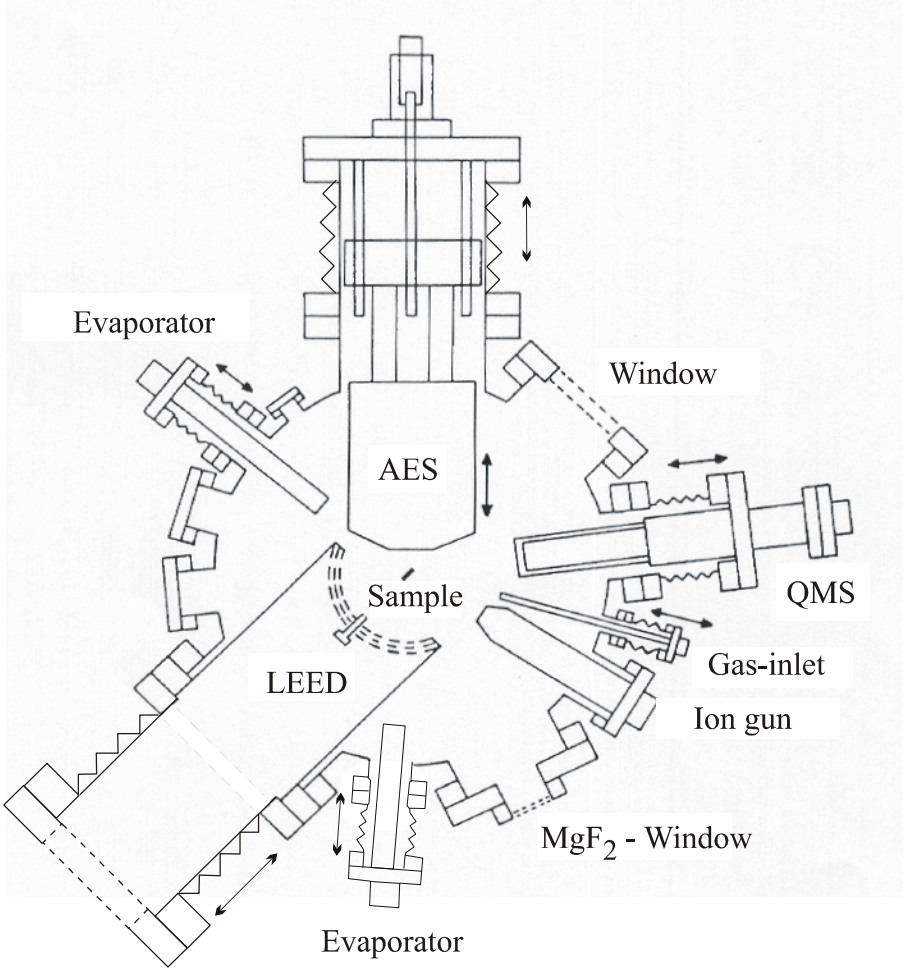

Fig. 4.1. The upper level of the UHV System.

The apparatus has two levels, between which the sample is transferred by means of a manipulator. In the lower level, which is lined with a double-cylinder made of μ-metal is located the EEL-Spectrometer. In the upper level (Fig. 4.1) are housed an AES spectrometer, a LEED optics and a QMS. All components of this chamber are linearly movable in order to be positioned in front of the sample. Besides this are mounted also an ion gun, a window and quartz glass tube for local letting in of process gases and two evaporators as well. The gas inlet system can be separated completely from the recipient with a shut-off valve and can be pumped separately with a small turbo pump and a rotary pump. The used gases, Ar for ion sputtering and O_2 for oxidation have a purity of above 99.9%. The

composition of the gases and of the rest gas could be observed by QMS. For pressure measurements there is an ionization manometer available and a gas-friction vacuummeter in the gas-inlet system. The manipulator is rotatable with 360° around its axis and the sample can be transferred between the two levels. The sample was heated by electron bombardment on its back side and was cooled down by liquid nitrogen. The sample temperature was measured by means of a W-type thermocouple (WRe3%/WRe25%) directly attached to the sample. The sample has a hat-form and it is mounted in an appropriated sample holder.

4.1.2 UHV STM-OMICRON Apparatus

The OMICRON VT STM is an UHV scanning probe microscope (SPM) system for topographic spectroscopic imaging of solid surface with atomic resolution and for surface preparation and analysis. The system consists in a STM chamber, a preparation chamber and a fast entry lock chamber (Fig. 4.2). The preparation chamber basically serves for cleaning and preparation of the sample surface.

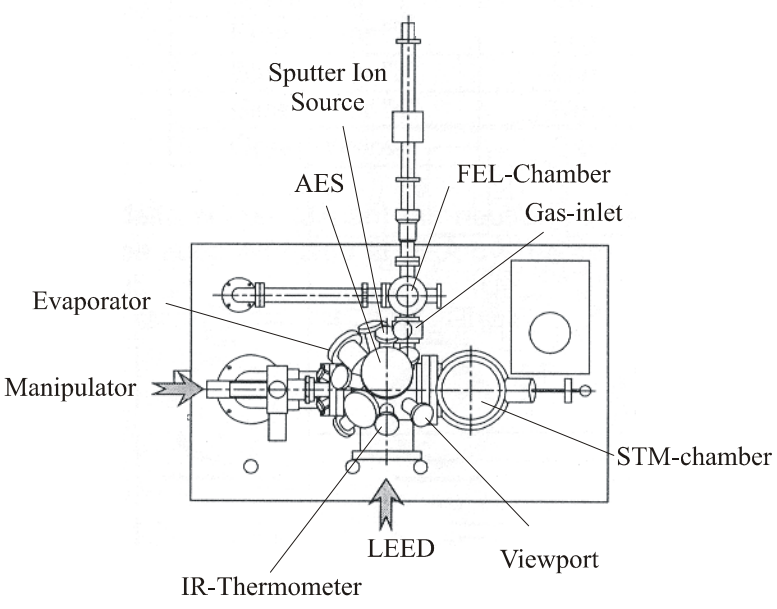

Fig. 4.2. The OMICRON VT STM Apparatus

It is equipped with a cylindrical mirror analyzer (CMA) for AES, a three-grid LEED optics, an ion-gun, a QMS, and a home made Ga evaporator. The analysis chamber houses a Variable Temperature Scanning Tunneling Microscope (OMICRON VT STM), which can be operated in the temperature range between 25 and 1300 K. AES spectra were recorded in the integral mode. The sample was heated by means of a solid-state PBN (pyrolytic boron nitride) heating element and the temperature was measured by means of an Infrared Thermometer. The UHV apparatus is pumped by an ion getter pump and a titanium sublimation pump (TSP). A turbo-molecular pump with a rotary pump is used to pump the vacuum chambers down from atmospheric pressure or after sputtering. Usually the fast entry lock chamber is pumped via a bypass. Gases can be admitted by a leak valve to the UHV apparatus.

4.2 The Measuring Techniques

4.2.1 The EEL Spectrometer

The lower level of the UHV apparatus I houses an EEL-Spectrometer, type Ulti 100. This is a state-of-the art instrument developed by Ibach and coworkers [100]. Fig. 4.3 shows a photography of the EEL-Spectrometer. The thermally emitted (LaB_6 – cathode) electron beam is focused by the lenses (A_1 – A_3) into the entrance slit of the premonochromator, which consist in an optimized cylindrical capacitor. After the premonochromator a main monochromator is located. A detailed description of the spectrometer and the numerical simulations can be found in Ref. [100]. The capacitors, based on 127° deflectors, are made of high-purity copper and are coated with a graphite layer. The entrance and outlet electron optical components of the scattering chamber are provided with symmetric lenses (B_1, B_2 and B_3, B_4, respectively).The scattered electrons which have suffered an energy loss (gain) are accelerated (decelerated) to the pass energy of the analyzer by an appropriate biasing of all the potentials on the

analyzer side. After passing the one-stage analyzer the electrons are detected by a channeltron (counting mode). The uptake of the channeltron counting rate as a function of the potential of the analyzer provides the EEL spectrum. The tunning and the data acquisition is operated by computer control.

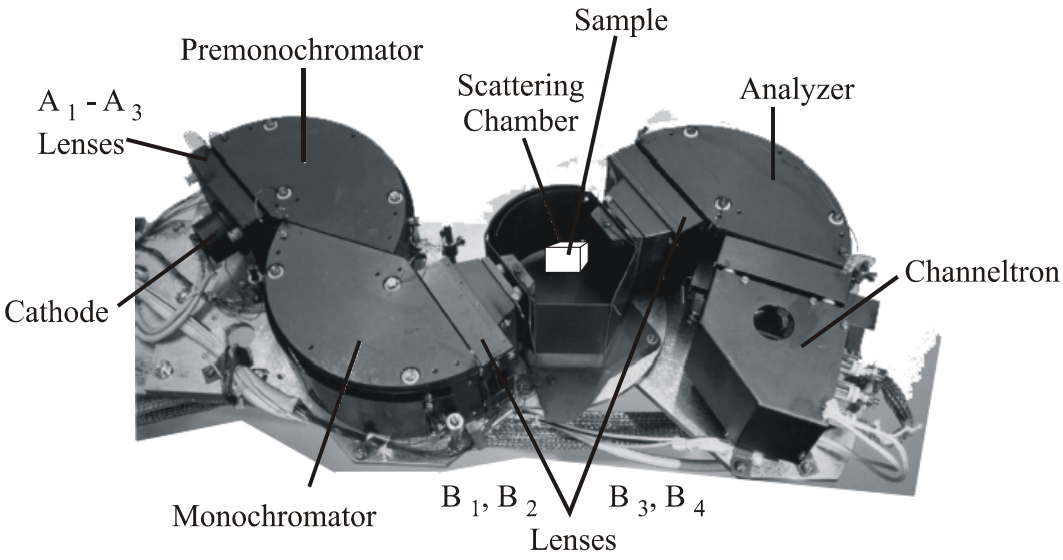

Fig: 4.3. The EEL-Spectrometer, type Ulti 100.

4.2.2 The Auger Electron Spectrometer

For the AES characterization of the samples we used a PHI CMA-Auger-System. Figure 4.4 shows a typical AES system. The primary electrons are emitted by an electron gun which is integrated into the CMA on its central axis. The AES electrons and some backscattered electrons entering from a directed entrance into a certain cone (with an apex angle of 42°18.5´) are filtered as a function of their energy by two concentric cylinders onto the detector. The electric field determining the pass energy is radially directed between the concentric cylinders.

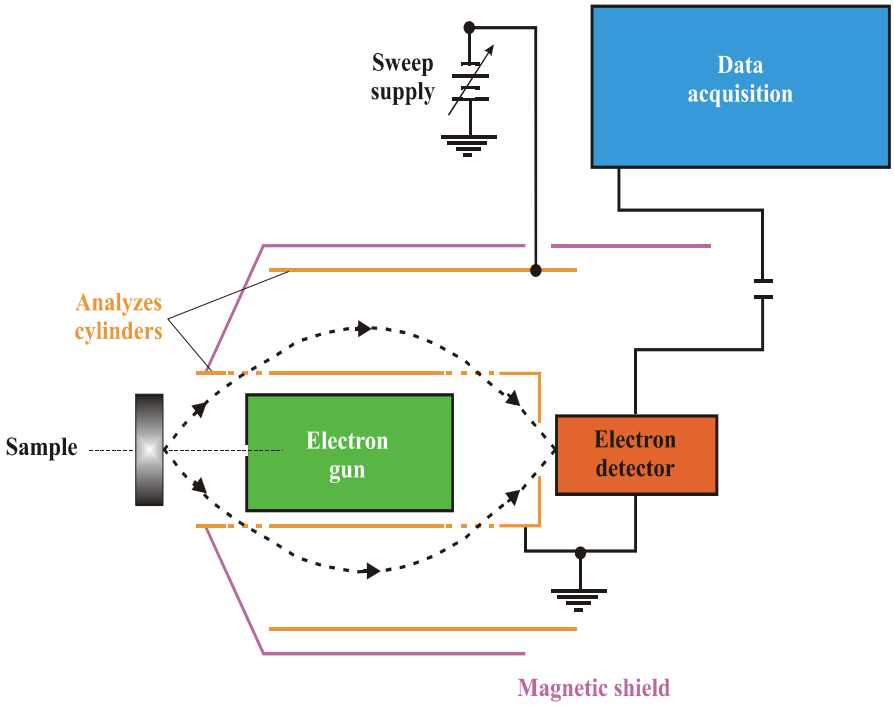

Fig. 4.4. A typical arrangement of a cylindrical mirror analyzer (CMA) for AES. The primary electrons are emitted by an electron gun, located on the central axis.

4.2.3 The LEED Optics

The LEED apparatus used in our experiments is a 3-mesh commercial rear view LEED system (VG RVL 900). A schematic of the LEED optics [46] is shown in Fig 4.5. The electron gun (VG LEG24) uses electrostatic focusing for the electron beam. Electrons are emitted by the heated filament (Thoria coated) and collimated by the Wehnelt cylinder which has a small negative bias with respect to the filament. The primary energy (10 – 500 eV) is determined by the acceleration voltage i.e. the voltage between the filament and the sample. The lenses B and C are used to focus the electron beam. The incident electrons are diffracted by the surface of the sample and are backscattered to the fluorescent screen. The screen is at a high positive potential with respect to the sample. The apertures A and D, the grids in front of the fluorescent screen and in front of the sample are

grounded. Thus, a field free region between the sample and the screen exists. This is important to prevent electrostatic deflection of the electrons. Besides elastic scattering, inelastic scattering also occurs at the sample surface and on the grid in front of the sample, thus giving rise to electrons of lower energy. These electrons produce a relatively homogeneous background illumination of the screen. This background is suppressed by applying a somewhat negative potential to the middle grid.

The images are recorded using photo camera at a distance of approximately 70 cm from the screen.

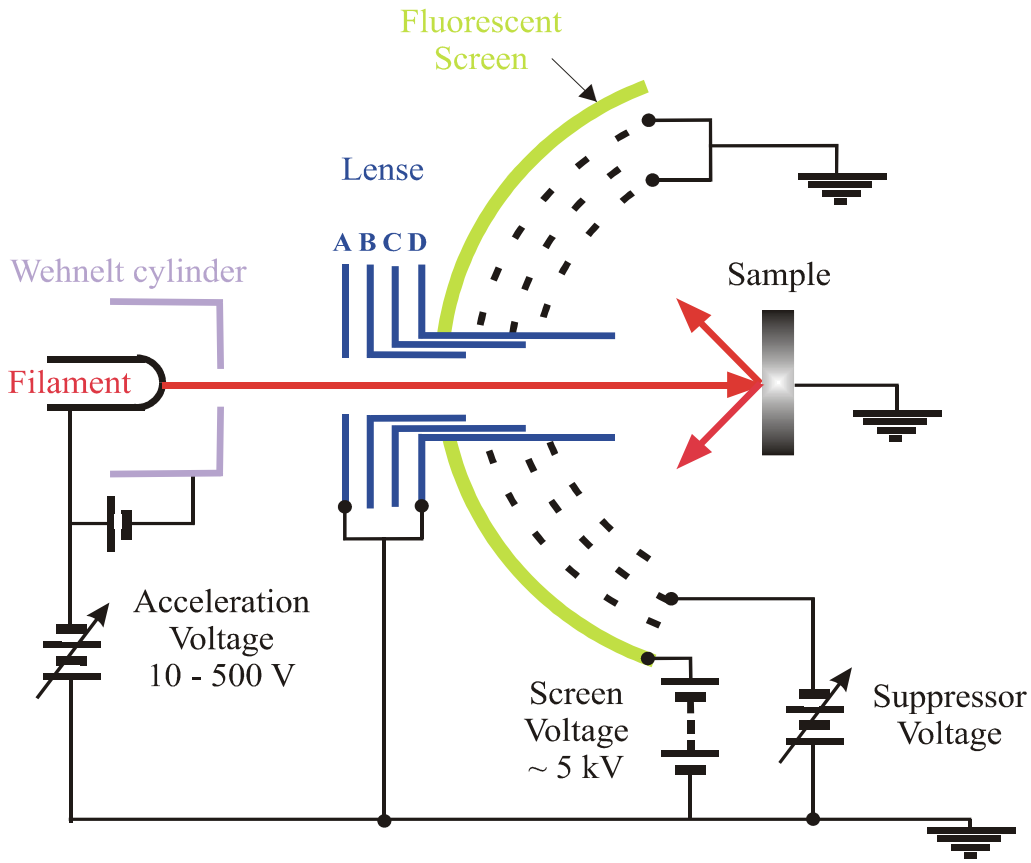

Fig. 4.5. A schematics of the LEED optics.

4.2.4 The Scanning Tunneling Microscope

For the investigations of the topography of the surface we have used an Omicron Variable Temperature STM (VT STM) with cooling and heating facilities to cover a temperature range from 25 to 1300 K. Any temperature within the specified range can be selected by combining cooling and heating procedures. A view of the STM is shown in Fig. 4.6.

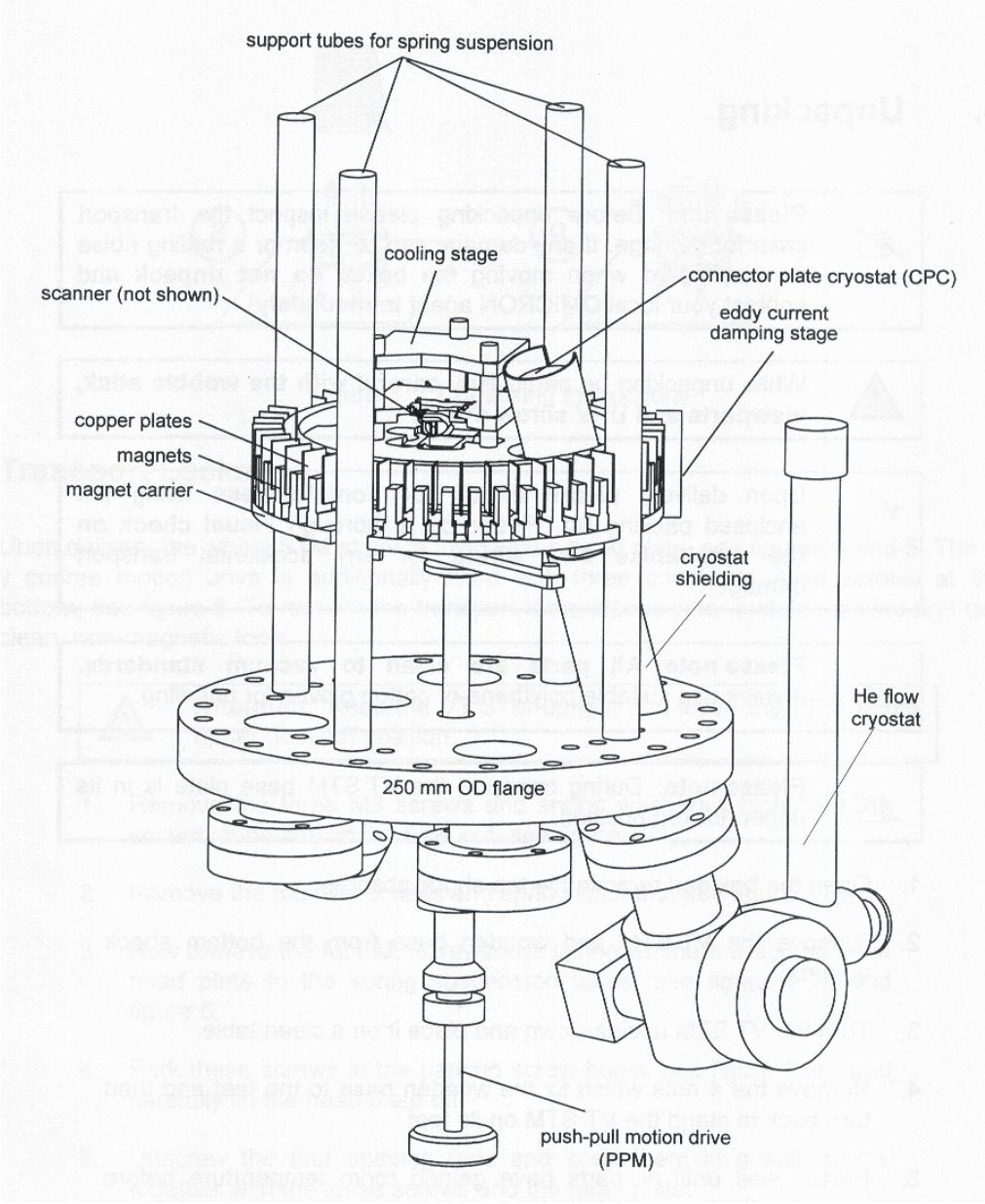

Fig. 4.6. A view of the VT STM microscope.

Chapter 5

Outline of the Materials

The main topic of the present work is the preparation and characterization of ultra thin oxide and metal layers on substrates of ferromagnetic metals and oxides, respectively. In order to facilitate the discussion about the multilayer systems the used materials are presented at a glance. This Chapter contains a description of the material properties, which are significant for our investigations and has no pretensions for explicitly.

5.1 The Single Crystalline Substrates

The multilayers were grown on the surface of Cu(111) and Ni(100) single crystals.

5.1.1 Cu(111)

Copper is a reddish colored, malleable, ductile transition metal. It is an excellent conductor of both electricity and heat. Typically is used for semiconductor seed layers, flexible circuits, contacts, junction films in IC's. Copper exhibits cubic face centered (fcc) crystal structure with a lattice constant of 3.61 Å [101].

The crystal we are dealing with was cutted along the (111) plane. In Fig. 5.1 are shown the fcc structure (a) and the (111) surface plane (b) of copper, where **a** is the lattice constant of copper in real space, while $\mathbf{a_{(111)}}$ is the lattice constant of the (111) unit cell. The melting point of copper is 1357.6 K and this gives the possibility for annealing the sample up to 1200 K.

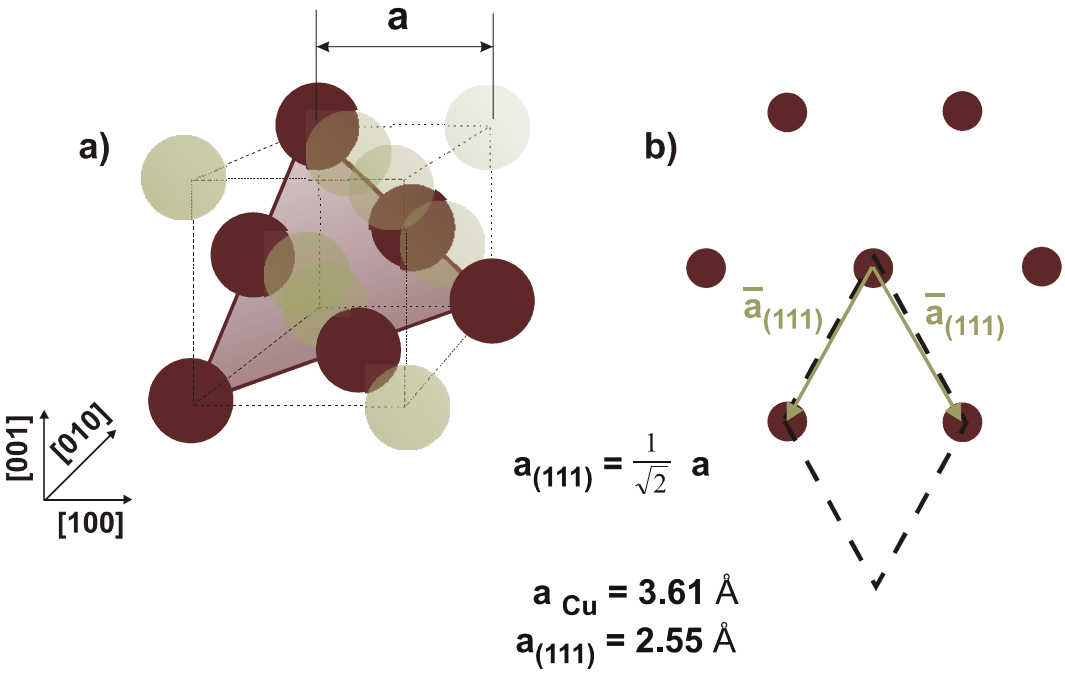

Fig. 5.1. Surface structure of Cu(111): a) the fcc structure of Cu; b) the (111) plane of Cu.

5.1.2 Ni(100)

Iron, nickel, cobalt and some of the rare earths exhibits a unique magnetic behavior – ferromagnetism. They possess a so called long range ordering phenomenon at the atomic level which causes the unpaired electron spins to line up parallel with each other in a region called domain. Within the domain, the magnetic field is intense, but in a bulk sample the material will usually be non

magnetic, because the domains are randomly oriented with respect to each another.

Nickel is a hard, malleable, ductile metal. Besides its applications as ferromagnetic films, nickel is also used for memory elements and diffusion barriers and in the catalysis.

Nickel exhibits a cubic face centered crystal structure with a lattice constant of 3.52 Å [101]. In Fig. 5.2 are shown the fcc structure of Ni (a) and the (100) surface layer (b), where **a** is the lattice constant of nickel in real space, while $\mathbf{a_{(100)}}$ is the lattice constant of the (100) unit cell. Its melting point is 1726 K and therefore a nickel substrate is suitable for studies in a large temperature range.

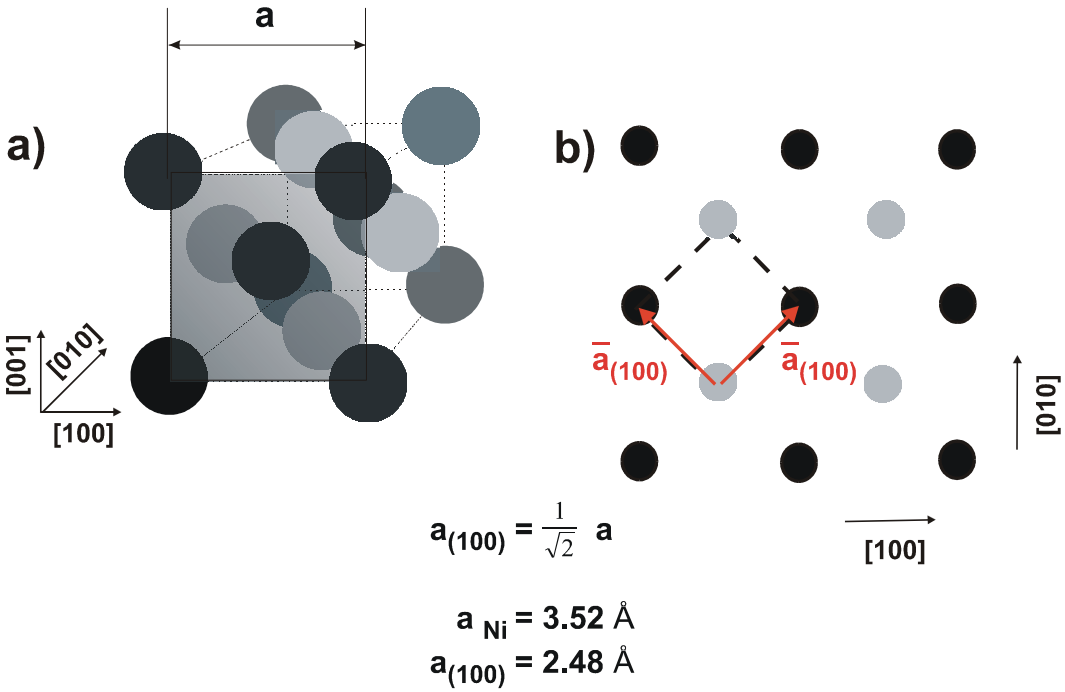

Fig. 5.2. Surface structure of Ni(100): a) the fcc structure of Ni; b) the (100) plane with its unit cell.

5.2 Cobalt

Two different structures are known for Co: the cubic face centered (fcc) and hexagonal (hcp) structure [101-104]. The lattice constant of the fcc structure is 3.544 Å, while the hexagonal one has lattice constants of 2.507 Å and 4.069 Å [101]. The hexagonal structure is stable up to around 700 K [101], above this temperature the fcc structure is formed. Cobalt has a melting point at 1765 K.

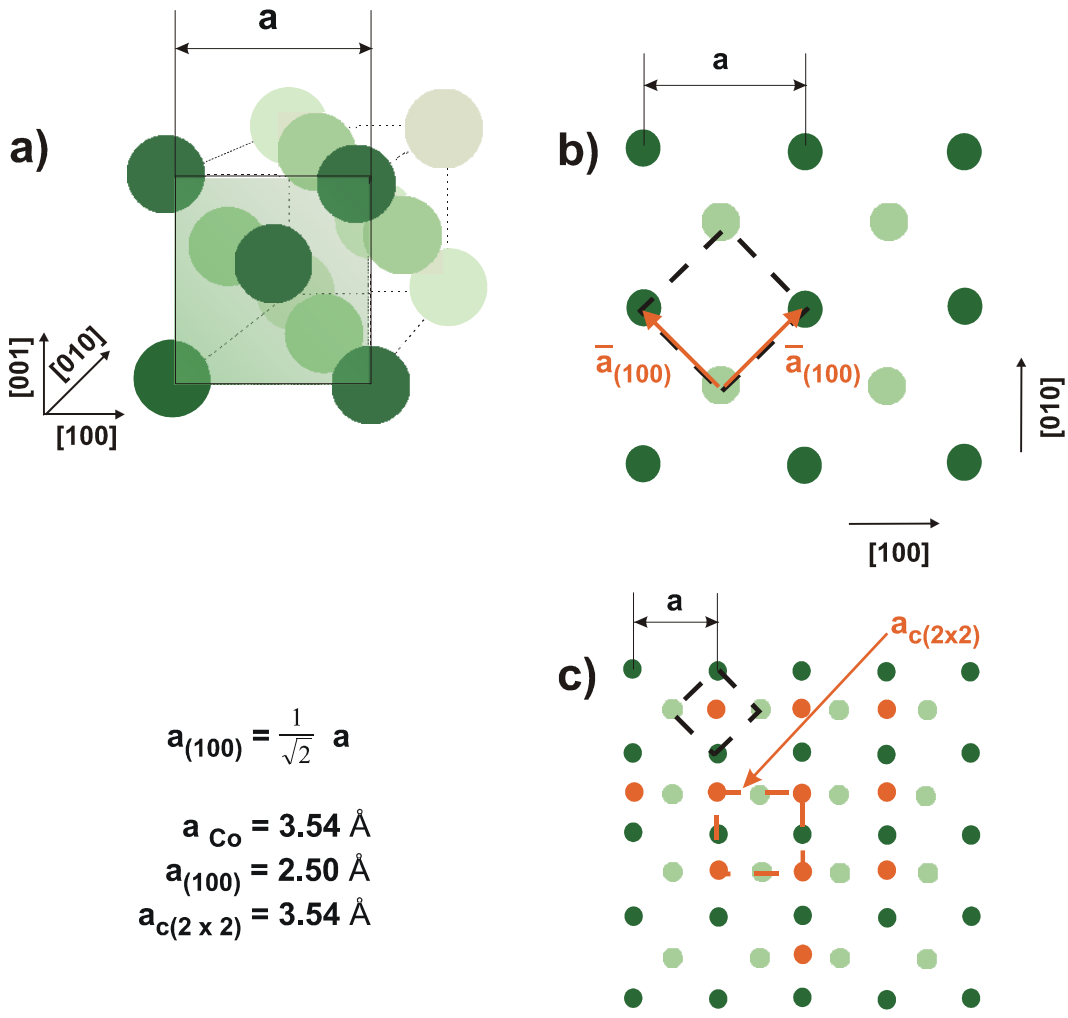

Fig 5.3 a) The structure of the fcc Co; b) The (100) surface with the unit cell; c) the c(2×2) – reconstruction of the (100) surface of fcc-Co.

Fig 5.3 shows the structure of fcc Co (a), the (100) surface with its unit cell (b) and the c(2×2) reconstruction of the (100) surface. In this work only the growth of fcc Co was found.

5.3 Oxides of Al and Ga

Al oxide is one of the most investigated materials, because of its great importance for the material science and catalysis. There are at least 14 known phases of Al_2O_3. Already in 1798 Greville described an Al mineral from India, which is called "corundum" [105]. This is the purest and the most stable α-Al_2O_3 phase. This oxide is also the final product of the dehydratation of the natural aluminiumhydroxide, which are trihydroxides Al_2O_3. $3H_2O$ (gibbsite/hydrargillite bayerite, nordstrandite) and the Al oxide – hydroxides Al_2O_3. H_2O (diaspore, boehmite) [106]. At the dehydratation of this hydroxides many different modifications of the Al oxide occur which have different crystal structure and lattice constants. Bellow are schematically presented some series of dehydratations [107]:

- ☞ Oxide-Hydroxide
  - ♦ Diaspore $\xrightarrow{450^\circ} a - Al_2O_3$
  - ♦ Boehmite $\xrightarrow{450^\circ} g \xrightarrow{600^\circ} d \xrightarrow{1000^\circ} q \xrightarrow{1200^\circ} a - Al_2O_3$
- ☞ Trihydroxide
  - ♦ Hydrargillite $\xrightarrow{250^\circ} c \xrightarrow{900^\circ} k \xrightarrow{1200^\circ} a - Al_2O_3$

    180° ↘ dry Atmosphere

    Boehmite $\xrightarrow{450^\circ} g$ ……

    180° ↗ dry Atmosphere
  - ♦ Bayerite $\xrightarrow{250^\circ} h \xrightarrow{850^\circ} q \xrightarrow{1200^\circ} a - Al_2O_3$

    in high-vacuum:

♦ $\left\{\begin{matrix}\text{Nordstrandite}\\ \text{Bayerite}\\ \text{Hydrargillite}\end{matrix}\right\} \xrightarrow{200^\circ} r \xrightarrow{400^\circ} g \xrightarrow{750^\circ} q \xrightarrow{1200^\circ} a - Al_2O_3$

There are also two more series of phase transformation, which do not begin with hydroxide, i.e they are not dehydratation reactions (a = amorph)

☞ $a - Al_2O_3 + \text{Ion - Implantation} \longrightarrow \text{a} - Al_2O_3 \xrightarrow{950^\circ} g - Al_2O_3$ [108]

☞ $\text{Al} \xrightarrow{+O_2} \text{a} - Al_2O_3 \xrightarrow{900^\circ} g - Al_2O_3$ [109]

In Table 5.1 are summarized some of the Al oxides. All alumina phases are based on closed packed oxygen lattice – either *hexagonal closed packed (hcp)* or *face-centered cubic (fcc)*. The Al^{3+} ions occupy different *octahedral* or *tetrahedral* positions in the oxygen lattice. The α-Al_2O_3 belongs to the so called *ABAB…* group. The oxygen ions form the *hcp* structure and the Al^{3+} ions occupy only *octahedral* positions. The γ-, γ'- and θ-Al_2O_3 belong to the *ABCABC…* group. In this case the oxygen ions form the *fcc* structure and the Al^{3+} ions occupy both the *octahedral* and *tetrahedral* positions. The γ-Al_2O_3 has a “defect spinel” structure with 32 oxygen atoms per unit cell.

Table 5.1. Crystal structures of some Al oxide phases [110]**.**

Name	Spacial Group	a, b, c [Å] ß	Oxygen sublattice	Al^{3+} positions	Remarks
α-Al_2O_3	hexagonal D_{3d}^6	a=4.7589 c=12.991	hcp	octahedral	"Corundum"
κ-Al_2O_3	hexagonal	a=9.71 c=17.86		octahedral + tetrahedral	
γ´-Al_2O_3	cubic	a=3.95		octahedral + tetrahedral	Spinel-type
γ-Al_2O_3	cubic O_h^7	a=7.911	fcc	octahedral + tetrahedral	Spinel-type
δ-Al_2O_3	tetragonal	a=7.96 c=11.70	fcc	octahedral + tetrahedral	distorted Spinel-type
θ-Al_2O_3	monoclinic C_{2h}^3	a=2.92 b=5.64 c=11.83 ß=103°	fcc	octahedral + tetrahedral	isomorphic with β-Ga_2O_3
β-Al_2O_3	hexagonal	a=5.60 c=22.50		octahedral + tetrahedral	

The γ´-Al_2O_3 has also a spinel structure but the unit cell is only half of the γ-Al_2O_3 unit cell. Fig. 5.4 shows a simplified spinel structure. There are indicated the octahedral, the tetrahedral sites of Al^{3+} and the fcc structure of O^{2-} ions. One corner of the tetrahedral coincide with one corner of the cube while the basal planes coincide with the faces of the octahedra.

The γ´-Al_2O_3 phase is which we met in our work.

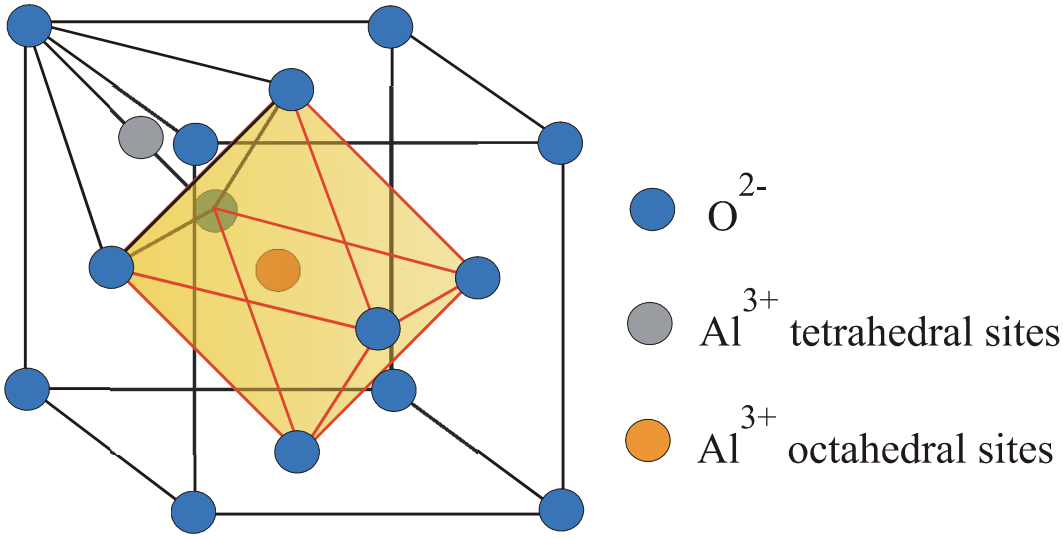

Fig. 5.4. A simplified representation of a spinel structure.

Ga_2O_3 also like Al_2O_3 exists in different phases [110], based on the closed packed oxygen structures. The Ga^{3+} ions can occupied different vacancies in this structure with *octahedral* or *tetrahedral* symmetry. There are at least 5 known phases of Ga_2O_3 [111].

In Table 5.2 are summarized some of the Ga oxides.

Most of the Ga_2O_3 phases are isomorphic to the appropriate Al_2O_3 phases. Thus, for example α-Ga_2O_3 has a corundum structure (α-Al_2O_3) with lattice constants of a = 4.983 and c = 13.43, and belongs to the *ABAB*…group. The Ga^{3+} ions occupy exclusively the *octahedral* interstices. A second group of Ga oxides shows *ABCABC*… stacking sequence. In this case the oxygen atoms are forming a *fcc* sublattice and Ga^{3+} ions occupy *octahedral* as well as *tetrahedral* sites. The modifications of γ-Ga_2O_3, δ-Ga_2O_3 and β-Ga_2O_3 belong to this group.

In this studies the growth of thin films of γ'-Ga_2O_3 and β-Ga_2O_3 is observed. For the Ga oxide arise larger interlayer distances than those of Al oxide, because the lattice constants of Ga_2O_3 are slightly larger than those of the corresponding Al_2O_3 phases.

Table 5.2. Crystal structures of some Ga oxide phases.

Name	Spacial Group	a, b, c [Å] β	Oxygen sublattice	Occupied interstices	Remarks
α-Ga_2O_3	hexagonal	a=4.983 c=13.43	hcp	octahedral	"Corundum" isomorph to α-Al_2O_3
β-Ga_2O_3	monoclinic	a=3.04 b=5.80 c=12.23 ß=103.7°	fcc	octahedral + tetrahedral	Ga-O distances: 1.octahedral pos. 1.935 to 2.074 2 tetrahedral pos. 1.833 to 1.863
γ-Ga_2O_3	cubic	a=8.22	fcc	octahedral + tetrahedral	Spinel-structure $MgAl_2O_4$-type isomorph to γ -Al_2O_3
γ´-Ga_2O_3	cubic	a=4.11	fcc	octahedral + tetrahedral	Spinel-type
δ-Ga_2O_3	cubic	a=9.52	fcc	octahedral + tetrahedral	isomorph to δ -Al_2O_3

5.4 The Surface Alloy of Ni-Ga

We have also studied the growth of Ga on Ni(100) at room temperature and the thermostability of the system. In order to understand the growth processes we need to know what kind of alloys and structures are possible to be formed.

The surface alloy of the Ga-Ni system exhibits several stable bulk forms. Their constitution was studied during the years by means of thermal, microscopic and X-ray methods [112-117]. Different intermediate phases were identified. Fig. 5.5 shows the Ni-Ga phase diagram [118].

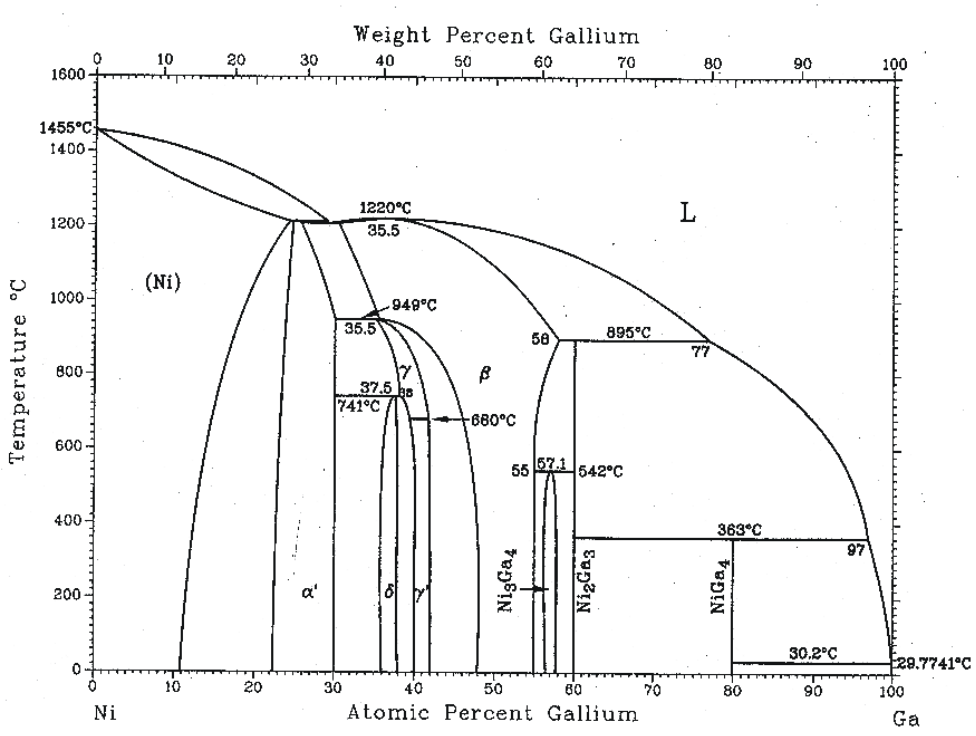

Fig. 5.5. Ni-Ga phase diagram [118].

Six intermediate phases – β, δ, γ, γ´, β´, and ε – were reported by Hellner [112]. For perspicuousness of the information the crystal structures of the Ni-Ga are summarized in Table 5.3.

Table 5.3. Crystal structures of some Ni-Ga phases.

Name	Prototype	Spacial Group	Composition, at. % Ga	a, b, c [Å]	Remarks
α´- Ni_3Ga	Cu_3Au	$L1_2$	26	a=3.5850	
β-NiGa	CsCl	B2	50	a=2.873	
γ -Ni_3Ga_2	NiAs	$B8_1$	35.5	a=4.002 c=4.988	
δ -Ni_5Ga_3	Pt_5Ga_3		36	a=3.76 c=3.39	
γ´-Ni_3Ga_2			41	a=13.785 b=7.883 c=8.457	Additional to the B^8 lines
Ni_3Ga_4	Ni_3Ga_4		55.5	a=11.41	
β-Ni_2Ga_3	Ni_2Al_3	$D5_{13}$	60	a=4.05 c=4.89	
ε-$NiGa_4$	Cu_5Zn_8	$D8_2$	70	a=8.42	
Ga	Ga	A11	100	a=4.51 b=7.64 c=4.51	Pure Ga (Below the melting point 302.91 K)

Chapter 6

Setup of the Evaporators

A large number of techniques have been elaborated on the basis of physical vapor deposition [119-121] to obtain reproducible results in UHV conditions. One of the most widely used type of evaporation source is based on electron bombardment: electrons are accelerated by means of high electrostatic fields (1 – 5 kV) and focused onto a small spot of an evaporant thus causing a local vaporization. In this manner, considerable rates are easily reached without melting the target completely.

Ideally, the beam source should be a Knudsen cell containing vapor and condensed phase at equilibrium. In this case the flux F at the substrate can be calculated from the equilibrium vapor pressure *p(T)* in the cell at temperature *T*. The flux $F\left(\frac{1}{s.cm^2}\right)$ of the exiting beam depends on the vapor pressure *p(T)* by the equation [46]:

$$F = \frac{p(T)a}{pL^2\sqrt{2pmkT}}, \qquad (6.1)$$

where *a* is the area of the cell aperture in cm^2, *L* the distance to the substrate in cm and *m* – the mass of the species. Convenient growth rates in MBE are 1 – 10 ML/s i.e. 1 – 10 Å/s. With typical geometrical factors like *L* = 5 cm and *a* = 0.5 cm^2 the equilibrium vapor pressure in the cell has to be in the range of 10^{-2} – 10^{-3} mbar. The temperatures needed to establish these pressures can be evaluated from the

vapor pressure plotted as a function of the cell temperature [46]. For Al and Ga, temperatures of 1500 K and 1300 K, respectively are needed to achieve a vapor pressure of 10^{-2} mbar, and these temperatures are far above the melting point.
In the deposition experiments performed in this work much lower deposition rates (~ 0.03 ML/s) are used, because of the interest in the growth of ultra thin layers. Thus, the vapor pressure in the cell can be about 100 times lower (10^{-4} mbar) which corresponds to a cell temperature of 1250 and 1100 K for Al and Ga, respectively. In the following the evaporators used for the deposition of Ga, Al, Ni and Co in this work are briefly described.
The calibration of the evaporators with respect to the deposition rate as a function of power supply, time or simultaneously measured ion flux were performed in a separate chamber, which contains a quartz microbalance. The amount of the deposited material determined by the quartz microbalance is declared here as the *nominal* film thickness in Å. The *effective* thickness of the film was determined by AES.

6.1 The Triple Solid State Evaporator

In order to grow films of Co and Ga oxides as well as Al oxides, we have used a triple evaporator type OMICRON EFM 3T (Evaporator with Integral Flux Monitor). Ga atoms as well as atoms of Al and Ni were evaporated from a crucible, and Co from a rod. This is achieved by electron bombardment heating. At a given electron emission current (I_{EM}) and acceleration voltage (HV) the integrated flux monitor detects the simultaneously during evaporation generated ion flux (I_{FM}) which is directly proportional to the flow of the evaporated particles. Once calibrated, the flux monitor releases from the necessity of a quartz thickness monitor by continuously monitoring the deposition rate (r). The flux monitor also operates with the shutter closed, thus allowing to pre-set the deposition rate. The evaporation cell is surrounded by a water-cooled copper cylinder. This and the fact, that only a restricted part of the evaporant is heated,

permits to keep the background pressure during evaporation in the low 10^{-10} mbar range.

The triple evaporator EFM 3T houses three completely separated evaporation cells. Each cell has an independent electron bombardment heater.

In many investigations performed in our research group it was observed that Ga and Al atoms are desorbed by heating samples (single crystals) of CoGa and NiAl, respectively. Therefore, we pestled pieces of CoGa as well as NiAl, and filled two different crucibles of the triple evaporator. In this way a “solid state evaporator” for Ga and Al (Ni+Al) was developed. On which condition the pure element only Ga or Al is vaporized from the respective alloy will be specified in the following sections. Our modification of the construction of the EFM 3T evaporator pertains to the design of the crucible only. This design is shown in Fig. 6.1. A small molybdenum cup (crucible) with the size according to scale and adapted to the EFM 3T construction, was spot welded to the molybdenum rod. In order to suffice with the heating capacity this rod shall be made as long and as thin as possible. In front of the cup was spot welded a grid made from a wire of Mo (0.4 mm) in order to keep the smithereens back during “tip down” handling of the evaporator. The W-cathode was placed 2 mm behind the exit of the crucible.

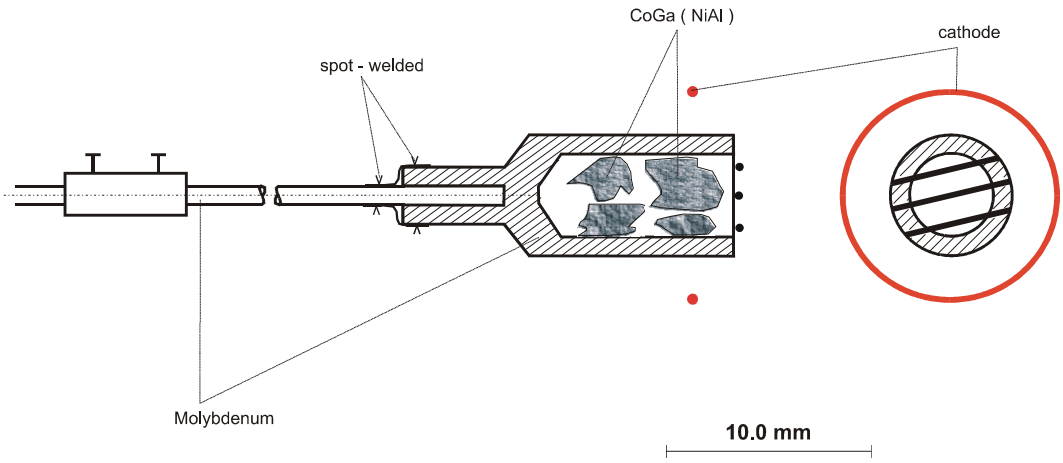

Fig. 6.1. Technical sketch of the molybdenum cup (crucible) – cross section and front view.

Table 6.1. Evaporator settings and deposition rate for the three evaporants Ga, Ni+Al and Co.

Evaporant	Ga atoms from CoGa		Ni+Al atoms from NiAl		Co	
Setting / Parameter	A	B	A	B	A	B
High Voltage (HV, V)	900	900	900	900	1000	1000
Filament Current (I_{FIL}, A)	2.4	2.4	2.2	2.2	2.9	2.85
Emission Current (I_{EM}, mA)	20.0	18.5	30.0	28.0	13.0	12.0
Flux Monitor (I_{FM}, μA)	2.000	1.000	1.100	0.450	0.080	0.035
Deposition Rate (r, Å/minute)	2.0	1.2	1.8	0.9	1.5	0.8

First, the calibration of the evaporators was performed by means of a quartz microbalance. We found two different settings (**A** and **B**) of parameters for each evaporant, at which two different deposition rates were obtained. They are summarized in Table 6.1.

6.1.1.The Solid State Evaporator of Ga

Fig. 6.2. shows two calibration curves, taken at the settings **A** (solid circles) and **B** (open circles). The nominal thickness was determined using a quartz microbalance. As expected, the nominal thickness increases linearly with time. With the setting **A** the evaporation rate is 2.0 Å/min and with the setting **B** it is 1.2 Å/min.

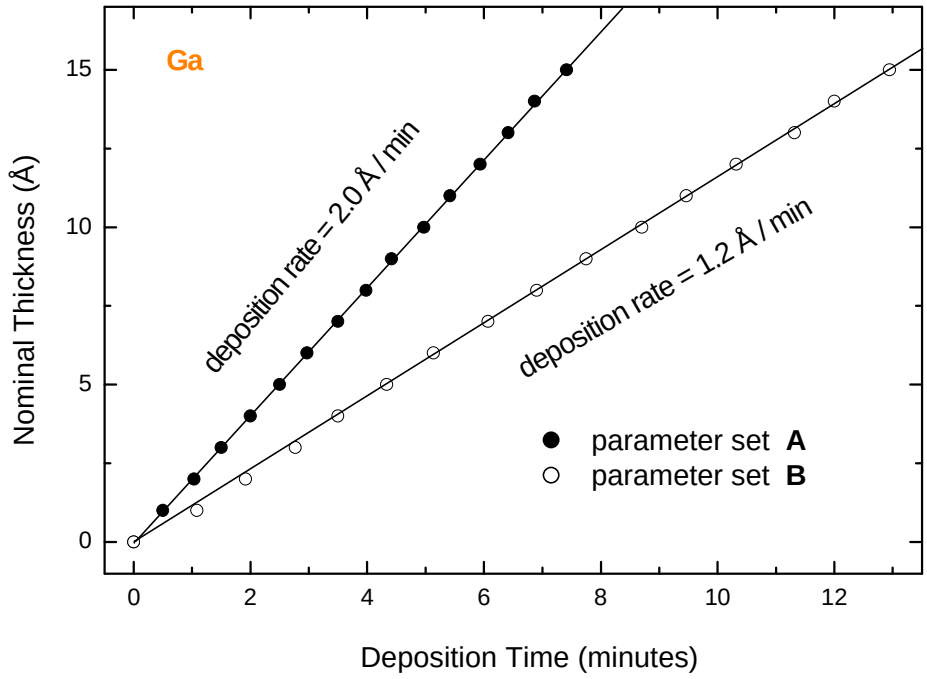

Fig. 6.2. The nominal thickness of the Ga layer measured with the quartz microbalance for the parameter setting A (solid circles) and B (open circles).

Fig. 6.3 shows a differentiated AES spectrum of Ni(100) taken after deposition of Ga at 80 K under the conditions of the parameter setting **B:** After 25 minutes the nominal thickness amounts to 30 Å and the LMM and MNN transitions of Ni vanished completely (Fig.6.3). The AES spectrum shows the MNN transitions of

Ga between 10 and 110 eV as well as its LMM transitions between 830 and 1097 eV. In Section 8 the determination and the relation between nominal and effective thickness is described in detail. There are no traces of cobalt. Deposition at the parameter setting **A** showed the same result – no measurable amount of cobalt is deposited. Thus, by using the "Solid State Evaporator" it is possible to grow a Ga layer, free of Co (in the limits of the AES sensitivity).

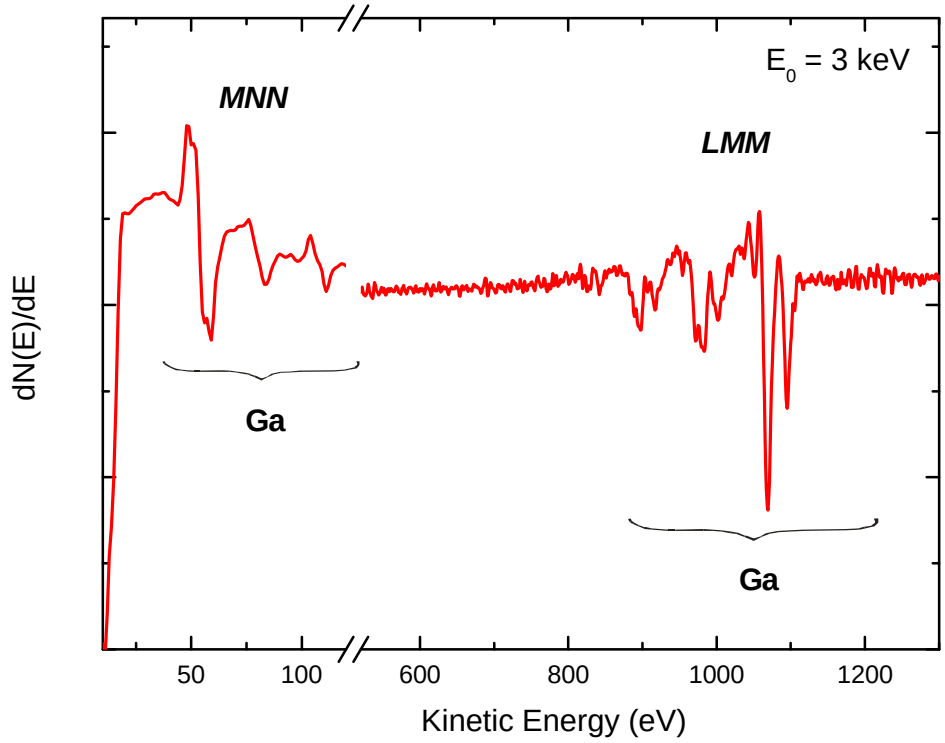

Fig. 6.3. AES spectrum of Ga/Ni(100)

In a different experiment D. A. Kovacs [122] has measured the thermal desorption of Ga and Co from a CoGa sample (single crystal) by means of Mass Spectrometry (MS). In Figure 6.4 the MS intensities of the two gallium isotopes (^{69}Ga and ^{71}Ga) and the cobalt isotope (^{59}Co) are presented as a function of the annealing temperature.

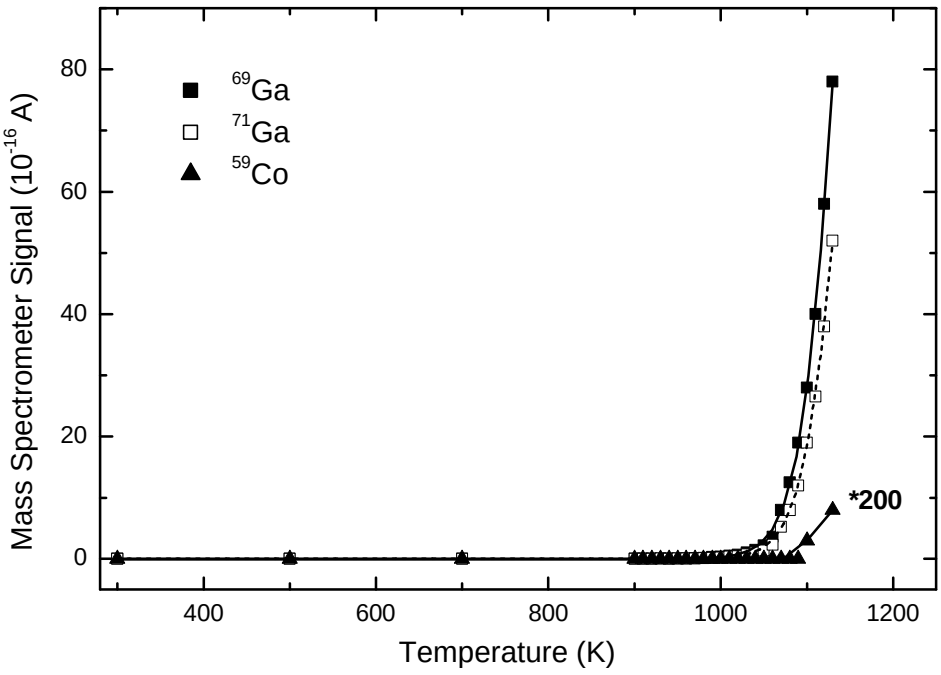

Fig. 6.4. The mass spectrometer signals of Ga (^{69}Ga and ^{71}Ga) and cobalt (^{59}Co) as a function of the annealing temperature of CoGa(100) [122]**.**

The desorption of gallium atoms from the surface starts at ~ 950 K, and the desorption of cobalt at ~ 1100 K. The Co signal was multiplied by 200, because it is very weak in comparison to those of Ga. Thus, the temperature of the crucible filled with CoGa should be between 950 and 1100 K, in order to evaporate Ga only. At 1100 K the Co signal is about thousand times smaller than that of Ga.

6.1.2 The Solid State Evaporator of Ni+Al

The next two figures present the results obtained by using the second crucible of the EFM 3T, which was filled with smithereens of a NiAl crystal. In this case both elements Ni and Al are evaporated simultaneously with the settings we have used according to Table 6.1. Fig. 6.5. shows two calibration curves, taken at the settings **A** (solid circles) and **B** (open circles), which were measured by the quartz microbalance at room temperature. As expected, the nominal thickness increases linearly with deposition time. The nominal deposition rates are 1.8 Å/min and 0.9 Å/min by using the settings **A** and **B**, respectively. In order to determine the nominal thickness by the quartz microbalance the density of Al was used. Therefore, the nominal thickness shown in Fig. 6.5 represents an upper limit for the total Ni+Al layer and by considering the actual composition of the Ni+Al deposit the value of the nominal thickness would be lower.

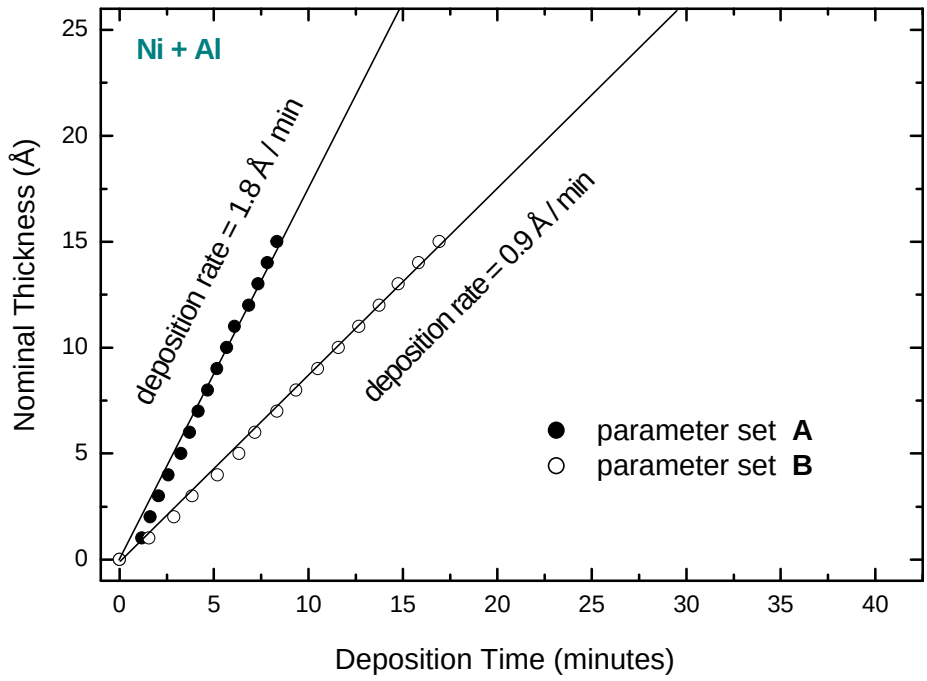

Fig. 6.5. The nominal thickness of the Ni+Al layer measured by the quartz microbalance for the parameter setting A (solid circles) and B (open circles).

Fig. 6.6. shows an AES spectrum taken from a Cu(111) surface, after a nominal deposition of 30 Å of Ni+Al under setting **A** (deposition time ~ 17 min.). No Cu signals are observed anymore and therefore the effective thickness of the deposited layer could not be determined. The AES spectrum exhibits the transitions of both elements Al and Ni. The atomic ratio between Ni and Al in the deposited layer was determined by comparison of the AES data of bulk NiAl [123] to the data of Fig. 6.6. For a single crystal of NiAl (50% Ni, 50% Al) the ratio between the intensity of the KLL transition of Al at 1396 eV and that of the LMM transition of Ni at 848 eV was found to be $I_{Al} / I_{Ni} = 0.22$ [89].

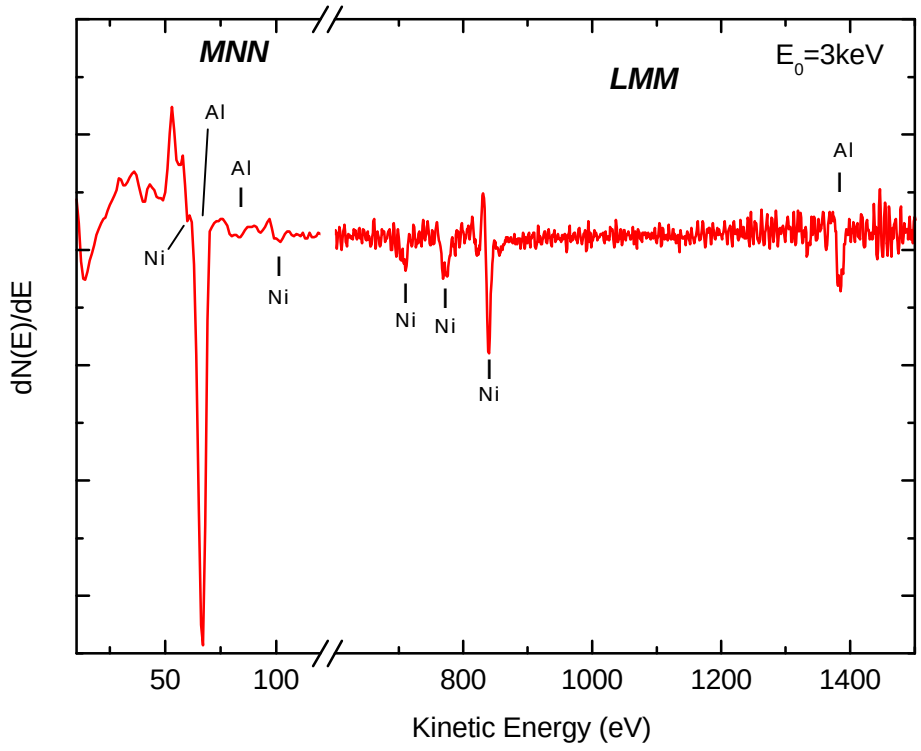

Fig. 6.6. AES spectrum of 30 Å of Ni+Al deposited on Cu(111).

In the experiment described here this ratio amounts to 0.46 and therefore, the atomic ratio between Ni and Al in the overlayer is estimated to be Ni:Al~1:2 with the understanding that the spatial distribution of Ni and Al in the overlayer is homogeneous through the whole thickness. This ratio has to be considered as a very approximate one. In Ref. [89] a thick NiAl single crystal was used, while in this case here a thin layer is produced in which the actual spatial distribution of Ni and Al is not known. Also we have to point out that the composition of the deposit has to be checked each time by AES, because the condition of the pestled CoGa and NiAl is changing with evaporation time. For the crucible filled with pestled NiAl A. Wehner [124] observed that the composition of the deposited layer crucially depends on the parameter setting. By a slight change of the parameters it was also possible to evaporate Al only, at least it was not possible to detect Ni with AES. The best way presumably is to determine the desorption temperatures of Al and Ni by Thermal Desorption Spectroscopy (TDS). However, such an experiment could not be performed in the course of this work.

6.1.3 The Evaporator of Co

Cobalt is evaporated from a high purity rod with a diameter of 2 mm mounted in the third position of the triple evaporator. Fig. 6.7. shows two calibration curves, taken at the settings **A** (solid circles) and **B** (open circles). The nominal thickness depends linearly on the deposition time. With the setting **A** an evaporation rate of 1.5 Å/min was found and with the setting **B** the rate is 0.8 Å/min.

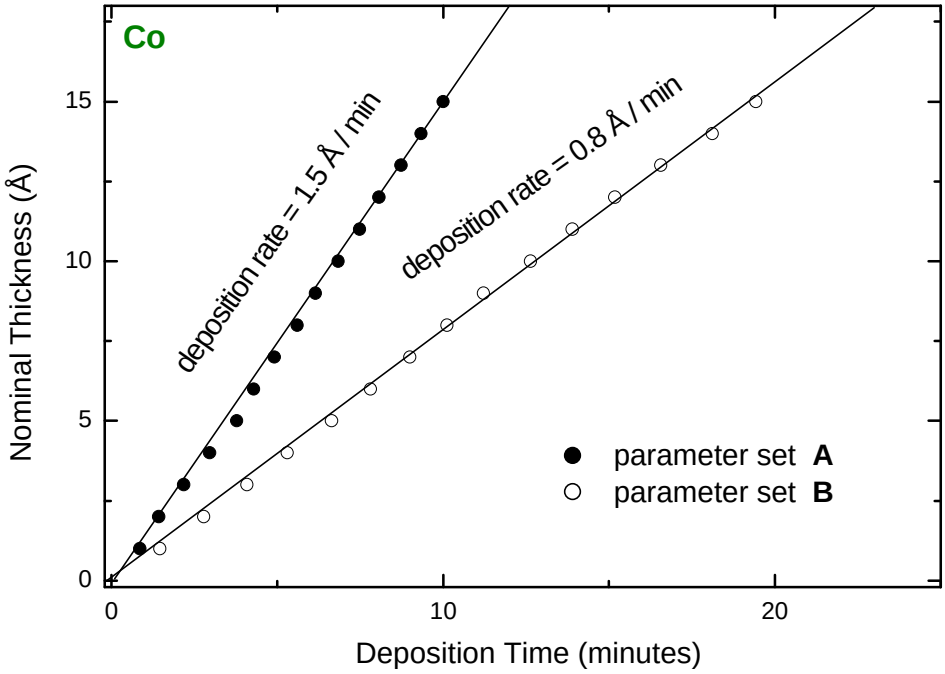

Fig. 6.7. The nominal thickness of the Co layer measured with the quartz microbalance for the parameter setting A (solid circles) and B (open circles).

6.2 An Evaporation Source Based on Pure Ga

A home build Ga evaporator was used in the OMICRON apparatus. Its design is based on the principles which are described in detail in Ref. [125] for the construction of aluminium evaporator, such as reproducibility, long-life, time-independent deposition rate, no measurable codeposition of any support-material, extremely low degas rate for operation at less than 2×10^{-10} mbar. This requires to minimize the necessary electrical energy, in order to avoid the warming-up of the supporting material and, in turn, it allows to manage without water-cool the instrument. It is designed for upward evaporation and can be inclined – accordingly to the inner diameter of the installed (one end closed) alumina tube – as long as the capillary forces keep the liquid inside.

A schematic of the crucible construction is given in Fig. 6.8. The WRe3% filament for resistive heating (0.25 mm f, total length about 200 mm) is wound around the alumina crucible (inner/outer diameter 1.5/3.2 mm, length 11 mm). The spiralic ends of the filament are spot welded to two supporting molybdenum feed rods which on their part are electrically isolated, fixed to a thick copper made base plate. If required, this crucible unit can be easily dissambled from the evaporator and replaced by a crucible for different material. The further support of the base plate is as well made from thick copper for good heat conductivity to the UHV-flange of the apparatus. No extra coolant is required. The evaporated Ga is collimated by an 8 mm f orifice in the housing (as well made from copper and attached to the copper support), which is 7 mm in front of the alumina tube. It can be closed by a shutter.

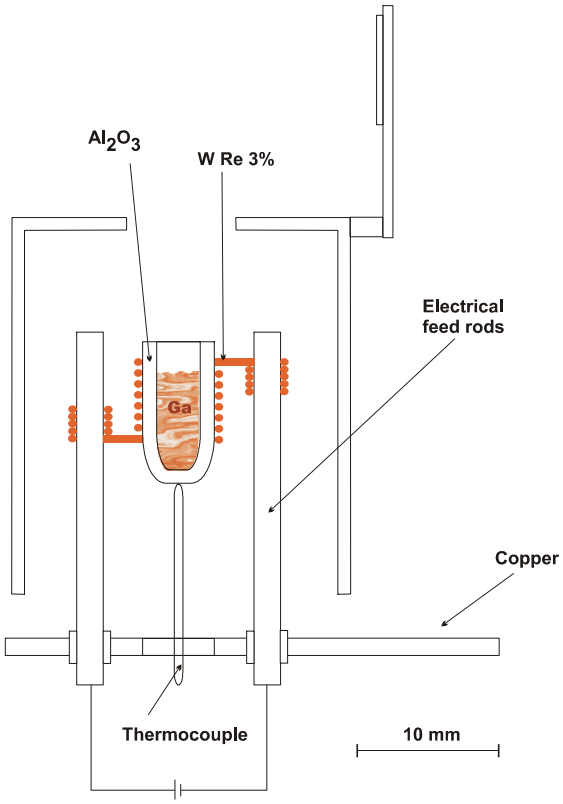

Fig. 6.8. A schematic of the construction of the Ga evaporation source.

Besides the wound around filament the crucible is additionally supported by means of a bifilar alumina tube for the Ni-NiCr thermocouple from below. It is very important, that Ga is one of the few elements which can be evaporated from an Al_2O_3 crucible without dissociation of the oxide below 1370 K. In order to establish a Ga vapor pressure of 10^{-4} mbar, as mentioned above, the temperature of Ga should be ~ 1100 K [46] which is below the temperature, when the oxygen from the Al_2O_3 crucible is attached to the evaporant in measurable amounts [126]. Fig. 6.9 shows two calibration curves, taken at I_{FIL} = 2,1 A (solid circles) and I_{FIL} = 2,0 A and (open circles). The nominal thickness depends linearly on the evaporation time. At a filament current of 2.1 A, an deposition rate of 3.3 Å/min is achieved while at 2.0 A the evaporation rate is reduced to 1.7 Å/min. The composition of the corresponding Ga layers was checked by AES, but no traces of codeposited elements were found in the limits of the AES sensitivity.

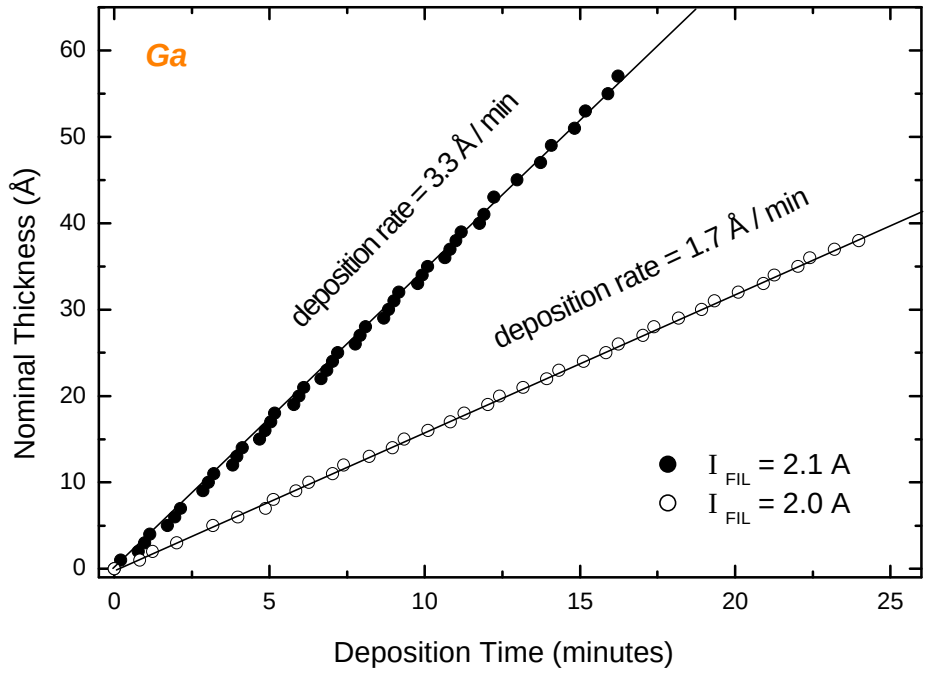

Fig. 6.9. Calibration curves of the deposition of Ga: I_{FIL} = 2,1 A (solid circles) and I_{FIL} = 2,0 A (open circles).

Chapter 7

The Growth of Ultra Thin Al_2O_3 Films on Cu(111)

Well-ordered, thin films Al_2O_3 were grown in the temperature range from 700 to 1200 K on different metallic surfaces, e.g. Re(0001) [127] and Ru(0001) [128] as well as on surfaces of intermetallic alloys, e.g. Ni_3Al (111) [87, 88], Ni_3Al (100) [88], NiAl (111) [89], NiAl (110) [90, 91] and NiAl(100) [86, 92, 129]. Different phases of the Al_2O_3 layers grow depending on the structure of the substrate surface and on the annealing or oxidation temperature. The Al_2O_3 thin films were characterized by Auger electron spectroscopy (AES) [86, 130-132] high-resolution electron energy loss spectroscopy (EELS) [86, 87, 89, 92, 127, 133-138], low energy electron diffraction (LEED) [6, 86-90, 127, 129-131, 133, 138-140], transmission electron microscopy (TEM) [91], X-ray Photoelectron Spectroscopy (XPS) [6, 88, 127, 132, 141], low energy ion scattering (LEIS) [127, 142] and scanning tunneling microscopy (STM) [129, 131, 138, 143-146]. It was found that the surface Al_2O_3 film is terminated with oxygen. Ab initio calculations [136] performed for a 5 Å thick Al_2O_3 (0001) film on the Al(111) and Mo(110) substrates have suggested that the tetrahedral coordinated Al^{3+} ions are located nearly in the same plane as the oxygen ions, for electroneutrality. Since the radius of the O^{2-} ions (1.40 Å) is much larger than the radius of the Al^{3+} ions (0.53 Å), one expects that the surface properties of the oxide is dominated by the oxygen anions [147].

This Chapter deals with the preparation of a well-ordered ultra thin aluminum oxide film on top of the Cu(111) surface. The experiments were performed in the UHV-apparatus I (see Section 4.1.1). The alumina film was prepared by the oxidation of Al atoms which were deposited simultaneously with Ni atoms on Cu(111). The AES investigations provide data concerning the deposition of a Ni+Al layer and the growth of ultra thin Al_2O_3 on Cu(111). The structure of the surface of the thin Al_2O_3 film was studied by LEED. By means of EELS the vibration properties of the oxide film are analyzed.

7.1 Clean Cu(111) Surface

The Cu(111) sample has a diameter of 8 mm and a thickness of 2.5 mm and it was polished mechanically and oriented within an accuracy of 30′. In UHV, the sample was heated by electron bombardment. The main impurities on the Cu(111) surface were sulfur, carbon, and oxygen. They were removed by repeated cycles of Ar^+ - ion sputtering (1 keV, 1 μA) and subsequent annealing to 870 K. The cleanliness of the sample was checked by AES. Fig. 7.1 shows the AES spectrum of clean Cu(111). The MNN Auger transitions of Cu at 20, 60 and 105 eV are clearly resolved. In the high energy region, the AES spectrum of Cu(111) exhibits the LMM multiplet in the energy interval between 731 and 940 eV. The clean sample exhibits a sharp (1×1) LEED pattern, which is also shown in Fig. 7.1.

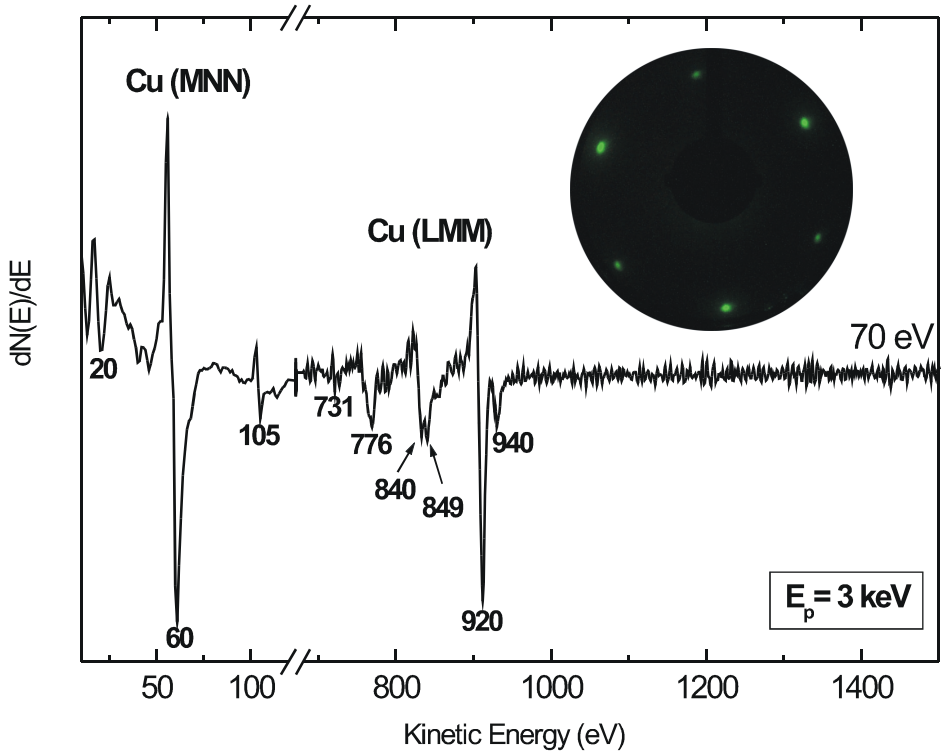

Figure 7.1. AES spectrum of the clean Cu(111) surface and its LEED pattern which shows a (1×1) structure (E_p=70 eV)

7.2 Deposition of Al and Ni on Cu(111)

Ni and Al were simultaneously deposited on Cu(111) substrate by evaporation from a crucible filled with pestle pieces of NiAl. The evaporator and the deposition process are described in Section 6.1.2. By heating of the crucible both elements Al and Ni were evaporated. In this experiment the setting B of the evaporator was used which gives a deposition rate of 0.9 Å/min.

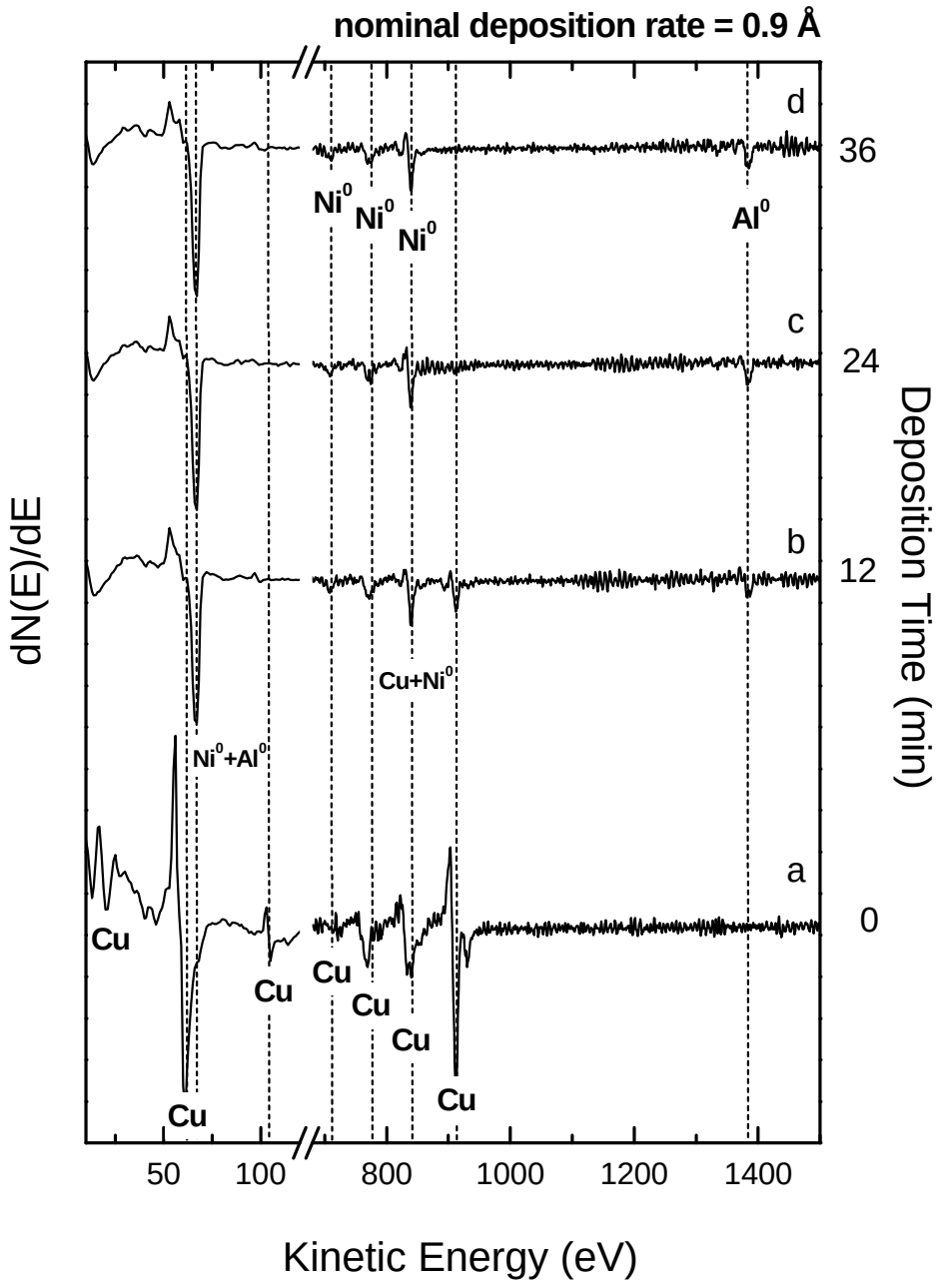

Figure 7. 2 AES spectra recorded at 300 K during deposition of the Ni+Al layers on Cu(111).

Fig. 7.2 shows a set of AES spectra of Cu(111) as a function of deposition time of the Ni+Al layer at 300 K. Spectrum (a) of the clean Cu(111) sample is shown for comparison. During the deposition process the p-to-p intensity of the $Cu_{(920\ eV)}$ transition decreases and vanishes completely for a deposition time of 24 minutes, which corresponds to about 20 Å according to the nominal deposition rate of 0.9 Å/min. During the deposition the AES signals of the $Ni_{(848\ eV)}$- and $Al_{(1396\ eV)}$-transitions appear simultaneously (spectrum (b)) and the p-to-p intensity increases up to a deposition time of 24 minutes (spectrum (c)). The IMFP for electrons with an energy of 920 eV (Cu(LMM)) through a Ni+Al layer is not known. By using the formula of Seah and Dench (1.13) the IMFP was estimated to be 18 Å [50, 148, 149]. Thus, only thickness of layers which are smaller than this value can be determined. The decrease of the intensity of the $Cu_{(920\ eV)}$ transition as a function of deposition time was used to determine the effective thickness of the deposited layer. After a deposition time of 12 min, the effective thickness of the film amounts to 17 Å. Changes of the AES signal of Cu (MNN) at 60 eV, of Al (LMM) at 68 and of Ni (MNN) at 61 eV during the Ni+Al deposition are clearly observed. The AES transitions of $Cu_{(20\ eV)}$ $Cu_{(60\ eV)}$ $Cu_{(105\ eV)}$ are vanished completely after a deposition time of a 12 min and those of $Ni_{(61\ eV)}$ and $Al_{(68\ eV)}$ transitions appear. The disappearance of the AES signals of Cu is due to the fact that the IMFP of the Cu electrons with low kinetic energy is smaller than the thickness of the overlayer ($l \cong 6.4\text{Å}$ for $Cu_{(20\,eV)}$; $l \cong 5.0\text{Å}$ for $Cu_{(60\,eV)}$ and $l \cong 6.1\text{Å}$ for $Cu_{(105\,eV)}$, these values are calculated by using equation (1.13) [50, 148, 149]). The spectra taken after a deposition time of 24 and 36 min are very similar. This is expected for layers with a thickness larger than 18 Å and a homogenous distribution of the two deposited elements (Ni and Al). The atomic ratio between Ni and Al in the deposited overlayer was determined by comparison of the AES data of bulk NiAl to the data of Fig. 7.2 (d). For a single crystal of NiAl (50% Ni, 50% Al) the ratio between the intensity of the Al KLL transition at 1396 eV and that of the Ni LMM transition at 848 eV was found to be I_{Al} / I_{Ni}=0.22 [89, 123]. In the present experiment this ratio amounts to 0.46 and

therefore, the atomic ratio between Ni and Al in the overlayer is estimated to be Ni:Al=1:2. However, this ratio has to be considered very approximately. In the former investigations of bulk NiAl a single crystal [89, 123] was used while in this case a thin layer with randomly distributed Al and Ni atoms is present therefore, which the real spatial distribution of Ni and Al is not known. The spatial distribution of Ni and Al in the overlayer was assumed to be homogeneous over the whole thickness.

The evolution of the AES transitions of Cu, Al and Ni is also represented in Fig. 7.3 which shows the p-to-p intensities of the AES transitions of $Cu_{(920\ eV)}$ $Ni_{(848\ eV)}$ and $Al_{(1396\ eV)}$ as a function of deposition time. During the Ni+Al deposition the p-to-p intensity of $Cu_{(920\ eV)}$ decreases strongly while the p-to-p intensity of $Ni_{(848\ eV)}$ and $Al_{(1396\ eV)}$ is increasing. After 24 minutes of deposition, the intensity of $Ni_{(848\ eV)}$ and $Al_{(1396\ eV)}$ reach a constant value, which is due to the fact that the film thickness (thickness > 18 Å) is already larger, than the IMFP of the $Cu_{(920\ eV)}$ electrons and only the transitions of $Ni_{(848\ eV)}$ and $Al_{(1396\ eV)}$ are observed.

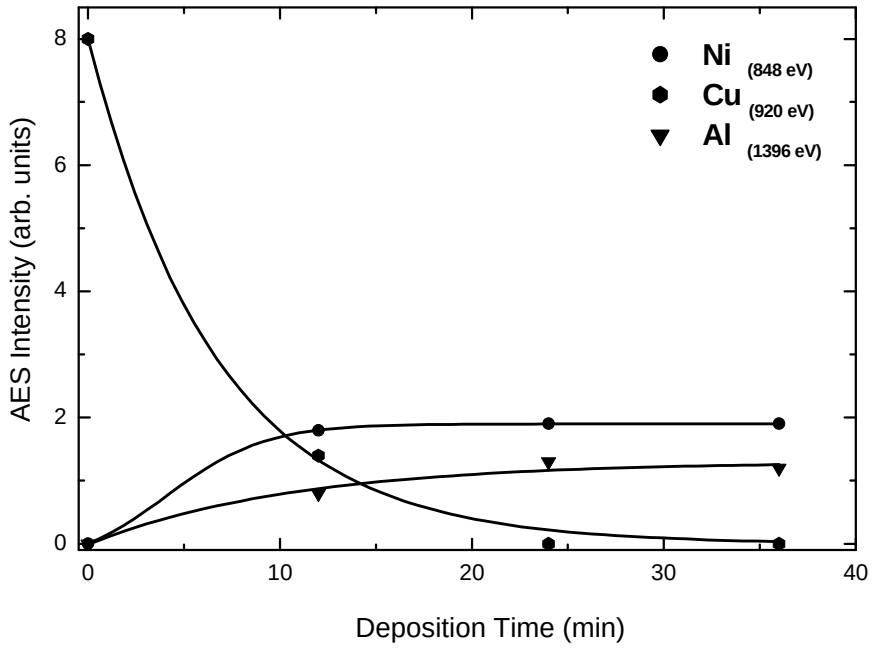

Figure 7. 3. The p-to-p intensity of the AES transitions of $Ni_{(848\ eV)}$ (●), $Al_{(1396\ eV)}$ (▼) and $Cu_{(920\ eV)}$ (⬢) as a function of deposition time.

7.3 Oxidation

7.3.1 AES

The oxidation of Ni+Al layer grown on the Cu(111) surface was performed at 300 K. The Ni+Al layer was exposed to O_2 until a saturation level was reached.

Fig. 7.4 shows two AES spectra of a 30 Å thick Ni+Al overlayer on Cu(111): (a) before and (b) after oxidation at 300 K, with 1500 L of oxygen. As we will show below, 1500 L represents saturation exposure. Spectrum (a) which was recorded before exposing the surface to oxygen shows the Ni LMM triplet, the AES transitions of Al (KLL) and the AES transitions of Ni at 61 eV and Al at 68 eV.

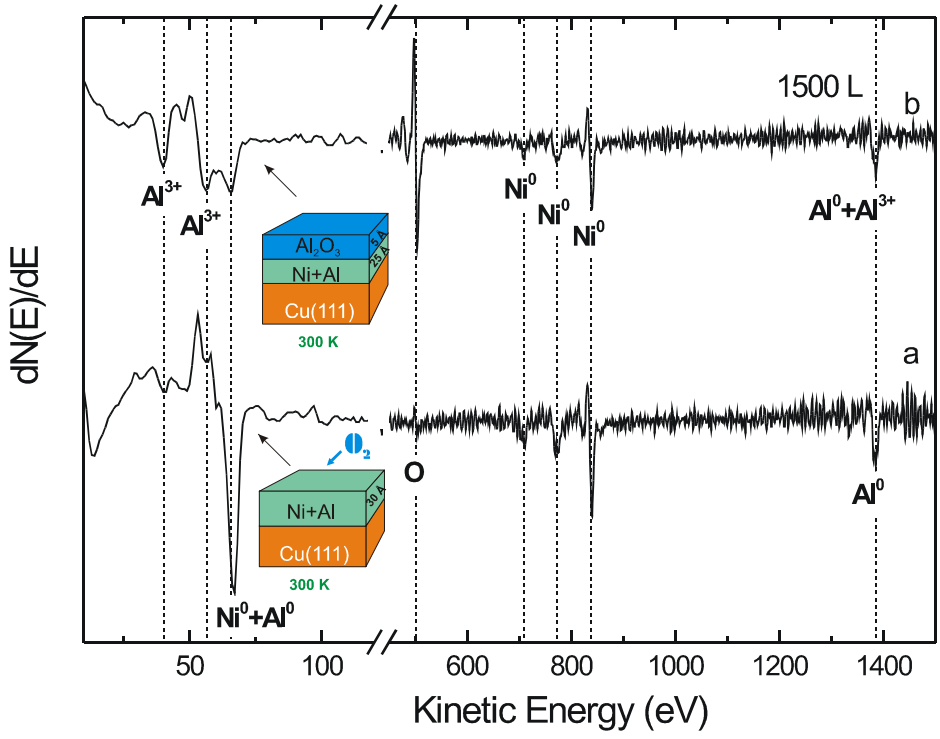

Figure 7. 4 Two AES spectra of Ni+Al grown on Cu(111) recorded at 300 K before (a) and after (b) oxidation of the Ni+Al layers with 1500 L at 300 K on Cu(111). A sketch of the oxidation procedure is also shown.

These later two transitions are not resolved and overlap. In addition, a small AES signal of oxygen is observed, which results from adsorption from the residual gas. After oxidation with 1500 L the spectrum shows a intense signal of the O (KLL) transition. In the low energy region (10 – 110 eV) the characteristic transitions of Al^{3+} at 35 eV and 53 eV appear. The p-to-p intensity of the transitions of Ni at 848 eV and Al at 1396 eV is decreased with respect to those in spectrum (a). A small signal around 68 eV is also visible which indicates that not all the Al and Ni atoms of the Ni+Al layer were oxidized. The KLL transition of Al initially at 1396 eV is shifted to 1378 eV, which together with the appearance of the signals of Al^{3+} (at 35 and 53 eV) are due to the oxidation of the aluminum atoms and to the formation of Al^{3+} ions, which suggests the growth of an Al_2O_3 layer on the surface.

Fig. 7.5 shows the p-to-p ratios $I_{O(503\,eV)}/I_{Al(1378\,eV)}$, $I_{O(503\,eV)}/I_{Ni(848\,eV)}$ and $I_{Ni(848\,eV)}/I_{Al(1378\,eV)}$ as a function of oxygen exposure. The partial pressure of oxygen was kept at 1×10^{-6} mbar. Both curves $I_{O(503\,eV)}/I_{Ni(848\,eV)}$ and $I_{O(503\,eV)}/I_{Al(1378\,eV)}$ have the same behavior. For oxygen exposure <100 L the uptake curves increase strongly, while after an exposure of about 200 L the curves become flatter and at around 500 L a saturation level is reached. This is typical for the growth of a thin oxide film in the regime of low oxidation temperatures. According to Cabrera-Mott the criterion for the low temperature oxidation is the term $qaE > kT$ [99], where q is the ionic charge, a is the half distance between two equilibrium places for the ions in the oxide, E is the electric field and k is the Boltzmann constant. This mechanism is also called electric field-supported growth. There is an inverse-logarithmical growing law for the dependence of the film thickness x on the time t:

$$\frac{x_1}{x} = K'' - \ln t \qquad \text{with } x_1, K'' = const..$$

In Fig. 7.5b is represented the ratio $I_{O(503\,eV)}/I_{Al(1378\,eV)}$ as a function of oxygen exposure in a logarithmic scale dependence. The perfect logarithmic dependence

confirms the field-supported growth mode. The ratio $I_{Ni(848\,eV)}/I_{Al(1378\,eV)}$ decreases, because of decreasing of the amount of Ni atoms in the oxide overlayer, i.e only the Al atoms of the Ni+Al layer are oxidized, which will be shown below. Based on the AES data the thickness q of the Al_2O_3 layer was estimated to be ~5 Å.

The ratio $I_{O(503\,eV)}/I_{Al(1378\,eV)}$ at saturation amounts to ~4.5, a value which was also found for the oxidation of $Ni_3Al(100)$ at 300 K [150].

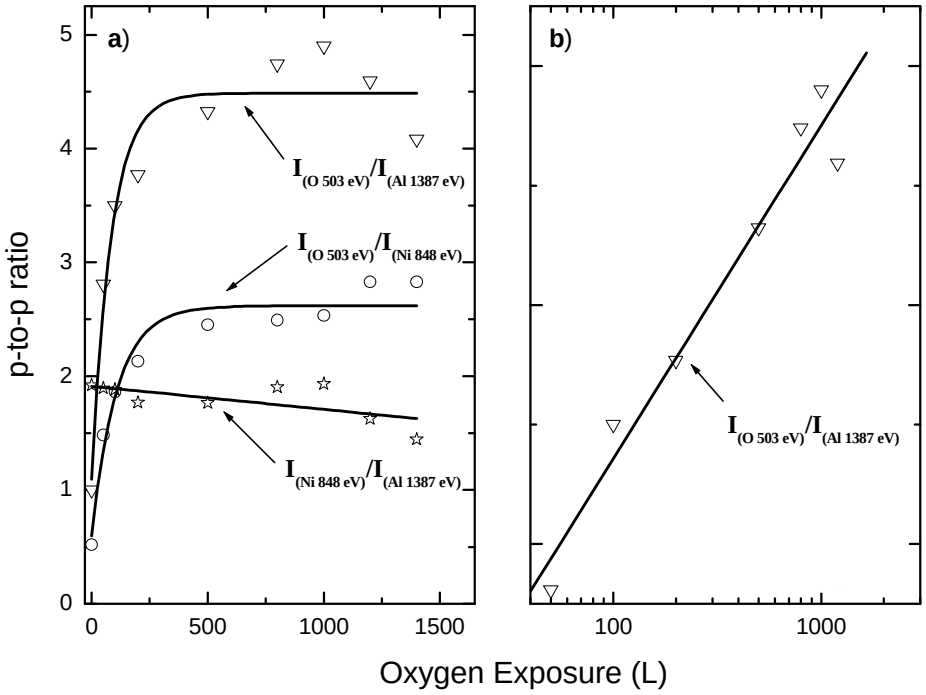

Figure 7. 5. Oxygen uptake curves of oxidation at 300 K. The AES ratios of $I_{O(503\,eV)}/I_{Al(1378\,eV)}$ (▽), $I_{O(503\,eV)}/I_{Ni(848\,eV)}$ (○) and $I_{Ni(848\,eV)}/I_{Al(1378\,eV)}$ (☆) are represented as a function of oxygen exposure: (a) linear and (b) logarithmic dependence.

Based on the experimental findings represented in Fig. 7.4 and 7.5 the following scenario is suggested (sketched as a model in Fig. 7.4): Oxidation at 300 K with an oxygen exposure above 200 L leads to the formation of an aluminum oxide overlayer. However, not the whole Ni+Al layer seems to be oxidized, and only the Al atoms are involved in the oxidation process. Thus, between the Cu(111) substrate and the Al_2O_3 layer a ~25 Å thick interface layer remains, which consists in Ni atoms and unoxidized Al atoms.

Afterwards, the trilayer system Al_2O_3/Ni+Al/Cu(111) was annealed in steps of 100 K, at each temperature for 2 min, up to ~1200 K. Fig. 7.6 shows the p-to-p intensity of the AES transitions as a function of the annealing temperature. It illustrates the behavior of the ultra thin Al_2O_3 film and the interface layer by annealing the system Al_2O_3/Ni+Al/Cu(111). During annealing the p-to-p intensity of the $Cu_{(920\ eV)}$ transition increases while all other decrease. This is explained by the diffusion of Cu atoms to the interface layer, which starts immediately above 300 K and/or by the diffusion of atoms the Ni+Al interface layer into the Cu(111) substrate. Up to 700 K, no signal of the AES transition of Cu at 60 eV is observed which suggests that the Cu atoms have diffused only in the Ni+Al interlayer and not on the top of the oxide layer. Up to 700 K the p-to-p intensities of $Ni_{(848\ eV)}$, $Al_{(1378\ eV)}$ and $O_{(503\ eV)}$ remain constant. After annealing at 900 K the $Ni_{(848\ eV)}$ transition is strongly diminished and after annealing at 1100 K it disappears completely, whereas the intensity of the of aluminum and oxygen decreases by approximately 50% and 30%, respectively. At 900 K, a week Cu signal at 60 eV is also observed, which increases simultaneously with that one at 920 eV. Thus, after annealing above 900 K the total thickness of the overlayer has decreased or some Cu atoms have diffused in the upper part of the interface layer. Therefore, Cu atoms are located just below the Al_2O_3 layer. The $Al^{3+}{}_{(1387\ eV)}$+$Al^{0}{}_{(1396\ eV)}$ transition decreases continuously with increasing of the temperature. Unfortunately, these both transitions can not be clearly resolved.

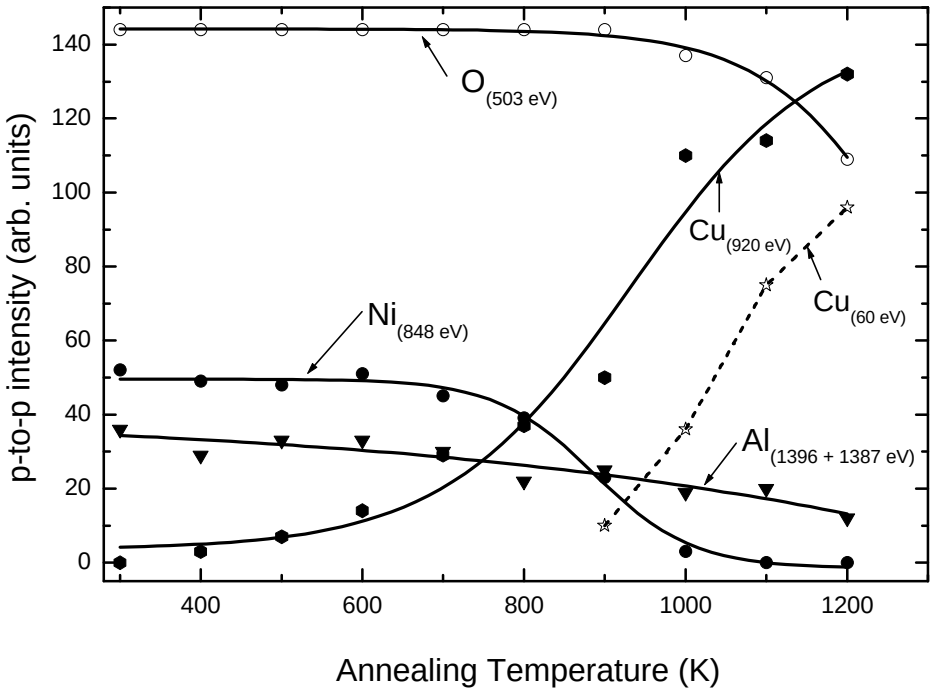

Fig. 7.6. The p-to-p intensity of the AES transitions of $O_{(503\ eV)}$ (○), $Cu_{(920\ eV)}$ (⬢), $Cu_{(60\ eV)}$ (☆), $Ni_{(848\ eV)}$ (●) and $Al_{(1396\ +\ 1387\ eV)}$ (▼) as a function of annealing temperature.

The decrease of the AES signals of $Al_{(1396\ eV)}$ and of $Ni_{(848\ eV)}$ shows that all the Ni and the Al atoms of the Ni+Al interlayer have diffused into the substrate. This is in agreement with the increase of the intensity of the Cu transitions at 920 and 60 eV.

In Fig. 7.7 are shown some typical AES spectra obtained after annealing at 900 and 1200 K. The spectrum (a) in Fig. 7.7 shows the AES spectrum of the Al_2O_3/Ni+Al/Cu(111) system. After annealing at 900 K, the Ni-triplet and the Cu-triplet overlap, but the signals of the Ni transitions still dominate. In the low energy region small signals of the Cu transitions at 20 and 60 eV appear. The AES signals of oxygen and aluminum at 503 and 1387 eV, respectively, have almost the same intensity as those of spectrum (a). Taking into account the

relative intensity of the transitions of bare Cu at 920, 840 and 849 eV, the p-to-p intensity at 848 eV can be attributed to about 40% of Cu and 60% of Ni. This corresponds to a smaller amount of Ni in comparison to the initial amount. Consequently, by annealing up to 900 K Ni atoms diffuse in part into the Cu substrate. By annealing above 300 K (see Fig. 7.6) the Cu transitions at higher kinetic energy appear again and increase continuously during the step-by-step heating, while the intensity of the $Ni_{(848\ eV)}$ transition decreases and disappears completely at 1200 K. This can be explained by a diffusion of Ni into the substrate. After annealing at 1200 K, the p-to-p intensity of the KLL transitions of Al and $O_{(503\ eV)}$ transitions also decreased: for example, the intensity of the O and Al transition at 1200 K corresponds to 50% of the intensity at 300 K. The decrease of the signal of the KLL transitions of Al is definitely related to the diffusion of the Al atoms of the Ni+Al interlayer into the Cu(111) substrate.

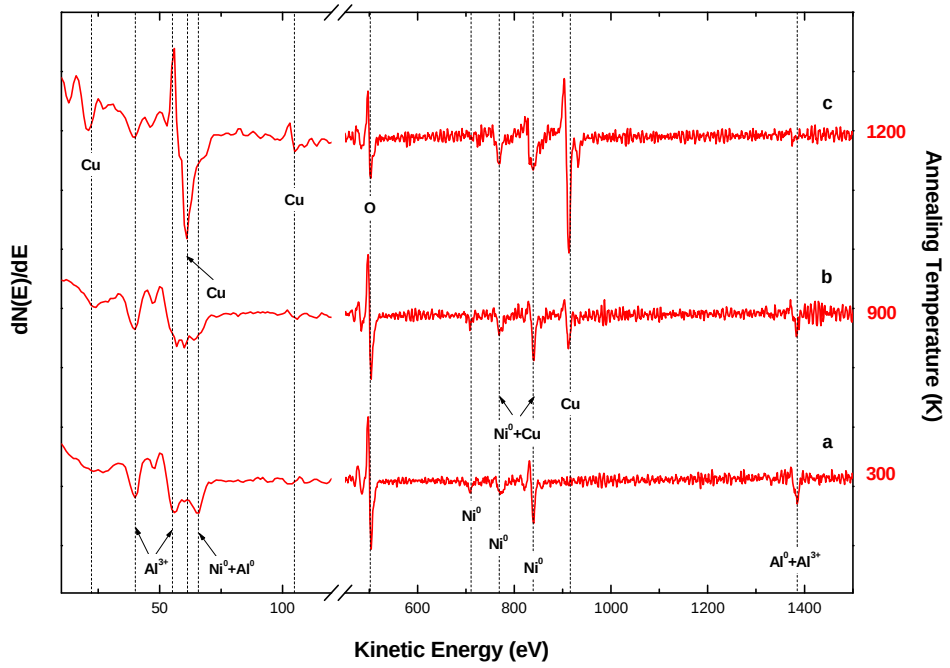

Figure 7. 7 AES spectra of the Al_2O_3/Ni+Al/Cu(111) system at 300, 900 and 1200 K.

At this temperature Al_2O_3 persists on the surface. At 1200 K (Fig. 7.7 (c)), all the AES transitions of Ni in the low and high energy region disappeared, suggesting that the total amount of Ni have diffused into the bulk of Cu. From the AES spectra (c) we can draw also another conclusion: In the high energy region the Al KLL transitions occurs clearly at 1387 eV without a signal at 1396 eV. Thus only Al^{3+} - ions are present which together with the oxygen ions form the thin Al oxide layer.

The shape of the low-energy transitions is changed also during the annealing process. Starting from 300 K (spectrum (a)) the intensity of the $Ni_{(61)}$ and $Al_{(68)}$ transitions decrease and disappear completely at ~900 K (spectrum (b)). This suggests also that Ni and the metallic Al atoms diffuse into the substrate. For annealing up to 1200 K the p-to-p intensity of the Al^{3+} transitions at 35 eV and 53 eV is also decreased, but still present (spectrum (c)). The $Cu_{(60)}$ transition occurs above 900 K (spectrum (c)) and increases up to 1200 K (spectrum (c)). This shows that after annealing above 900 K the total thickness of the overlayer has decreased to about 5 Å which corresponds to the Al_2O_3 layer or some Cu atoms are segregated to top layers below the oxide. However, the EELS measurements, which we present below, show that a "clean" Al_2O_3 remains on the Cu(111) surface, and therefore, Cu atoms do not segregate on the top of the oxide.

7.3.2 LEED

By deposition of a Ni+Al layer at 300 K the LEED pattern becomes diffuse, but the substrate spots can be seen up to a nominal deposition of ~10 Å. This suggests that the Ni+Al layer grows in three-dimensional islands on Cu(111). Above a nominal deposition of 10 Å of Ni+Al the substrate diffraction spots vanish completely and the LEED screen exhibits only diffuse illumination. During oxidation at room temperature the LEED pattern remains diffuse showing that an amorphous oxide layer is formed. Similar results are reported for the room-temperature oxidation of NiAl(001) [86, 129, 151], NiAl(110) [152], and

NiAl(111) [89]. After annealing to 900 K, a very weak LEED pattern was observed. After annealing to 1200 K, the LEED pattern shows a complicated structure which can be identified with a hexagonal structure. (Fig. 7.8a). A schematic representation of the LEED pattern is shown in Fig. 7.8b. By comparison with the lattice constant of Cu(111), the lattice constant of the hexagonal structure is determined to be 3.1 ± 0.1 Å.

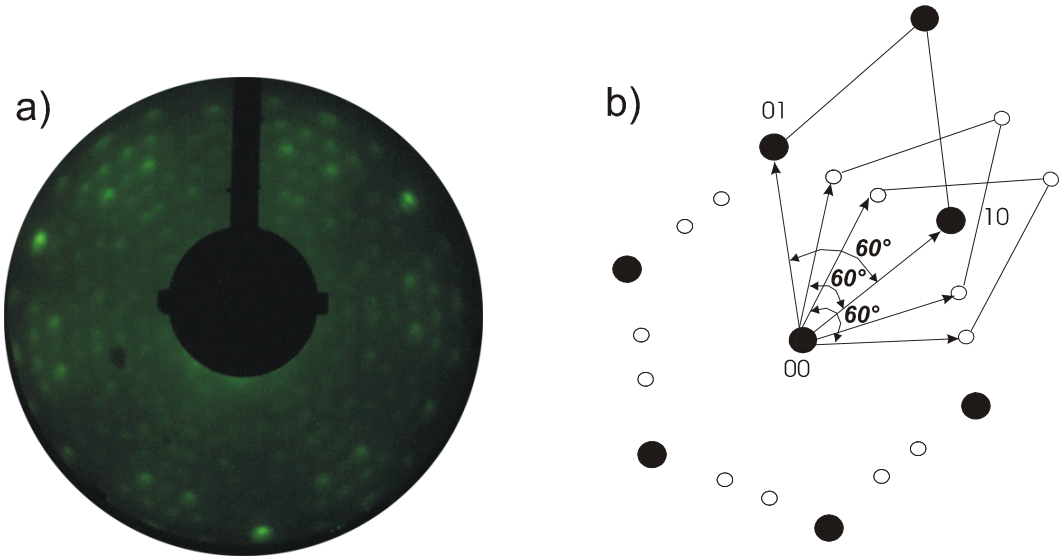

Figure 7. 8 (a) LEED pattern of the ordered ultra thin aluminum oxide layer after annealing at 1200 K, E = 70 eV; (b) schematic representation of the pattern.

The hexagonal structure results from a (111) plane of the γ- and γ´-Al_2O_3 phase or from α-Al_2O_3. The latter phase can be ruled out due to the observed three losses in the EELS investigations (see Section 7.3.3). The lattice constant of ~3 Å suggests an oxygen termination of the Al_2O_3 layer which was observed for most of the thin films of Al_2O_3. The agreement of the lattice constant estimated from LEED with the length of the basis vectors of the (111) plane of γ´-Al_2O_3 suggest

that the oxide grows with the (111) plane parallel to the surface plane. The growth of thin layers of γ- and/or γ´-Al_2O_3 layer was reported for the oxidation at elevated temperature of NiAl(110) [90], NiAl(111) [89], Ni_3Al(111) [88], and FeAl(111) [127], and for Al layers deposited on Re(0001) [127] and Ru(0001) [128]. The main diffraction spots can be simulated by two hexagonal or nearly hexagonal lattices grown in two domains rotated by 15°. Most of the low intensity Bragg spots could be a result of multiple diffraction effects and could not be reproduced by a simple simulation which took into account only geometrical effects. On the other hand, the presence of low intensity spots observed close to the center of the LEED pattern suggests that a superstructure with a large unit cell could be present on the surface as well. In a DFT (Density Functional Theory) study [153] it was shown that the top layer could consist in nearly coplanar Al^{3+} and O^{2-} ions. The ordering of an Al_2O_3 film after annealing at 1200 K was observed also in earlier studies by oxidation of NiAl(001) [86, 92], Ni_3Al(111) [88] and NiAl(110) [90].

7.3.3 EELS

The growth Al_2O_3 on Cu(111) was also investigated by EELS. Fig. 7.9 shows an EEL spectrum after oxidation of a 10 Å thick Ni+Al overlayer on Cu(111) at 300 K and subsequent annealing to 1200 K. The EEL spectrum exhibits three broad losses at 410 (ν_1), 620 (ν_2) and 885 cm^{-1}(ν_3). The frequency of these losses corresponds to that found for thin Al_2O_3 layer grown on NiAl(111) (426, 635 and 885 cm^{-1}) [89], on NiAl(001) (420, 603 and 896 cm^{-1}) [86, 92, 138], and on Ni_3Al(111) (440, 648 and 910 cm^{-1}) [84]. Therefore, we conclude that on Cu(111) also only Al_2O_3 is formed. No evidence for a Ni or Cu oxide is found.

Based on the enthalpies of formation of Al_2O_3 $\left(\Delta H_f = -1675.7 kJmol^{-1}\right)$, NiO $\left(\Delta H_f = -240.8 kJmol^{-1}\right)$ [78], CuO $\left(\Delta H_f = -157.3 kJmol^{-1}\right)$, and Cu_2O $\left(\Delta H_f = -168.6 kJmol^{-1}\right)$ the oxidation of aluminum is thermodynamically more favorable. Hence, one expects that only aluminum is oxidized in a Ni+Al layer.

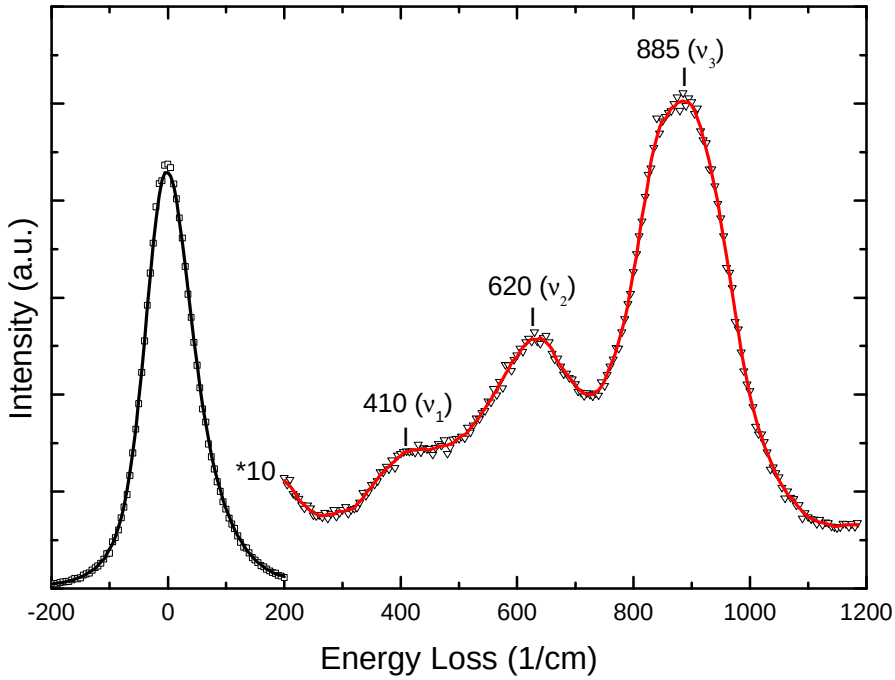

Fig. 7.9. EEL spectrum of the ordered ultra thin aluminum oxide layer after annealing at 1200 K.

In general, it is also possible that the oxide, formed at ~ 300 K, consist in a mixture of both nickel oxide and Al_2O_3. Becker et al. [87], have reported that EELS measurements have revealed the presence of energy losses that correspond to nickel-oxygen bonds for adsorption of oxygen at room temperature on a $Ni_3Al(111)$ surface. Furthermore, these authors have found that the EELS losses associated with Ni-O bonds [87] disappear when the oxide was heated above 800 K. The EEL spectrum taken after annealing to 1200 K is typical for Al_2O_3, and therefore, after annealing to this temperature, no Ni-oxide is present in the overlayer, which is consistent with the study of Becker et al. [87]. Aluminum oxide exists in the form of several phases in different temperature ranges [84]. Room-temperature oxidation of Ni+Al alloys yields an amorphous aluminum oxide (a-Al_2O_3), phase in which Al^{3+} cations are tetrahedral coordinated [86].

Upon annealing at temperatures in the range between 700 and 1200 K and depending on the substrate surface the amorphous phase usually is transformed into a γ-like Al_2O_3 phase, which consists of octahedral and tetrahedral coordinated aluminum cations arranged in a fcc oxygen sublattice [86]. EEL spectra of thin alumina films of the γ-like Al_2O_3 phase and θ-Al_2O_3 phase on metal substrates show commonly three distinct phonon features in the frequency regions of 380 – 430 cm^{-1}, 620 – 660 cm^{-1}, and 850 – 900 cm^{-1} with slightly different relative loss intensities between the modes [89, 90, 127, 135]. These modes are related to different alumina phases, in which Al^{3+} ions occupy both octahedral and tetrahedral sites in an oxygen fcc lattice. Therefore, we conclude that in the case of Al_2O_3 on Cu(111) the Al oxide belongs to a γ-like phase (probably γ´-Al_2O_3) and the oxide grows with the (111) plane parallel to the Cu(111) surface. However, the exact knowledge of the oxide phase and structure and, based on that, lattice-dynamic calculation would be a great help for a detailed explanation of the three loss features.

Summary

The scenario, described in this Chapter is schematically presented as a model in Fig. 7.10. At 300 K, a Ni+Al layer grows disordered on the Cu(111) surface, with an atomic ratio of Ni:Al = 1:2. Up to 10 Å,

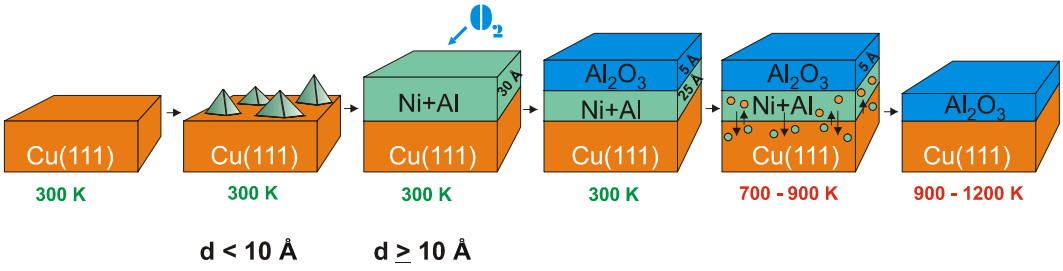

Fig. 7.10. Schematic model of the growth of ultra thin Al_2O_3 films on Cu(111).

Ni+Al grows in 3D clusters on the surface afterwards the whole surface is covered with a Ni+Al overlayer.

Oxidation at 300 K leads to the formation of an amorphous aluminum oxide and a trilayer system Al_2O_3/(Ni+Al)/Cu(111) is established. After annealing to ~ 900 K, an ultra thin well-ordered Al_2O_3 is grown, while the atoms of Ni and metallic Al start to diffuse into the volume of the Cu(111) substrate. Simultaneously, some Cu atoms diffuse to the top layers on the Ni+Al interlayer. The complex LEED pattern reveals an ordering of the aluminum oxide. The AES, LEED and EELS investigation of an oxidized Ni+Al overlayer on Cu(111) at elevated temperature show that an ultra thin overlayer of γ-like Al_2O_3 grows on Cu(111).

Chapter 8

Growth of Ultra Thin Ga_2O_3 Films on Ni(100)

Most of the insulating layers (tunneling barrier) in TMR structures consist in Al_2O_3 which in the bulk has a band gap of ~ 8 eV. An alternative to the Al_2O_3 layers are Ga_2O_3 layers. Ga_2O_3 has in the bulk a band gap of 4.5 eV and consists in various phases which are isomorph to the corresponding Al_2O_3 phases. An advantage of using Ga_2O_3 instead of Al_2O_3 consist in the fact that much lower temperature are needed for the formation of well-ordered (crystalline) Ga_2O_3 thin layers.

Thin films of Ga oxide grow by the oxidation of the surfaces of GaAs [154], CoGa [84, 93-95] and GaN epilayers [155]. On CoGa, during the oxidation process, Ga atoms segregate from the bulk to the surface and react with adsorbed oxygen. Oxidation of CoGa (100) in the temperature range at 600 – 900 K leads to the formation of well-ordered β-Ga_2O_3, which grows in two domains, which are perpendicular to each other [84, 94, 95, 156]. The vibrational properties and the structure of β-Ga_2O_3 on CoGa (100) [94, 156] and θ-Al_2O_3 on NiAl (100) [86] are very similar. At 770 K, a well-ordered thin Ga_2O_3 film grows on CoGa(110) which has a hexagonal structure [93].

Ga_2O_3 exists in different modifications, all of which are based on the close-packed oxygen lattice (See Section 5.2). The most important are α-Ga_2O_3, β-Ga_2O_3 and γ-Ga_2O_3. The α-Ga_2O_3 is metastable and has a hexagonal corundum structure with the lattice constants $a = 4.98\text{Å}$ and $c = 13.43\text{Å}$. At 920 K, it

transforms into the β-Ga_2O_3 phase [110]. The stable β-Ga_2O_3 phase has a monoclinic structure and is isomorphic to θ-Al_2O_3. The corresponding lattice constants amount to: $a = 3.04\text{Å}$, $b = 5.80\text{Å}$, $c = 12.23\text{Å}$, and $b = 103.7°$ [157, 158]. The γ-Ga_2O_3 phase is isomorphic to γ-Al_2O_3 and has a cubic lattice with a spinel structure ($MgAl_2O_4$-type) with a lattice constant $a = 8.22\text{Å}$ [110]. In analogy to γ´-Al_2O_3, a γ´-Ga_2O_3 may exist which has also a spinel structure but the unit cell is only half of that of γ-Ga_2O_3 (See Section 5.2).

Ga presents a complicate phase diagram with many stable and metastable phases. Under normal conditions the stable bulk phase is α-Ga which presents a remarkable coexistence of metallic and covalent character [103, 159, 160]. The growth of Ga nanoparticles on silica at 100 K was studied under the influence of irradiation with 1 μs pulses of a 1.55 μm diode laser with a peak power of 17 mW at rate of 1 kHz. The irradiation results in the formation of Ga nanoparticles with a narrow size distribution [161].

The question which is addressed in this Chapter is how does a thin films of Ga_2O_3 (amorphous and crystalline) of few Å grow on a ferromagnetic substrate. As a substrate a single crystal of Ni was used which was cut in the direction of the (100) plane. First, Ga was deposited on the Ni(100) surface and afterwards oxidized. The growth temperature of Ga was 80 K in one experiment and 300 K in the other. The investigations were performed by means of high-resolution electron energy loss spectroscopy (EELS), low-energy electron diffraction (LEED), Auger electron spectroscopy (AES), and Scanning Tunneling Microscopy (STM).

This Chapter is organized as follows: Section 8.1 presents the clean Ni(100) surface. Section 8.2 deals with growth of Ga_2O_3 at 80 K. The consecutive subsections 8.2.1 and 8.2.2. track down the growth of Ga layer at 80 K and the oxidation behavior of Ga. In Section 8.3 are presented the growth of Ga on Ni(100) at 300 K (Subsection 8.3.1) and the oxidation of Ga film (Subsection 8.3.2).

8.1 Clean Ni(100) Surface and the c(2´2) - O - Ni(100)

8.1.1 Clean Ni(100)

The Ni (100) sample has a diameter of 8 mm and a thickness of 2.5 mm for the experiments in the UHV System I and a diameter of 3 mm and a thickness of 2 mm for the experiments in the UHV-OMICRON apparatus. The samples were polished mechanically and oriented with a precision of 0.5°. The main impurities on the Ni (100) surface were sulfur, carbon, and oxygen, which were removed by repeated cycles of Ar^+ - ion sputtering (1 keV, ~1.0 μA) and subsequent annealing at 1200 (UHV I) and 950 K (UHV OMICRON).

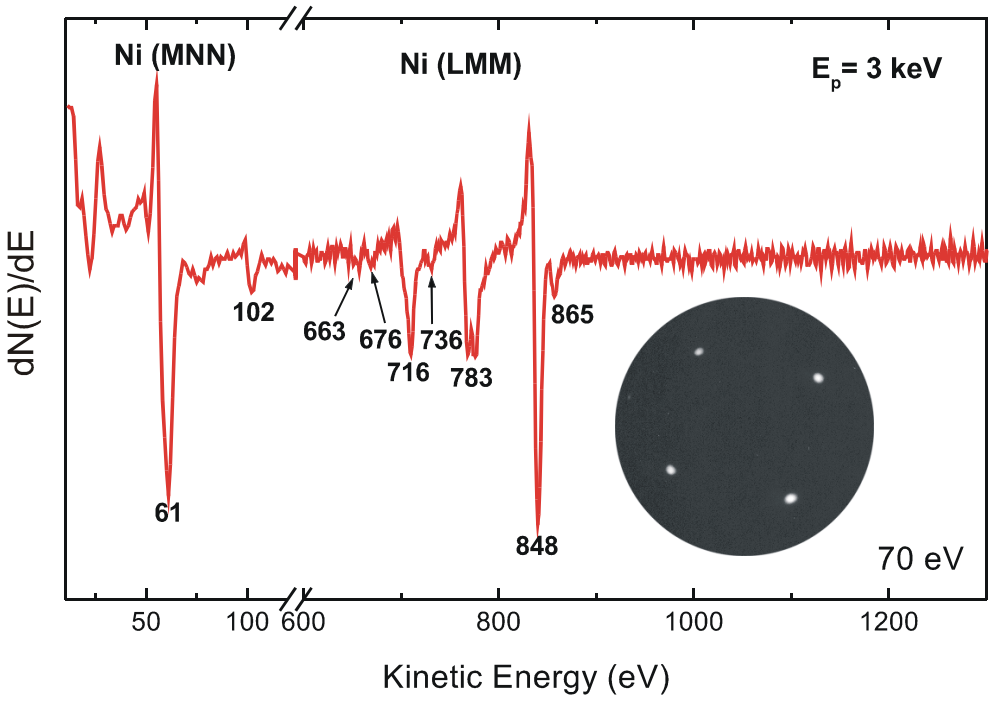

Figure 8.1. AES spectrum of the clean Ni(100) surface and the LEED pattern showing a (1×1) structure (E_p=70 eV)

The cleanliness of the sample was checked by AES and further evidenced by the formation of a sharp (1×1) LEED pattern.

Fig. 8.1 shows a typical AES spectrum of the clean Ni(100). The MNN Auger transitions of Ni at 61 and 102 eV are clearly resolved. In the high energy region, the AES spectrum of Ni(100) exhibits a multiplet (LMM) in the energy interval between 663 and 865 eV with the most intensive transition at 848 eV. The clean sample exhibits a sharp (1×1) LEED pattern, shown also in Fig. 8.1.

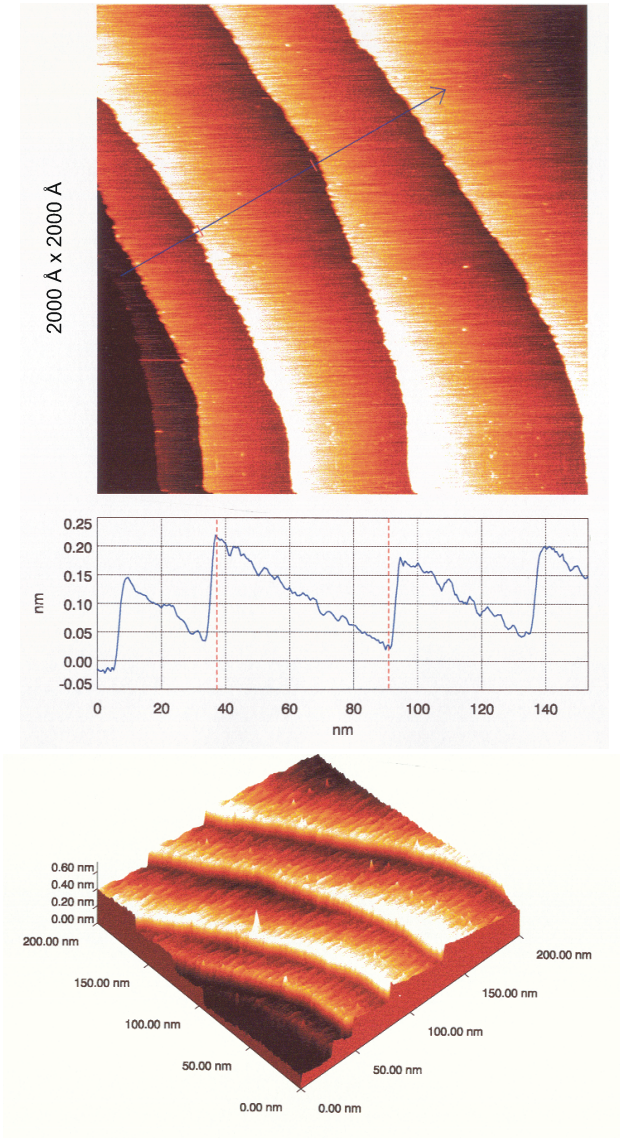

Figure 8.2. The topography of the clean Ni(100) surface (2000 Å × 2000 Å; U_t = 10 mV; I_t = 0.6 nA): a) 2D image with line profile; b) 3D image

The clean Ni(100) exhibits large terraces of several hundred Å. Fig. 8.2 shows a large scale 2D and 3D STM images of the Ni(100) surface. From the line scan the average terrace width of this surface was measured to be around 400 Å, although terraces of more than 1000 Å extension as well as regions with high step density were also found.

The terraces were separated by mono-atomic steps of ~1.72 Å height.

8.1.2 The c(2×2) – O – Structure on Ni(100)

In order to get better intermixing of the deposited Ga layer with oxygen first, a c(2×2) oxygen overlayer was prepared on Ni(100) by adsorption of 80 L of O_2 at room temperature and subsequent annealing at 420 K [162].

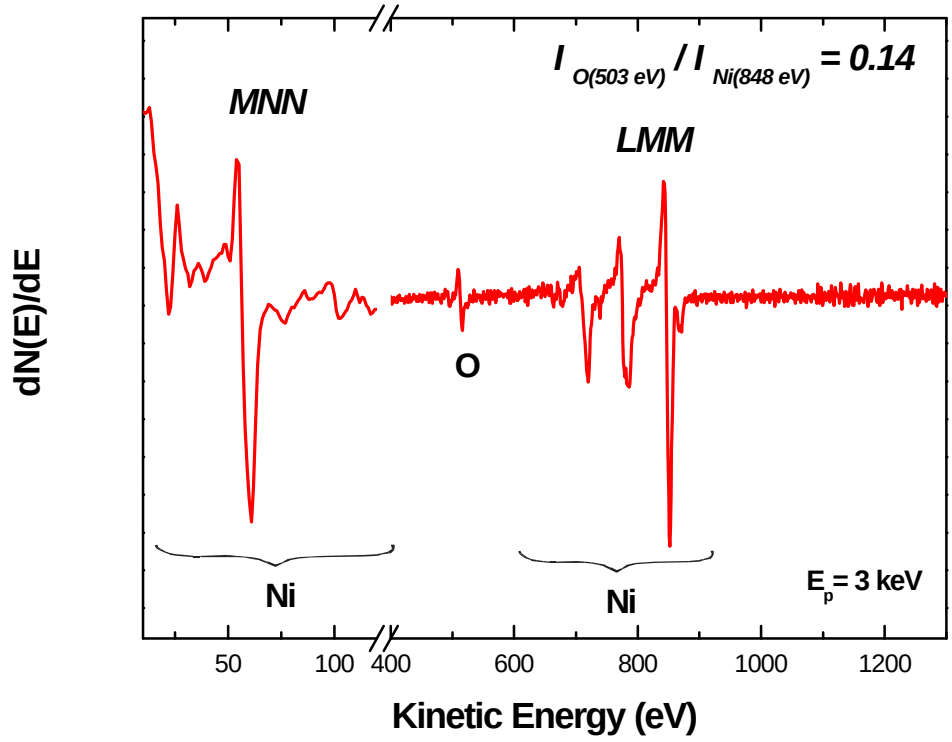

Fig. 8.3 The AES spectrum of the O-c(2×2)/Ni(100) surface.

Fig. 8.3 shows the AES spectrum of the O-c(2×2)/Ni(100) surface. The peak-to-peak (p-to-p) ratio of $I_{O(503eV)}/I_{Ni(848eV)}$ is 0.14, which corresponds to the coverage of $q_0 \sim 0.5$.

Fig. 8.4 shows a EEL spectrum of the O-c(2×2)/Ni(100) surface and an LEED pattern. The EEL spectrum exhibits two losses at 270 and 330 cm^{-1} which agree with the losses (265 and 306 cm^{-1}) found by Franchy at al. [162] for the O-c(2×2) overlayer on Ni(100). The LEED pattern shows a typical c(2×2) structure. Thus, the EEL spectrum, the LEED pattern and the AES data are used as a reference for a well prepared c(2×2) overlayer of oxygen on Ni(100).

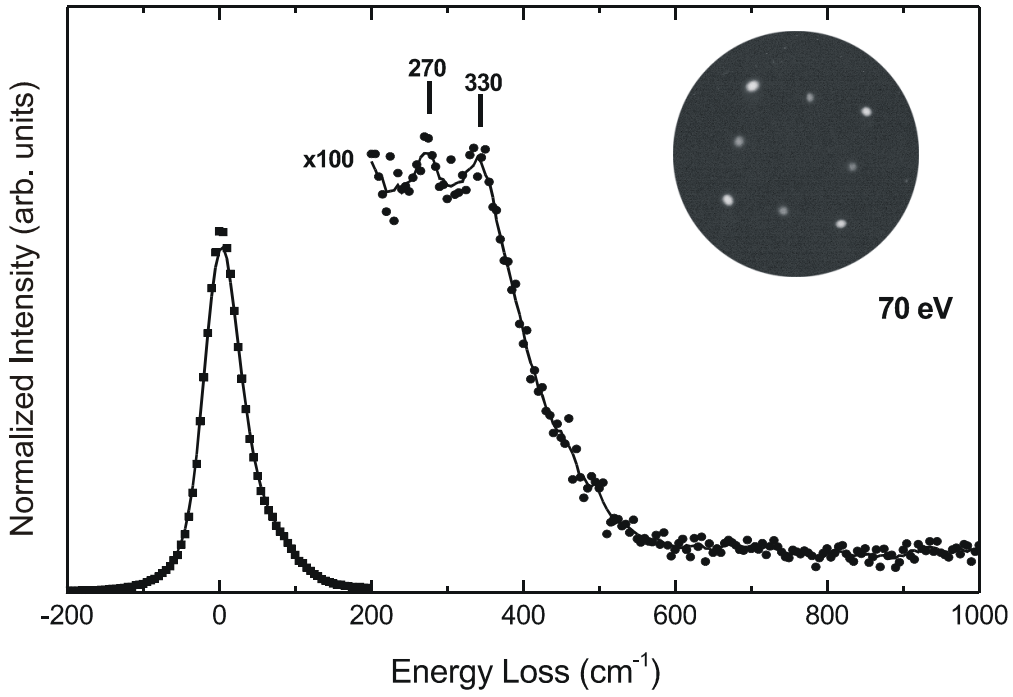

Fig. 8.4 The EEL spectrum and the LEED pattern of the O-c(2×2)/Ni(100) surface.

8.2 Growth of Ga_2O_3 Films at 80 K

8.2.1 Deposition of Ga on O-c(2×2)/Ni(100) at 80 K

Ga was deposited at 80 K on Ni(100) by evaporation from a crucible filled with pestled CoGa (See Section 6.1). Fig. 8.5 shows an AES spectrum of O-c(2×2)/Ni(100) surface after deposition of 30 Å (nominal thickness) Ga at 80 K. The evaporator (see Section 6.1.1) was operated with the parameter set **B** with a rate of 1.2 Å/min. After the deposition of Ga with a nominal thickness of 30 Å the Ni LMM and MNN transitions vanished completely. The intensity of the O KLL transition at 503 eV changes only by a factor of 0.8 (Fig. 8.5).

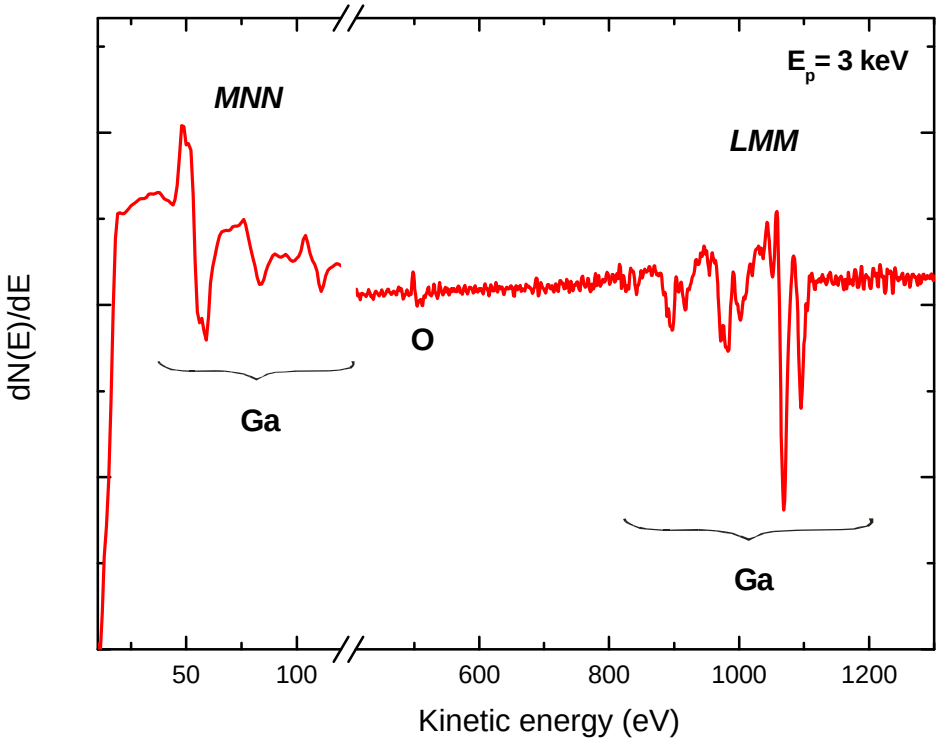

Fig. 8.5. AES spectrum of 30 Å of Ga deposited at 80 K on O-c(2x2)/Ni(100).

This suggests that at 80 K oxygen atoms from the O-c(2×2) overlayer (coverage q_0 ~ 0.5) diffuse into the Ga layer. The AES spectrum shows the Ga MNN transitions at 55, 81, 108 eV and the Ga LMM transitions between 830 and 1097 eV.

The IMFP for electrons with an energy of 848 eV (Ni(LMM)) through a Ga layer is not known. By using the formula of Seah and Dench (Equation 1.13) the IMFP was estimated to be 18 Å [50, 148, 149]. Thus, only thicknesses of layers which are thinner than this value can be determined. Fig. 8.6 shows the p-to-p intensity of the Auger transitions of $Ni_{(848\ eV)}$, $O_{(503\ eV)}$ and $Ga_{(1070\ eV)}$ as a function of the deposition time. During Ga deposition the intensity of $Ni_{(848\ eV)}$ decreases, while the signal of $Ga_{(1070\ eV)}$ increases. After a deposition time of 15 min, the effective thickness of the film amounts to 18 Å.

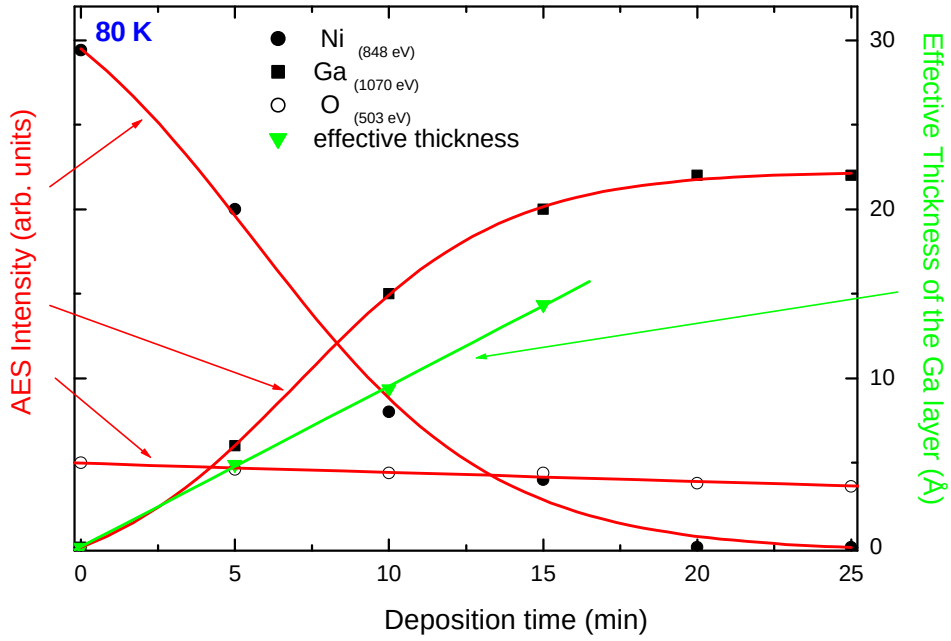

Figure 8.6. The p-to-p intensity of the AES transitions of $Ni_{(848\ eV)}$ (●),$O_{(503\ eV)}$ (○), $Ga_{(1070\ eV)}$ (■), and the effective thickness of the Ga layer as a function of the deposition time of Ga.

The $Ni_{(848\ eV)}$ signal vanishes completely for a deposition time of 20 minutes, which according to the estimated effective deposition rate of 1.2 Å/min, corresponds to a nominal thickness of 24 Å. The $O_{(503\ eV)}$ signal decreases a little during the whole deposition time of the Ga. This is a result of the diffusion of oxygen atoms from the c(2×2)-structure into the Ga layer. On the right side of the figure 8.6. is shown the effective thickness of the Ga layer as a function of the deposition time. The effective thickness was calculated from the decrease of the intensity of the $Ni_{(848\ eV)}$ transition. The effective thickness of the Ga layer depends linearly on the deposition time. From the linear part of the curve, the effective deposition rate of 1.2 Å/min was estimated, which is equal to the deposition rate determined by the quartz microbalance (Section 6.1.1).

8.2.2 Oxidation

The oxidation of the Ga layer with an effective thickness of 30 Å on the top of O-c(2×2)-Ni(100) was performed in two steps. First, the Ga layer was oxidized at 80 K, after that the Ga oxide layer was annealed in steps of 100 K up to 700 K. At 700 K the layer was exposed again to oxygen.

8.2.2.1 AES

At 80 K, a ~ 30 Å thick Ga layer was oxidized with oxygen until a saturation level has been reached. Fig 8.7 shows the p-to-p intensity of the AES transitions as a function of oxygen exposure. Two different LMM Auger transitions of Ga are resolved: the transition of metallic $Ga^0_{(1070\ eV)}$ and the transition of ionic $Ga^{3+}_{(1066\ eV)}$, which is formed during the oxidation. With increasing of oxygen exposure, the intensity of the $Ga^{3+}_{(1066\ eV)}$ increases at the expense of the intensity of the $Ga^0_{(1070\ eV)}$ which decreases simultaneously. This is due to the transformation of the metallic Ga^0 atoms into Ga^{3+} ions. Both the signals of LMM transitions of $Ga^{3+}_{(1066\ eV)}$ and of KLL transition of $O_{(503\ eV)}$ increase with increasing of the oxygen exposure up to ~ 1000 L.

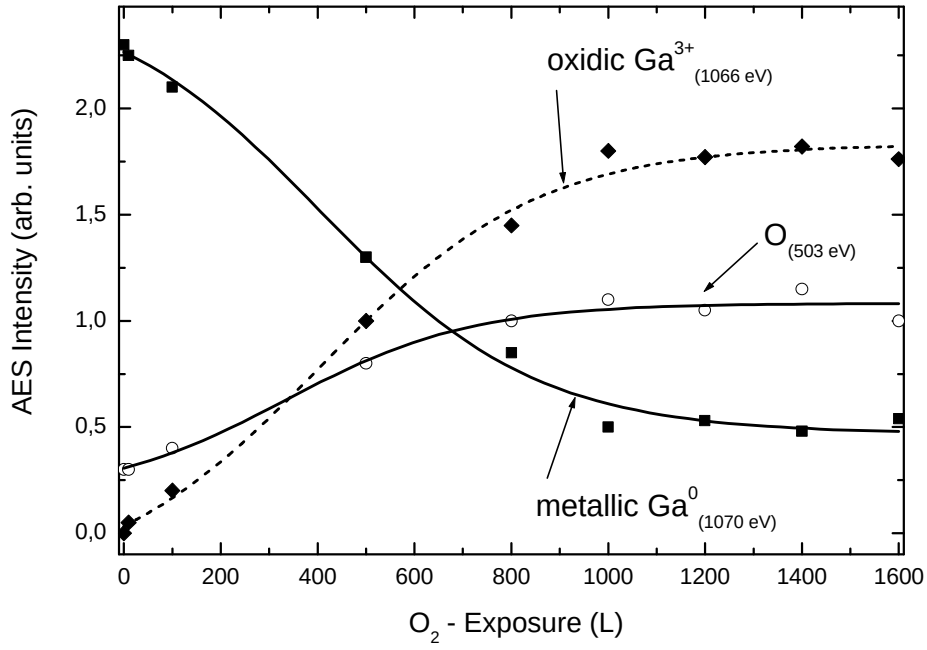

Fig. 8.7. The p-to-p intensity of the AES transitions of $O_{(503\ eV)}$, $Ga^{0}_{(1070\ eV)}$ and $Ga^{3+}_{(1066\ eV)}$ as a function of O_2 exposure at 80 K.

Above this exposure the signals remain constant, which shows that a saturation level is reached. Two AES one before (a) and one after (b) oxidation at 80 K with 1600 L of oxygen are shown in Fig. 8.8. Spectrum (a) shows the LMM multiplet of the metallic Ga between 830 and 1097 eV as well as the transitions in the low energy region at 55, 81 and 108 eV and a small oxygen signal which originates from oxygen atoms from the c(2×2) oxygen which have segregated to the surface. After oxidation all the transitions are shifted to lower energies (spectrum (b)) which is caused by the transformation of the Ga^0 atoms into Ga^{3+} ions. The oxygen transition at 503 eV can be used as a reference point (evidence), to determine the energy of the AES transitions. The values of the transitions of the Ga^{3+} ions are as follows:

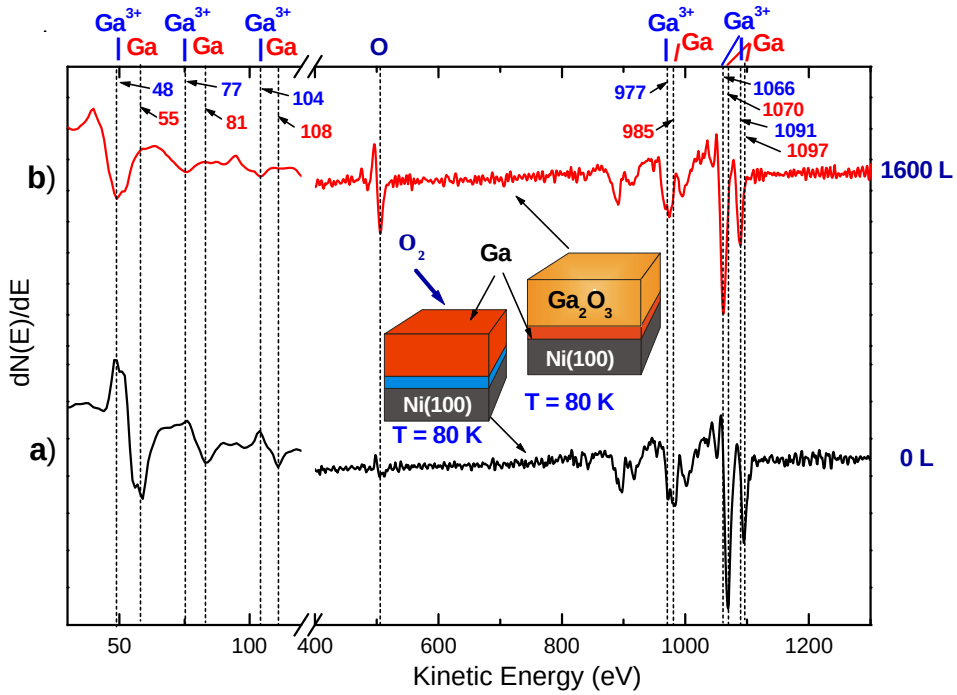

Fig. 8.8. Two AES spectra: (a) before and (b) after oxidation of the Ga layer with 1600 L at 80 K on Ni(100). A model of the oxidation feature is also shown. The interlayer represents the O-c(2x2) structure on Ni(100).

- MNN transitions at 48, 77 and 104 eV;
- LMM transitions at 977, 1066 and 1091 eV.

To our knowledge there are no data about the shifts of the binding energy (X-ray data) or of the kinetic energy of AES transitions due to the transition from the neutral to ionic state of Ga. Therefore, the absolute values of the AES energies of the ionic Ga^{3+} states have to be considered with precaution. In the low energy region no signals of the neutral Ga atoms are observed anymore. This suggests that a Ga_2O_3 layer with a thickness of at least ~ 5 Å (the IMFP in this region) is present. The signals of the LMM transitions of metallic Ga^0 and of Ga^{3+} are may be convoluted and therefore it seems that between the Ga_2O_3 layer and the Ni(100) substrate a interlayer of Ga may exists.

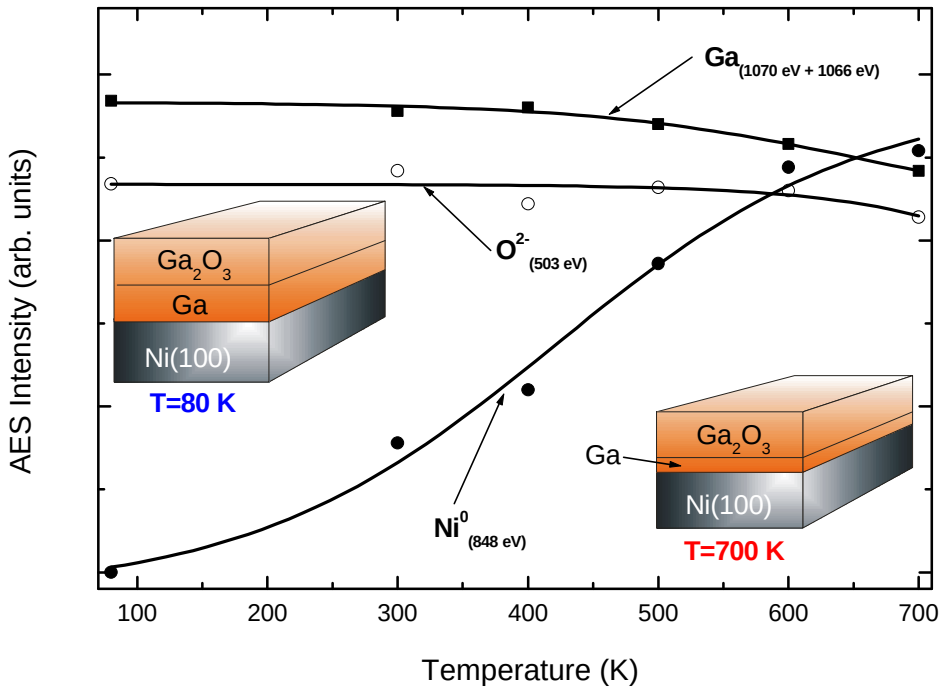

Fig. 8.9. The p-to-p intensity of the AES transitions of $O_{(503\ eV)}$, $Ni_{(848\ eV)}$, and $Ga_{(1066\ +\ 1070\ eV)}$ as a function of annealing temperature. The solid lines represent a guide for the eyes. The models show the changes of the Ga_2O_3/Ga/Ni system.

After oxidation at 80 K the grown Ga oxide on Ni(100) was annealed step by step up to 700 K. Fig. 8.9 shows the evolution of the p-to-p intensity of the $Ni_{(848\ eV)}$, $Ga_{(1070\ +\ 1066\ eV)}$, and $O_{(503\ eV)}$ AES transitions during annealing. With increasing of the temperature, the $Ni_{(848\ eV)}$ signal starts to increase. The AES intensities of the $Ga_{(1070\ +\ 1066\ eV)}$ and $O_{(503\ eV)}$ transitions show a stable behavior with a small decrease after 500 K. Thus, Ga_2O_3 is stable in this temperature region and the small decrease is may be due to the diffusion of unoxidized Ga atoms into the Ni substrate, or to the ordering of the oxide layer. From the increase of the intensity of the $Ni_{(848\ eV)}$ AES transitions, the thickness of the Ga_2O_3 is calculated and it amounts to ~ 15 Å after annealing at 700 K.

Fig. 8.10 shows an overview of the evolution of the AES ratio intensity of O/Ga (a) during oxidation at 80 K, (b) during annealing between 80 and 700 K, and (c) during oxidation at 700 K. The O/Ga p-to-p ratio during the oxidation at 80 K (plot (a)) shows that above 1000 L a saturation level is reached. During annealing of the Ga oxide the O/Ga p-to-p ratio remains constant (plot (b)). The appearance of the $Ni_{(848\ eV)}$ transition at 300 K and the increase of its AES signal with temperature leads to a decrease of the O/Ni p-to-p ratio (plot (b)). May be the Ga_2O_3 layer contains also some unoxidized Ga atoms. The presence of such atoms is confirmed by the further oxidation at 700 K (plot (c)). The AES p-to-p ratio of O/Ga increases with the increase of oxygen exposure up to ~ 500 L. Above this exposure a saturation level is reached.

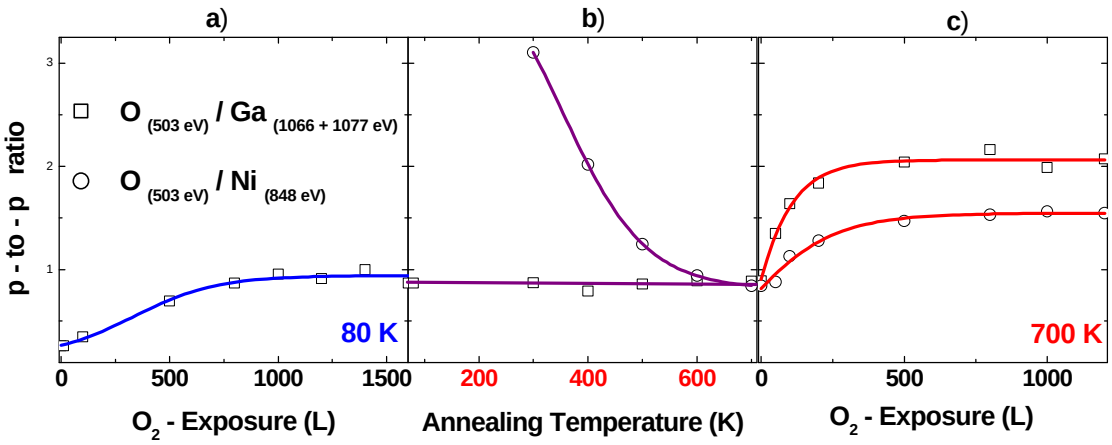

Fig. 8.10. O/Ga p-to-p ratio as a function of a) O_2 exposure at 80 K; b) annealing temperature in the range between 80 – 700 K; c) O_2 exposure at 700 K. In addition, in plots b) and c) the dependence of the O/Ni – ratio is shown.

The thermal stability of grown Ga oxide was also studied. Fig. 8.11. shows the intensity of the $Ni_{(848\ eV)}$, $Ga^{3+}{}_{(1066\ eV)}$ and $O_{(503\ eV)}$ AES transitions as a function of

the annealing temperature. Up to around 950 K both $O_{(503\ eV)}$ and $Ga^{3+}{}_{(1066\ eV)}$ signals remain almost constant which suggests that the Ga_2O_3 is thermostable. Simultaneously, the $Ni_{(848\ eV)}$ signal increases continuously with temperature, which could be either because the thickness of the overlayer is decreasing, or because the Ga oxide becomes better ordered.

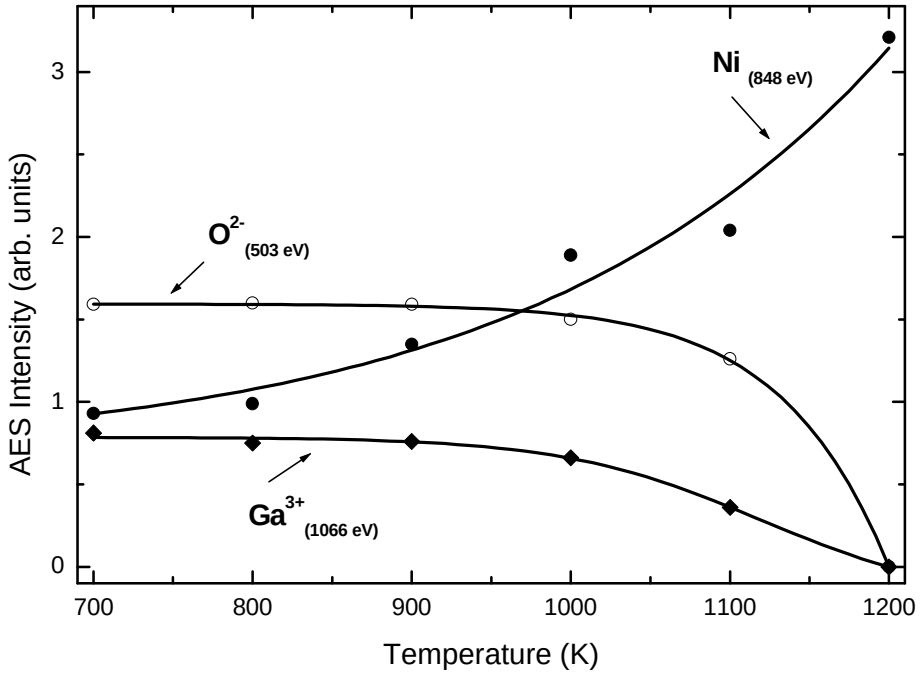

Fig. 8.11. The AES intensity of the AES transitions of $Ni_{(848\ eV)}$ (●),$O_{(503\ eV)}$ (○) and $Ga^{3+}{}_{(1066\ eV)}$ (◆) as a function of the annealing temperature.

After annealing above 950 K the intensity of $Ga^{3+}{}_{(1066\ eV)}$ and $O_{(503\ eV)}$ transitions starts to decrease faster while that of $Ni_{(848\ eV)}$ is still increasing. From the increase of the intensity of the AES $Ni_{(848\ eV)}$ transition the effective thickness of the Ga_2O_3 layer, after annealing at 950 K, is estimated to be ~ 5.5 Å. At 1200 K, the Ga_2O_3 is decomposed and desorbed from the surface and an AES spectrum of clean Ni surface was found.

8.2.2.2 EELS

The growth and the vibrational properties of Ga oxide in the temperature range between 80 and 1200 K were also studied by EELS.

Fig. 8.12 shows two EEL spectra: (bottom) after deposition of a 30 Å thick Ga layer on the O-c(2×2) layer on Ni(100) at 80 K and (top) after exposing this Ga layer to 1500 L of oxygen at 80 K. In the bottom spectrum the intensity of the elastic beam is very low (~ 10^3 c/s) and no certain loss can be observed. This is not surprising, because the Ga layer is not ordered and scattering from such a surface always gives a low intensity and a broad angular distribution. No loss corresponding to covalent stretching mode of Ga dimers at 7 THz (~ 234 cm^{-1}) [163, 164] could be resolved. The spectrum at top is obtained after exposing the Ga layer at 80 K to 1500 L of O_2 which corresponds to the saturation level. The EEL spectrum exhibits a broad loss feature between 450 and 900 cm^{-1}. Such a loss feature corresponds to vibrations of different Ga-O bonds.

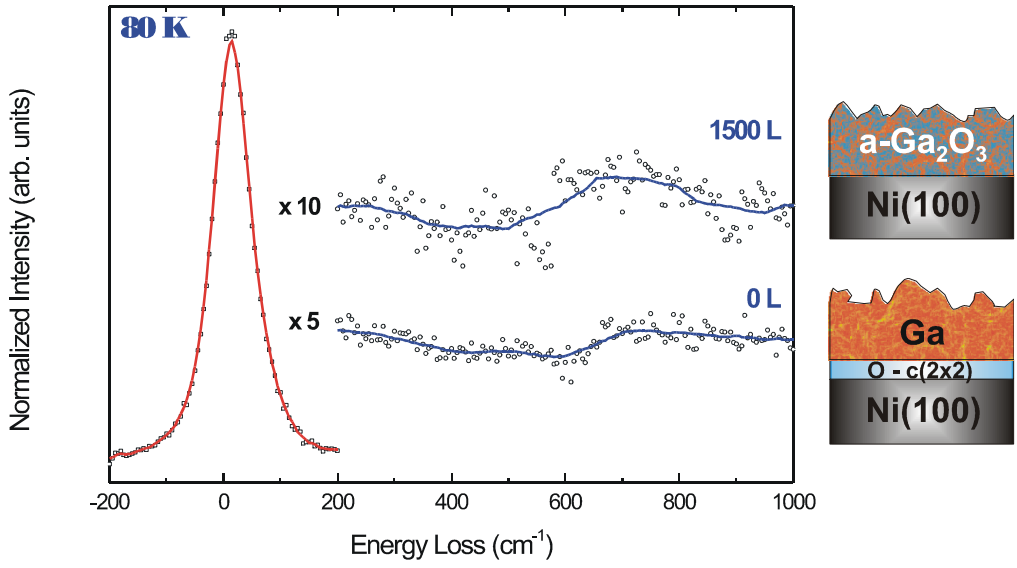

Fig. 8.12. EEL spectra of Ga-O/Ni(100) as a function of oxygen exposure at 80 K

However, the shape of this loss feature does not permit to assign some certain loss to a specific Ga-O bond. The models on the right side of Fig. 8.12 show the scenario which may takes place at 80 K: The Ga layer is unordered and the exposure to oxygen leads to the penetration of oxygen into the Ga layer where an amorphous Ga oxide grows.

Fig. 8.13 shows EEL spectra after oxidation at 80 K of the Ga layer on Ni(100) as a function of the annealing temperature.

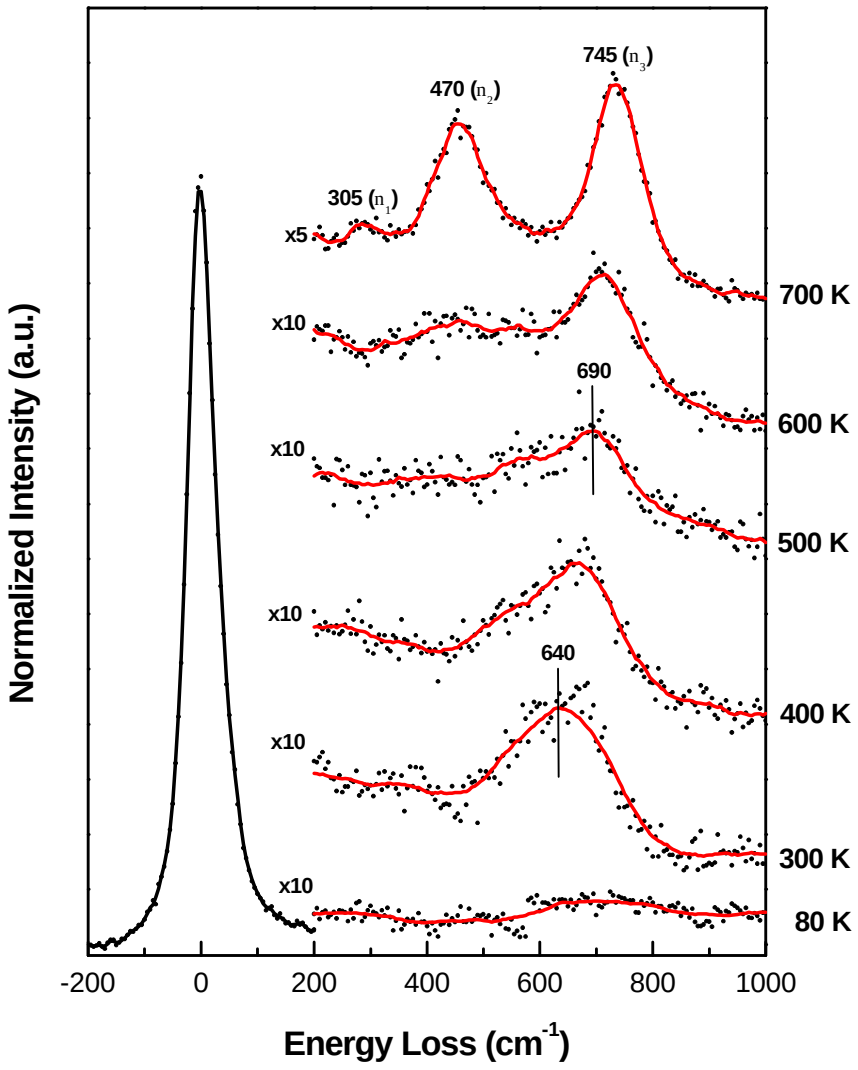

Fig. 8.13. EEL spectra of the O-Ga/O-c(2´2)/Ni(100) system as a function of annealing temperature.

At 300 K, the EEL spectrum shows a broad loss feature which, during annealing to 500 K shifts from 640 to 690 cm^{-1}. EEL spectra of a-Ga_2O_3 (amorphous Ga_2O_3) grown at 300 K [95] exhibit usually two losses at ~ 400 and 690 cm^{-1}. However, the oxidation at 80 K and annealing at 300 K leads to EEL spectra which shows only one broad loss at ~ 640 cm^{-1}.

The frequency of 677 cm^{-1} found for the vibrational excitation of the diatomic Ga-O bond observed in the EEL spectrum of Ga oxide on GaAs(100) [154] is similar to the frequency of the loss found in our EEL spectrum. Therefore we assign this loss to vibrational excitations of Ga-O bonds in the Ga oxide structure. Taking also into account that a diffuse LEED pattern was found, we readily conclude that, after oxidation at 80 K and also after annealing at room temperature, an amorphous Ga oxide is formed. After annealing at 600 K new losses develop and at 700 K intense losses at 305 (ν_1), 470 (ν_2) and 745 cm^{-1} (ν_3) occur. These intence losses are Fuchs-Kliewer (FK-) modes of Ga_2O_3. FK-phonons are typical for insulating or semiconducting thin layers on metal surfaces [43, 44].

After annealing at 700 K, the sample was again exposed to oxygen. Fig. 8.14a shows EEL spectra of the sample as a function of oxygen exposure. The intensities of the elastic beam and of the losses increase with increasing oxygen exposures and the losses became sharper.

For oxygen exposure above 200 L, in addition to the vibrational losses at 305 (ν_1), 470 (ν_2) and 745 cm^{-1} (ν_3), multiple losses at 1215 ($\nu_2+\nu_3$) and at 1490 cm^{-1} ($\nu_3+\nu_3$), and gain peaks at -305 (ν_1), -470 (ν_2) and -745 cm^{-1} (ν_3) occur. By a comparison of the frequencies of these losses with the frequencies of the losses found for β-Ga_2O_3 on CoGa(100) [94] and γ′-Ga_2O_3 on CoGa(110) [93] and CoGa(111) [165], the formation of a well-ordered Ga_2O_3 is concluded. In general, the formation of Ga_2O_3 is thermodynamically favored in comparison to the formation of NiO, because the heat of formation $\left(\Delta H_f(Ga_2O_3) = -1080 kJmol^{-1}\right)$ [166] is higher than the corresponding value for NiO $\left(\Delta H_f(NiO) = -240 kJmol^{-1}\right)$ [78].

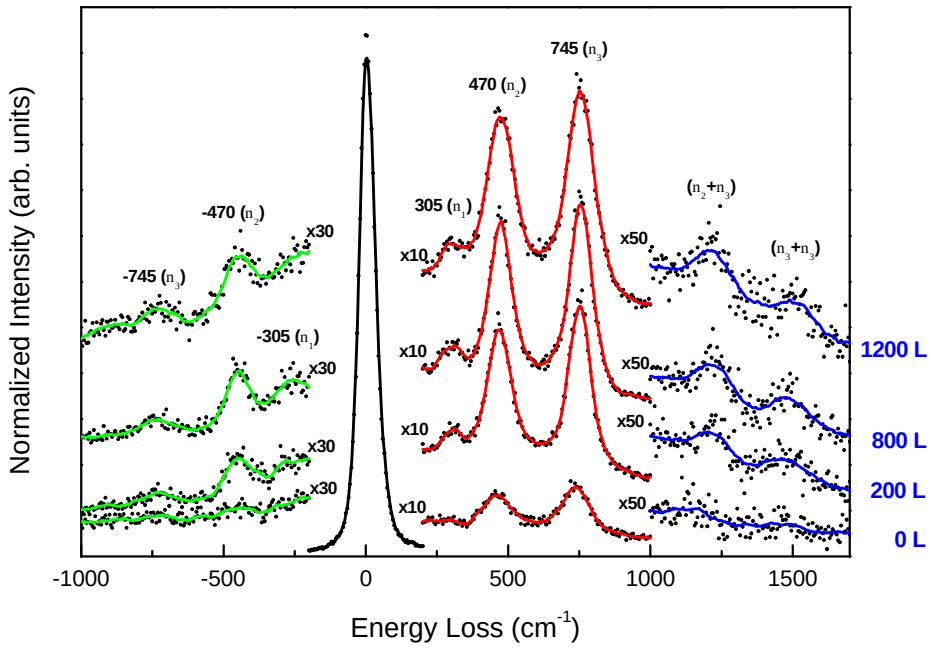

Fig. 8.14. (a). EEL spectra of Ga_2O_3/Ni(100) as a function of oxygen exposure at 700 K.

Table 8.1 shows an overview of the characteristic frequencies of the losses found in EELS experiments for amorphous and well-ordered Ga_2O_3 layers grown on various substrates. For amorphous Ga_2O_3 (a-Ga_2O_3) layers grown at 300 K, always two losses are found in the frequency range between 430 and 510 and at around 690 cm^{-1}. In the case of Ga_2O_3 grown at 300 K on CoGa(110), the EEL spectra exhibits three losses [93]. This suggests, that at 300 K a mixture of domains of a-Ga_2O_3 and γ-Ga_2O_3 may coexist on the surface. In general, for a-Ga_2O_3, only two modes are expected due to the solely tetrahedral coordination of the Ga^{3+} ions. Two IR modes are also predicted by the group theory. However, in the investigations of the oxidation of Ga at 80 K only one loss was found. This suggests, that the grown oxide is not stoichiometric or may be the oxygen atoms are only chemisorbed on the Ga layer. Only after annealing at 700 K, the EEL

spectra exhibits the well known losses of well-ordered thin films of Ga_2O_3 with three losses at 305, 470 and 745 cm^{-1} which are identical to those found for γ´-Ga_2O_3 on CoGa(110) (see Table 8.1 and [93]).

Table 8.1. The characteristic frequencies of the optical phonons for some thin Ga_2O_3 layers on various substrates.

System	Frequency of the losses (cm^{-1})				Temperature (K)	Ref.
a-Ga_2O_3/CoGa(001)	400			690	300	[95]
a-Ga_2O_3/CoGa(110)	435	510		705	300	[93]
a-Ga_2O_3/Ni(100)		640			80	This work
β-Ga_2O_3/CoGa(001)	305	455	645	785	700	[94]
γ´-Ga_2O_3/CoGa(110)	305	470	605	745	770	[93]
Ga_2O_3/CoGa(111)	300	470	640	730	800	[165]
γ´-Ga_2O_3/Ni(100)	305	470		745		This work

In order to verify the proposed type of oxide, the experimental EEL spectrum was compared to calculations for a model of a Ga_2O_3 layer on a Ni(100) substrate based on the dielectric theory [167, 168] (see Section 1.2.1.3). The dielectrical theory permits the calculation of an EEL spectrum, by using the transversal optical phonons $w_{TO,n}$ [169], e_0, and e_∞ [29] of Ga_2O_3 which are known from infrared spectroscopy. The thickness d of the Ga_2O_3 film is a free parameter and was assumed to be 7Å. The values of the fitting parameters $w_{TO,n}$ – the frequency of the transversal optical phonons, Q_n – the oscillator strength and the damping constant $g/w_{TO,n}$ are summarized in Table 8.2. The calculated spectrum shown in Fig. 8.14(b) (solid line) reproduces very well the measured spectrum (dotted line) concerning the frequencies of the losses and their relative intensities.

Table 8.2. Values of the parameters used in the calculations.

n	$w_{TO,n}(cm^{-1})$ [169]	Q_n	$g/w_{TO,n}$
1	285	1.4	0.0993
2	402	1.5	0.0674
3	605	0.04	0.0496
4	680	0.6	0.0420

$d = 7$Å , $e_0 = 7.15$, $e_\infty = 3.61$ [29]; g = *0,03*, w_p = *55000* s^{-1}

This confirms that on Ni(100) a Ga_2O_3 layer is formed. The frequencies of the losses found in this work are very similar to those of the Ga_2O_3 layer grown on CoGa(110) and CoGa(111) which strongly suggests that the same Ga_2O_3 phase is present.

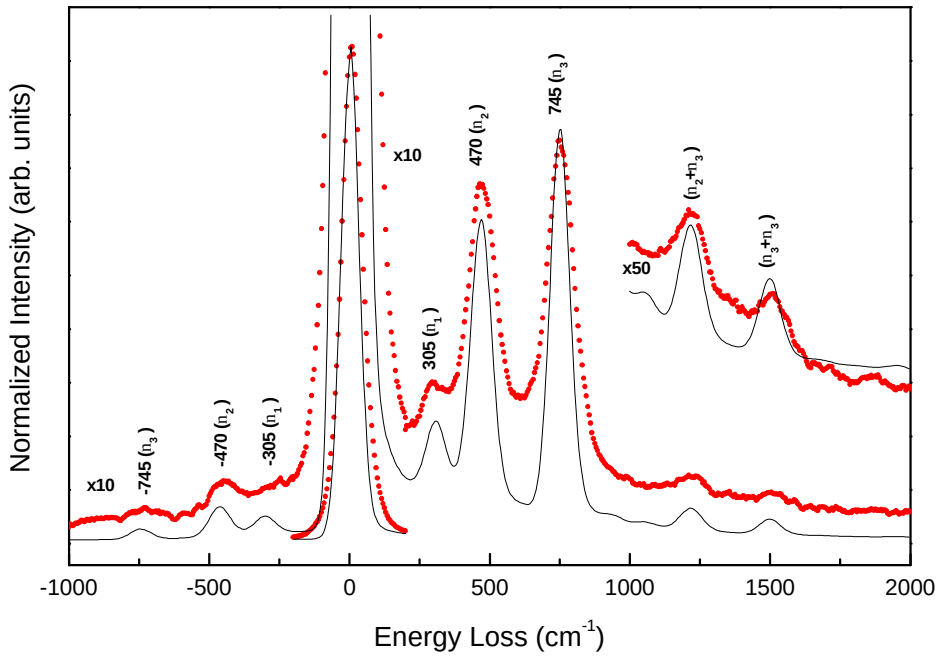

Fig. 8.14 (b). Measured (doted line) and calculated (solid line) EEL spectra of Ga_2O_3/Ni(100).

After oxidation at 700 K, the Ga_2O_3 /Ni(100) system was gradually annealed up to 1200 K. Fig. 8.15 shows EEL spectra as a function of the annealing temperature. The intensity of the elastic beam and that of the loss at 470 (ν_2) increases with increasing annealing temperature up to 900 K. At 900 K, the intensity of the loss 470cm^{-1} (ν_2) exceeds that of the loss at 745 cm^{-1} (ν_3). After annealing at 1000 K a new loss at 660 cm^{-1} occurs, which shifts to 620 cm^{-1} by annealing to 1100 K and the intensity of the loss at 745 cm^{-1} (ν_3) is decreased. The frequencies in the range between 620 and 660 cm^{-1} are typical for excitation of Ga-O bonds in a Ga oxide structure [84]. The change of the frequencies of the losses and the appearance of a new loss between 1000 – 1100 K shows that in this temperature range a structural change in the Ga oxide occurs. This finding is different to that of Ga_2O_3 grown on surfaces of intermetallic alloys. It seems that the substrate atoms play a different role, may be some of the Ni atoms diffuse into the Ga_2O_3 layer and new structures of mixed Ga-Ni-oxide are built.

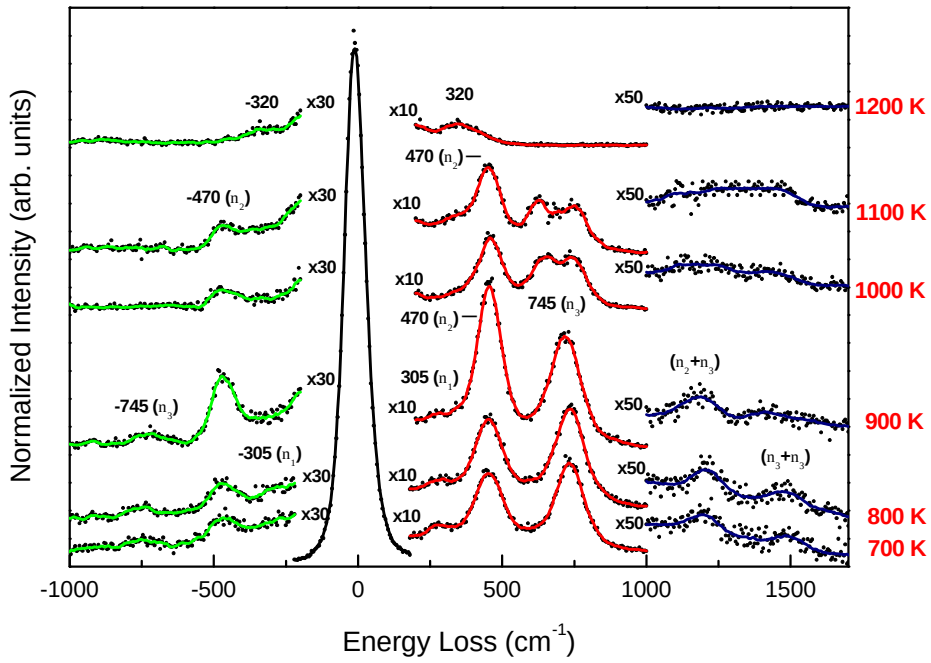

Fig. 8.15. EEL spectra of Ga_2O_3/Ni(100) as a function of annealing temperature.

After annealing at 1200 K, the Ga_2O_3 film is completely destroyed, and in the EEL spectrum only a broad loss at 321 cm^{-1} can be observed. May be some oxygen atoms remain on the surface and form a p(2×2) like oxygen structure on Ni(100). The LEED pattern shows a diffuse p(2×2) structure and confirms this assumption. However, this loss is very broad, which suggests that this is not a perfect, clean O-p(2×2) structure.

8.2.2.3 LEED

The formation of Ga oxide on Ni(100) was also studied by LEED. Fig. 8.16 (a) shows the LEED pattern and schematic representation of the c(2×2) oxygen structure (asterix) on the Ni(100) substrate (open circle). After deposition of Ga on the c(2×2)-O/Ni(100) surface and oxidation at 80 K an amorphous Ga_2O_3 grows, which exhibits a diffuse LEED pattern. Fig. 8.16 (b) presents the LEED pattern of Ga oxide after annealing at 700 K and oxidation at this temperature. The LEED pattern of this Ga oxide shows a weak diffuse ring structure, which is indicative of a Ga oxide layer with domains with hexagonal structure randomly orientated with respect to the Ni(100) substrate. The lattice constant of the hexagonal unit cell deduced from the ring diameter is ~2.8 ± 0.5 Å, a value that is close to the typical oxygen-oxygen spacing observed for different modifications of Al_2O_3 [170-172]. The existence of more or less distorted hexagonal oxygen layers is a common feature of nearly all of the many phases of Al_2O_3 [170-172]. Most of the Ga_2O_3 phases are isomorphic to the appropriate Al_2O_3 phases, therefore, the same oxygen-oxygen spacing is also present in Ga_2O_3. This spacing is approximately twice the value of the O^{2-} ionic radius (1.4 Å). A reasonable interpretation is therefore, that the observed hexagonal structure corresponds to compact hexagonal planes of oxygen ions. In fact, the structure of all known bulk Ga oxides is based on compact *fcc* or *hcp* oxygen lattices. In γ´-Ga_2O_3 the side of the cubic unit cell is 4.1 Å, therefore the basis vectors along the (111) plane are 2.91 Å long (See Table 5.2). Concequently, the Ga_2O_3 phase observed on Ni(100)

can be interpreted in terms of γ´-Ga_2O_3 which grows with the (111) plane parallel to the substrate (100) surface plane. The LEED data are in a good agreement with the finding in the EEL measurement which shows that a well-ordered Ga_2O_3 is formed on Ni(100) at 700 K.

After annealing at 1100 K, a new structure develops (solid circle (Fig. 8.16 (c)) which may result from the top layer of an ultra thin film of β-Ga_2O_3 on Ni(100) (open circle (Fig. 8.16 (c)). In addition to the Ni(100) Bragg reflections, spots of a (2×1) structure of two domains which are rotated by 90° are observed. The lattice constants of the (2×1) structure amount to $a = 3.1 \pm 0.1$Å and $b = 6.2 \pm 0.1$Å . The lattice constants of the unit mesh of the top layer of the monoclinic β-Ga_2O_3 are $a_{b-Ga_2O_3} = 3.04$Å and $b = 5.80$Å which agree well with the (2×1) LEED pattern. In one direction $\left(a_{b-Ga_2O_3} \sim a_{(2\times1)}\right)$ there is an almost perfect coincidence, while in the second direction the lattice mismatch amounts to ~ 6 %.

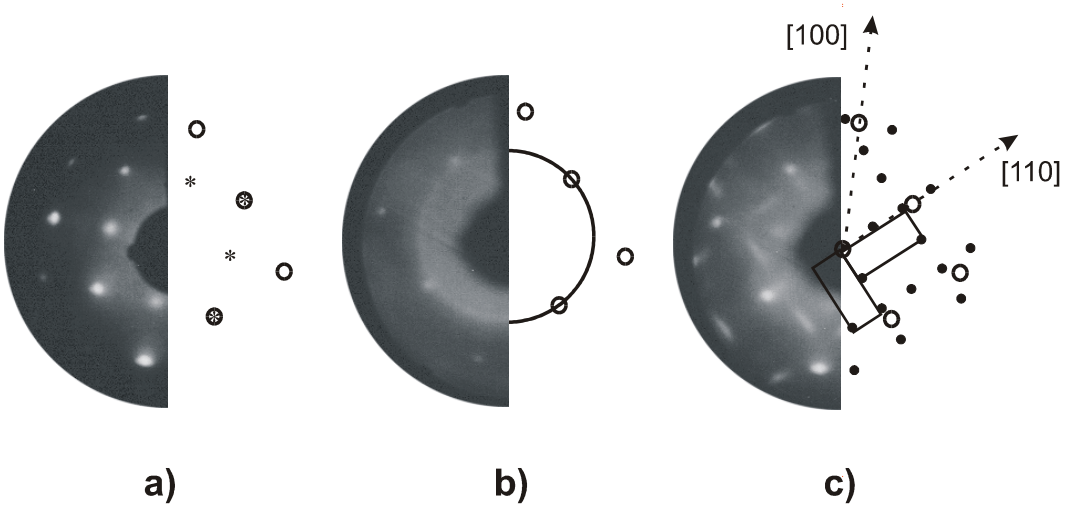

Fig. 8.16. LEED pattern of: a) O-c(2x2)/Ni(100) surface; b) Ga_2O_3/Ni(100) after oxidation at 700 K; c) the ultra thin b-Ga_2O_3 layer after annealing at 1100 K, E_p=122 eV. On the left side of the figures are shown the LEED pattern. The second half (right side) shows a schematic of the LEED pattern.

Thus, a slightly distorted (expanded) surface structure of the ultra thin β-Ga_2O_3 layer may results. The oxide structure is in coincidence with the substrate structure $\left(5\times\frac{\sqrt{2}}{2}a_{Ni}=4\times a_{Ga_2O_3}\right)$ in the $[110]$ direction, while in the the $[1\bar{1}0]$ direction, in which the second basis vector points, the coincidence with the unit mesh of Ni(100) is $\left(5\times\frac{\sqrt{2}}{2}a_{Ni}=2\times b_{Ga_2O_3}\right)$.

8.3. Growth of Ga_2O_3 Films at 300 K

8.3.1 Deposition of Ga on Ni(100)

At 300 K, Ga was deposited on the clean Ni (100) surface in the OMICRON – UHV apparatus. Fig. 8.17 shows the peak-to-peak (p-to-p) intensity of the Auger transitions of $Ni_{(848\ eV)}$ and $Ga_{(1070\ eV)}$ as a function of deposition time. During Ga deposition the p-to-p intensity of $Ni_{(848\ eV)}$ decreases while the p-to-p intensity of $Ga_{(1070\ eV)}$ is increasing. After 15 minutes deposition the effective thickness of the Ga film was estimated to be 15 Å.

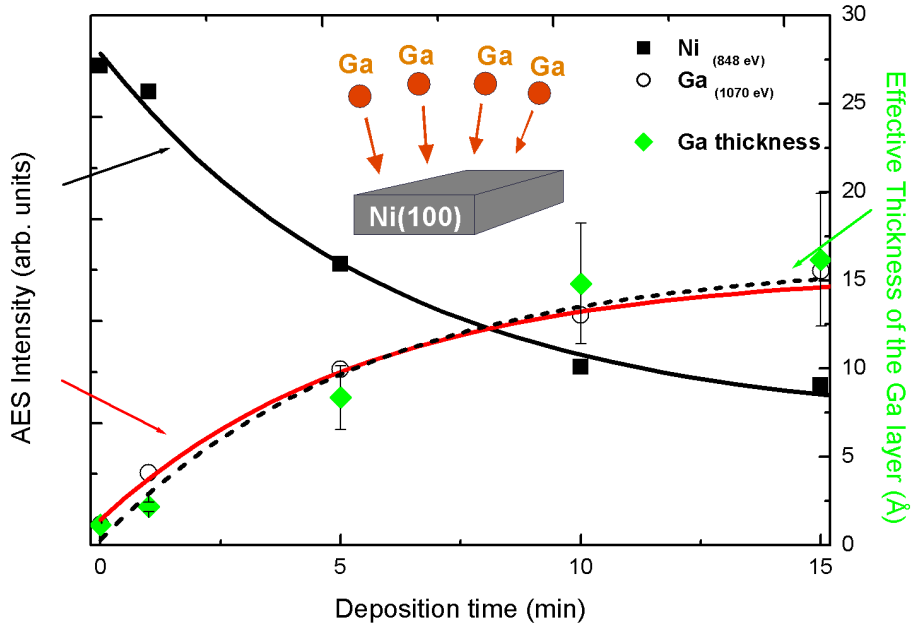

Fig. 8.17. The p-to-p intensity of the AES transitions of $Ni_{(848)}$ (■)and $Ga_{(1070)}$ (○) during deposition of the Ga layers on Ni(100) at 300 K and the thickness (◆) of the Ga layer, calculated from the AES spectra.

On the right side of the graphic is plotted the effective thickness of the Ga layer as a function of the deposition time, which was estimated from the AES data (equation (1.13)). Up to a deposition time of 10 min, the thickness of the Ga layer increases linearly, for larger deposition a smaller increase is observed. The reason of the smaller increase of the Ga AES signal could not be clarified in this study. For a larger deposition time some large clusters (bubbles) of Ga are formed on the surface, which could be observed on some STM images. One example is shown in Fig. 8.18 which presents a STM image of Ga clusters. The diameter of the "bubbles" extends up to 2000 Å. This large drops which are formed on the surface, may induce an incorrect determination of the effective thickness, due to an inhomogeneous distribution of Ga on the surface. Large clusters were also observed in the study of Ga on silica at 100 K [161].

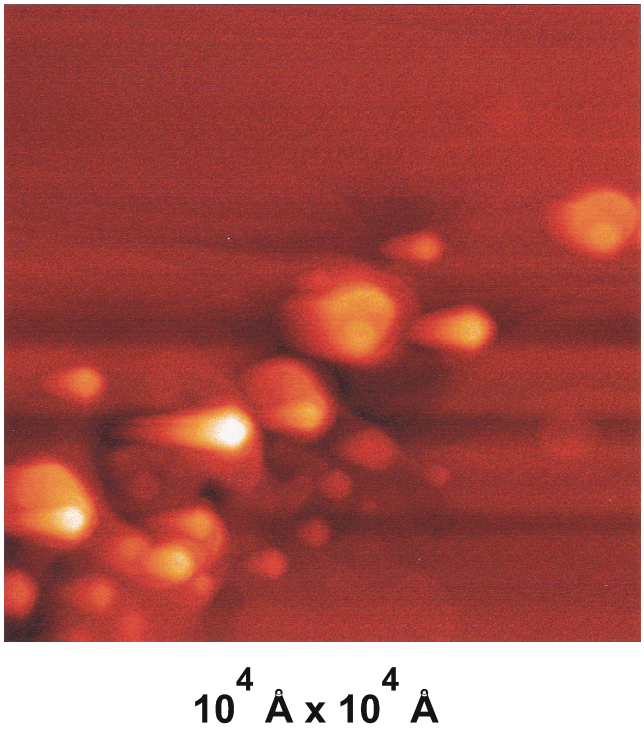

Fig. 8.18. STM image of Ga clusters ("drops") with scanned area of 10^4 Å ´ 10^4 Å (U_t = 1.5 V, I_t = 3.0nA).

Electron Induced Desorption (EID) of Ga atoms caused by the electron beam of the Auger gun (3 kV, 1 μA) may also lead to an incorrect determination of the effective thickness.

After a nominal deposition of 15 Å of Ga, a diffuse illumination of the LEED screen is observed, which indicates that at 300 K a disordered Ga film is formed. At 300 K, no ordered LEED pattern can be expected due to the large mobility of the Ga atoms close to the low melting temperature of Ga (302.91 K).

Fig. 8.19a presents a STM image with a scanned area of 1000 Å × 1000 Å taken after a nominal deposition of 0.02 Å of Ga on Ni(100) at room temperature. This figure shows that Ga grows in small two-dimensional islands on the Ni (100) surface. A line scan was performed in order to estimate the size and the height of the islands. They are around 20 Å in diameter with a height of 1.2 Å above the Ni surface. This height suggest that the Ga atoms are sitting in fourfold hollow sites on Ni(100). A model of the Ga atoms, sitting in fourfold hollow sites of the Ni(100) is drawn in Fig. 8.19c. The distance between two fourfold hollow sites on Ni(100) amounts to 2.48 Å. In the orthorhombic α-Ga phase (a = 4.5107, b = 4.5167, c = 7.6448 Å) the distance between two Ga atoms in a "dimer" is 2.465 Å and a X-ray diffraction study suggests that the covalent bond in the dimer is expanded [173]. Such a covalent dimer bond seems to be also possible on the Ni(100) surface for Ga atoms sitting in fourfold hollow sites which are separated by a distance which is close to the distance between two Ga atoms in a dimer. Fig. 8.19b shows the distribution of the Ga islands after deposition of 0.02 Å of Ga at 300 K. The distribution exhibits a maximum of the island size centered at ~ 380 $Å^2$. After a nominal deposition of 0.02 Å of Ga about 2% of the Ni(100) surface is covered by Ga atoms. The two-dimensional (Frank-van der Merwe) growth of Ga on the Ni(100) surface results to the large difference between the surface free energies of Ga $\left(g^{0}_{Ga} = 720 mJ/m^2\right)$ and Ni $\left(g^{0}_{Ni} = 2364 mJ/m^2\right)$.

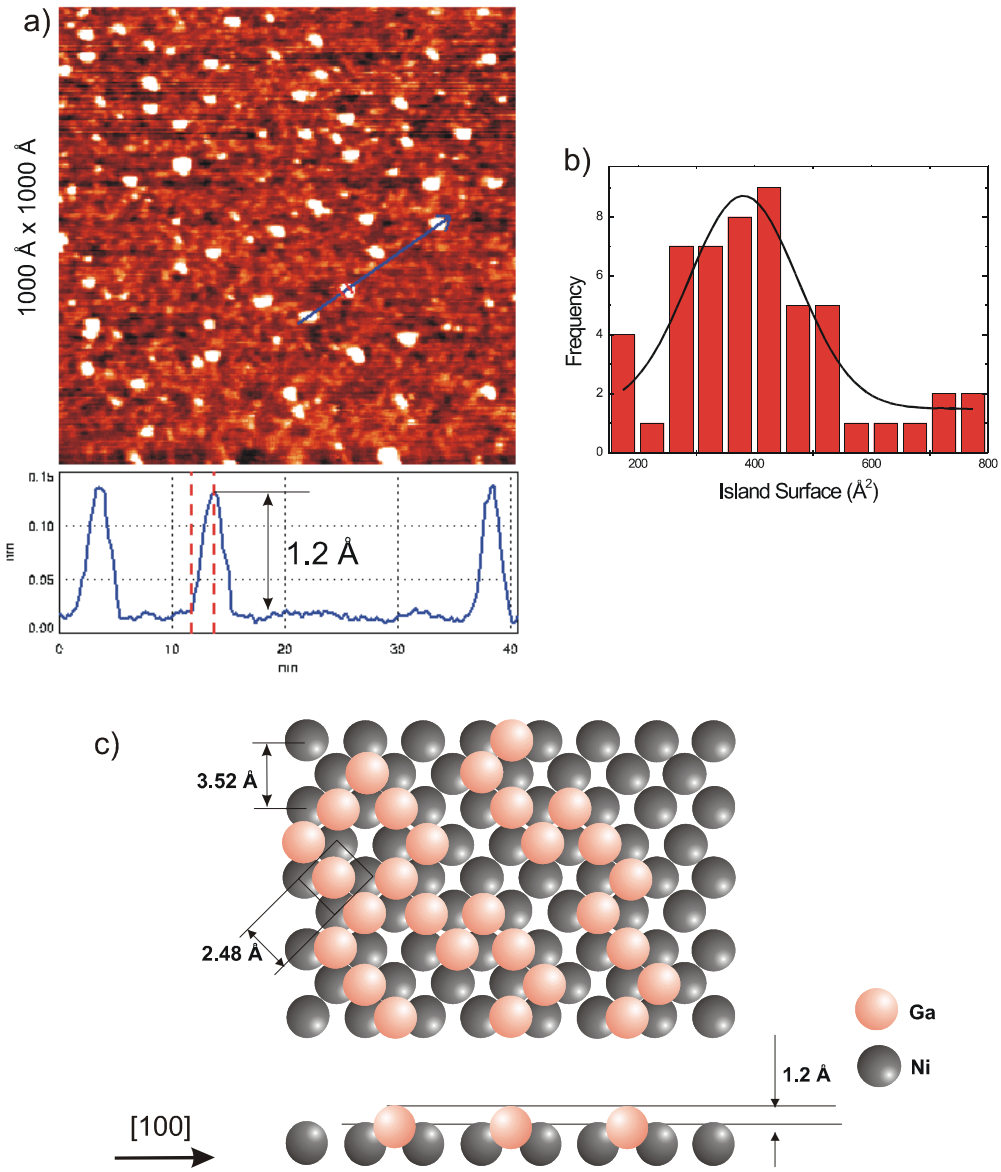

Fig. 8.19. a) STM image (1000 Å ´ 1000 Å) with the line scan along the arrow, taken after a deposition of 0.02 Å of Ga 300 K (U_t = 1.5 V, I_t = 4.0 nA); b) The distribution of the Ga islands; c) A model of the Ga atoms, sitting in fourfold hollow sites on Ni(100).

Fig. 8.20 shows a STM image with a scanned area of 1000 Å × 1000 Å after a nominal deposition of 1.5 Å of Ga. Three terraces of Ga are observed on the STM image which are denoted by A, B and C. The black holes represent the terrace C and may correspond to Ga free areas i.e. areas of the clean Ni(100) surface. The step height between terrace C and B amounts to 2.1 Å. The terrace B covers about 85 % of the surface. On terrace B the third terrace A is located which is separated by a step height of ~1.1 Å. The terrace A covers about 10 % of the surface (with respect to the Ni(100) surface). A nominal thickness of 1.0 Å should correspond to one complete monolayer of Ga, therefore, the over whole sum of the terraces B and C may correspond to 1.5 ML.

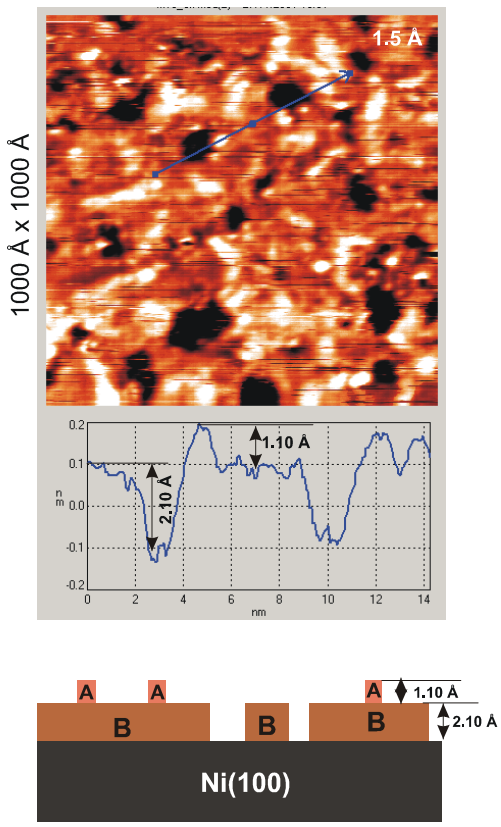

Fig. 8.20. STM image (1000 Å ´ 1000 Å) with the line scan along the arrow, taken after a deposition of 1.5 Å of Ga and a model of the terraces on the Ni(100) surface (U_t = 1.0 V, I_t = 0.8 nA).

However, a smaller coverage is observed (~1 ML) which may result by the agglomeration of Ga "bubbles" on some areas. A model of the terraces of Ga on the Ni(100) surface is also shown in Fig. 8.20.

Fig. 8.21 shows two STM images taken after a nominal deposition of 4.5 Å (Fig. 8.21a) and 15.0 Å of Ga (Fig. 8.21b) on Ni(100), respectively. On both figures three terraces can be recognized. Two of them B and A are not completely filled. They are marked by A and B on the models. C_i represent the already completed Ga layers.

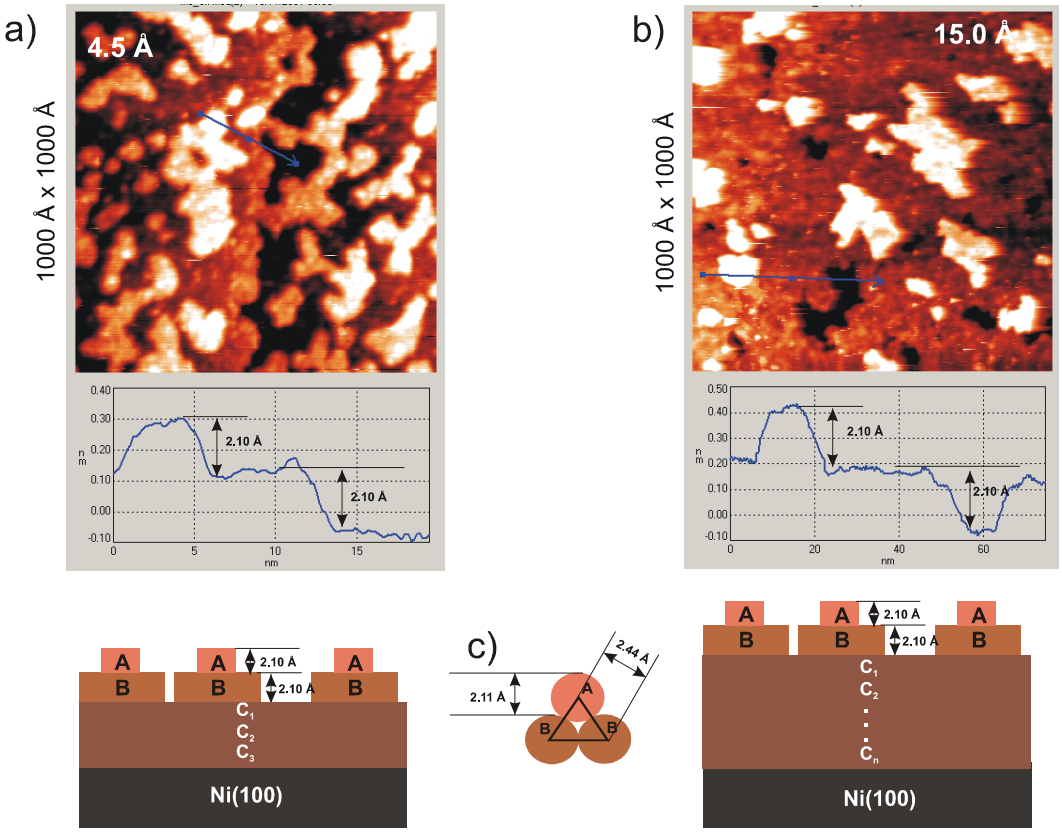

Fig. 8.21. STM images with a scanned area of 1000 Å ´ 1000 Å taken after deposition of Ga on Ni(100) with a nominal thickness of 4.5 Å (a) (U_t = - 1.4 V, I_t = 0.42 nA) and 15.0 Å (b) (U_t = 0.24 V, I_t = 0.24 nA). Under the STM images are sketched appropriate models. c) A model of the arrangement of the Ga atoms.

For a nominal thickness of 4.5 Å, three completed layers are expected below the two layers A- and B-, (see the model in Fig. 8.21a). After a nominal deposition of 15.0 Å, there are many completed layers (C_n - the model on Fig. 8.21b). On both STM images (a) and (b) it is not possible to recognize if the terrace C_i are defect free or not. The step height between the terraces is as follow: B over C = 2.10 Å, A over B = 2.10 Å. This distance suggests that the Ga atoms are sitting between two neighboring Ga atoms (bridge sites) as shown in the sketch. However we have to point out that such a distance is not found in the α-Ga phase. Züger and Dürig [174] found that the (010) surface shows steps which are 3.8 Å high. This distance is one-half of the unit cell of α-Ga and no steps of 1.9 Å (or $c/4$) are found. In our case the distance between the terraces is closer to $c/4$ which would corresponds to a splitting of the metallic bilayer in the α-Ga structure. On the other hand it is questionable, if the Ga atoms are growing with the α-phase and with the (010) surface of the α-Ga structure parallel to the Ni(100) surface. The sketch in Fig. 8.21c represents a model of the arrangement of the Ga atoms towards to each other. In the model the calculated height between two Ga terraces is 2.11 Å, which is in a good agreement with the measured one ~ 2.10 Å.

8.3.2 Oxidation

At 300 K, a Ga layer with an effective thickness of 15 Å was oxidized until saturation.

8.3.2.1 AES

Fig. 8.22 shows the p-to-p intensity of the AES transitions as a function of oxygen exposure at 300 K. The p-to-p intensity of $Ni_{(848\ eV)}$ decreases continuously which is due to the increasing of the film thickness during the oxidation process. In Fig. 8.22 two different AES transitions of Ga are presented, first the LMM transitions of the metallic $Ga^0_{(1070\ eV)}$ and secondly from the ionic $Ga^{3+}_{(1066\ eV)}$ which is formed during the oxidation. With increasing oxygen exposure the p-to-p

intensity of $O_{(503\ eV)}$ increases and that of the metallic $Ga^0_{(1070\ eV)}$ decreases. This decrease is due to the transformation of metallic Ga^0 atoms into Ga^{3+} ions. Thus the AES intensity of Ga^{3+} is increasing during oxygen exposure. The signal of oxygen is increasing up to 1000 L. Above 1000 L a saturation level is eventually reached. After an exposure of 1400 L of oxygen the AES intensity of $Ga^0_{(1070\ eV)}$ decreased to approximately 50% of its initial value. This suggests that only a part of the Ga layer is oxidized, while an unoxidized Ga layer remains as an interface layer. After oxidation at 300 K, the total thickness of the overlayer consisting of metallic Ga^0 and Ga_2O_3 is determined to be ~ 18 Å.

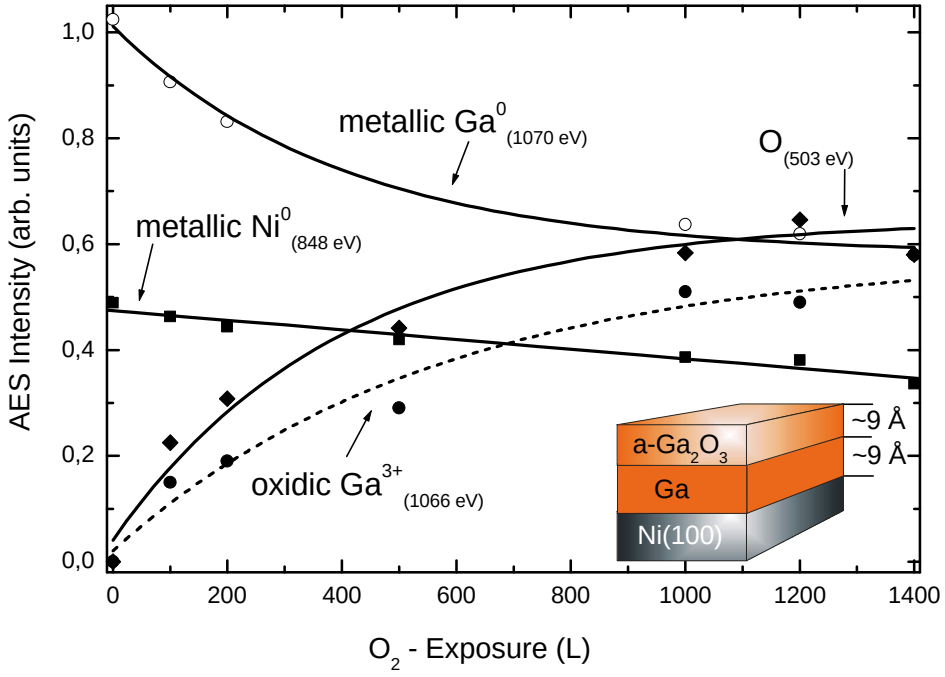

Fig. 8.22. The p-to-p intensity of the AES transitions of $O_{(503)}$(◆), $Ni_{(848)}$(■), metallic $Ga_{(1070)}$(○) and $Ga_{(1066)}$(●) as a function of O_2 exposure at 300 K. The solid lines represent a guide for the eyes. A model of the Ga_2O_3/Ga/Ni(100) system is also shown.

The thickness of the oxide layer and of the metallic Ga interface layer is approximately equal. However we have to point out that the deconvolution of the Ga^0 signal at 1070 eV and of the Ga^{3+} signal at 1066 eV can be done only with a large error. Therefore, the values of the thickness has to be considered with care. The inset of Fig. 8.22 shows a model of the system which indicates, that the overlayer consists of two parts: a metallic Ga interface layer and a top layer of Ga_2O_3, both layers with a thickness of ~9 Å. The oxidation process is also clearly illustrated in Fig. 8.23 which shows two typical AES spectra: (a) after a nominal deposition of 15 Å of Ga at 300 K and (b) after oxidation with 1400 L with O_2 at 300 K. After oxidation the shape of AES transitions in the low energy region is changed drastically. The intensity of Ga^0 transitions at 51, 55, 81 and 108 eV are diminished and AES transitions of Ga^{3+} at 45, 48, 77, and 104 eV are observed. A change of the LMM Ga transitions is also observed, the intensity of Ga^0 transitions at 1070 and 1097 eV are diminished and transitions of Ga^{3+} at 1066 and 1094 eV, respectively, have developed. By comparison of the signals of the LMM transition of Ga at ~1070 eV in the spectra (a) and (b) two aspects are observed: first, the p-to-p intensity in spectrum (a) is much higher than that in spectrum (b) and second, in spectrum (b) there are two transitions at 1070 and 1066 eV. It is difficult to deconvolute these two transitions perfectly, and therefore an overlap of both signals is observed. If the total amount of Ga is oxidized, only the transition at 1066 eV would be present with an intensity which is approximately equal to that of the Ga signal at 1070 eV in spectrum (a). Thus, the apparent decrease of the signal at 1070 eV is a result of the appearance of two AES transitions at 1066 and 1070 eV. The argument, discussed above holds also for the AES transition at 1097 eV. All these changes are due to the oxidation of a part of the gallium atoms and to the formation of Ga^{3+} ions. Taking into account that at 300 K no ordered LEED pattern is observed, we readily conclude that, an amorphous Ga oxide is formed. However, not all the Ga atoms are oxidized and thus, the amorphous Ga oxide is located on an interface layer of metallic Ga, which is situated between the Ga_2O_3 layer and the Ni substrate.

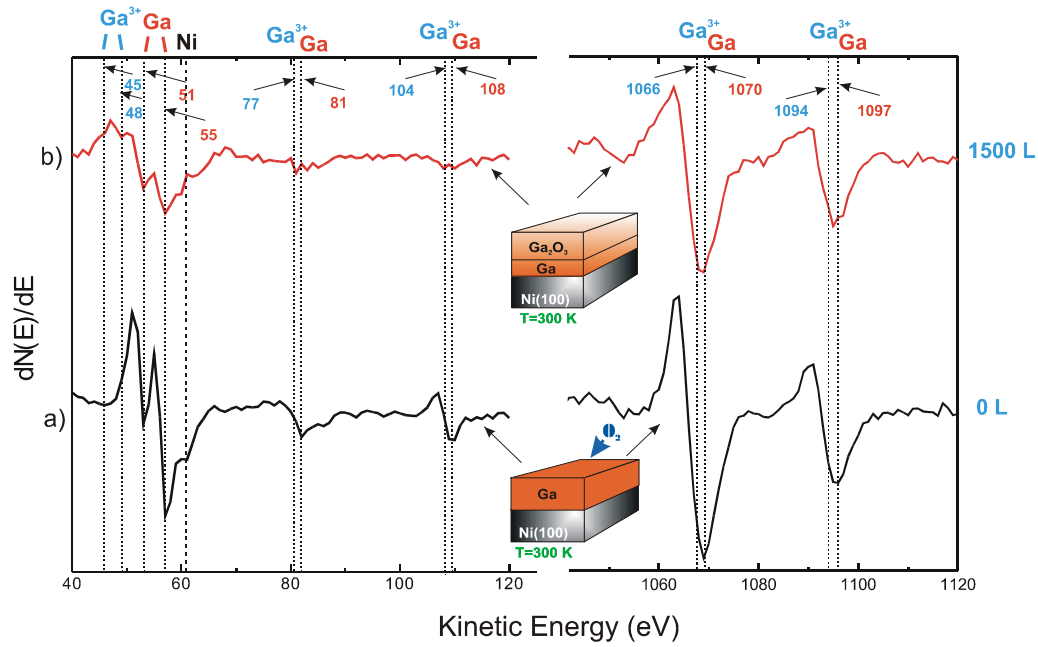

Fig. 8.23. Two AES spectra recorded at 300 K: a) before and b) after oxidation of the Ga layer on Ni(100). A sketch of the oxidation is also shown.

Such an interface layer was also observed in Section 8.2.2.1, where a Ga layer was oxidized at 80 K.

Fig. 8.24 shows the p-to-p intensity of the AES transitions of $O_{(503\ eV)}$, $Ni^{0}_{(848\ eV)}$ and $Ga_{(1070\ eV\ +\ 1066\ eV)}$ as a function of annealing temperature. We have to consider that the AES signal is measured with a CMA and this implies that only electrons which are emitted under an angle of 42 ± 2° are detected. It seems that the emission angles for AES electrons after ordering are changed. If some of these emission directions coincide with the CMA angle of 42° it is understandable why during the annealing between 300 and 600 K the signals of Ga and O are increasing and passing through a broad maximum. Otherwise (if the angle does not coincide these directions) the signals will decrease or remain constant even though the film thickness remains constant. The same phenomena was also observed by Schmitz et al. [175]. However, even with the increase of the Ga and O intensity, the total thickness of the overlayer is decreasing. This is shown by the

increase of the AES intensity of $Ni_{(848\ eV)}$. After further annealing the AES signals of Ga and O decrease and above 700 K Ga signal reaches a value which is constant up to ~850 K. Above ~900 K the AES signal decreases further. This evolution suggests that the Ga atoms from the interlayer diffuse into the Ni substrate and the most stable phase of the Ga_2O_3 seems to be between 700 and 850 K. Such a behavior was also observed after deposition of Ga at 80 K and oxidation (see Section 8.2.2.1). During annealing in the temperature range between 300 and 900 K the Ni signal increase continuously which suggest that the thickness of the layers grown on Ni(100) is diminishing. For instance, after annealing at 700 K, the thickness of the layers above Ni(100) (the oxide and the remaining metallic Ga) amount to ~16 Å. At 900 K the thickness of the overlayer is strongly reduced (~3 Å).

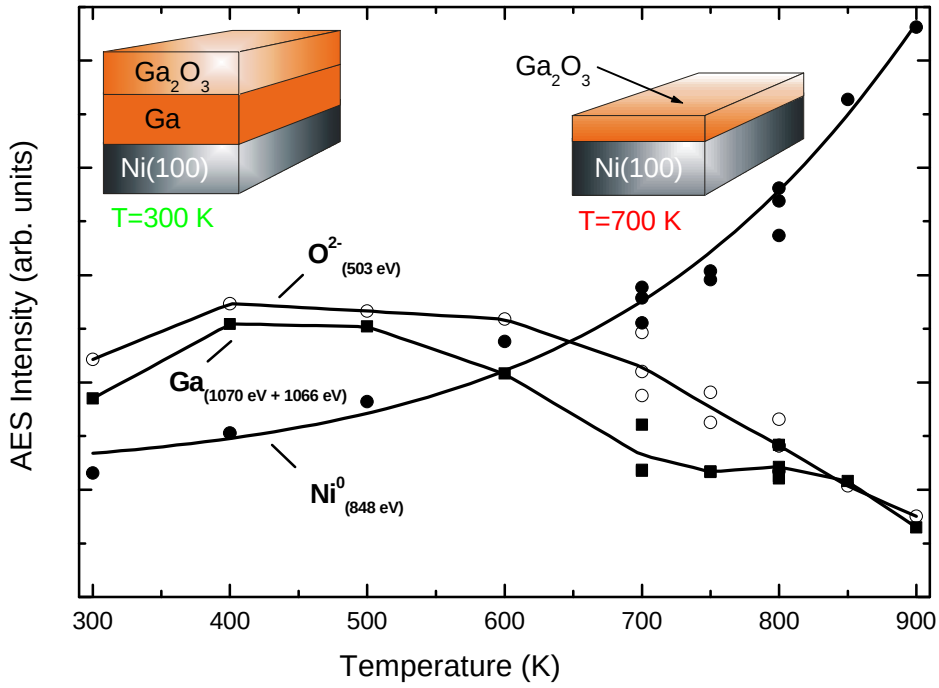

Fig. 8.24. The p-to-p intensity of the AES transitions of $O_{(503\ eV)}$, $Ni_{(848\ eV)}$, and $Ga_{(1070\ eV)}$ and $Ga_{(1066\ eV)}$ as a function of the annealing temperature. The solid lines represent a guide for the eyes. The models show schematically the changes of the Ga_2O_3/Ga/Ni system.

8.3.2.2 LEED

Fig. 8.25a shows a LEED pattern of the clean Ni(100) which exhibits a (1x1) structure. After deposition of 15Å of Ga the substrate diffraction spots vanish completely and the LEED screen exhibits only diffuse illumination. During oxidation at room temperature, the LEED pattern is still diffuse showing that an amorphous oxide layer is formed. A similar behavior was reported for the room-temperature oxidation of CoGa(100) [94, 95, 138, 176], and CoGa(110) [93].

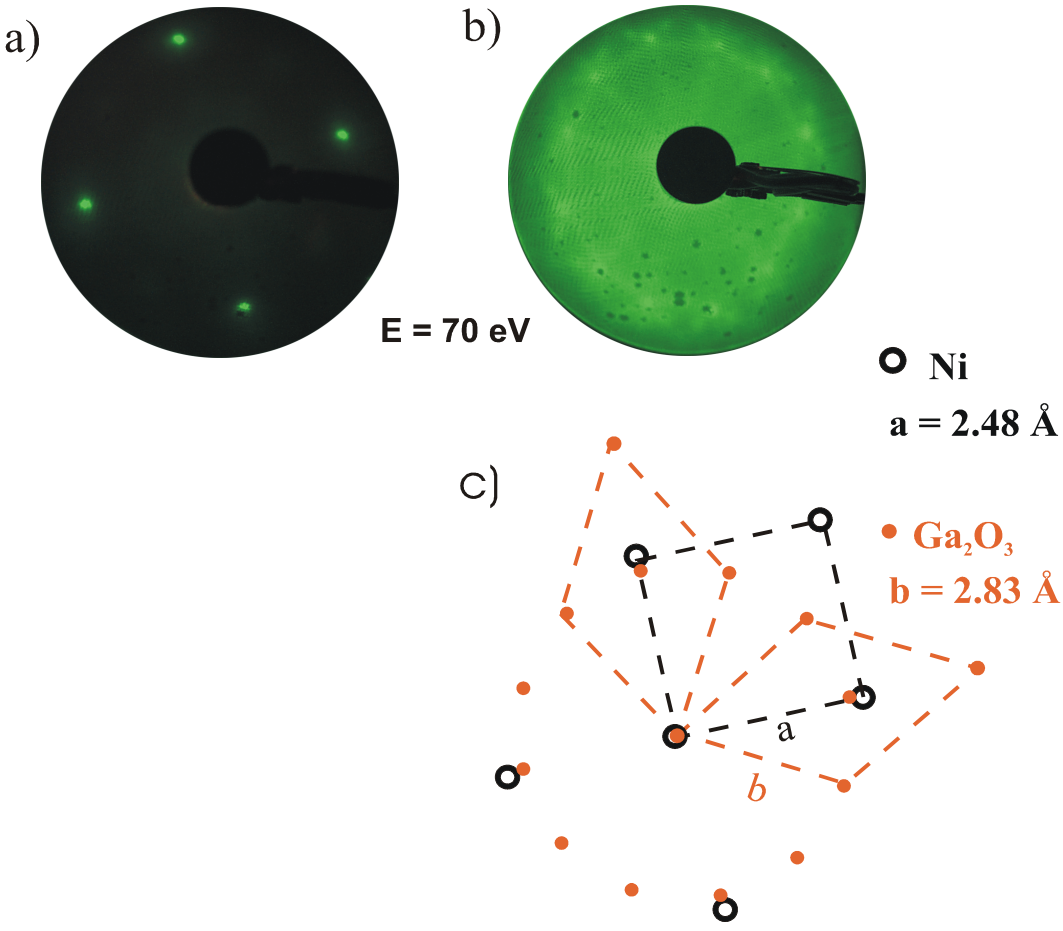

Fig. 8.25. LEED pattern of: a) the clean Ni(100) surface; b) of the gallium oxide layer after annealing at 700 K, E = 70 eV; c) A schematic of the Ni(100) and Ga_2O_3 unit cells in the reciprocal space.

The gallium oxide film which is formed after annealing at 700 K shows a 12-fold ring structure, which can be explained by two domains with hexagonal structure, which are rotated by 90° with respect to each other (Fig. 8.25b). The lattice constant of the hexagonal unit cell is determined to be 2.83 ± 0.05 Å. A similar structure of the thin Ga_2O_3 layer was found in Section 8.2, where an amorphous Ga_2O_3 layer was grown at 80 K and annealed at 700 K [177]. The hexagonal structure of Ga_2O_3 can be explained by the formation of γ′-Ga_2O_3 layer which grows with the (111) plane parallel to the (100) surface of Ni. In Fig. 8.25c a schematic of the Ni(100) and Ga_2O_3 unit cells in the reciprocal spece are shown. The presence of low intensity spots observed close to the center of the LEED pattern suggests that a superstructure with a large unit cell could also be present on the surface.

8.3.2.3 STM

The growth of the Ga oxide layer on Ni(100) was also investigated by STM. The STM images are taken directly at the respective annealing temperature by scanning the same surface area. The STM images of the amorphous Ga_2O_3 which is formed at 300 K exhibit small Ga oxide islands (not shown here) with a very rough surface. Afterwards the amorphous Ga oxide layer was gradually annealed. During annealing between 300 and 800 K an ordering of Ga oxide is observed and the oxide is transformed into the well-ordered γ′-Ga_2O_3 phase. Simultaneously the Ga oxide islands grow (coalesce) together. Fig. 8.26 shows STM images with a scanned area of 1500 Å × 1500 Å of Ga_2O_3 on Ni(100), taken during the step-by-step annealing. The roughness of the surface is shown by a line scan located below the images. The first image taken at 500 K shows a rough surface with black areas, which correspond to holes about 2 Å deep. Three different terraces are observed which are separated by steps with a height of ~ 2 Å. The black areas belong to the deepest terrace.

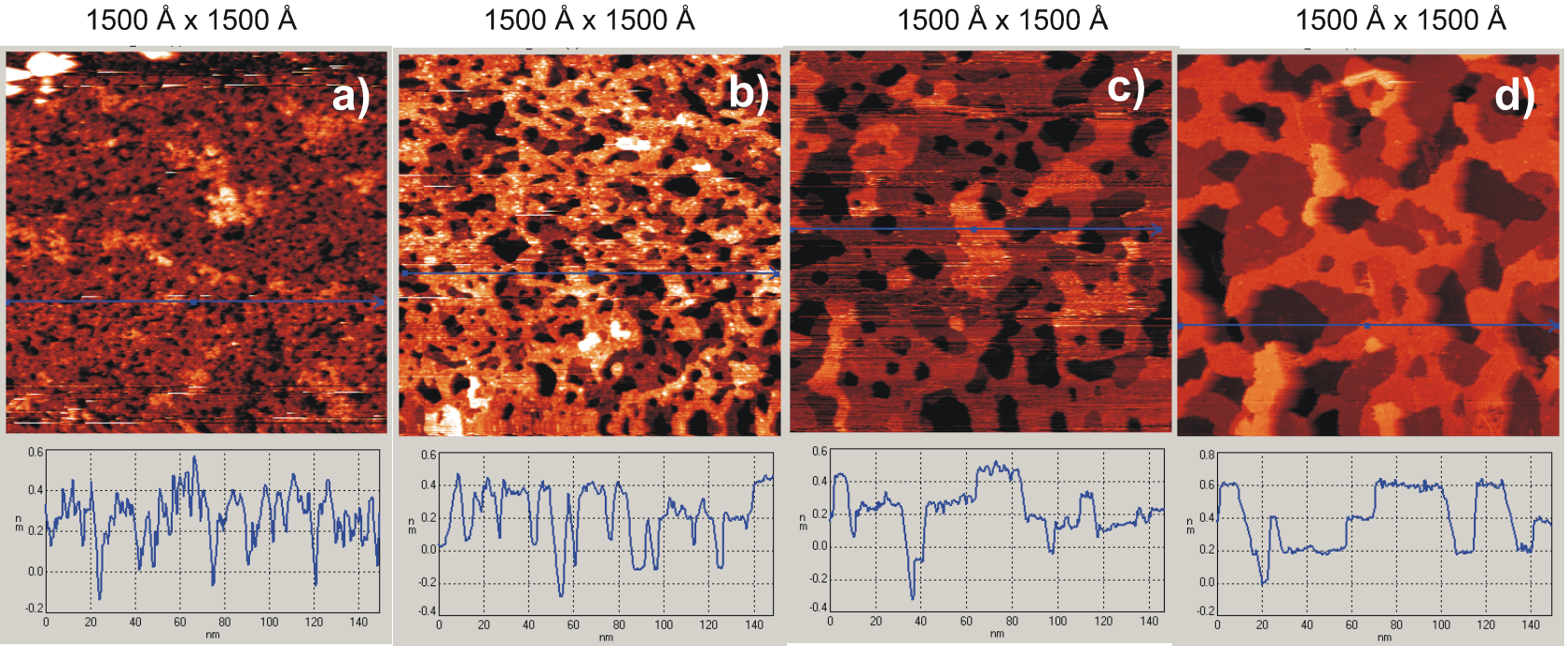

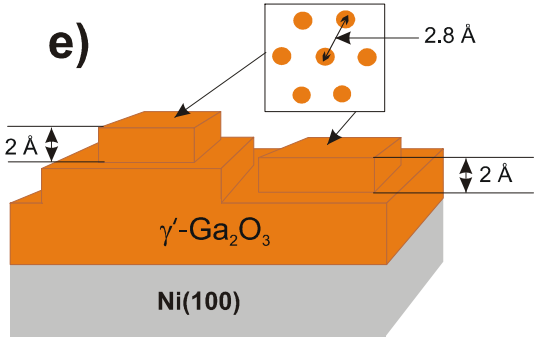

Fig. 8.26. STM images with line scan along the arrows, taken after annealing
a) at 500 K (U_t = 1.6 V, I_t = 0.6 nA),
b) at 600 K (U_t = 1.6 V, I_t = 0.4 nA),
c) at 700 K (U_t = 1.6 V, I_t = 0.4 nA);
d) at 800 K (U_t = 0.9 V, I_t = 0.3 nA);
e) a model of the γ′-Ga2O3 layer on Ni(100) which was obtained after annealing at 700 K.

On the top two terraces (brown and orange) a smooth morphology is found with a roughness of ~ 3 Å. After annealing at 600 K, the size of the terraces increases and the holes which are 2 Å deep can be more easily recognized. At 700 K , the morphology of the surface is changed: large terraces are developed which are very smooth and flat. The terraces have an irregular shape. The black holes (lowest terrace) already observed at 500 and 600 K are now larger. The larger size of the black holes is a result of the coalescence of the oxide terraces. The step height between the terraces is determined to be about 2 Å. Already, the LEED data have suggest that the well-ordered Ga oxide grown at 700 K corresponds to the γ′-Ga_2O_3 phase, which grows with the (111) plane parallel to the (100) surface of Ni. The STM and LEED data suggest that all the terraces are formed with the (111) plane of γ′- Ga_2O_3 phase parallel to the Ni(100) surface. The distance between two (111) planes of oxygen in the γ′- Ga_2O_3 structure is about 2 Å . Therefore, is not surprising, that the step height between two terraces is ~2 Å. On the other hand the formation of large terraces, larger than the transfer width of LEED permits the observation of a LEED structure. After annealing at 800 K the terraces and the black holes, respectively became even larger, which is a result of a further coalescence of the oxide terraces with the temperature. They still have an irregular shape (Fig. 8.26d). On Fig. 8.26e a model of the surface after annealing at 700 K is drawn. On the sketch are noticed the step height of the terraces and a scheme of the γ′- Ga_2O_3(111) lattice. After annealing at 900 K, the terrace structure of the oxide starts to be destroyed. We found places, where the oxide structure was present, but also regions, where no oxide was observed. Taking into account the diminished Ga and O AES signals and the still present LEED pattern, we readily conclude, that the Ni surface is partially covered by Ga oxide.

Fig. 8.27 shows a STM image with a scanned area of 300 Å × 300 Å after annealing at 700 K and after cooling down to 300 K. On the STM image only one terrace is observed. The network of streaks which form angles of 60° or 120° with respect to each other suggests that the streaks result from a hexagonal superstructures. From the distance between the streaks, the periodicity of the

superstructure amount to ~15, ~21 and ~29 Å. The STM image in Fig. 8.27 was taken at a bias voltage of U_t = - 0.7 V which is different from that used in Fig. 8.26. The Zoom In (50 Å × 60 Å) shows atomically resolved strikes, where hexagonal unit cells with a lattice constant of ~3.8 ± 0.5 Å are observed.

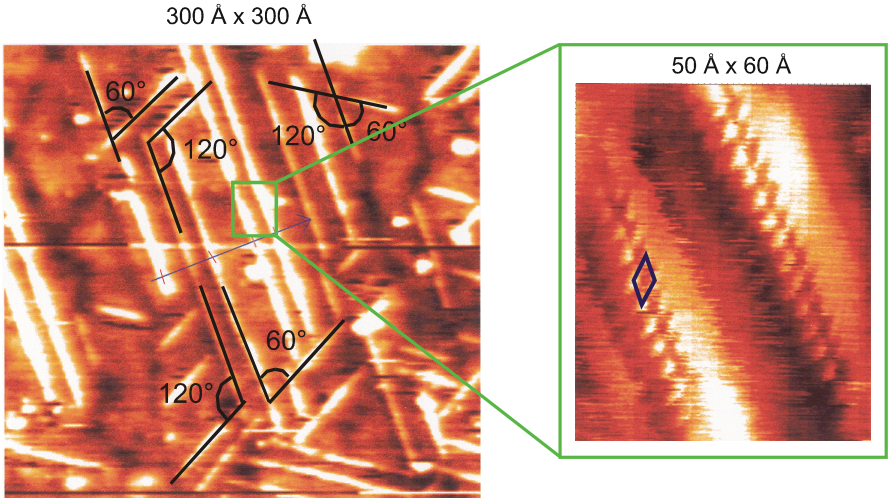

Fig. 8.27. STM image with a scanned area of 300 Å ´ 300 Å and Zoom In image with of an area of 50 Å ´ 60 Å, after annealing at 700 K (U_t = - 0.7 V, I_t = 0.4 nA). The angles and the distances between the streaks and one of the hexagonal unit cells are schematically shown.

This lattice constant is larger than that determined from the LEED data. Nevertheless, we believe that the discrepancy may result from a deficient calibration.

Summary

Ga was deposited on Ni(100) in two different procedures: first, Ga was deposited at 80 K on a Ni(100) substrate, which was covered with a c(2×2)-oxygen overlayer and secondly, Ga was deposited at 300 K directly on Ni(100).

Ga grows disordered on the O-c(2×2)/Ni(100) surface at 80 K. Oxygen adsorption at 80 K leads to the formation of an amorphous Ga oxide which seems to be non stoichiometric. After annealing and oxidation at ~ 700 K, the LEED pattern of the Ga oxide film shows a ring structure of randomly oriented and distorted hexagonal domains. By annealing at 1100 K, ultra thin layers of β-Ga_2O_3 are formed. At 1200 K, the Ga oxide is decomposed and desorbed from the surface.

At 300 K and low nominal deposition, Ga grows as two-dimensional islands on Ni(100). Oxidation at 300 K leads to the growth of an amorphous Ga oxide. Annealing up to 700 K leads to the formation of a well-ordered thin film of γ'-Ga_2O_3, The LEED pattern of Ga_2O_3/Ni(100) shows a 12-fold ring structure which corresponds two hexagonal domains, which are rotated by 90° with respect to each other. During annealing between 300 and 800 K coalescence of the Ga_2O_3 islands takes place and the amorphous Ga_2O_3 transforms into the well-ordered γ'-Ga_2O_3 phase.

Chapter 9

Preparation of a TMR – Model System e.g. Au/Co/Ga_2O_3/Ni(100)

In most of the experiments on spin-polarized tunneling in ferromagnetic (FM)–insulator (I)–ferromagnetic (FM) tunnel junctions, polycrystalline transition metals and amorphous oxides are used as FM and I layers, respectively.

The success of FM–I–FM tunneling depends critically on the properties and the quality of the insulating tunnel barrier [13, 178]. Tunneling is extremely interface sensitive, because it displays the band structure of the electrodes surfaces close to the tunneling barrier [179-183]. The recent breakthrough in observing a TMR of nearly 20% in planar FM–I–FM junctions was possible mostly with tunnel barriers made of Al_2O_3, and to a limited extent with AlN and MgO barriers [13, 23]. Other barrier materials, such as HfO_2 and $SrTiO_3$, with lanthanum peroxide as the FM electrodes, have also been described [184-186].

This Chapter deals with a basic research in which the growth and characterization of a TMR – model system is performed under well defined conditions. The first FM electrode is a Ni single crystal with (100) orientation. A thin film of Ga_2O_3 is grown as tunneling barrier. The second FM electrode is a thin layer of Co which is deposited on top of the Ga_2O_3 layer. The growth of the multilayers was performed in UHV apparatus I. The characterization was performed by means of Auger Electron Spectroscopy (AES), Low Energy Electron Diffraction (LEED) and High Resolution Electron Energy Loss Spectroscopy (EELS).

The clean Ni(100) surface was already described in Chapter 8. The AES spectrum and the LEED pattern of clean Ni(100) surface are shown in Fig. 8.1. A STM image of the surface is presented in Fig. 8.2. The growth and the properties of the Ga_2O_3 layer is described in Section 8 and will not be repeated here. In this Chapter we present the growth of the Co layer, as the second FM electrode, on the top of a well-ordered 7 Å thick γ'-Ga_2O_3(111) layer which was prepared on Ni(100).

9.1 Growth and Properties of the Cobalt Ferromagnetic Layer

9.1.1 Deposition of the Co Film

The deposition of Co was performed by evaporation from a cobalt rod which was heated by electron bombardment. By using the set **B** of parameters a deposition rate of 0.8 Å/minute is obtained (see Section 6.1.3). Figure 9.1 shows the p-to-p intensities of the AES transitions of $Ni_{(848\ eV)}$, $Ga^{3+}{}_{(1066\ eV)}$, $O_{(503\ eV)}$ and $Co_{(775\ eV)}$ as a function of deposition time. As a function of the deposition time the signal of the AES transition of $Co_{(775\ eV)}$ increases and the intensities of the other transitions of $Ni_{(848\ eV)}$, $Ga^{3+}{}_{(1066\ eV)}$ and $O_{(503\ eV)}$ decrease. After a deposition time of 35 min, the intensity of the $Ni_{(848\ eV)}$ transitions vanished completely, while that of $Ga^{3+}{}_{(1066\ eV)}$ is decreased, by 60 %. The explanation is the following: The AES electrons of $Ga^{3+}{}_{(1066\ eV)}$ have a IMFP of ~ 17 Å in Co, while the Ni electrons with an energy of 848 eV have a IMFP of ~ 14 Å [50, 148, 149]. The $Ni_{(848\ eV)}$ electrons have to pass the Ga_2O_3 layer (~ 7 Å) and the Co layer which after a deposition time of 35 minutes has an effective thickness of ~ 10 Å. Hence, electrons of the $Ni_{(848\ eV)}$ transition can not pass elastically the Ga_2O_3 and Co layers. The intensity of the transition of Ga^{3+} electrons at 1066 eV decreases

continuously during the deposition of Co and is almost zero after deposition of 55 minutes. In this case the $Ga^{3+}_{(1066\,eV)}$ electrons have to pass only the Co layer.
The decrease of the AES signal of $Ga^{3+}_{(1066\,eV)}$ was used to determine the effective thickness (*d*) of the Co overlayer $\left(l \cong 17\text{Å for Ga}_{(1066\,eV)}\right)$. The effective film thickness after a nominal deposition of 16 Å was estimated to be 8 Å. After a deposition time of 55 minutes the effective thickness is estimated to be ~ 13 Å. In addition, the AES signal of the $O_{(503\,eV)}$ transition was also used to determine the effective thickness of the Co layer.

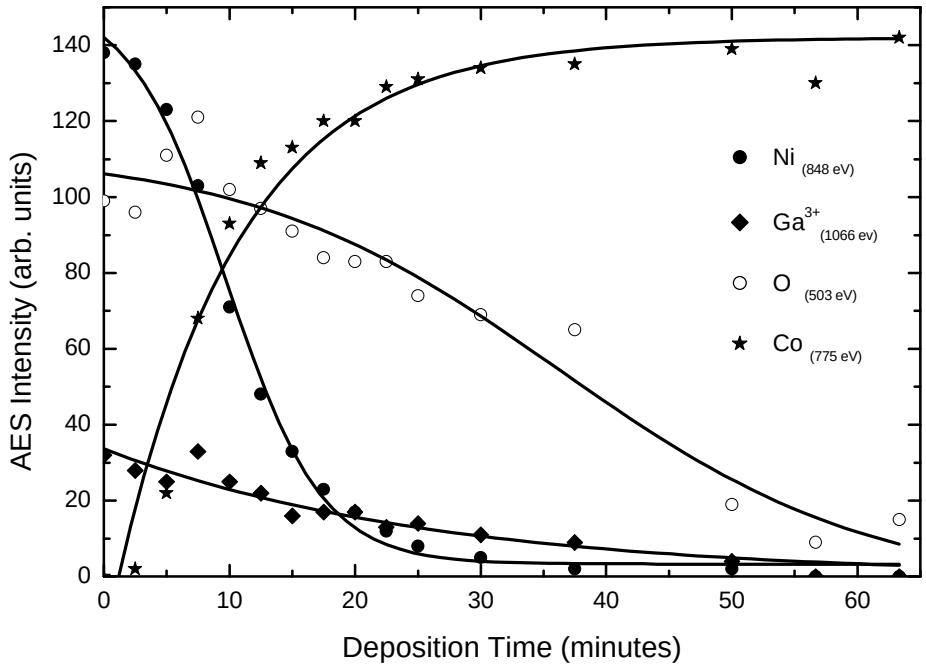

Fig. 9.1a. The p-to-p intensity of the AES transitions of $Co_{(775\,eV)}$ (★), $Ni_{(848\,eV)}$ (●), $Ga^{3+}_{(1066\,eV)}$ (◆) and $O_{(503\,eV)}$ (○) as a function of the deposition time of Co. The solid lines represent a guide for the eyes.

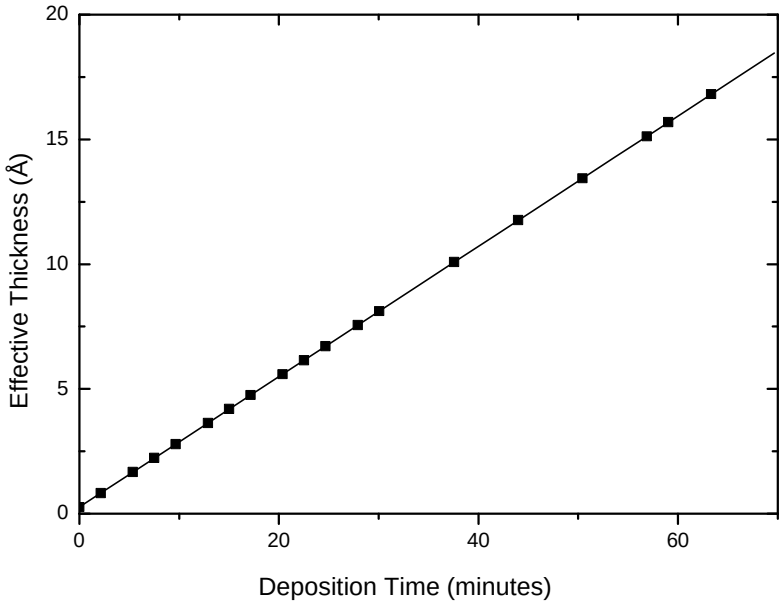

Fig. 9.1b. The effective thickness of the Co layer as a function of the deposition time.

Using the oxygen transition $\left(l \cong 9.3\text{Å} \text{ for } O_{(503\,eV)}\right)$ [148], the effective thickness of the Co layer after deposition of 55 minutes is estimated to be ~ 12.5 Å, which is in a good agreement with the estimated thickness on the base of $Ga^{3+}_{(1066\ eV)}$ transition. The effective thickness of the Co layer as a function of the deposition time is shown in Fig. 9.1b.

Fig. 9.2 shows EEL spectra of the Ga_2O_3 layer on Ni(100) as a function of the effective thickness of the Co layer. The Co layer was deposited in a stepwise manner on the Ga_2O_3 surface up to the final effective thickness of 25 Å. The spectrum at the bottom represents the well-ordered Ga_2O_3 on Ni(100) (see also Chapter 8). It exhibits losses at 305 (ν_1), 470 (ν_2) and 745 cm^{-1} (ν_3). The intensities of the two losses at 470 cm^{-1} (ν_2) and 745 cm^{-1} (ν_3) decrease about ten times after deposition of only 1.5 Å of Co. The loss at 305 cm^{-1} (ν_1) is not observed anymore. When 3 Å of Co was deposited the intensity of the losses

decreases twenty times with respect to the bottom spectra and a very broad loss feature between 600 and 800 cm^{-1} develops. This loss feature originates from the loss at ~ 745 cm^{-1} and a new loss around 680 cm^{-1} occurs. After deposition of 5 Å of Co, the new loss at 680 cm^{-1} shifts to ~ 650 cm^{-1} and the loss at 745 cm^{-1} shifts to ~ 780 cm^{-1}. However, these two losses are not resolved and only a very broad loss feature is observed in the frequency region between 550 and 800 cm^{-1}. This suggest that many losses occur in this energy region – they could result from the same bonding structure which may are slightly different in the bond length and angles (inhomogeneous broadening). On the other hand the frequency of the FK-phonons of CoO is lying between 523 and 565 cm^{-1} [187, 188] and may be some Co-O bonds result. It is interesting to notice that a similar loss structure was found by solely annealing the Ga_2O_3 films on Ni(100) at T ≥ 1000 K (see Fig. 8.15). As already mentioned in Section 8.2.2.2, may be some atoms of Co (in this case) diffuse into the Ga_2O_3 layer and a new structure (mixed oxide) is built.

After deposition of Co with a effective thickness of 10 Å further shifts of frequency 650 cm^{-1} and 780 cm^{-1} appear and the intensity decreases further, while after 15 Å all losses are disappeared, which is due to the screening of the dipoles of the oxide by the metallic layer.

What can be learned from the EELS investigations?

- ✓ Structure (growth mode) of the Co layer.

With increasing the amount of deposited Co up to 10 Å the intensities of the EELS losses of the Ga_2O_3 decrease but are not zero. This suggest that Co grows in 3D-islands on the surface which leaves part of the Ga_2O_3 surface free of Co. From this area which becomes smaller and smaller the EELS losses are observed. This is in agreement with the LEED observation: after deposition of Co with an effective thickness smaller than 15 Å the LEED screen exhibits diffuse illumination. Above this thickness of the Co deposit the whole surface is covered with Co and the EELS losses are screened.

- ✓ Loss features in the EEL spectra of the Ga_2O_3 layer.

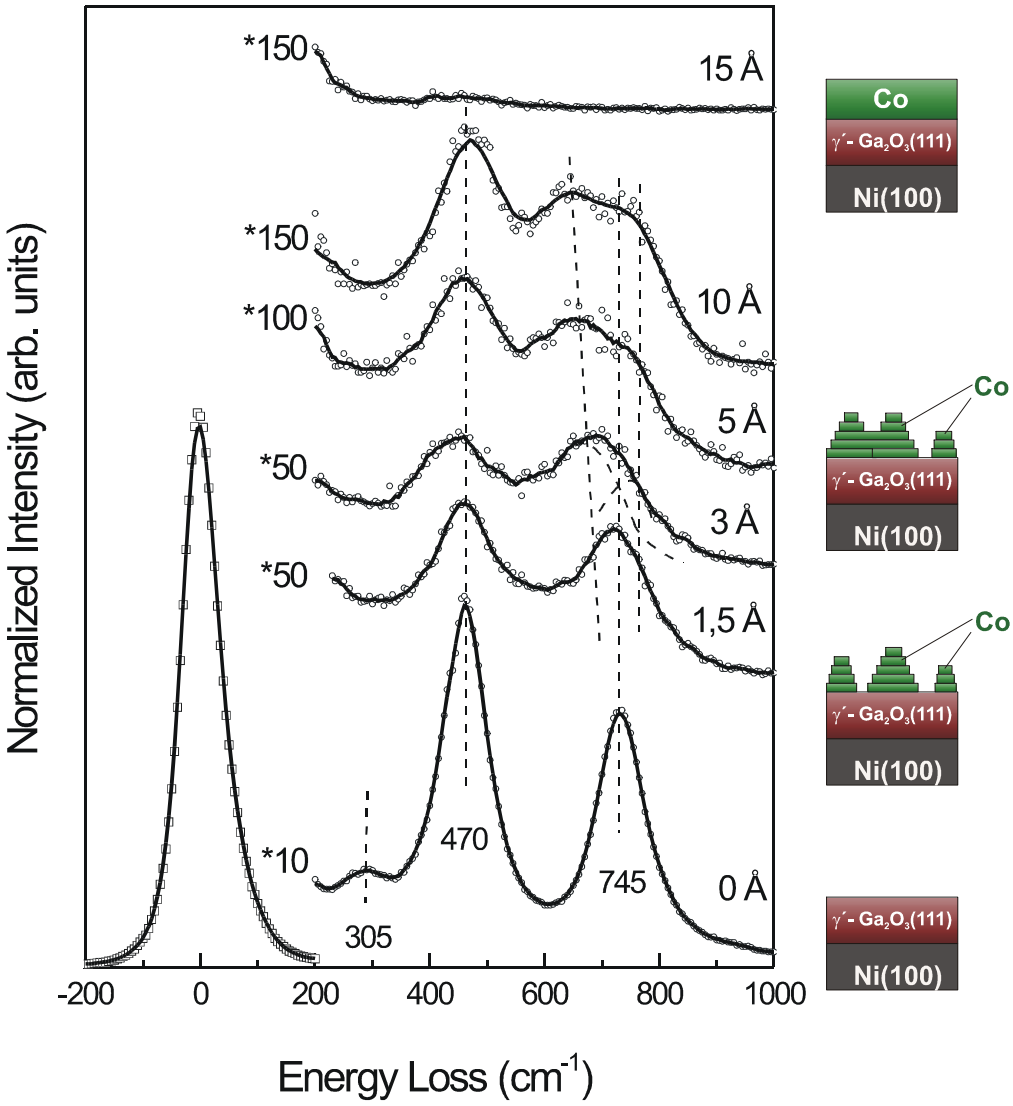

Fig. 9.2. EEL spectra of g´-Ga_2O_3/Ni(100) as a function of the effective thickness of the deposited Co overlayer.

During Co deposition the intensities of all losses are decreasing. The week loss at 305 cm^{-1} vanish after a deposition of 1.5 Å, while the other one only after deposition of ~15 Å. This later effect is explained by the screening of the dipoles of Ga_2O_3 by the Co layer. The new losses in the frequency region between 550

and 800 cm^{-1} which can not be resolved could be a result of the interaction of the Co clusters with the underlying Ga_2O_3 layer or by diffusion of some Co atoms into the Ga_2O_3 layer and the formation of a new structure (mixed Ga-Co oxide). It is clearly observed that especially the loss at 745 cm^{-1} is influenced by the Co deposit, according to the discussion above.

From a thermodynamical point of view a cluster (3D) growth of Co on γ´-Ga_2O_3(111) is expected, because of the difference between the surface free energies of Ga_2O_3 and cobalt. For Ga_2O_3 the value of the surface free energy is not known, but the similarity between Ga_2O_3 and Al_2O_3 allow us to use the value of surface free energy of Al_2O_3 for comparison. Depending on the structure of Al_2O_3 the surface free energy is between 650 and 925 mJ/m^2 [74]. These values are considerable smaller then one of the cobalt (1870 mJ/m^2). Thus, a 3D growth (V-W) is expected. On the right side of Fig. 9.2 a growth scenario of the trilayer structure is shown.

9.1.2 The Thermostability of the Co/Ga_2O_3/Ni(100) System

The stability of the multilayer Co(25Å)/Ga_2O_3(7Å)/Ni(100) system was investigated in the temperature range between 300 and 1200 K. The sample was annealed in steps of 100 K and the intensities of the AES transition of $Co_{(775\ eV)}$ was studied as function of the annealing temperature. The results are plotted on Fig. 9.3. During the annealing up to 1100 K, the AES intensity of $Co_{(775\ eV)}$ is constant and no other changes were observed. After annealing at 1200 K the intensity of the Co transition is strongly decreased, while the triplet of the Ni NMM transitions appear and the LEED pattern shows the structure of the clean Ni(100) surface.

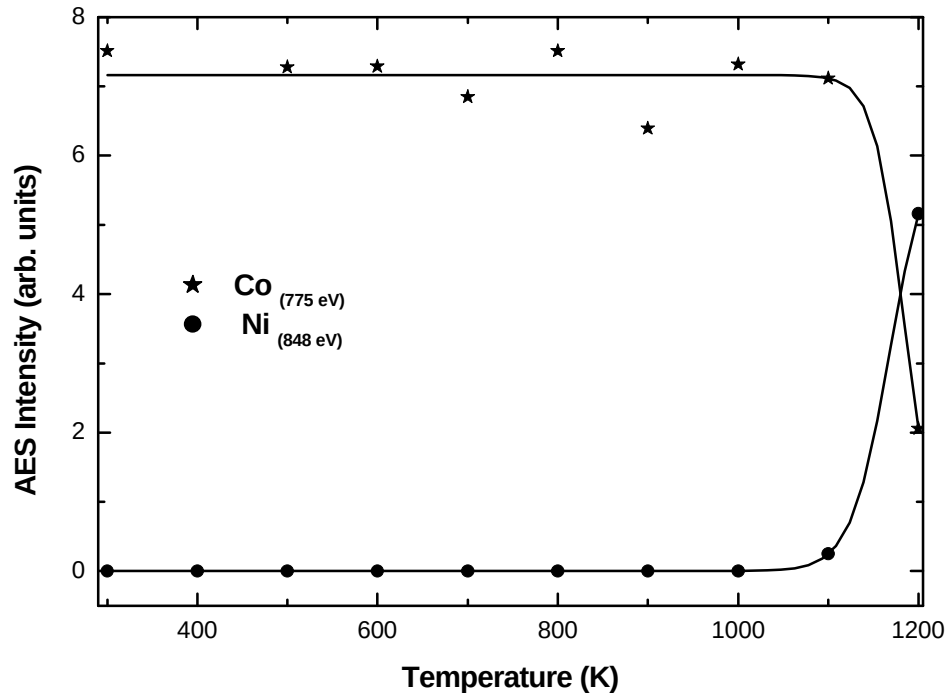

Fig. 9.3. The p-to-p intensity of the Auger transitions of $Co_{(775\ eV)}$ (★) and $Ni_{(848\ eV)}$ (●)after every step of annealing. The solid lines represent a guide for the eyes.

The decrease of the intensity of the Co transitions is related to the decomposition and desorption of the Ga_2O_3 layer which takes place above 1100 K [177]. Simultaneously, Co diffuses into the substrate. The thermostability of the $Co/Ga_2O_3/Ni(100)$ system was also investigated by EELS. During annealing only the elastically reflected electrons are observed and no losses. This suggests that the Co film is stable on the surface and the Co atoms do not segregate through the Ga oxide film into the substrate. This represents a variance to the $Co/Al_2O_3/NiAl(Ni_3Al)$ systems, where at around 700 K a diffusion of the Co atoms through the Al_2O_3 was observed [150, 189].

Fig. 9.4 shows LEED patterns which were obtained as follows: a) is the LEED pattern of randomly orientated domains of γ´-Ga_2O_3(111), grown on Ni(100) and shows a weak ring structure (see Section 8.2).

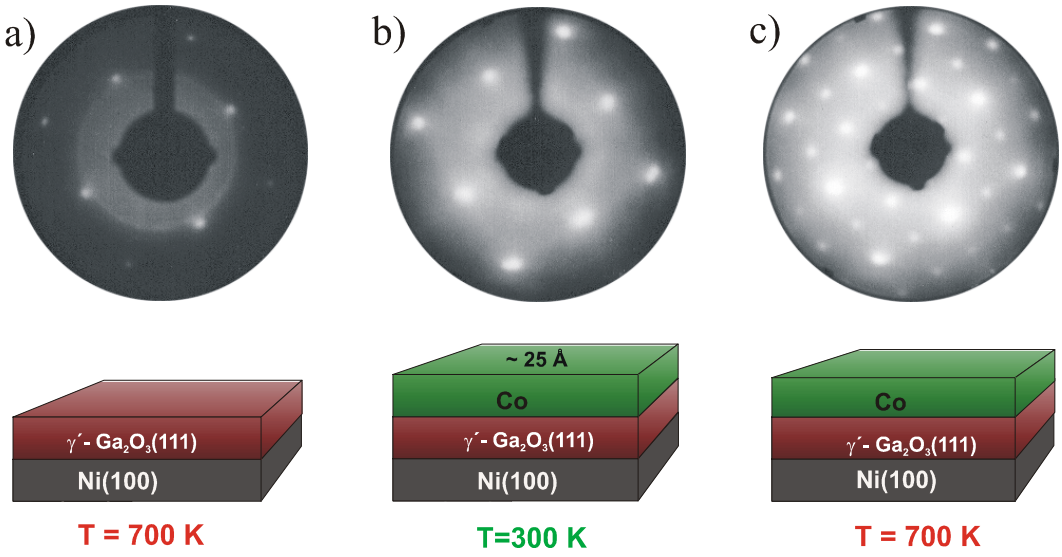

Fig. 9.4. LEED pattern and models of the growth of the Co/Ga_2O_3/Ni(100) system: a) g´-Ga_2O_3/Ni(100); b) Co(25Å)/Ga_2O_3/Ni(100) at room temperature; c) Co/Ga_2O_3/Ni(100) system after annealing at 700 K. The LEED images were taken at energy of 122 eV.

After deposition of 25 Å of Co at 300 K the LEED pattern (b) exhibits a quadratic structure with a lattice constant of ~ 2.48 ± 0.05 Å which is similar to that of the unit cell of Ni(100). The Brag reflections appear on a diffuse background. This structure corresponds to a fcc Co(100) surface. This suggests that such a thick Co layer grows ordered on the γ´-Ga_2O_3 layer. Actually, because of the cluster growth mode of the Co on the Ga_2O_3 it is not possible to get perfectly well-ordered thin Co layer. The Co clusters have to become large enough in order to

coalescence and to form ordered surfaces measurable by LEED. During annealing the LEED spots became sharper and structural changes develops. After annealing to 700 K the LEED pattern of the Co layer shows another quadratic pattern with an unit cell which has a lattice constant of 3.54 Å. Thus, the LEED pattern corresponds to the c(2×2) reconstruction of the (100) surface of fcc Co (see Section 5.2).

9.2 Growth of an Au Layer on $Co/Ga_2O_3/Ni(100)$

The growth of an Au cap layer on the Co layer was investigated by AES and LEED. A gold layer with a nominal thickness of 50 Å was evaporated on the top of the Co layer at 300 K. Fig. 9.5 shows the AES spectrum and the LEED pattern of the deposited Au layer. The AES spectrum exhibits only the gold transitions.

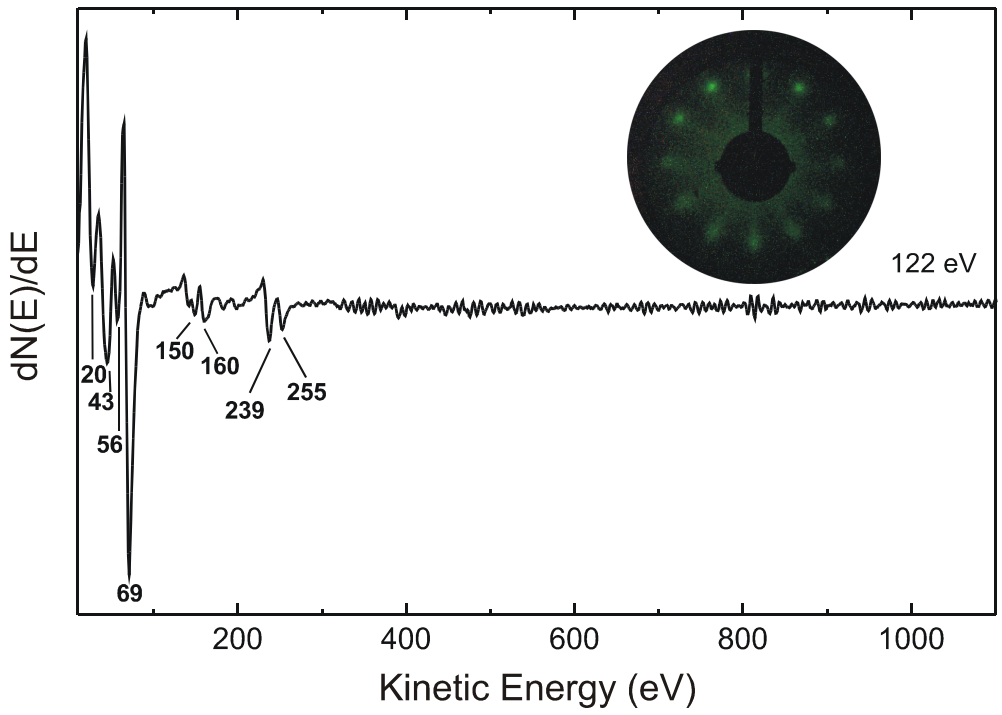

Fig 9.5. AES spectrum and LEED pattern of the $Au(50\ Å)/Co(25\ Å)/Ga_2O_3(7\ Å)/Ni(100)$ system.

The LEED pattern was taken at energy of 122 eV and shows a 12 fold ring structure. This 12 fold ring structure is explained by two hexagonal domains, which are rotated by 90° with respect to each other. Therefore, Au grows with the (111)-plane parallel to the (100) surface of fcc Co. The lattice constant was estimated to be 3.52 ± 0.15 Å which corresponds to that of the unit cell of the Au(111) plane.

9.3 The TMR - Model System

The main purpose of our investigations was to study the growth and properties of a TMR – model system. Especially, we wanted to find conditions for an epitaxial growth of a well-ordered (crystalline) tunnel barrier and of the second FM layer. With other words we have studied:

- ✓ the growing properties;
- ✓ the oxidation behavior;
- ✓ the thermal stability

of the ferromagnetic electrodes and the insulating tunnel barrier as well, like it is shown in Fig. 9.6.

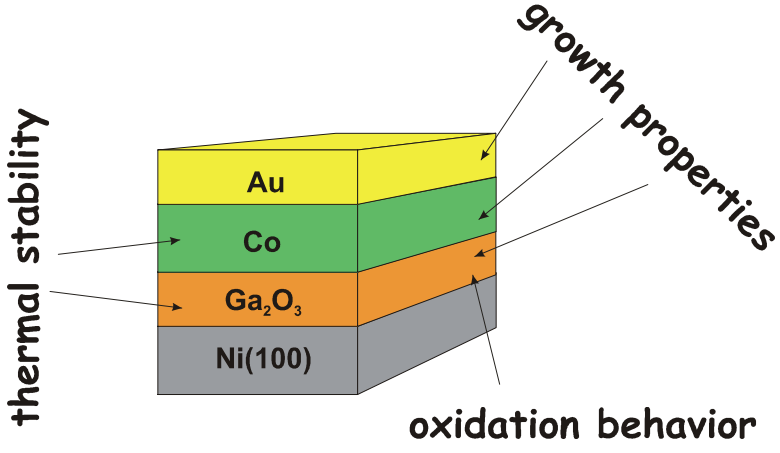

Fig. 9.6. Schematic presentation of the performed study.

We have performed several experiments with different thickness of the Ga_2O_3 tunnel barrier and every time we obtained very similar growing properties, oxidation behavior and thermal stability as well. The transport properties (tunneling current) of this TMR system was not studied. For this a structuring of the surface (by lithography) is necessary which could not be done in our institute. Also, at 300 K electrons pass easy through the ultra thin Ga_2O_3 layer. Thus, transport measurements on a structured surface at low temperature are necessary in order to get information if such a structure has a potential of applications.

Summary

The scenario, described in this Chapter is schematically presented in Fig. 9.7. A TMR model system was grown on a ferromagnetic single crystalline substrate (Ni(100)). First, a 7 Å thick was grown on Ni(100). Co was deposited at 300 K on the Ga_2O_3 layer.

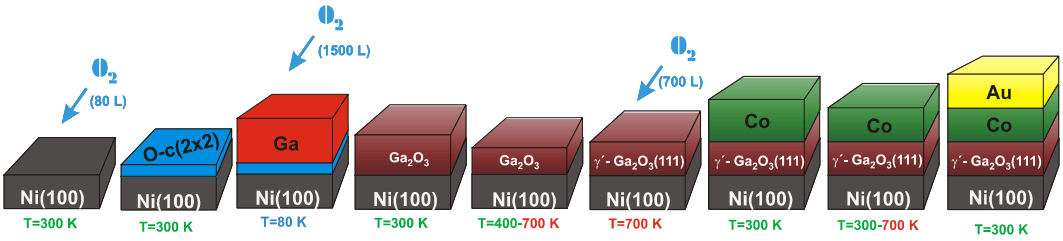

Fig. 9.7. The schematic of the grown TMR system

It was found, that a 25 Å thick Co layer grows ordered with the (100) plane of the fcc Co parallel to the Ni(100) surface. The Co layer covers completely the Ga_2O_3 surface and screens perfectly the dipoles of the Ga_2O_3 layer. After annealing at 700 K, the Co(100) surface is reconstructed and shows a c(2×2) structure.

At 300 K, Au grows ordered on the c(2×2)-Co(100) surface. The LEED pattern shows a twelve fold ring structure which is explained by two domains with hexagonal structure, which are rotated by 90° with respect to each other.

Chapter 10

The Formation of a Ni_3Ga Surface Alloy – a STM, LEED and AES Study

Intermetallic compounds such as transition-metal aluminides and silicides have attracted much attention in resent years, particularly as high-temperature structural materials [30]. Ordered compounds with a $L1_2$ (prototype Cu_3Au) structure belong to a group of intermetallic phases and typically, they are formed in alloys of Ni, Fe and Pt. The nickel-containing compounds of the type Ni_3X (X=Al, Ga, In, Pd) are the most promising materials for engineering applications due to their excellent mechanical parameters and their corrosion resistance. Binary intermetallic compounds that contain a transition metal and a group-III metal display also interesting electronic and magnetic properties. For instance, Ni_3Al possess a weak itinerant ferromagnetism with T_C = 71 K and a small magnetic moment (0.23 mB per cell) [31], while Ni_3Ga is an exchange enhanced paramagnetic alloy [32], and Ni_3In is nonmagnetic.

In this Chapter some aspects of the formation of a surface alloy of Ni_3Ga are presented. The data in this Chapter should be considered as preliminary results, further investigations are necessary to elucidate this complex problem. The investigations were performed in the OMICRON UHV apparatus and Ga was evaporated from a “Solid State Evaporation” source of Ga.

10.1 STM Investigations

Ga was deposited at 300 K, on the clean Ni(100) surface, with different coverages of Ga: 10%, 30% and 90%. This coverage was determined by STM. Afterwards, the sample was annealed step by step and the surface morphology was investigated by means of STM, AES and LEED.

- **Ni(100) covered with 10% Ga**

Fig. 10.1 shows a STM image of Ni (100) covered with 10% Ga. As already discussed in Section 8.3, Ga grows in small two-dimensional islands on the Ni(100) surface. The two-dimensional growth (Frank - Van der Merve) of Ga on Ni(100) is explained by the large difference between the surface free energy of Ga

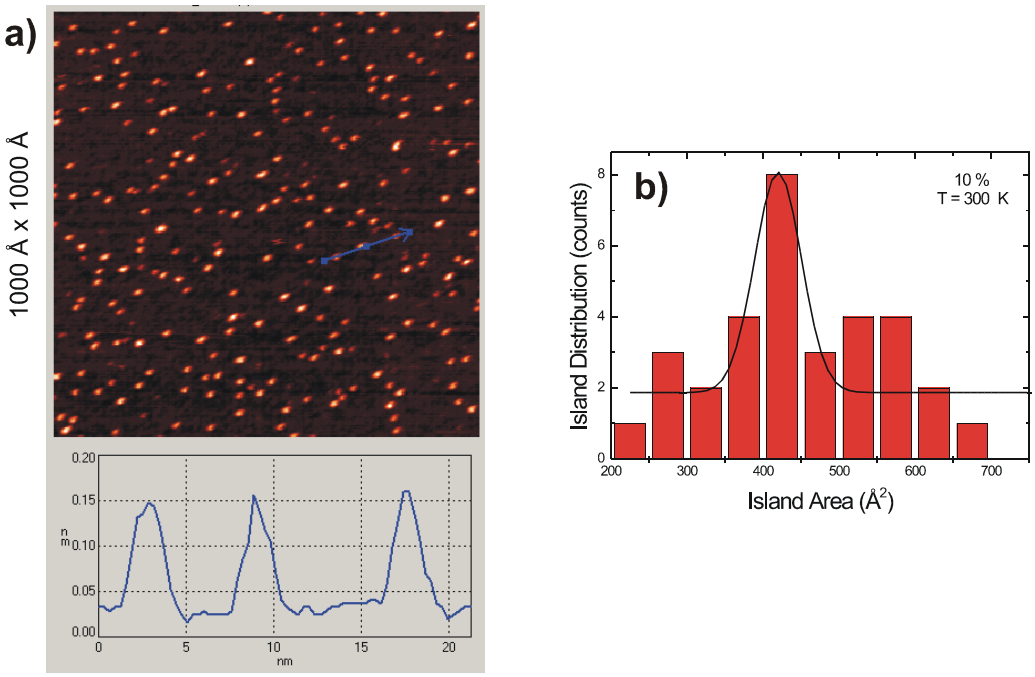

Fig. 10.1. a) STM image with a line scan of the Ni(100) surface covered with 10 % of Ga (U_t = 1.0 V, I_t = 2.0 nA); b) The island distributions as a function of the islands area.

$\left(g^{0}_{Ga} = 720mJ/m^2\right)$ and Ni $\left(g^{0}_{Ni} = 2364mJ/m^2\right)$. A line scan below the image shows the profile of the islands which have a height of ~1.2 Å. This height suggest that the Ga atoms are sitting in fourfold hollow sites on Ni(100 (see Section 8.3.1)). A model of the Ga atoms, sitting in fourfold hollow sites of the Ni(100) is drawn in Fig. 8.19c. The distribution of the islands is shown in Fig. 10.1b. The distribution has a maximum which is centred at around 380 Å^2.

Fig. 10.2 and Fig. 10.3 show the morphology of the surface after deposition of 10% of Ga and subsequent annealing at 400 and 483 K, respectively. During annealing at 400 K, some Ga islands coalesce but larger islands grow mainly by a mass transport (diffusion) from small islands to the larger one. The coalescence of the islands plays the main role at larger densities of the islands.

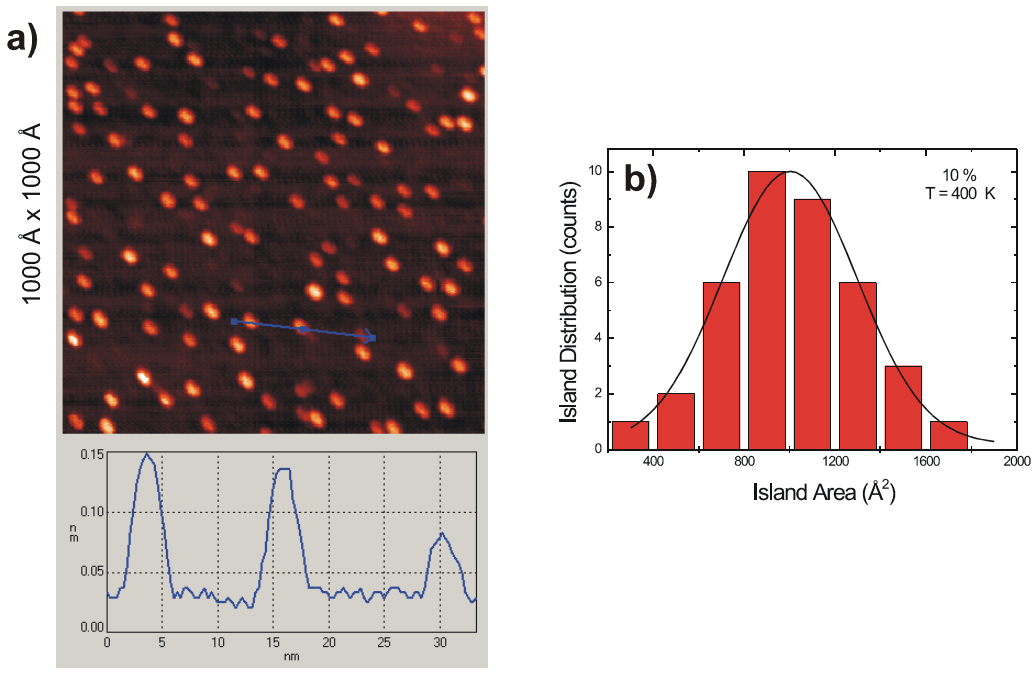

Fig. 10.2. a) STM image with a line scan of the Ni(100) surface covered initially with 10 % of Ga and annealed at 400 K (U_t = 1.0 V, I_t = 2.0 nA); b) The island distributions as a function of the islands area.

After annealing at 400 K, two different kind of islands are found with two different heights of 0.6 and 1.2 Å. Thus the Ga atoms are sitting in fourfold hollow sites on Ni(100) as well as, may be due to the annealing, some of the islands diffuse into the substrate surface and therefore a smaller height of 0.6 Å develops.

At 400 K, the maximum of the distribution of the island area (Gaussian) is centered at around 1000 $Å^2$ (Fig. 10.2b) and the islands cover still ~ 10 % of the surface, while after annealing at 483 K the island have a size of the order of 3000 $Å^2$ (Fig. 10.3b). Now, the islands cover only 2 % of the surface, which suggests that a part of the Ga atoms are diffused into the substrate. After annealing at higher temperature and/or as a function of the annealing time at 400 K the Ga islands disappear from the surface by diffusion of the Ga atoms into the substrate. The STM measurements were performed at 300 K after every step of annealing.

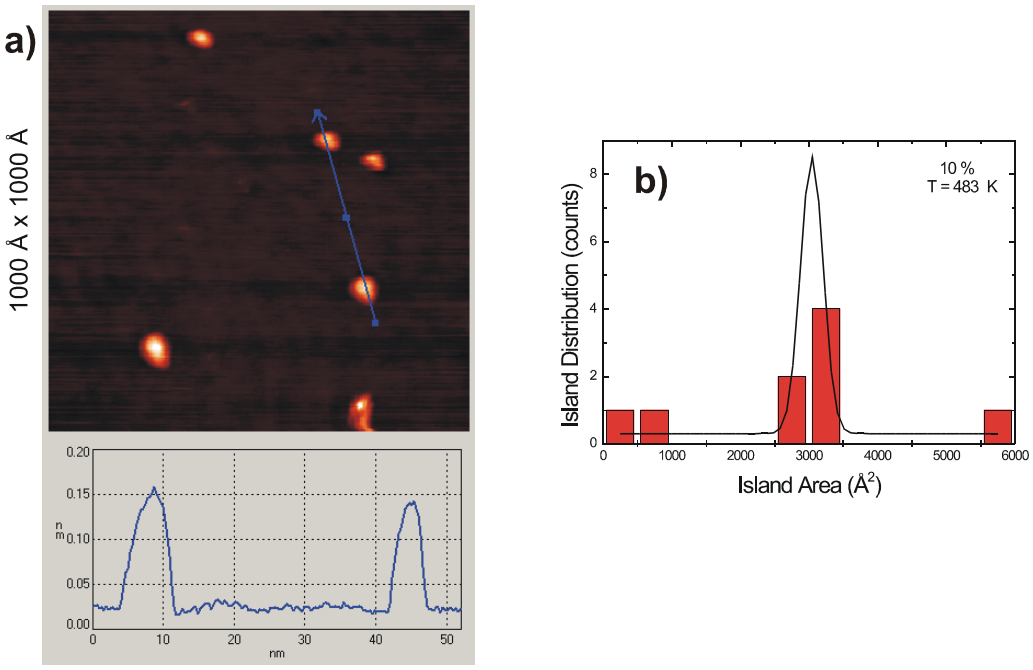

Fig. 10.3. a) STM image with a line scan of the Ni(100) surface covered initially with 10 % of Ga and annealed at 483 K (U_t = 1.0 V, I_t = 2.0 nA); b) The island distributions as a function of the islands area.

- **Ni(100) covered with 30% Ga**

Fig. 10.4a shows a STM image of the Ni(100) surface, which is covered with 30% of Ga. A line scan of the image shows the roughness of the surface with a maximal deviation of ~ 1.2 Å which corresponds to the height of the two-dimensional islands. The large density of the islands does not permit to determine precisely the shape of single islands. Fig. 10.4b shows the distribution of the island area with a maximum centered at ~ 350 $Å^2$. Thus, the distribution of the islands is similar for both coverage (10% and 30 %) of the Ni(100) surface with Ga.

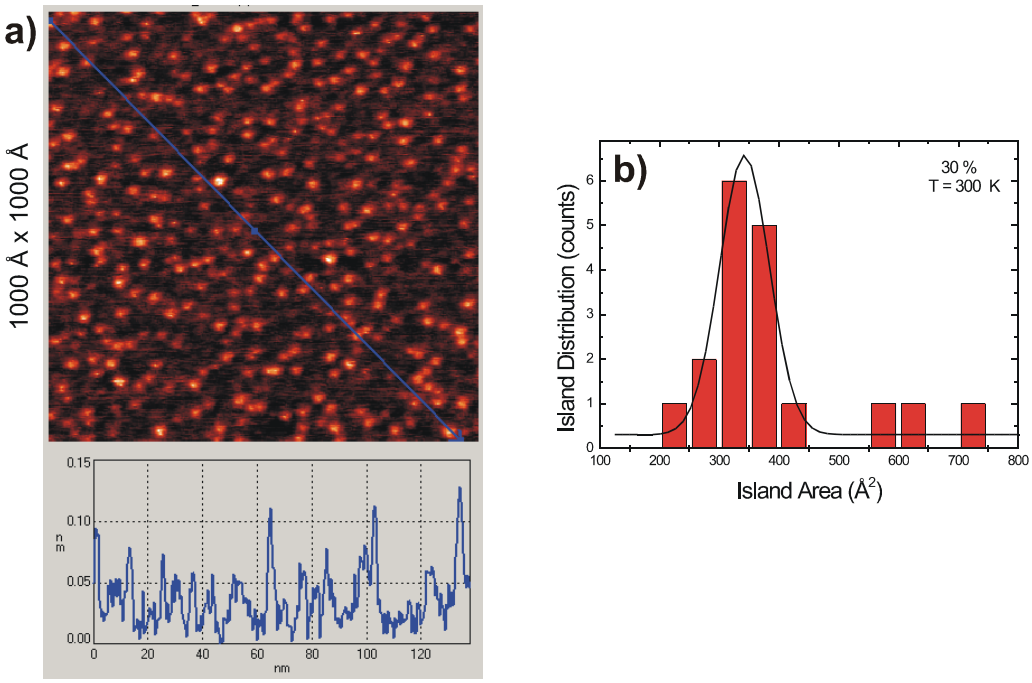

Fig. 10.4. a) STM image with a line scan of the Ni(100) surface covered with 30 % of Ga at 300 K (U_t = 2.0 V, I_t = 0.3 nA); b) The island distributions as a function of the islands area.

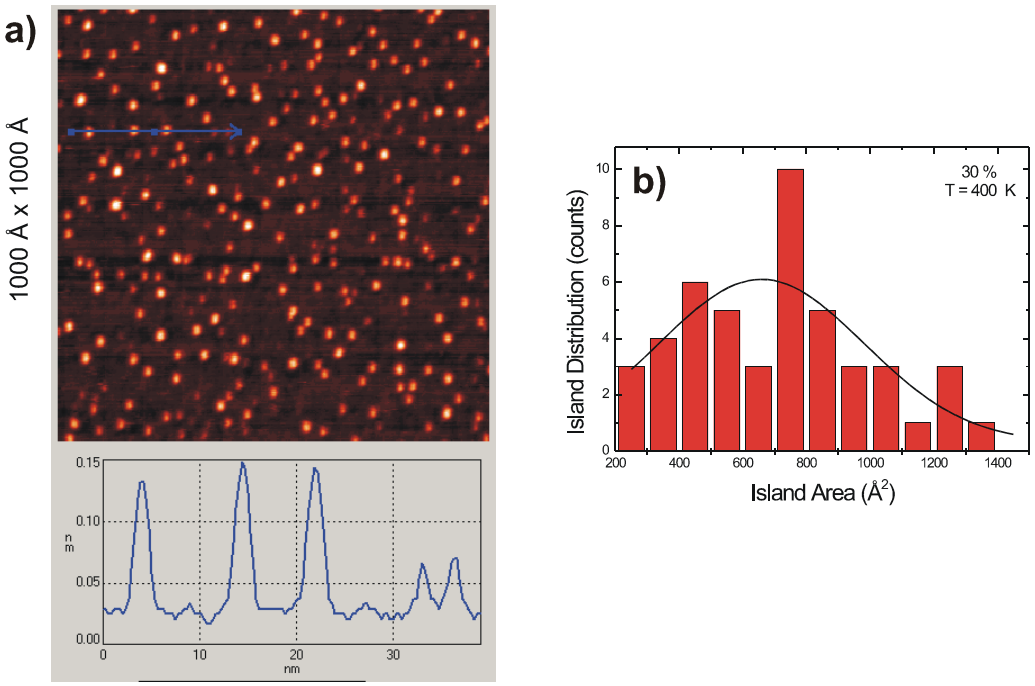

Fig. 10.5. a) STM image with a line scan of the Ni(100) surface covered initially with 30 % of Ga and annealed at 400 K (U_t = 0.5 V, I_t = 1.5 nA); b) The island distributions as a function of the islands area.

After annealing at 400 K some islands coalesce and larger islands grow also by a mass transport (diffusion) from smaller islands to the large one. The maximum of the distribution of the islands is centered at ~ 700 Å^2 (Fig. 10.5b). The surface is still covered with ~ 30 % of Ga which shows that no diffusion of Ga atoms into the substrate sets in up to 400 K. A line scan of the STM image (Fig. 10.5a) shows the presence only of two-dimensional islands with heights of 0.6 and 1.2 Å. The STM measurement was performed at 400 K.

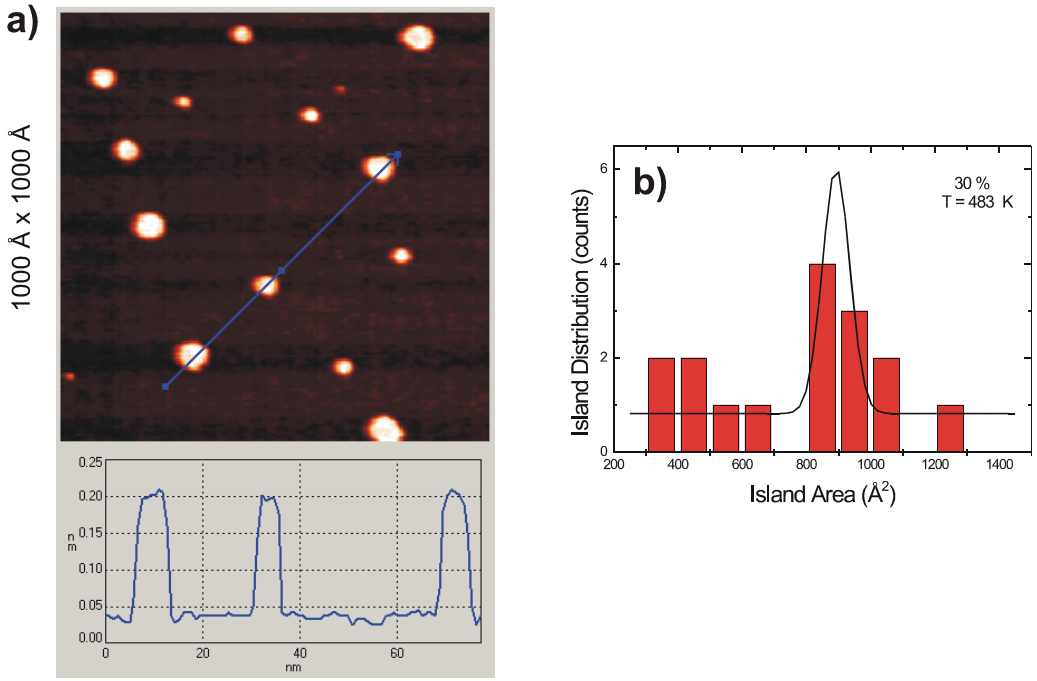

Fig. 10.6. a) STM image with a line scan of the Ni(100) surface covered initially with 30 % of Ga and annealed at 483 K (U_t = 0.4 V, I_t = 2.0 nA); b) The island distributions as a function of the islands area.

Afterwards the sample was annealed at 483 K and the STM image shows only large islands (see Fig. 10.6a). The most frequently found islands have areas of ~ 700 Å^2 (Fig. 10.6b) and now the islands cover only about 6 % of the surface. Thus, subsequently with the enlargement of the islands a diffusion of Ga atoms into the Ni substrate takes place. Only 2D islands with a height of 1.5 Å are found (see the line scan below the image).The STM image was taken at 483 K.

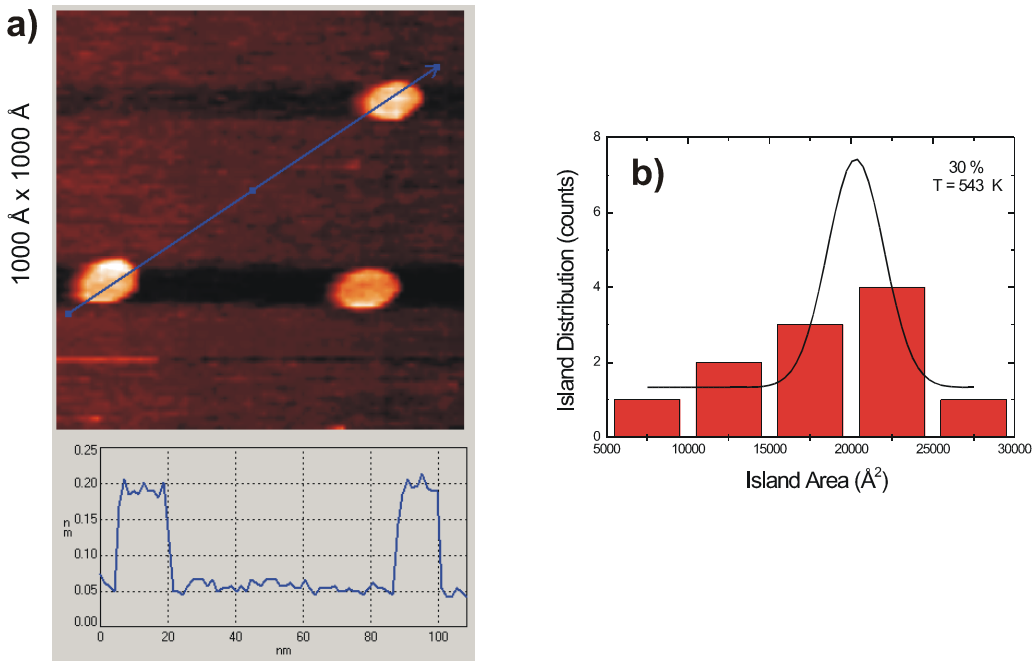

Fig. 10.7. a) STM image with a line scan of the Ni(100) surface covered initially with 30 % of Ga and annealed at 543 K (U_t = 1.5 V, I_t = 1.5 nA); b) The distributions of the islands as a function of the islands area.

After annealing at 543 K large 2D islands are found with a height of 1.5 Å. (Fig. 10.7a) and the maximum of the distribution of the islands is located at ~ 2×10^4 $Å^2$ (Fig. 10.7b). The STM image was taken at 543 K.

As in the first case (10%) by annealing at higher temperatures (and/or as a function of longer annealing time) all the islands disappear from the surface by diffusion of the Ga atoms into the Ni substrate.

- **Ni(100) covered with 90% Ga**

Fig. 10.8a shows a STM image taken of Ni(100) surface covered with ~ 90 % of Ga at 300 K. The distribution of the islands is again centered around ~ 350 $Å^2$ (Fig. 10.8b) and the surface shows a rough morphology. The roughness amounts to ~ 1 Å

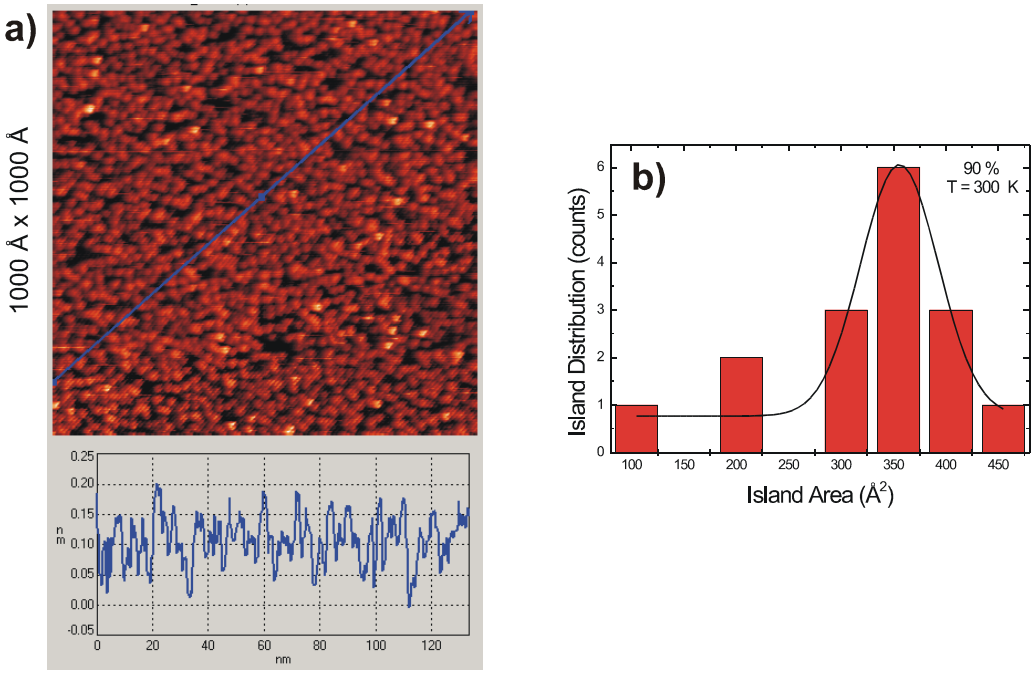

Fig. 10.8. a) STM image with a line scan of the Ni(100) surface covered with 90 % of Ga at 300 K (U_t = -1.8 V, I_t = 0.25 nA); b) The island distributions as a function of the islands area.

After annealing at 400 K, the STM image in Fig. 10.9a was found. The island grow by coalescence and diffusion (mass transport) from small islands to large one and the distribution has a maximum centered at ~ 450 $Å^2$ (Fig. 10.9b). May be at this density of the islands the coalescence of them play the main role in the growth of larger islands. Line scan shows that the surface has a roughness with a maximal deviation of ~ 1 Å. The STM image was taken at 400 K.

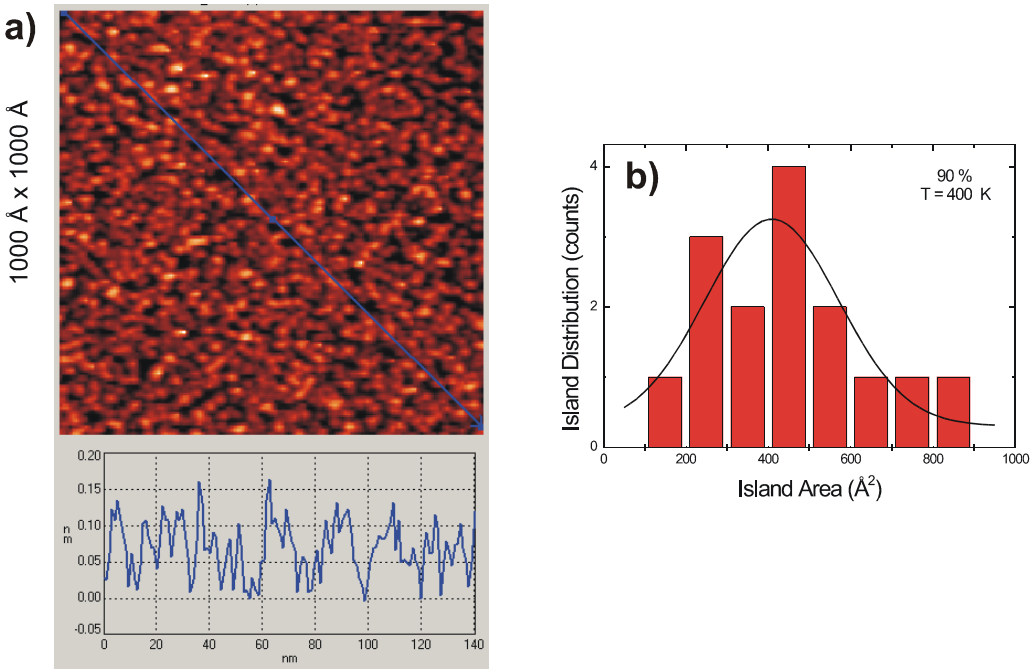

Fig. 10.9. a) STM image with a line scan of the Ni(100) surface covered with 90 % of Ga and annealed at 400 K (U_t = -1.8 V, I_t = 1.0 nA); b) The island distributions as a function of the islands area.

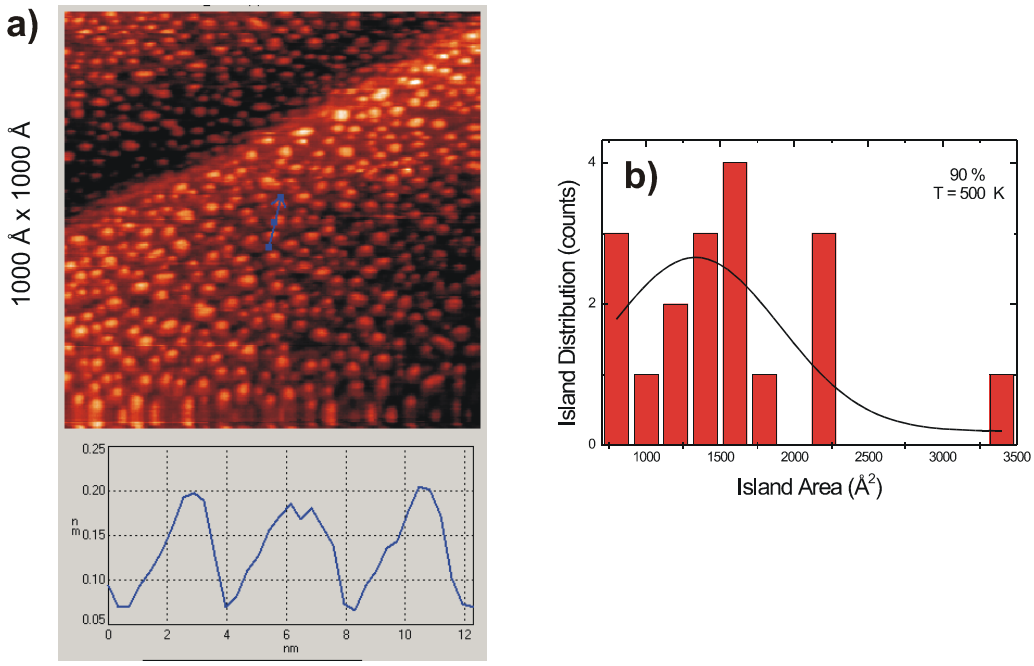

Fig. 10.10. a) STM image with a line scan of the Ni(100) surface covered initially with 90 % of Ga and annealed at 500 K (U_t = -1.8 V, I_t = 0.3 nA); b) The island distributions as a function of the islands area.

Fig. 10.10a shows a STM image after annealing at 500 K. The Ga coverage (initially 90 %) on the surface is decreased to ~ 80 %. The distribution of the islands exhibits a broad structure between 1000 and 1500 $Å^2$ (Fig. 10.10b). The islands are about 1.2 Å high which represents the height of 2D Ga islands. The STM image was taken at 500 K.

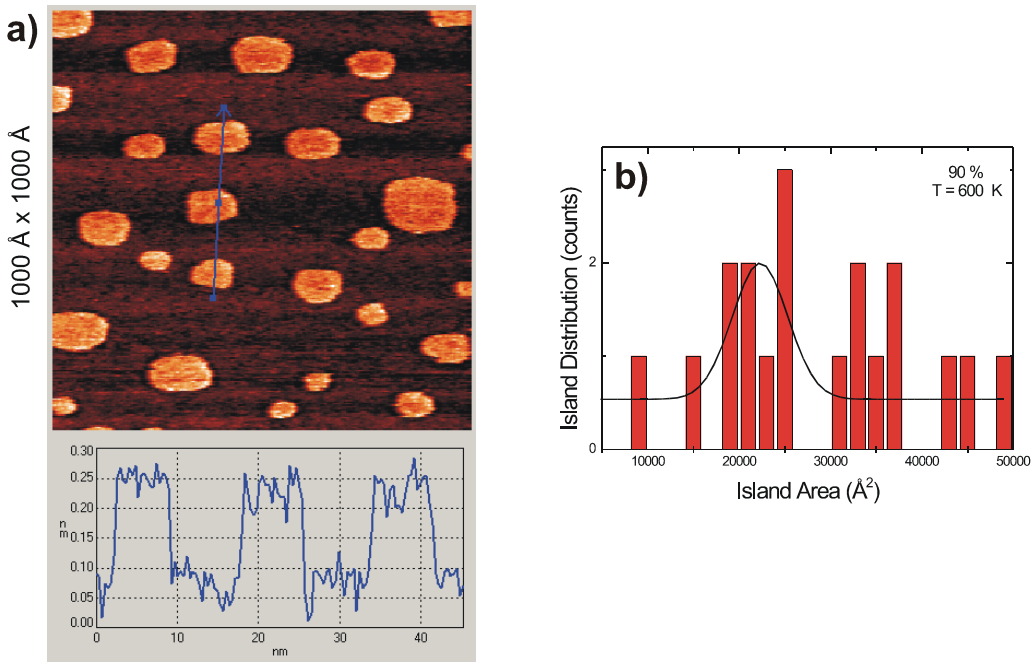

Fig. 10.11. a) STM image with a line scan of the Ni(100) surface covered initially with 90 % of Ga and annealed at 600 K (U_t = 2.0 V, I_t = 0.6 nA); b) The island distributions as a function of the islands area.

After annealing at 600 K the 2D Ga islands cover about 30 % (Fig. 10.11a) of the surface and only very large islands of the order of 23×10^3 Å^2 (Fig. 10.11b) are observed. The height amounts to 1.2 Å. The surface of the islands is very flat. The decrease of the coverage of the Ni(100) surface is an unequivocal evidence of the diffusion of the Ga atoms into the substrate. The STM image was taken at 600 K.

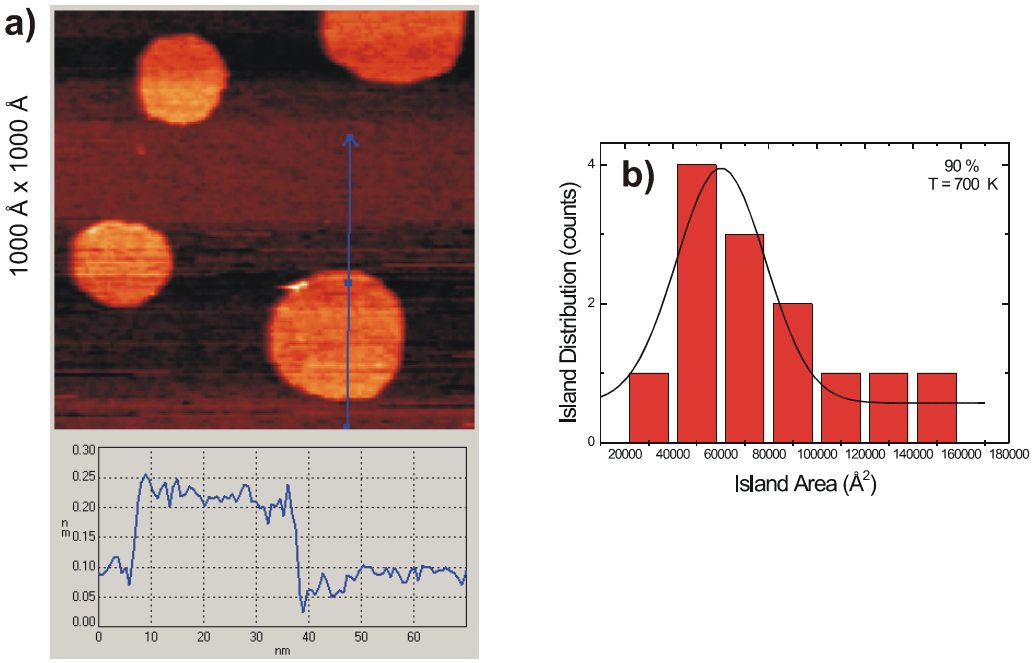

Fig. 10.12. a) STM image with a line scan of the Ni(100) surface covered initially with 90 % of Ga and annealed at 700 K (U_t = 2.4 V, I_t = 0.5 nA); b) The distribution of the islands with a maximum centered at ~ 6 ´ 10^4 Å^2.

Fig. 10.12a shows the morphology of the surface after annealing at 700 K. The Ga 2D islands occupy ~ 20 % of the surface. Only three islands are shown in the image, because the shown area is only 1000 Å × 1000 Å. The height of the islands amounts to ~ 1.2 Å (see the line scan below the image). The STM image was taken at 300 K. The islands have an area of about 6 × 10^4 Å^2. Two phenomenon which are observed already for annealing above 400 K are responsible for the development of the larger islands at 700 K which have a total area which is smaller as that after annealing at 600 K. At first, the Ga atoms diffuse along the surface and from small islands to the larger one and larger islands are built. On the other hand a diffusion of the Ga atoms into the Ni substrate takes place which implies that the total coverage is decreasing.

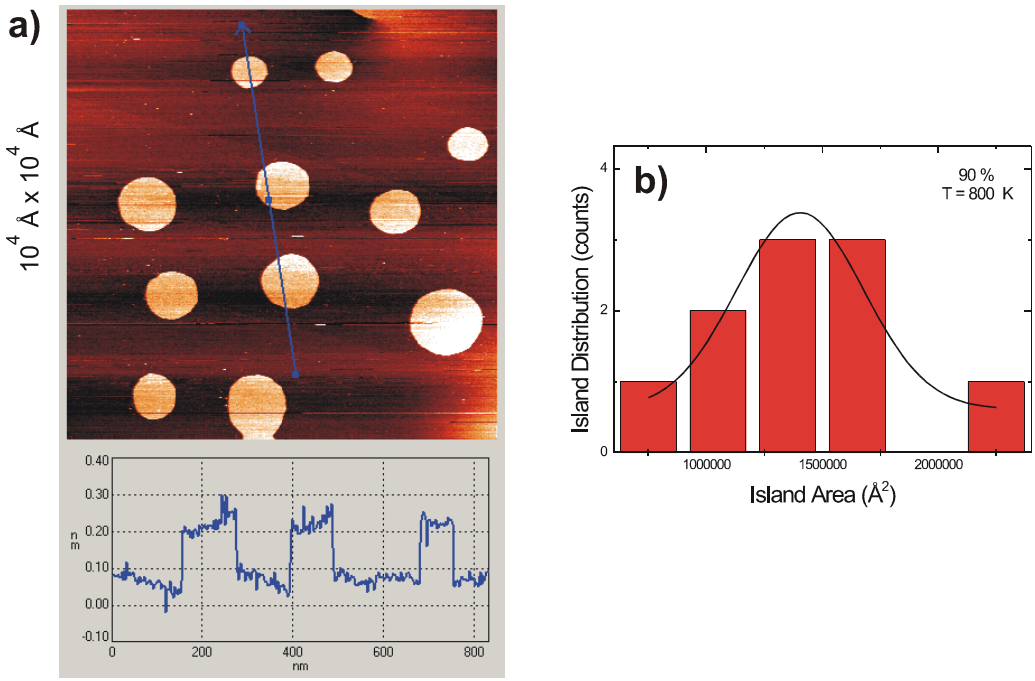

Fig. 10.13. a) STM image with a line scan of the Ni(100) surface covered initially with 90 % of Ga and annealed at 800 K (U_t = 1.0 V, I_t = 0.6 nA); b) The distribution of the islands with a maximum centered at ~ 1.5 ´ 10^6 Å^2.

These two phenomena can be observed also by annealing at 800 K. Annealing at 800 K results in very large "moons" (Fig. 10.13), which cover ~ 15 % of the surface. The area of the "moon" is of about 1.5×10^6 Å^2. A line scan of the STM image shows, that the height of the "moons" is ~ 1.2 Å. The STM image was taken at 300 K.

- **The shape of the islands**

A careful inspection of the "moons" shows that the shape of the islands is not perfect round, a rather quadratic shape is found. Such a quadratic shape of islands is expected due to the growth on a (100) surface. For T > 0 K the corners and the edges of quadratic islands are more or less rounded.

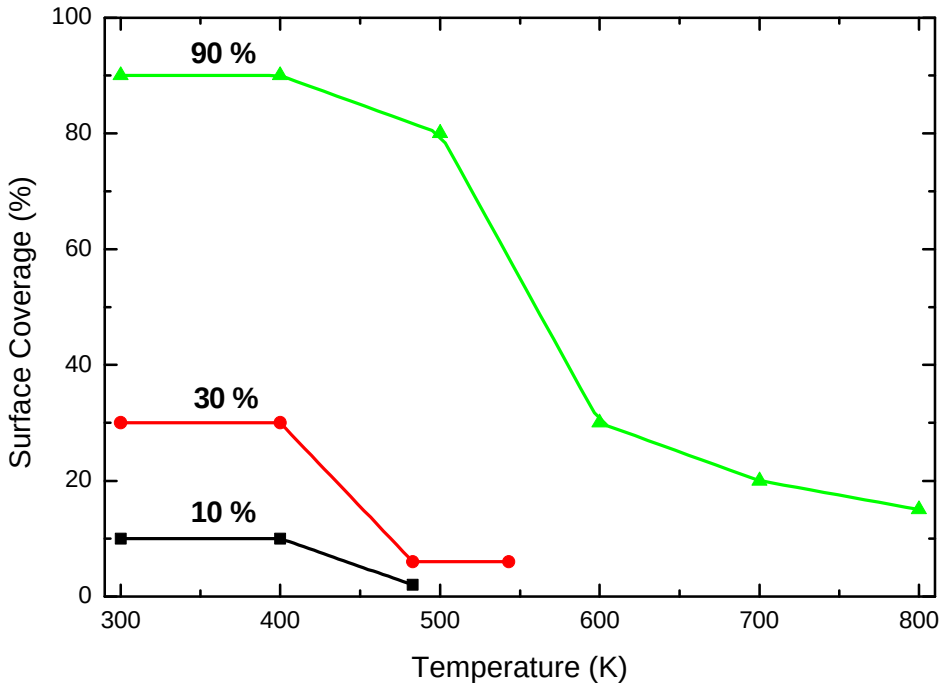

Fig. 10.14. The surface coverage of Ga as a function of the annealing temperature.

In Fig. 10.14 is plotted the surface coverage of Ga as a function of the annealing temperature. Between 300 and 400 K the amount of Ga on the surface (the area of the Ni(100) surface covered with Ga islands) remains constant, while after annealing at ~ 500 K the Ga amount decreases five times for the initial deposition of 10% and 30% of Ga. For an initial coverage of 90% of Ga the Ni(100) surface covered with Ga decreased to 80 %. Above 550 K, the evolution of the Ga islands was investigated only after the initial coverage of 90 % of Ga. Between 500 and 600 K a strong decrease of the surface coverage with Ga is observed. Between 600 and 800 K the surface coverage decreases continuously, but slowly to a final value of ~ 15 % at 800 K. Thus, up to 400 K only diffusion of Ga atoms along the surface takes place. Above 400 K the diffusion of the Ga atoms into the substrate

sets in and is accelerated when the annealing temperature exceeds 500 K. In the course of this PhD work, the diffusion phenomenon was not investigated in more details. This phenomenon will be studied in forthcoming investigations. Here, the intention was to clarify, if a well-ordered Ni-Ga surface alloy is built. Therefore, after annealing the structure of the surface was analysed by means of STM and LEED.

After annealing at 700 K, it was possible to determine with atomic resolution the structure of the surface. The STM measurement was performed at 300 K. Fig. 10.15a shows a STM image which exhibits a quadratic lattice. The quadratic lattice permits to determine the surface unit cell and from the line scan the lattice constant was determined to be 3.8 ± 0.5 Å.

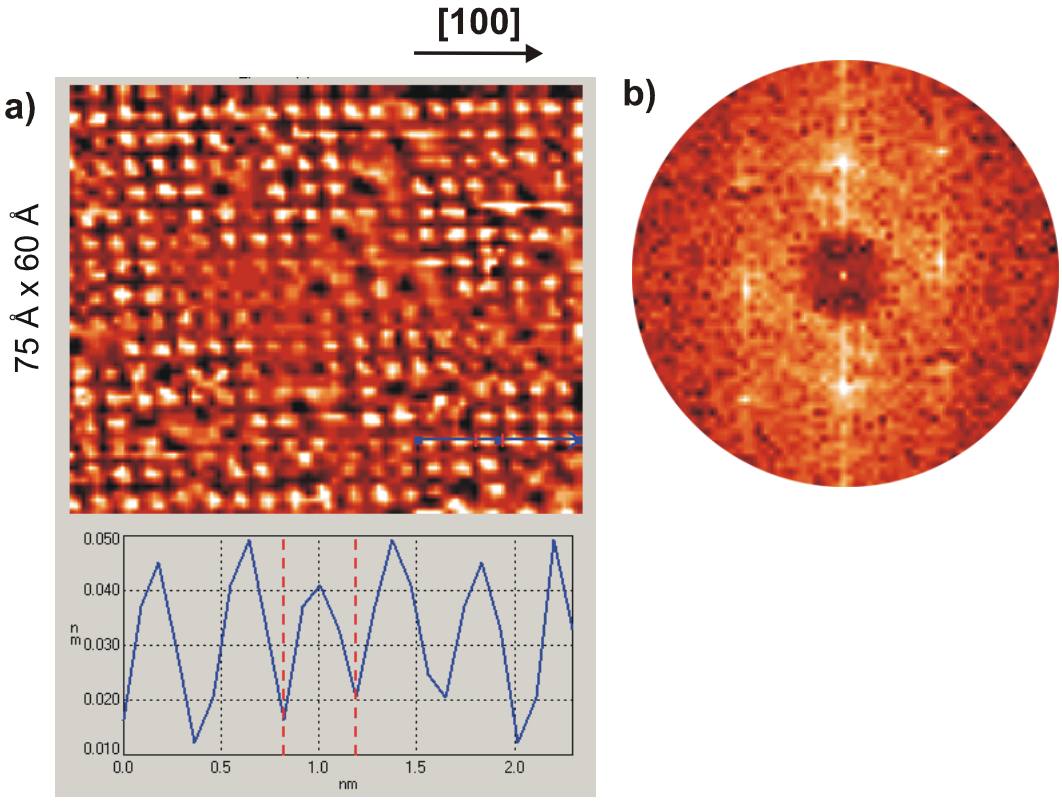

Fig. 10.15. a) STM image with a scanned area of 75 Å ´ 60 Å, taken after annealing at 700 K (U_t = 0.7 V, I_t = 0.4 nA), b) Fourier transformation of the STM image.

By performing a Fourier transformation of the real space image, an image in the reciprocal space is found and represented in Fig. 10.15b. This image shows a slightly distorted quadratic symmetry which can be considered as a confirmation of a quadratic lattice. The STM image in Fig. 10.15 was taken outside of the “moons”. Inside it was not possible to obtain a STM image with an atomic resolution.

10.2 LEED and AES Investigations

After annealing at 700 K, the surface was also investigated by LEED and AES. Fig. 10.16 shows a LEED pattern of the clean Ni(100) surface (a) and of Ga on Ni(100) after annealing at 700 K (b). The LEED pattern exhibits a c(2×2) structure with respect to the Ni(100) surface.

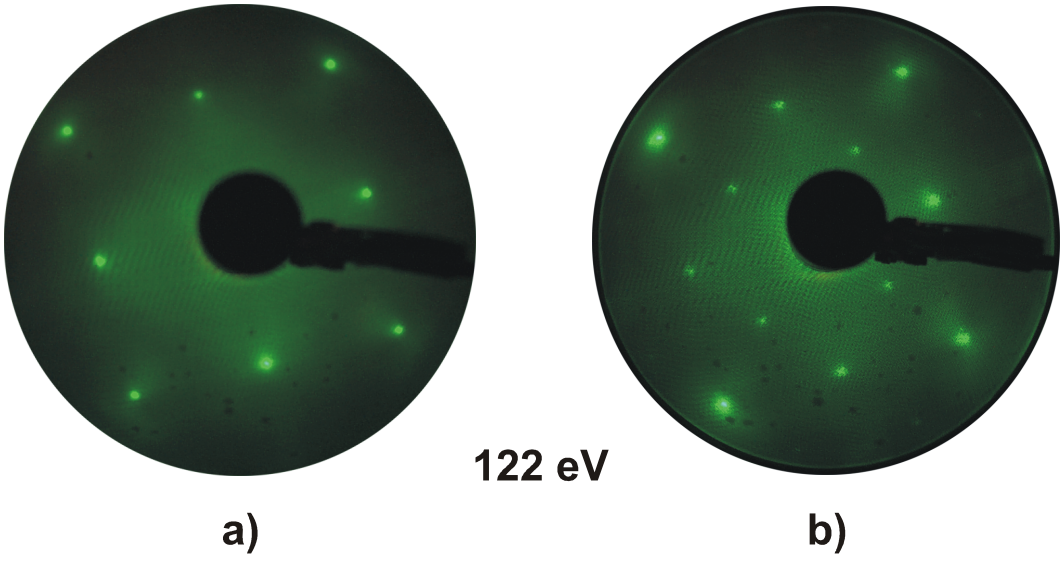

Fig. 10.16. LEED pattern of: a) the clean Ni(100) surface; b) the a´-**Ni_3Ga(100) overlayer on Ni(100) (E_P = 122 eV).**

This can be explained: a) by a reconstruction of the Ni (100) surface induced by Ga atoms which have diffused into the substrate, or b) by the formation of an ordered Ni-Ga surface alloy. The basic vector of the quadratic unit cell amounts to 3.52 Å, a value which in the limits of the experimental accuracy corresponds to the lattice constant of α´-Ni_3Ga(100) (See Table 5.3) and also to the lattice constant of Ni. From the STM and LEED data alone it is not possible to determine the surface composition and to discriminate between a reconstruction of the Ni(100) and a surface alloy. However, it is very difficult to determine the surface structure of a clean Ni(100) with atomic resolution, while STM images with atomic resolution of the surface of CoGa alloys are easily obtained [95, 190]. The same is true in this case – at a bias voltage of the tip of U_t = + 0.7 V the structure of the surface could be determined easily with atomic resolution. This is an evidence which suggests that an α´-Ni_3Ga surface alloy may be formed.

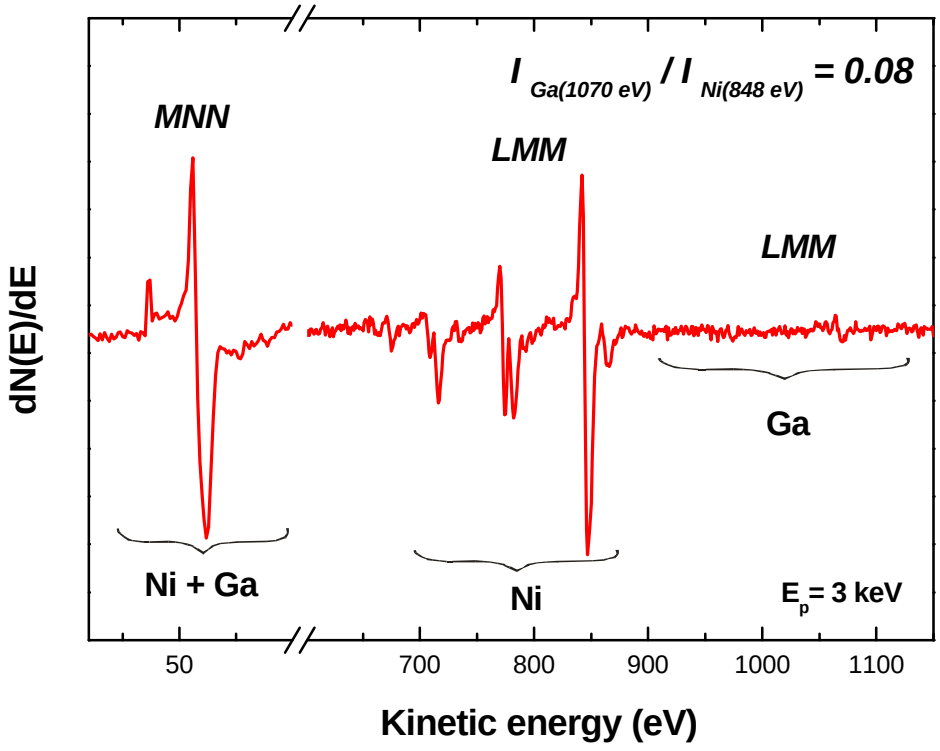

Fig. 10.17. AES spectrum of a thin layer of a´-**Ni_3Ga grown on Ni(100).**

Fig. 10.17. shows an AES spectrum after annealing at 700 K in which the LMM transitions of Ni and Ga are observed. The MNN transitions of both elements overlap. Nevertheless the presence of the Ga transitions demonstrate clearly that Ga atoms are located in the surface layers. This evidence and the ordered LEED pattern again suggest, that the formation of a α´-Ni_3Ga surface alloy is very likely. The LEED structure can be explained by the surface alloy of α´-Ni_3Ga which grows with the (100) plane parallel to the (100) surface of Ni. In this case the [100] direction of the $Ni_3Ga(100)$ surface is aligned in the [110] direction of the Ni(100) surface. The p-to-p ratio $I_{Ga(1070eV)}/I_{Ni(848eV)}$ is determined to be 0.08. This value is very low, but for a thin layer of α´-Ni_3Ga the $Ni_{(848\ eV)}$ signal results in a large part from the Ni substrate.

The formation of a thin α´-Ni_3Ga alloy on Ni(100) is similar to the growth of another Ni_3X alloys, namely Ni_3Al. After deposition of Al on Ni(100) and annealing to ~ 1150 K a thin film of Ni_3Al grows with the (100) plane parallel to the (100) surface of the Ni substrate [124, 142, 191] also with the [100] direction of the $Ni_3Ga(100)$ surface aligned in the [110] direction of the Ni(100) surface.

Summary

At 300 K, Ga grows in two-dimensional islands on the Ni(100). Annealing above 400 K leads to an enlargement of the islands by diffusion of Ga atoms on the surface of Ni. For T ≥ 400 K, a diffusion of Ga atoms into the substrate sets in. For T > 500 K, the diffusion process is strongly enhanced. Annealing to 700 – 800 K, for a Ni(100) surface which initially was covered with 90% of Ga leads to the formation of an α´-Ni_3Ga surface alloy which grows with the (100) plane parallel to the (100) surface of Ni.

As already mentioned in the introduction, the data presented here should be considered preliminary. Especially the diffusion phenomena along the surface and into the surface need to be investigated more precisely as a function of the temperature and annealing time.

Summary

The purpose of this work was the growth and characterization of thin films of Al- and Ga- oxide on Cu(111) and Ni(100), respectively. In a second step a TMR model system consisting in Au/Co/Ga_2O_3/Ni(100) was grown and the properties of the individual layers were determinated. The last part of the Thesis deals with the formation of a thin α'-Ni_3Ga surface alloy on Ni(100). In order to deposit Al(Ni), Ga, Co and Au appropriate evaporators were developed and calibrated. Ga and Ni+Al were evaporated from heated crucibles filled with pestled pieces of CoGa and NiAl, respectively.

- **The clean Cu(111) and Ni(100) surface**

The LEED pattern of the clean Cu(111) and Ni(100) surface shows a (1×1) structure. Only the Ni(100) surface was analyzed with STM. The STM images of the Ni(100) surface display flat and large terraces (400 Å) separated by monoatomic steps.

- **Al_2O_3 /Cu(111)**

At 300 K, a Ni+Al layer grows disordered on the Cu(111) surface, with an atomic ratio of Ni:Al = 1:2. Up to 10 Å, Ni+Al grows in 3D clusters on the surface afterwards the whole surface is covered with a Ni+Al overlayer. Oxidation at 300 K leads to the formation of an amorphous aluminum oxide and a trilayer system Al_2O_3/Ni+Al/Cu(111) is established. After annealing to ~ 900 K, an ultra thin well-ordered Al_2O_3 is grown, while the Ni and metallic Al atoms diffuse into the Cu(111) substrate. The complex LEED pattern reveals the formation of a γ'-Al_2O_3 phase which grows with the (111) plane parallel to the Cu(111) surface.

- **Ga_2O_3 /Ni(100)**

Ga was deposited on Ni(100) in two different procedures: first, Ga was deposited at 80 K on a Ni(100) substrate, which was covered with a c(2×2)-oxygen overlayer and secondly, Ga was deposited at 300 K directly on Ni(100).

Ga grows disordered on the O-c(2×2)/Ni(100) surface at 80 K. Oxygen adsorption at 80 K leads to the formation of an amorphous Ga oxide which seems to be non stoichiometric. After annealing and oxidation at ~ 700 K, the LEED pattern of the Ga oxide film shows a ring structure of randomly oriented and distorted hexagonal domains. By annealing at 1100 K, ultra thin layers of β-Ga_2O_3 are formed. At 1200 K, the Ga oxide is decomposed and desorbed from the surface.

At 300 K and low nominal deposition, Ga grows as two-dimensional islands on Ni(100). Oxidation at 300 K leads to the growth of an amorphous Ga oxide. Annealing up to 700 K leads to the formation of a well-ordered thin film of γ′-Ga_2O_3, The LEED pattern of Ga_2O_3/Ni(100) shows a 12-fold ring structure which corresponds two hexagonal domains, which are rotated by 90° with respect to each other. During annealing between 300 and 800 K coalescence of the Ga_2O_3 islands takes place and the amorphous Ga_2O_3 transforms into the well-ordered γ′-Ga_2O_3 phase.

- **Au/Co/Ga_2O_3 /Ni(100)**

A TMR model system was grown on a ferromagnetic single crystalline substrate (Ni(100)). First, a 7 Å thick was grown on Ni(100). Co was deposited at 300 K on the Ga_2O_3 layer. It was found, that a 25 Å thick Co layer grows ordered with the (100) plane of the fcc Co parallel to the Ni(100) surface. The Co layer covers completely the Ga_2O_3 surface and screens perfectly the dipoles of the Ga_2O_3 layer. After annealing at 700 K, the Co(100) surface is reconstructed and shows a c(2×2) structure.

At 300 K, Au grows ordered on the c(2×2)-Co(100) surface. The LEED pattern shows a twelvefold ring structure which is explained by two domains with hexagonal structure, which are rotated by 90° with respect to each other.

- a´-**Ni_3Ga /Ni(100)**

At 300 K, Ga grows in two-dimensional islands on the Ni(100). Annealing above 400 K leads to an enlargement of the islands by diffusion of Ga atoms on the surface of Ni. For T ≥ 400 K, a diffusion of Ga atoms into the substrate sets in. For T > 500 K, the diffusion process is strongly enhanced. Annealing to 700 – 800 K, of a Ni(100) surface which initially was covered with 90% of Ga leads to the formation of an α´-Ni_3Ga surface alloy which grows with the (100) plane parallel to the (100) surface of Ni.

References

[1] M. Henzler and W. Göpel, Oberflächenphysik des Festkörpers. Stuttgart: Teubner Studienbücher Physik, 1994.

[2] A. Atkinson, Rev. Mod. Phys. 57 (1985) 437.

[3] V. E. Heinrich and P. A. Cox, Cambridge University Press (1994).

[4] S. Nakamura, M. Senoh, S. Nagahama, N. Iwasa, T. Yamada, H. Kiyoku, and Y. Sugimoto, Appl. Phys. Lett. 68 (1996) 2105.

[5] D. Walker, A. Saxler, P. Kung, X. Zhang, M. Hamilton, J. Diaz, and M. Razeghi, Appl. Phys. Lett. 72 (1998) 3303.

[6] A. Sandell, J. Libuda, M. Bäumer, and H.-J. Freund, Surf. Sci. 346 (1996) 108.

[7] D. L. Cocke, E. D. Johnson, and R. P. Merrill, Catal. Rev. Sci. Eng. 26 (1984) 163.

[8] F. Winkelmann, S. Wohlrab, J. Libuda, M. Bäumer, D. Cappus, M. Menges, K. Al-shamery, H. Kuhlenboeck, and H.-J. Freund, Surf. Sci. 307-309 (1994) 1148.

[9] B. Heinrich, K. B. Urquhart, A. S. Arrott, J. F. Cochran, K. Myrtle, and S. T. Purcell, Phys. Rev. Lett. 59 (1987) 1756.

[10] B. T. Jonker, K.-H. Walker, E. Kisker, G. A. Prinz, and C. Carbone, Phys. Rev. Lett. 57 (1986) 142.

[11] C. Liu, E. R. Moog, and S. D. Bader, Phys. Rev. Lett. 60 (1988) 2422.

[12] T. Miyazaki and N. Tezuka, J. Magn. Magn. Mater. 139 (1995) L231.

[13] J. S. Moodera, L. R. Kinder, T. M. Wong, and R. Meservey, Phys. Rev. Lett. 74 (1995) 3273.

[14] J. S. Moodera and G. Mathon, J. Magn. Magn. Mater. 200 (1999) 248.

[15] K. Inomata, J. Magn. Soc. Jpn. 23 (1999) 1826.

[16] M. Julliere, Phys. Lett. 54 (1975) 225.

[17] Y. Suezawa and Y. Gondo, presented at International Symposium Physics of Magnetic Materia, Sendai, MAG-18, 1987.

[18] W. Wulfhekel, M. Klaua, D. Ullmann, F. Zavaliche, and J. Kirschner, Appl. Phis. Lett. 78 (2001) 509.

[19] Y. Suezawa, F. Takahashi, and Y. Gondo, Jpn. J. Appl. Phys. Part 2: 31 (1992) L1415.

[20] H. Brückl, J. Schmalhorst, and G. Reiss, Appl. Phis. Lett. 78 (2001) 1113.

[21] D. J. Keavney, S. Park, and C. M. Falko, Appl. Phis. Lett. 78 (2001) 234.

[22] S. Cardoso, P. P. Freitas, C. d. Jesus, and J. C. Soares, J. Appl. Phys. 87 (2000) 6058.

[23] J. S. Moodera, L. R. Kinder, J. Nowak, P. LeClair, and R. Meservey, Appl. Phys. Lett. 69 (1996) 708.

[24] J. S. Moodera, L. R. Kinder, T. M. Wong, and R. Meservey, Phys. Rev. Lett. 75 (1998) 3273.

[25] Z. Li, C. d. Groot, and J. H. Moodera, Appl. Phys. Lett. 77 (2000) 3630.

[26] M. Fleischer and H. Meixner, Sensors Actuators B 5 (1992) 115.

[27] M. Fleischer and H. Meixner, Sensors Actuators B 6 (1992) 257.

[28] A. Callegari, P. D. Hoh, D. A. Buchanan, and D. Lacey, Appl. Phys. Lett. 54 (1989) 332.

[29] M. Passlack, N. E. J. Hunt, E. F. Schubert, G. J. Zydzik, M. Hong, J. P. Mannaerts, R. L. Opila, and R. L. Fischer, Appl. Phys. Lett. 64 (1994) 2715.

[30] J. H. Westbrook and R. L. Fleischer, Intermetallic Compounds: Principles and Practice. New York: Wiley, 1995.

[31] B. I. Min, A. J. Freeman, and H. J. F. Jansen, Phys. Rev. B 37 (1988) 6757.

[32] N. R. Bernhoeft, G. G. Lonzarich, P. W. Mitchell, and D. M. Paul, Phys. Rev. Lett. 62 (1989) 657.

[33] G. H. Vurens, M. Salmeron, and G. A. Somorjai, Prog. Surf. Sci. 2 (1990) 333.

[34] S. C. Street, C. Xu, and D. W. Goodman, Annu. Rev. Phys. Chem. 48 (1997) 43.

[35] N. W. Robinson, The physical principles of Ultra-high Vacuum Systems and Equipment: Chapman & Hall, 1968.

[36] T. A. Delchar, Vacuum Physics and Techniques: Chapman & Hall, 1993.

[37] D. P. Woodruff and T. A. Delchar, Modern Techniques of Surface Science. Cambridge, 1994.

[38] F. M. Propst and T. C. Piper, J. Vac. Sci. Technol. 4 (1967) 53.

[39] H. Ibach, Phys. Rev. Lett. 27 (1971) 253.

[40] H. Ibach, J. Vac. Sci. Technol. 9 (1972) 713.

[41] H. Ibach and D. L. Mills, Electron Energy Loss Spectroscopy and Surface Vibrations: Academic, New York, 1982.

[42] R. F. Willis, A. A. Lucas, and G. D. Mahan, The chemical physics of solid surfaces and heterogeneous catalysis edited by D.A. King and D.P. Woodruff, 2 (1983) 61.

[43] K. L. Kliewer and R. Fuchs, Phys. Rev. 144 (1966) 495.

[44] K. L. Kliewer and R. Fuchs, Adv. Chem. Phys. 27 (1974) 355.

[45] H. Ibach, Electron Energy Loss Spectrometers: Springer Series in Surface Science, Springer, Berlin, 1990.

[46] H. Lüth, Surfaces and Interfaces of Solid Materials, Third ed. Springer Verlag, Berlin, Heidelberg, 1998.

[47] H. Ibach, Interaction of Atoms and Molecules with Solid Surface: Plenum Press, New York, 1990.

[48] R. Fleming, http://www.cea.com/cai/augtheo/caiatheo.htm.

[49] G. Somorjai, Chemistry in two dimension: Surface, 1 ed. Ithaca and London: Cornell University Press, 1981.

[50] M. P. Seah and W. A. Dench, Surf. Interface Anal. 1 (1979) 2-10.

[51] J. B. Hudson, Surface Science: Stoneham, MA: Butterworth-Heinemann, 1992.

[52] J. Tersoff and N. D. Lang, Theory of Scanning Tunneling Microscopy, vol. 27. Boston, MA: Academic Press, 1993.

[53] G. Binning, H. Rohrer, C. Gerber, and E. Weibel, Phys. Rev. Lett. 49 (1982) 57.

[54] G. Binning and H. Rohrer, Phys. Acta 55 (1982) 726.

[55] C. Bai, Scanning tunneling microscopy and its applications, vol. 32. Berlin: Springer Verlag, 1995.

[56] R. H. Fowler and L. Nordheim, Proc. R. Soc. London A 119 (1928) 173.

[57] J. M. Daughton, J. Appl. Phys. 81 (1997) 3758.

[58] S. S. P. Parkin, K. P. Roche, M. G. Samant, P. M. Rice, R. B. Beyers, R. E. Scheurlein, E. J. O'Sullivan, S. L. Brown, J. Bucchigano, D. W. Abraham, Y. L. M. Rooks, P. L. Trouilloud, R. A. Wanner, and W. J. Gallagher, J. Appl. Phys. 85 (1999) 5828.

[59] S. Tehrani, J. M. Slaughter, E. Chen, M. Durlam, J. Shi, and M. DeHerrera, IEEE Trans. Magn. 35 (1999) 2814.

[60] R. E. Scheuerlein, Proceedings of the International Non-Volatile Memory Technology Conference, New York (1998) 47.

[61] H. Boeve, J. Das, C. Bruynseraede, J. D. Boeck, and G. Borghs, J. Appl. Phys. 85 (1999) 4779.

[62] R. C. Sousa, P. P. Freitas, V. Chu, and J. P. Conde, Appl. Phis. Lett. 74 (1999) 3893.

[63] J. M. Daughton, Thin Solid Films 216 (1992) 162.

[64] G. Binasch, P. Grünberg, F. Saurenbach, and W. Zinn, Phys. Rev. B 39 (1989) 4828.

[65] M. N. Baibich, J. M. Broto, A. Fert, F. N. V. Dau, and F. Petroff, Phys. Rev. Lett. 61 (1988) 2472.

[66] C. H. Tsang, R. E. F. Jr., T. Lin, D. E. Heim, B. A. Gurney, and M. L. Williams, IBM J. of Recearch and Developement 42 (1998) 103.

[67] S. Mengel, Technologiefrüherkennung, Technologieanalyse Magnetismus, Bd. 2, XMR-Technologien (VDI Technologiezentrum Physikalische Technologien, Düsseldorf), 1997.

[68] J. G. Simmons, J. Appl. Phys. 3 (1963) 1793.

[69] R. Schelten, in 30. IFF-Ferienschule: Magnetische Schichtsysteme, Forschungszentrum Jülich GmbH, 1999.

[70] F. Montaigne, PhD thesis, in *University Paris Orsay*, 1999.

[71] E. Bauer, Z. Kristallogr. 110 (1958) 372.

[72] E. Bauer and H. Poppa, Thin Solid Films 12 (1972) 167.

[73] R. Kern, G. L. Lay, and J. J. Metois, Current Topics in Material Science, vol. 3. Amsterdam: North-Holland, 1979.

[74] D. Chatain, I. Rivollet, and N. Eustathopoulos, J. Chim. Phys. 83 (1986) 561.

[75] L. Z. Mezey and J. Giber, Jpn. J. Appl. Phys. 21 (1982) 1569.

[76] C. T. Campbell, Surf. Sci. Rep. 27 (1997) 1.

[77] J. Nakamura, J. A. Rodriguez, and C. T. Campbell, J. Condens. Matter 1 (1989) SB149.

[78] D. R. Lide, Handbook of Chemistry and Physics. Boca Raton, FL: CRC Press, 1994.

[79] H. Z. Cummins, Fundamental Problems in Statistical Mechanics VII: North-Holand, 1990.

[80] G. Ehrlich and F. Hudda, J. Chem. Phys. 44 (1966) 1039.

[81] R. L. Schwoebel and E. J. Shipsey, J. Appl. Phys. 37 (1966) 3682.

[82] J. Krug, Physica A 313 (2002) 47.

[83] P. Feibelman, Phys. Rev. Lett. 81 (1998) 168.

[84] R. Franchy, Surf. Sci. Rep. 38 (2000) 195.

[85] H.-J. Freund, H. Kuhlenbeck, and V. Staemmler, Rep. Prog. Phys 59 (1996) 283.

[86] P. Gassmann, R. Franchy, and H. Ibach, Surf. Sci. 319 (1994) 95.

[87] C. Becker, J. Kandler, H. Raaf, R. Linke, T. Pelster, M. Draeger, M. Tanemura, and K. Wandelt, J. Vac. Sci. Technol. A 16 (1998) 1000.

[88] U. Bardi, A. Atrei, and G. Rovida, Surf. Sci. 268 (1992) 87.

[89] R. Franchy, J. Masuch, and P. Gassmann, Appl. Surf. Sci. 93 (1996) 317.

[90] R. M. Jaeger, H. Kuhlenbeck, H.-J. Freund, M. Wuttig, W. Hoffmann, R. Franchy, and H. Ibach, Surf. Sci. 259 (1991) 235.

[91] M. Klimenkov, S. Nepijko, H. Kuhlenbeck, and H.-J. Freund, Surf. Sci. 385 (1997) 66.

[92] P. Gassmann, R. Franchy, and H. Ibach, J. Electron Spectrosc. Relat. Phenom. 64/65 (1993) 315.

[93] A. März and R. Franchy, Surf. Sci. 466 (2000) 54.

[94] G. Schmitz, P. Gasmann, and R. Franchy, J. Appl. Phys. 83 (1998) 2533.

[95] G. Schmitz, P. Gasmann, and R. Franchy, Surf. Sci. 397 (1998) 339.

[96] F. P. Fehlner, Low-Temperature Oxidation. Wiley, New York, 1986.

[97] N. F. Mott, Trans. Faraday Soc. 43 (1947) L1705.

[98] C. Wagner, Z. Physik. Chem. B 21 (1933) 25.

[99] N. Cabrera and N. F. Mott, Rep. Prog. Phys 12 (1948-49) 163.

[100] H. Ibach, Electron Energy Loss Spectrometers - The Technology of High Performance: Springer, Berlin, 1991.

[101] Landoldt-Börnstein: Structure Data of Elements and Intermetallic Phases, vol. New Series Bd. III/6: Springer Verlag, 1971.

[102] American Institut of Physics Handbook, Third ed: McGraw-Hill Book Company, 1971.

[103] R. W. G. Wyckoff, Crystal Structure, vol. I, 2nd ed: Wiley, New York, 1962.

[104] E. Preuss, B. Krahl-Urban, and R. Butz, Laue Atlas; Plotted Laue Back-Reflection Patterns of the Elements, the Compounds RX and RX2. Düsseldorf: Bertelsmann Universitätsverlag, 1974.

[105] C. Greville, Encyclopedia Britanica. Chicago, 1910.

[106] B. C. Lippens and S. S. Steggerda, Phisical and Chemical Aspects of Adsorbents and Catalysts. New York: Academic Press, 1970.

[107] K. Wefers and G. M. Bell, Oxides and Hydroxides of Aluminum, Nr. 19 in ALCOA Technical Paper. St. Louis: Aluminum Company of America, 1972.

[108] P. Gassmann, J. Boysen, G. Schmitz, F. Bartolucci, and R. Franchy, Solid State Commun. 97 (1996) 1.

[109] A. I. Taub and R. L. Fleischer, Science 243 (1989) 616.

[110] W. Pies and A. Weiss, in: V.K.-H. Hellwege, A.M. Hellwege (Eds.), Landolt-Börnstein "Zahlenwerte und Funktionen aus Naturwissenschaften und Technik", vol. III/7b: Springer, Berlin, 1975.

[111] R. P. Elliott, Constitution of binary alloys, vol. XXXII,877 S. New York: MacGraw Hill, 1965.

[112] E. Hellner, Z. Metallkunde 41 (1950) 480.

[113] W. B. Pearson, Nature 173 (1954) 364.

[114] W. B. Pearson, Can. J. Phys. 35 (1957) 1228.

[115] W. Michel, Ann. Physik 11 (1963) 321.

[116] M. Ellner, J. Less-Common Met. 19 (1969) 294.

[117] P. Feschotte and P. Eggimann, J. Less-Common Met. 63 (1979) 15.

[118] T. B. Massalski, Binary Alloy Phase Diagrams, 2 ed: William W. Scott jr. ASM International, 1992.

[119] L. Holland, Vacuum deposition of Thin Films. London: Chapman and Hall, 1961.

[120] R. Glang, Handbook of Thin Film Technology. New York: McGraw-Hill, 1970.

[121] R. F. Bunshah, Deposition Technologies for Thin Films and Coatings. Park Ridge, NJ: Noyes, 1982.

[122] A.-D. Kovacs, PhD Thesis, In preparation.

[123] R. Franchy, M. Wuttig, and H. Ibach, Surf. Sci. 189/190 (1987) 438.

[124] A. Wehner, Y. Jeliazova, and R. Franchy, Submited to Surf. Sci.

[125] W. J. Wytenburg and R. M. Lambert, J. Vac. Sci. Techn. A 10 (1992) 3597.

[126] D. V. Rigney, Vacuum Coating, vol. 5, Ninth ed: Metals-Park,OH : American Society for Metals, 1985.

[127] Y. Wu, E. Garfunkel, and T. E. Madey, Surf. Sci. 365 (1996) 337.

[128] Y. Wu, H.-S. Tao, E. Garfunkel, and T. E. Madey, Surf. Sci. 336 (1995) 123.

[129] R.-P. Blum and H. Niehus, Appl. Phys. A 66 (1998) S529.

[130] M. Vermeersch, F. Malengreau, R. Sporken, and R. Caudano, Surf. Sci. 323 (1995) 175.

[131] S. G. Addepalli, B. Ekstrom, N. P. Magtoto, J.-S. Lin, and J. A. Kelber, Surf. Sci. 442 (1999) 385.

[132] R. Jansen, B. Davis, C. T. Tanaka, and J. S. Moodera, Surf. Sci. 463 (2000) 109-114.

[133] I. Costina and R. Franchy, Appl. Phys. Lett. 78 (2001) 4139.

[134] P. J. Chen, M. L. Colaianni, and J. T. Yates, Phys. Rev. B 41 (1990) 8025.

[135] M. B. Lee, J.-H. Lee, B. G. Frederick, and N. V. Richardson, Surf. Sci. 448 (2000) L207-L212.

[136] D. R. Jennison, C. Verdozzi, P. A. Schultz, and M. P. Sears, Phys. Rev. B 59 (1999) R15605.

[137] J. L. Erskine and R. L. Strong, Phys. Rev. B 25 (1982) 5547.

[138] R. Franchy, G. Schmitz, P. Gassmann, and F. Bartolucci, Appl. Phys. A 65 (1997) 551.

[139] Q. Guo, D. Y. Kim, S. C. Street, and D. W. Goodman, J. Vac. Sci. Technol. A 17 (1999) 1887.

[140] J. Toofan and P. R. Watson, Surf. Sci. 401 (1998) 162.

[141] C. Palacio and A. Arranz, J. Phys. Chem. B 104 (2000) 9647.

[142] D. J. O'Connor, M. Draeger, A. M. Molenbroek, and Y. G. Shen, Surf. Sci. 357-358 (1996) 202.

[143] A. Rosenhahn, J. Schneider, C. Becker, and K. Wandelt, Appl. Surf. Sci. 142 (1999) 169.

[144] R.-P. Blum, D. Ahlbehrendt, and H. Niehus, Surf. Sci. 396 (1998) 176.

[145] A. Rosenhahn, J. Schneider, J. Kandler, C. Becker, and K. Wandelt, Surf. Sci. 433-435 (1999) 705.

[146] T. Bertrams, A. Brodde, and H. Neddermeyer, J. Vac. Sci. Technol. B 12 (1994) 2122.

[147] P. J. Chen and D. W. Goodman, Surf. Sci. 312 (1994) L767.

[148] S. Tanuma, C. J. Powell, and D. R. Penn, Surf. Interface Anal. 17 (1991) 927.

[149] C. J. Powell, A. Jablonski, I. S. Tilinin, S. Tanuma, and D. R. Penn, J. Electron Spectrosc. 98-99 (1999) 1-15.

[150] I. Costina, PhD Thesis.: Heinrich-Heine-Universität Düsseldorf, 2002.

[151] R. Franchy, S. K. So, and P. Gassmann, Surf. Rev. Lett. 3 (1996) 1909.

[152] H. Isern and G. R. Castro, Surf. Sci. 211/212 (1989) 865.

[153] D. R. Jennison and A. Bogicevic, Surf. Sci. 464 (2000) 108.

[154] C. Huang, A. Ludviksson, and R. M. Martin, Surf. Sci. 265 (1992) 314.

[155] P. Chen, R. Zhang, X. F. Xu, Y. G. Zhou, Z. Z. Chen, S. Y. Xie, W. P. Li, and Y. D. Zheng, Appl. Phys. A 71 (2000) 191.

[156] R. Franchy, M. Eumann, and G. Schmitz, Surf. Sci. 470 (2001) 337.

[157] J. Åhman, G. Svensson, and J. Albertson, Acta Crystallogr., Sect. C 52 (1996) 1336.

[158] S. Geller, J. Chem. Phys. 33 (1960) 676.

[159] L. Bosio, J. Chem. Phys. 68 (1978) 122.

[160] X. G. Gong, G. L. Chiarotti, M. Parrinello, and E. Tosatti, Phys. Rev. B 43 (1991) 14277.

[161] K. F. MacDonald, V. A. Fedotov, S. Pochon, K. J. Ross, G. S. Stereus, N. I. Zheludev, W. S. Brocklesby, and V. I. Emelyanov, Appl. Phys. Lett. 80 (2002) 1643.

[162] R. Franchy, M. Wuttig, and H. Ibach, Surf. Sci. 203 (1988) 489.

[163] W. Reichardt, R. M. Nicklow, G. Dolling, and H. G. Smith, Bull. Am. Phys. Soc. 14 (1969) 378.

[164] Landoldt-Börnstein: Numerical Data and Functional Relationships in Science and Technology, vol. New Series Bd. III/13a: Springer Verlag, 1981.

[165] G. Schmitz, PhD Thesis. Univesität Düsseldorf, 1999.

[166] R. C. Weart and D. R. Lide, Handbook of Chemistry and Physics, 70th ed. Boca Raton, FL: CRC Press, 1989-1990.

[167] P. Lambin, J.-P. Vigneron, and A. A. Lucas, Phys. Rev. B 32 (1985) 8203.

[168] P. Lambin, J.-P. Vigneron, and A. A. Lucas, Comput. Phys. Commun. 60 (1990) 351.

[169] N. T. McDevitt, Spectrochem. Acta 20 (1964) 799.

[170] K. P. Sinha and A. P. B. Sinha, J. Phys. Chem. 61 (1957) 758.

[171] H. D. Megaw, Crystal Structures: A Working Approach. Philadelphia: Sanders, 1973.

[172] Gmelius Handbuch der anorganische Chemie, eigth ed. Weinheim: Verlag Chemie, 1953.

[173] D. A. Walko, I. K. Robinson, C. Grütter, and J. H. Bilgram, Phys. Rev. Lett. 81 (1998) 626.

[174] O. Züger and U. Dürig, Phys. Rev. B 46 (1992) 7319.

[175] G. Schmitz, M. Eumann, D. Stapel, and R. Franchy, Surf. Sci. 427-428 (1999) 91.

[176] F. M. Pan, C. Pflitsch, R. David, L. Verheij, and R. Franchy, Surf. Sci. 479 (2001) 191.

[177] Y. Jeliazova and R. Franchy, Surf. Sci. 502-503 (2002) 51.

[178] J. S. Moodera and L. R. Kinder, J. Appl. Phys. 79 (1996) 4724.

[179] I. Giaever, Phys. Rev. Lett. 5 (1960) 147.

[180] C. B. Duke, Tunneling in Solids. New York: Solid State Physics: Supplement 10, Academic, 1969.

[181] L. Solymar, Superconductive Tunneling and Applications. New York: Wiley-Interscience, 1972.

[182] E. L. Wolf, Principles of Tunneling Spectroscopy. Oxford: Clarendon, 1985.

[183] R. Meservey and P. M. Tedrow, Phys. Rep. 238 (1994) 173.

[184] C. E. Platt, B. Dieny, and A. E. Berkowitz, Appl. Phys. Lett. 69 (1996) 2291.

[185] Y. Lu, X. W. Li, G. Q. Gong, G. Xiao, A. Gupta, P. LeCoeur, J. Z. Sun, Y. Y. Wang, and V. P. David, Phys. Rev. B 54 (1996) R8357.

[186] J. Z. Sun, W. J. Gallagher, P. R. Duncombe, L. Krusin-Elbaum, R. A. Altman, A. Gupta, Y. Lu, G. Q. Gong, and G. Xiao, Appl. Phys. Lett. 69 (1996) 3266.

[187] M. Haßel and H.-J. Freund, Surf. Sci. 325 (1995) 163.

[188] M. Hassel, H. Kuhlenbeck, H.-j. Freund, S. Shi, A. Freitag, V. Staemmler, S. Lütkehoff, and M. Neumann, Chem. Phys. Lett. 240 (1995) 205.

[189] M. Bäumer and H.-J. Freund, Prog. Surf. Sci. 61 (1999) 127.

[190] F. M. Pan, C. Pflitsch, R. David, L. Verheij, and R. Franchy, Phys. Rev. B 63 (2001) 125414.

[191] S. H. Lu, D. Tian, Z. Q. Wang, Y. S. Li, and F. Jona, Solid State Commun. 67 (1988) 325.

Acknowledgments

Благодаря!

I would like to be able to find the most beautiful words in order to express my gratitude to my PhD tutor Prof. Dr. René Franchy.
Mr. Franchy, thank you for giving me the chance to see the fascinating world of the surface science through your eyes and through the eyes of the experimental methods, available in your group. I am grateful to you because during my stay in Jülich, you were not only a wonderful supervisor, but also a lovely person, whom I could ask any time for help, a kind of help which one needs when you are thousands of kilometers far away from your parents. Thank you, very much!

I would like to express my gratitude to Prof. Dr. Harald Ibach for giving me the possibility to make this PhD Thesis in the Institut für Schichten und Grenzflächen (ISG 3).

I am very grateful to Prof. Dr. Schierbaum for accepting to be the co-referee of my thesis.

My special thanks to Prof. Dr. Stavrev for facilitating my coming to Germany and readiness for help.
Моите специални благодарности към Проф. Д-р Ставрев, че улесни идването ми в Германия, както и за готовността му винаги да ми помогне.

I would like to thank to Dr. Rudolf David and Dr. Laurens Verheij for many helpful discussions and specially Dr. Rudolf David for the pleasant co-work and the many technical tips.

I address to Mrs. Christa Elsaesser my gratitude for welcoming me in her laboratory and patiently instructions.

I also thank to Mr. Udo Linke for the high-quality and fast preparation of the crystalline samples and for useful discussions.

Many thanks to Mr. Dieter Strobl and his team for the precisely and quickly done work.

Thank you also to Mr. Norbert Tiefes and to Mr. Rainer Rausch and their co-workers for the given hand.

Thank you to all the former and present fellows from the Magnetoelectronics group and from the whole ISG 3 as well (particularly to the “Mittagsrunde”), for the pleasant working atmosphere and for the help along my learning German.

Many thanks to our “Spielrunde” for the amicability and pleasant evenings in the small Jülich.

Also my thankfulness to the friendly members of BGM in Jülich.

My special thanks for their countenance to my old friends, which are always standing by me independently of the distance, to Desi for her help and critical reading of my thesis.
Моите специални благодарности към старите ми приятели за моралната подкрепа и затова, че са винаги с мен, независимо от разстоянието, на Деси за помощта и критичното прочитане на дисертациата ми.

On the end, but not on the last place, I would like to say: “My dear mom and dad, my darling sister, my grand- ma and pa (until he was between us), I thank you so

much for your understanding, supporting, patience and for your confidence in me!”

На края, но не на последно място, бих искала да кажа: ”Скъпи мамо и татко, мила сестричке, бабо и дядо (докато беше още между нас), безкрайна е моята благодарност за разбирането, подкрепата, търпението и за вярата ви в мен!”

Sincerely yours

Yanka

Искрено ваша

Янка